Title
Fabricating Germanium Interfaces for Battery Applications

Author
Serino, Andrew Clark

Publication Date
2017

UNIVERSITY OF CALIFORNIA

Los Angeles

Fabricating Germanium Interfaces for Battery Applications

A dissertation submitted in partial satisfaction of the
requirements for the degree Doctor of Philosophy
in Materials Science and Engineering

by

Andrew Clark Serino

2017

ABSTRACT OF THE DISSERTATION

Fabricating Germanium Interfaces for Battery Applications

by

Andrew Clark Serino

Doctor of Philosophy in Materials Science and Engineering

University of California, Los Angeles, 2017

Professor Paul S. Weiss, Co-Chair

Professor Bruce S. Dunn, Co-Chair

The experimental results presented herein detail the importance of material surfaces in device performance. We have demonstrated this importance by furthering and applying our understanding of germanium surfaces to a number of real-world applications. Pure and stable dispersions of germanane, an “all-surface” form of germanium, were created through solid-state synthesis followed by ultrasonication and centrifugation. These dispersions were used to fabricate germanane-based, high-performance, Li-ion anodes with capacities of ~1100 mA-h/g, capacity retention over 100 cycles, and Coulombic efficiency of 99%. Additionally, carborane monolayers were self-assembled on Ge(100) and Ge(111) surfaces through carboxylic acid tethers, and found to be capable of tuning the surface work function by ~0.4 eV without significantly affecting surface wettability. These capabilities are important for increasing device efficiency while minimizing complications associated with processing. Lastly, we introduce the

concept of the molecular battery, a possible design using a layer-by-layer deposition approach, and our steps toward its realization. In this pursuit, we explored the assembly of metal-organic coordination of carborane-based linkers, as well as the capabilities of a film of benzene-based linkers (<50 nm) as a Li-ion battery separator using a Ge anode as a tool for analyzing performance.

This dissertation of Andrew Clark Serino is approved.

Richard B. Kaner

Alexander M. Spokoyny

Bruce S. Dunn, Committee Co-Chair

Paul S. Weiss, Committee Co-Chair

University of California, Los Angeles

2017

For my family

TABLE OF CONTENTS

LIST OF FIGURES

LIST OF TABLES

LIST OF ABBREVIATIONS AND SYMBOLS

AFM	atomic force microscopy
BBC	1,3,5-Tris(4'-carboxy[1,1'-biphenyl]-4-yl)benzene
BTB	1,3,5-Tris(4- carboxyphenyl) benzene
BTC	1,3,5-benzenetricarboxylate
C10	1-decanethiol
C12	dodecanethiol
C8DT	1,8-octanedithiol
CB	carbon black
CF	carbon fiber
CV	cyclic voltammetry
DEC	diethyl carbonate
DI	deionized
EC	ethylene carbonate
EIS	electrochemical impedance spectroscopy
FEC	fluoroethylene carbonate
FWHM	full-width-half-max
GeH	germanane

HOMO	highest occupied molecular orbital
IP	in-plane
IPA	isopropanol
JCPDS	Joint Committee on Powder Diffraction Standards
LBL	layer-by-layer
LUMO	lowest occupied molecular orbital
M9	9-*m*-carborane
M9OH	9-OH-*m*-carborane
M9SH	9-SH-*m*-carborane
MHDA	16-mercaptohexadecanoic acid
MOF	metal organic framework
NMP	1-methyl-2-pyrrolidinone
O1COOH	1-COOH-*o*-carborane
O9	9-*o*-carborane
O9COOH	9-COOH-*o*-carborane
O9SH	9-SH-*o*-carborane
OCVD	organic chemical vapor deposition
OP	out-of-plane

PC	propylene carbonate
PCB	1-SH, 12-COOH *para*-carborane
PCB/B	PCB in benzene
PCB/E	PCB in ethanol
PET	polyethylene terephthalate
PPA	polyacrylic acid
SAMs	Self-assembled monolayers
SEI	solid-electrolyte-interphase
SurMOF	surface-anchored metal-organic framework
WF	work function
XPS	X-ray photoelectron spectroscopy
XRD	X-ray diffraction
Å	Ångströms
A	area
C	concentration of ions
cm	centimeter
E	electrode potential
E^o	standard potential

e	elementary charge
ED	energy density
ε	material permittivity
ε_o	permittivity of free space
F	Faraday’s constant
G	Gibbs Free Energy
K	Kelvin
k	Boltzmann constant
k_s	extinction coefficient
κ^{-1}	Debye length
M_m	molar mass
M	molar
m	meter
ml	milliliter
mm	millimeter
µm	micron
µS	microsiemens
N	number of electrons involved in the electrochemical reaction

nm	nanometer
n_s	index of refraction
ppm	parts per million
Q	reaction quotient
R	gas constant
R_{CT}	charge transfer resistance
R_{Ω}	contact resistance
rpm	rotations per minute
σ	conductivity
T	absolute temperature
t	thickness
v	volume
Ω	ohm
Z	charge of the ions

ACKNOWLEDGEMENTS

This dissertation marks the end of my Ph.D. program and the beginning of the next phase of my life. The road has been challenging, but extremely rewarding. I would be remiss if I did not thank the many people that helped me to get here.

First and foremost, I express an undying gratitude to my parents, Anthony and Lyla, and my sister, Nicole, who have been incredibly supportive of my academic aspirations and a guiding light throughout my life. They have always been there to push me to achieve my best, console me during difficult times, and celebrate my accomplishments with me.

I also thank my grandfather, Mostafa El-Sayed, for his example and enthusiasm for science and nanotechnology, which led me to the lab of Prof. Paul Weiss, at Pennsylvania State University. It was there that I developed a taste for research under the advisement of Paul and his senior graduate students, Nate Hohman and Moonhee Kim. Nate and Moonhee so graciously took me under their wing, helped me to fit in and find my way. After I received my Bachelor in Science, I was invited to continue my work with Paul and pursue a Doctor of Philosophy from the University of California in Los Angeles. Based on my experiences as an undergraduate, I was excited to continue.

While UCLA is a long way from my home in New Jersey, I enjoyed the notion of continuing a family legacy, where my mother received her undergraduate education, my father conducted post-doctoral work as an NIH fellow, and my grandfather was a professor. Additionally, this provided me an opportunity to get closer to my extended family and close family friends in California. I'd like to extend a special thank you to Sherwin and Elaine Olken, who became my second family. It was reassuring to know that I had a warm home if it was ever needed.

UCLA provided a rich environment for learning; I was especially fortunate to work with people across multiple disciplines, especially, chemistry, physics, biochemistry, and engineering. A large number of unique and interesting people at UCLA helped to make my graduate school experience both entertaining and enlightening. I'd also like to thank the faculty, staff, visiting scholars, and collaborators that helped me along the way, specifically, Prof. Sarah Tolbert, Prof. Arlene Russell, Dr. Ignacio Martini, Dr. Sergey Prikhodko, Dr. Adam Stieg, Prof. Chris Barrett, Prof. Tomáš Baše, and Prof. Beth Anderson.

I'd like to thank the entirety of both the Weiss group and the Dunn group for their helpful guidance throughout the years, and I am grateful to have you as friends and members of my academic family. Specifically, I'd like to thank those members, both my senior and junior, who were more helpful to me then they may realize: Prof. Shelly Claridge, David McMillan, Prof. Heidi McMahon, Dr. Jeffrey Schwartz, Dr. Huan Cao, Prof. Sarawut Cheunkar, Dr. Andrew Guttentag, Dr. John Thomas, Garrett Wadsworth, Dr. Yuxi Zhao, Prof. Wei-Ssu Liao, Prof. Yuebing Zheng, Dr. Jesse Ko, Matt Lai, Jon Lau, Michael Yeung, Liban Saleh, Rafal Dziedzic, Harrison Mills, John Abendroth, Nako Nakatsuka, Kevin Cheung, Dr. Xiaobin Xu, Qing Yang, Chuanzhen Zhao, Jasson Belling, Liv Heidenreich, Gail Vinnacombe, and Dominik Stemer.

In closing, I would like to thank my committee members, Prof. Alexander Spokoyny and Prof. Richard Kaner for their guidance, stimulating discussions, and collaboration throughout my graduate career. Additionally, I express a deep gratitude to my co-advisor, Prof. Bruce Dunn. He was an enormous help throughout my graduate education with advice on projects, and through his stimulating and challenging lectures. Lastly, I would like to thank Prof. Paul S. Weiss, for not only guiding me through graduate years, but also through my time as an undergraduate. I am immensely grateful for those years, as the lessons learned are invaluable. His continued generosity, support, and advice have helped to build me into the person I am today.

Thank you, from the bottom of my heart, to those mentioned, and not mentioned, here, who helped to make my undergraduate and graduate journey such a remarkable time in my life.

VITA

Andrew Clark Serino attended Pennsylvania State University from 2006 to 2010, where he received a Bachelor of Science in Materials Science & Engineering, with a focus in Electronic and Photonic Materials. During his undergraduate education, he studied molecular interactions on gold surfaces using electroanalytical techniques under the direction of Professor Paul Weiss. Upon graduation, Andrew trained briefly in the lab of Professor Mostafa El-Sayed at the Georgia Institute of Technology, where he conducted research in the synthesis of gold, silver, and platinum nanoparticles, and explored the catalytic properties of platinum nanocages. In 2011, he was admitted into the Ph.D. program in the Department of Materials Science & Engineering at the University of California – Los Angeles, and joined the new lab of Professor Paul Weiss and the lab of Professor Bruce Dunn. Under their advisement, Andrew worked on showing the importance of surface control and its impact on various electronic applications, specifically in energy storage devices. During his time in graduate school, he was awarded the Dr. Ursula Mandel Scholarship.

PUBLICATIONS

Serino, AC; Anderson, ME; Dziedizic, RM; Saleh, LMA; Harrison Mills, Heidenreich, L; Spokoyny, AM; Dunn, BS; Weiss, PS. Work Function Control of Germanium through Carborane-Carboxylic Acid Surface Passivation. *In Revision.*

Serino, AC; Ko, JS; Yeung, MT; Schwartz, JJ; Kang, C; Tolbert, S; Kaner, R; Dunn, BS; Weiss PS. Lithium-Ion Insertion Properties of Solution-Exfoliated Germanane. ACS Nano 2017, 11, 7995.

Cao, HH; Nakatsuka, N; Liao, WS; **Serino, AC**; Cheunkar, S; Yang, H; Weiss, PS; Andrews, AM. Advancing Biocapture Substrates via Chemical Lift-Off Lithography. Chem. Mater. 2017, 29, 6829.

Ko, JS; Doan-Nguyen, VVT; Kim, HS; Muller, AG**; Serino, AC**; Weiss, PS; Dunn, BS. $Na_2Ti_3O_7$ Nanoplatelets and Nanosheets Derived from a Modified Exfoliation Process for Use as a High Capacity Sodium-Ion Negative Electrode; ACS Appl. Mater. Interfaces 2017, 9, 1416.

Cao, HH; Nakatsuka, N; **Serino, AC**; Liao, WS; Cheunkar, S; Yang, H; Weiss, PS; Andrews, AM. Controlled DNA Patterning by Chemical Lift-Off Lithography: Matrix Matters. ACS Nano 2015, 9, 11439.

Thomas, JC; Schwartz, JJ; Hohman, JN; Claridge, SA; Auluck, HS; **Serino, AC**; Spokoyny, AM; Tranf, G; Kelly, K; Mirkin, CA; Gilles, J; Osher, S; Weiss, PS. Defect-Tolerant Aligned Dipoles within TwoDimensional Plastic Lattices. ACS Nano 2015, 9, 4734.

Kim, J; Rim, YS; Liu, Y; **Serino, AC**; Thomas, JC; Chen, H; Yang, Y; Weiss, PS. Interface Control in Organic Electronics Using Mixed Monolayers of Carboranethiol Isomers. Nano Lett. 2014, 14, 2946.

Claridge, SA; Liao, WS; Thomas, JC; Zhao, Y; Cao, HH; Cheunkar, S; **Serino, AC**; Andrews, AM; Weiss, PS. From the Bottom Up: Dimensional Control and Characterization in Molecular Monolayers. Chem. Soc. Revs. 2013, 42, 2725.

Kim, M; Hohman, JN; **Serino, AC**; Weiss, PS. Structural Manipulation of Hydrogen-Bonding Networks in Amide-Containing Alkanethiolate Monolayers via Electrochemical Processing. J. Phys. Chem. C 2010, 114, 19744.

CHAPTER 1: Introduction

1.1: Lithium-Ion Batteries

Batteries have enabled the rapid development of portable electronics and reduction of our dependence on fossil fuels. Multiple battery chemistries have been adopted over the years, but none have been as influential as the lithium-ion battery, due to large energy-storage and cycle lifetime capabilities that result from Li's low atomic mass and volume. As a result, Li-ion batteries have impacted a number of industries, including entertainment, communications, transportation, and defense. While Li-ion batteries have dominated the energy-storage field, the rapid pace of advances requires increasingly more powerful energy-storage devices.

The principal function of lithium-ion and other battery systems is similar. A battery is comprised of two materials with different electrochemical potentials. For example, a common type of lithium-ion battery is depicted in **Figure 1.1**, with $LiCoO_2$ as the cathode and graphite as the anode with an ionically conductive, but electrically insulating separator between them. The overall battery chemistry involves two separate electrochemical reactions, one at the cathode (**Equation 1.1**) and the other at the anode (**Equation 1.2**).

$$CoO_2 + Li^+ + e^- \rightarrow LiCoO_2 \qquad E^o = 1\,V \qquad \textbf{(1.1)}$$

$$LiC_6 \rightarrow C_6 + Li^+ + e^- \qquad E^o = -3\,V \qquad \textbf{(1.2)}$$

In combination, they represent the overall electrochemical process (**Equation 1.3**).

$$CoO_2 + LiC_6 \rightarrow LiCoO_2 + C_6 \qquad E^o = 4\,V \qquad \textbf{(1.3)}$$

Each of these reactions has a corresponding standard potential (E^o), with ~1 V and -3 V for the cathode and anode, respectively. The overall standard cell potential is the sum of these potentials, 4 V, and describes the overall driving force within the battery. These potentials can be related to the chemical activity of the components through the Gibbs Free Energy (G, **Equation 1.4**) and the Nernst equations (**Equation 1.5**),

$$\Delta G = -nFE \tag{1.4}$$

$$E = E^o + \frac{RT}{nF}\ln Q, \tag{1.5}$$

where E is the electrode potential, R is the gas constant, n is the number of electrons involved in the electrochemical reaction, F is Faraday's constant, and Q is the reaction quotient.[1] Additionally, the theoretical maximum energy density (ED) for an electrode can be calculated (**Equation 1.6**),

$$ED = \frac{nF}{3.6M_m} \tag{1.6}$$

where M_m is the molar mass. For example, the theoretical energy density for graphite according to the reaction described in **Equation 1.2** is 372 mAh/g.

There are several approaches to improving Li-ion battery performance, for example, by improving the energy and power densities of the anode and/or cathode, or by improving electrolyte solution stabilities. Here, we focus specifically on the anode. Graphite is an excellent Li-ion anode material and has been used commercially for years.[2,3] Its popularity is due to its high capacity, good rate capability, good thermal stability, high Coulombic efficiency, low volume expansion, and high cycle lifetime. Improving upon this material has been a difficult task, leaving researchers to explore a number of different Li-ion chemistries. Materials like silicon and germanium have received much attention because of their high theoretical energy densities, 3578 and 1384 mAh/g, respectively.[4–6] These high energy density values coincide with a different type of reaction, specifically an alloying reaction where 4 Li^+ ions alloy with the host atom (Si or Ge).[5,7] Conversely, the lithium-graphite process is an intercalation reaction where 1 Li^+ ion sits at the center of a six-carbon ring.[3,8]

In comparing Si and Ge, the latter is more attractive for high power density applications due to its high electron and hole mobility (3.25× Si and 3.8× Si, respectively)[9,10] as well as its high lithium diffusivity (400× Si at room temperature).[11,12] Despite being more costly than some alternatives due to a lack of concentrated Ge ore deposits, defense and aerospace applications may still benefit from the unique high energy and power densities.

While Ge has its benefits, there are limitations preventing its implementation. For example, Ge undergoes a significant volume expansion (400%) during lithiation, which can cause stress-induced fracture and pulverization.[12,13] This degradation leads to two possible mechanisms for capacity loss: (*i*) physical separation of conductive components (*i.e.*, fracture of Ge materials or delamination of germanium from the current collector) and (*ii*) continuous build-up of an insulating solid-electrolyte-interphase (SEI). The latter occurs due to the instability of the electrolyte solution within the potential window of the anode that continues to grow as fractures expose new surfaces. This build-up results in electrical isolation of active material, Li diffusion limitations, and decreases in Coulombic efficiency.

Researchers have investigated ways to improve upon germanium's limitations through nano-structuring,[6,12,14] different electrolyte compositions,[14,15] and surface control.[15] The latter has been accomplished by organic passivation and proven useful for improving Li-ion anode stability. Yuan *et al.* have shown that by passivating Ge nanowires with alkanethiols increases the interaction strength with surrounding carbon-based filler components, which helps to hold the anode together through lithiation-induced volume expansion and contraction cycles.[15] This report exemplifies the importance of surface control for lithium-ion systems. Continued exploration of how the Ge surface is involved and can be manipulated will likely further improve lithium-ion anodes.

1.2: Germanium Surfaces

While germanium is a promising next-generation lithium-ion anode material, it plays an integral role in the fabrication of a wide range of devices, including transistors, photovoltaics, and sensors. Its low bandgap is useful for detecting and harvesting low-energy photons and its high carrier mobility leads to highly conductive devices. These advantages have directed research efforts into understanding how to control and to manipulate the physical and electronic properties of germanium to advance its implementation.

Silicon still dominates many industrial applications primarily due to its ease of processability, which is mainly attributed to its oxide (SiO_2). The inherent oxide serves as a stable, low-defect density passivation layer that offers facile manipulation through a number of different etch processes. Additionally, SiO_2 has a relatively high dielectric constant, which has been implemented in metal-oxide-semiconductor field-effect transistors.

Conversely, germanium's inherent oxide acts as a poor passivation layer due to a large defect density at the interface, which leads to a large number of electron trap states.[16] This is a result of the formation of a GeO_x natural oxide that forms when introduced to an O_2 environment. This oxide consists of +1 to +3 oxidation states, with little to no formation of the +4 state. Upon annealing at high temperatures (≥450 ˚C), the oxide layer is converted entirely to +2, and subsequently desorbs from the surface leaving behind an oxide-free surface.[16] Fabricating devices by implementing an oxide layer is complicated due to this thermal instability.

Several different oxide removal and surface passivation techniques have been explored in both gas- and solution-based systems. For this purpose, investigators have studied the effectiveness of hydrogen peroxide (H_2O_2), deionized water (DI), ammonium hydroxide, ammonium sulfide, halogenetic acids, oxynitride, oxysulfide, and organic ligands. Surfaces etched with halogenetic acids alone were found to have remnants of germanium oxide, which decreases the overall stability of the film. Therefore, rinses with H_2O_2 and DI followed by halogen deposition more effectively remove residual oxide and thus result in increased stability. Sulfur passivation with ammonium sulfide has proven to be a promising method for surface passivation, since surfaces were stable in ambient conditions over several days.

Organic passivation of semiconductor surfaces is one of the most active areas of research for surface control, with more work done on Si than Ge. These films covalently bind to the surface and offer control of surface energy, electronic, optical, and biological properties in addition to oxide control.[16–18] Several binding chemistries have been established including thiol, amine, and Grignard chemistry.[16,17] Of these, thiols have been shown to self-assemble readily upon oxide-free surfaces and are stable for several days due to the strength of the S-Ge bond;[16,17,19–22] and appear to be a promising method for organic passivation.

Self-assembled monolayers (SAMs) of thiols have been studied extensively on Au{111} due to the strong Au-S bond and stability of Au in ambient conditions. These studies have explored how substrate-surface and intermolecular interactions affect order and adhesion strength. For example, implementation of amide groups increases intermolecular interaction strength by incorporating hydrogen bonding networks, which forces molecules to pack more densely.[23,24] Additionally, surface properties can be altered through the incorporation of different head groups. For example, surface wettability can be altered by adding a methyl or hydroxyl group to the tail group, creating a hydrophobic or hydrophilic surface, respectively.[25] Lastly, electronic properties can be altered through the incorporation of surface normal dipole moments,[26] and altering the head group binding chemistry. A surface dipole acts as an image charge on the surface, shifting the surface work function, while head group covalent bonding alters the highest occupied molecular orbital (HOMO) and lowest occupied molecular orbital (LUMO).[27]

The thiol-gold system has provided an important platform for studying these features, however, studies of thiols on Ge are limited. Maboudian and coworkers demonstrated that 1-octadecanethiolate SAMs can be formed on hydrogen-passivated Ge(111). Bent and coworkers showed this deposition could be extended to halogenated Ge(111) and Ge(100) surfaces. Films created by first removing the oxide with H_2O_2 and DI rinses, passivating with HCl or HBr, then backfilling with octanethiol or octadecanethiol resulted in films that are stable in ambient conditions for several days.

Bent and coworkers also revealed a significant difference in halogen and sulfur concentrations between the two surfaces, which is attributed to the unique characteristics of the Ge(100) surface. In order to reduce the number of dangling bonds, the Ge(100) surface reconstructs into a 2 × 1 structure (**Figure 1.2**), resulting in the creation of surface dimers. The Ge(111) surface maintains a 1 × 1 structure upon functionalization.[16] The major difference in surface reactivity is attributed to the nucleophilic top Ge atom and the electrophilic bottom Ge atom. Therefore, the reactivity varies depending on the specific Ge atom, thus presenting an opportunity for differential functionalization (**Figure 1.3**) and interesting surface chemistries. A number of head groups (*i.e.*, hydroxyl, amine, and carboxylic acid) have been explored in vacuum to understand how the interesting surface chemistry of the Ge(100) surface can be exploited.[16,17] These head groups preferentially bind to the Ge(100) surface over the Ge(111) surface due to the different chemical environment of the surface dimer reconstruction. The carboxylic acid system was investigated in greater detail by Bent *et al*. and Kim *et al*.[28,29] who concluded that the carboxylic acid head group is capable of adopting several different binding orientations (**Figure 1.4**).[28,29] First, hydrogen dissociates from the OH group, opening a single oxygen to bind to the electrophilic atom on the dimer (monodentate). The second oxygen group can bind to a neighboring dimer's electrophilic atom (end bridged bidentate). At room temperature, surfaces tend to contain both monodentate and end-bridged bidentate configurations. The activation energy to bind to the nucleophilic atom on the dimer can be overcome by increasing the deposition temperature or adding an annealing step (400 K), allowing the carboxylic acid to bridge a single dimer (on-top bidentate).[28,29] These binding avenues create interesting alternatives to controlling binding orientations, binding energies, and subsequent surface properties.[30]

1.3: Molecular Battery

As consumer use of lithium-ion batteries continues to grow and the applicable markets expand, so do the battery requirements. Recently, there has been increasing demand for lithium-ion batteries with smaller volumetric impact to power increasingly smaller microelectromechanical devices (*i.e.*, smart dust mote).[31] These types of devices incorporate a collection of sensors, receivers, and transmitters, all of which require a power source. Typical battery architectures are impractical for powering these devices due to their large volumetric impact, where the battery becomes the largest component and limits how small the device can be. To solve this issue, researchers have incorporated three-dimensional architectures, such as repeating parallel plates or interdigitated pillars.[32–34]

While these three-dimensional architectures dramatically decrease the volumetric impact of the lithium-ion battery, there is still significant room for improvement for decreasing the size impact of the electrolyte separator. Since the electrolyte layer plays no role in energy storage and only acts as a means of ion transport, decreasing the size of this separator will increase the total energy storage per unit volume. However, decreasing the thickness of the electrolyte layer requires uniformity and structure, thus limiting materials to the solid-state.

Solid-state electrolyte systems have been explored extensively in an attempt to exploit their added safety benefits.[35–39] Common liquid Li-ion battery electrolytes consist of flammable organic solvents because of their superior stability with battery components and the potential ranges used. However, these batteries run the risk of catching fire, thereby limiting their potential applications. Incorporation of a solid-state electrolyte alleviates the flammability concern.

Both organic and inorganic solid-state electrolyte systems have been explored and each offers unique advantages. For example, organic systems tend to be less expensive, while inorganic systems tend to be more stable.[37,40] Initial research into these materials focused primarily on increasing ionic conductivity, as this was the key limitation to both organic and inorganic solid-state systems. To overcome low ionic conductivities, researchers incorporated conductive channels and amorphous structures to prevent ion-pathway impedance.[38] Additionally, the resistance due to ion transport impedance can be decreased by reducing the thickness of the electrolyte layer, and thus decreasing the ion transport path length.[41–43] **Equation 1.7** shows the relationship of ionic resistance (R) to path length (L), ionic resistivity (ρ), and surface area (A).

$$R = \frac{\rho L}{A} \tag{1.7}$$

Therefore, decreasing the thickness of the electrolyte layer through the incorporation of ultra-thin film solid-state systems will increase storage capacity per unit volume, safety, and stability as well as decrease resistance due to ionic transport limitations.

1.3.1: The Debye Length

Ideally, the electrolyte separator should be as thin as physically possible, approaching a thickness less than 50 nm. However, new phenomena start to emerge when approaching these length scales. One phenomenon is quantum tunneling, which involves electrons passing through a classical barrier at nanometer length scales, and is dependent on the potential applied. As the thickness of the barrier increases, the tunneling current becomes exponentially smaller.[44] This phenomenon creates a lower limit on the thickness of the electrolyte separator, as quantum tunneling would discharge the battery as electrons tunnel between electrodes across the separator.

A second phenomenon that emerges at these length scales is overlapping Debye lengths. Briefly, this phenomenon occurs when two electrodes with different potentials are brought into close proximity, causing their effective potentials to interact. The distance a potential extends from an electrode into the surrounding electrolyte is defined by the Debye length (κ^{-1} **Equation 1.8)**

$$\boldsymbol{\kappa^{-1}} = \sqrt{\frac{\boldsymbol{kT\varepsilon\varepsilon_{\circ}}}{\boldsymbol{2Cz^2e^2}}}\,, \qquad \textbf{(1.8)}$$

where k is the Boltzmann constant, T is absolute temperature, ε is the electrical permittivity of the material, $\varepsilon_{\circ}$ is the permittivity of free space, C is the concentration of ions, z is the charge of the ions, and e is the elementary charge.

The effect of the Debye length can be commonly seen with liquid electrolyte systems in the double-layer capacitance (**Figure 1.5**), which occurs in response to an applied potential.[1] This double-layer is comprised of several layers, inner and outer Helmholtz layers, and a diffuse layer. The inner layer corresponds to absorbed solvent molecules whose dipoles align with the applied potential. Solvated ions whose charge is opposite that of the applied potential absorb at the locus of the outer layer. The non-specifically absorbed components in solution are distributed throughout the diffuse layer. The thickness of the diffuse layer is described by the Debye length.[1]

While the Debye length is well understood for electrochemical systems,[1] more work is required to understand the effects of the overlapping Debye lengths that can occur at the nanoscale. This work extends into the field of nanoionics, which aims to understand ion transport at the nanoscale.[41] Recent work has both theoretically and experimentally explored the effects of potentials on ions at the nanoscale in liquid-sate electrolyte systems.[45–49] Results indicate that the activation energy for ion transport within the Debye length is increased.[50] This effect would have a negative impact on nanoscale battery performance. Some work has been done on exploring both inorganic[51–54] and organic[55–57] solid-state systems as well, however, not to the same extent as liquid-based systems. One key difference between liquid- and solid-state systems, is the larger carrier concentration, which has a significant impact on the Debye length. For example, an organic solid-state system that incorporates a lithium monocarborane salt, like the system tested by Udovic and coworkers,[58] with 1 ion per ~125 $Å^3$, would result in a concentration of 13.29 M. In comparison, typical liquid-based electrolytes have a concentration of ~1 M. Using **Equation 1.8**, this concentration difference would result in a decrease in the Debye length by a factor of ~3.6. While this estimates for a specific system, the general trend holds across liquid- and solid-state systems. This trend enables solid-state systems to attain thinner electrolyte separators than their liquid counterparts without any influence from overlapping Debye lengths (**Figure 1.6**).

1.3.2: Proposed Construction

Solid-state approaches appear to be ideal for decreasing the thickness of electrolyte separators. While both organic and inorganic systems have been explored, each has its own drawbacks. Current organic systems lack precise thickness control, which adds variability in assembly. Precise control of thickness is attainable for inorganic systems; they typically require the use of atomic layer deposition methods that are costly and difficult to perfect. Herein, we propose the creation of a "molecular battery" by applying layer-by-layer (LBL) control of the inorganic system to an organic system. This battery will enable the precise control of electronic and physical properties at the molecular scale to investigate how to maximize ionic conductivity and minimize overall thickness of the solid-state electrolyte layer. There are four major components (**Figure 1.6**) to the molecular battery: (*i*) the anode substrate, (*ii*) the foundation layer, (*iii*) the layered solid-state electrolyte, and (*iv*) the polymer cathode.

Anode

The anode itself is not within the scope of this project, however, there are important factors to consider. First, from a practical engineering perspective, it would be beneficial to use a high theoretical energy density material. Second, and more importantly, the anode must have the capacity for ordered, organic functionalization. As organic passivation on Ge surfaces is well-characterized, it provides a model system for exploring various separator structures. For these reasons, germanium is an ideal initial candidate for the anode.[59]

Foundation Layer

Designing a well-ordered, layer-by-layer structure requires control over assembly and the ability to minimize defects. The first layer, or the foundation layer, is an important first step in identifying and addressing defect sources, as any defects can propagate up through the layers. Additionally, the first layer is an important system to test the performance of different electronic or physical properties.

The thiol-Au system has been heavily studied with various tail groups[25] to understand how different tail groups affect assembly. For example, the dodecanethiol (C12) on Au{111} system adopts a 30° tilt from the surface normal, creating distinct grains and grain boundaries. This system would be non-ideal for the molecular battery due to the significamt number of defects, which provide access to the substrate. Conversely, carboranethiols assemble on Au{111} without any distinct grains and minimal defects. This assembly is due to the nearly spherical backbone and lack of surface tilt, resulting in what appears as close-packing of balls on a surface, anchored by a thiol head-group.[60] More information on carboranes can be found in **section 5.2**.

Layered Solid-State Electrolyte Layer-by-Layer

Constructing a solid-state, organic electrolyte with layer-by-layer (LBL) control provides a platform to study ionics at the nanometer scale in detail with each incremental layer and tune molecular properties to improve performance. Previously reported molecular layer deposition strategies of similar systems suggest that either (*i*) the COOH-NH_2 condensation reaction,[61] similar to an A-B-A-B layering process, or (*ii*) a layer-by-layer assembly of organics by metal-organic coordination[35,62–67] could produce ultra-thin films.

Polymer Cathode

The cathode is the last step in fabricating the full molecular battery, and is required for full-cell testing. A Li-host polymer is a good choice for the cathode material due to the temperature sensitivity of organics within the electrolyte layer that would add restrictions to processing. Polypyrrole has been heavily researched and is a good choice as the cathode material, due to its high cycle lifetime and storage capacity.[68,69] Several avenues exist for deposition, however the most promising method is organic chemical vapor deposition (OCVD).[70–73]

1.4: Thesis Overview

1.4.1: Processing of an All-Surface Germanium Nanomaterial

Germanane (GeH) is a two-dimensional form of germanium, which shows promise for a number of electronic devices, including transistors, supercapacitors, batteries, and photodetectors. The favorable properties of GeH stem from the two-dimensional structure. Unfortunately, current synthesis and exfoliation methods produce Ge particle impurities and suffer from low yields.[74–82] In order to capitalize on two-dimensional specific properties for large-scale devices, a method needs to be created to batch-purify and to exfoliate GeH. Here, we present a facile method for producing stable single-to-multi-sheet dispersions of pure germanane. Purity and degree of exfoliation were assessed with scanning electron microscopy, transmission electron microscopy, and Raman spectroscopy.

1.4.2: Germanane as a Lithium-Ion Anode Material

The high theoretical energy density of alloyed lithium and germanium ($Li_{15}Ge_4$), 1384 mAh/g, makes germanium a promising anode material for lithium-ion batteries. However, common alloy anode architectures suffer from long-term instability upon repetitive charge-discharge cycles that arise from stress-induced degradation upon lithiation (volume expansion >300%). Here, we explore the use of the two-dimensional nanosheet structure of germanane to mitigate stress from high volume expansion. We measured representative germanane battery electrodes to have a reversible Li-ion capacity of 1108 mAh/g when cycled between 0.1 to 2 V *vs.* Li/Li^+. These results indicate germanane anodes are capable of near-theoretical-maximum energy storage, perform well at high cycling rates, and can maintain capacity over 100 cycles.

1.4.3: Work Function Control of Germanium through Carboxyl-Carborane Surface Passivation

Self-assembled monolayers of functionalized carborane isomers with different dipole moments passivate germanium to modulate surface work function while maintaining chemical environment and surface energy. To identify head groups capable of monolayer formation on germanium surfaces, we studied thiol-, hydroxyl-, and carboxylic acid-terminated carboranes. Monolayers were successfully formed with carboxylic acid head groups instead of the archetypal thiol, suggesting that the carborane cluster significantly affects head group reactivity. Monolayer characterization included X-ray and ultraviolet photoelectron spectroscopies as well as contact angle goniometry. Using these carborane SAMs, the germanium surface work function was tailored by 0.4 eV without significant changes to wetting properties.[26]

1.4.4: Progress towards a Molecular Battery

Fabrication of the molecular battery requires development of a LBL approach for depositing organic molecules on a surface with 1−3 nm control to obtain a total thickness <50 nm. Here, we explore a LBL approach to assembling metal-organic coordinated films, specifically carborane-based organic linkers on Au{111} surfaces. Additionally, benzene-based organic linkers are explored on Au{111} and Ge(100) surfaces for Li-ion battery applications. Characterization methods include ellipsometry, atomic force microscopy, X-ray photoelectron spectroscopy, electrochemical impedance spectroscopy, and cyclic voltammetry. Results show that when common methods for LBL assembly were applied to functionalized carborane linkers, films reached a maximum thickness of ~10 Å, which corresponds to bilayer formation. The benzene-based linker, 1,3,5-tris(4'-carboxy[1,1'-biphenyl]-4-yl)benzene, shows promise as a Li-ion separator. This material exhibits electronic insulating and ionic conducting properties over the potential window of 0.05 to 2.5 V *vs.* Li^+/Li.

1.5: Prospects

The work presented herein aims to demonstrate the importance of material surfaces, especially in nanostructures, and how they can be manipulated to improve device performance. In doing so, we investigated an "all-surface" material, SAMs for surface property control, and molecular LBL for nanoscale Li-ion battery architectures. We envision that this work will further advance the Li-ion field, as well as a number of other device-based fields, including sensors, photovoltaics, transistors, and spintronics.

1.6: References

(1) Bard, A. J.; Faulkner, L. R. *Electrochemical Methods: Fundamentals and Applications*; 1st ed.; John Wiley & Sons, Inc.: New York, 1980.

(2) Etacheri, V.; Marom, R.; Elazari, R.; Salitra, G.; Aurbach, D.; Lu, L.; Yang, H.; Burnett, J.; Uhuegbu, C.; Chow, T. T.; Tachan, Z.; Ruhle, S.; Zaban, A.; Nazeeruddin, M. K.; Baranoff, E.; Graetzel, M.; Zhou, L.; Coup, D.; Zhan, F.; Jiang, L. J.; Scrosati, B.; *et al.* Challenges in the Development of Advanced Li-Ion Batteries: A Review. *Energy Environ. Sci.* **2011**, *4*, 3243.

(3) Goodenough, J. B.; Park, K.-S. The Li-Ion Rechargeable Battery: A Perspective. *J. Am. Chem. Soc.* **2013**, *135*, 1167–1176.

(4) Zhang, W.-J. A Review of the Electrochemical Performance of Alloy Anodes for Lithium-Ion Batteries. *J. Power Sources* **2011**, *196*, 13–24.

(5) Park, C.-M.; Kim, J.-H.; Kim, H.; Sohn, H.-J.; Nagaura, T.; Tozawa, K.; Dey, A. N.; Idota, Y.; Kubota, T.; Matsufuji, A.; Maekawa, Y.; Miyasaka, T.; Besenhard, J. O.; Yang, J.; Winter, M.; Winter, M.; Besenhard, J. O.; Spahr, M. E.; Novak, P.; Broussely, M.; Tarascon, J.-M.; *et al.* Li-Alloy Based Anode Materials for Li Secondary Batteries. *Chem. Soc. Rev.* **2010**, *39*, 3115.

(6) Goriparti, S.; Miele, E.; De Angelis, F.; Di Fabrizio, E.; Proietti Zaccaria, R.; Capiglia, C. Review on Recent Progress of Nanostructured Anode Materials for Li-Ion Batteries. *J. Power Sources* **2014**, *257*, 421–443.

(7) McDowell, M. T.; Lee, S. W.; Nix, W. D.; Cui, Y. 25th Anniversary Article: Understanding

the Lithiation of Silicon and Other Alloying Anodes for Lithium-Ion Batteries. *Adv. Mater.* **2013**, *25*, 4966–4985.

(8) Goodenough, J. B.; Kim, Y. Challenges for Rechargeable Li Batteries. *Chem. Mater.* **2010**, *22*, 587–603.

(9) Prince, M. B. Drift Mobilities in Semiconductors. II. Silicon. *Phys. Rev.* **1954**, *93*, 1204–1206.

(10) Prince, M. B. Drift Mobilities in Semiconductors. I. Germanium. *Phys. Rev.* **1953**, *92*, 681–687.

(11) McIlwrath, K.; Cui, Y.; Huggins, R. A.; Zhang, X. F.; Chan, C. K.; Peng, H.; Liu, G. High-Performance Lithium Battery Anodes Using Silicon Nanowires. *Nat. Nanotechnol.* **2008**, *3*, 31–35.

(12) Kennedy, T.; Mullane, E.; Geaney, H.; Osiak, M.; Dwyer, C. O.; Ryan, K. M. High-Performance Germanium Nanowire-Based Lithium-Ion Battery Anodes Extending over 1000 Cycles Through in Situ Formation of a Continuous Porous Network. **2014**, *14*, 716–723.

(13) Seng, K. H.; Guo, Z. P.; Liu, H. K.; Park, M. M.-H.; Cho, J.; Guo, Z. P.; Liu, H. K.; Cho, J. Self-Assembled Germanium/Carbon Nanostructures as High-Power Anode Material for the Lithium-Ion Battery. *Angew. Chemie Int. Ed.* **2012**, *51*, 5657–5661.

(14) Chockla, A. M.; Klavetter, K. C.; Mullins, C. B.; Korgel, B. A. Solution-Grown Germanium Nanowire Anodes for Lithium-Ion Batteries. *ACS Appl. Mater. Interfaces* **2012**, *4*, 4658–4664.

(15) Klavetter, K. C.; Wood, S. M.; Lin, Y.-M.; Snider, J. L.; Davy, N. C.; Chockla, A. M.; Romanovicz, D. K.; Korgel, B. A.; Lee, J.-W.; Heller, A.; Mullins, C. B. A High-Rate Germanium-Particle Slurry Cast Li-Ion Anode with High Coulombic Efficiency and Long Cycle Life. *J. Power Sources* **2013**, *238*, 123–136.

(16) Yuan, F.-W.; Yang, H.-J.; Tuan, H.-Y. Alkanethiol-Passivated Ge Nanowires as High-Performance Anode Materials for Lithium-Ion Batteries: The Role of Chemical Surface Functionalization. *ACS Nano* **2012**, *6*, 9932–9942.

(17) Loscutoff, P. W.; Bent, S. F. Reactivity of the Germanium Surface: Chemical Passivation and Functionalization. *Annu. Rev. Phys. Chem.* **2006**, *57*, 467–495.

(18) Kachian, J. S.; Wong, K. T.; Bent, S. F. Periodic Trends in Organic Functionalization of Group IV Semiconductor Surfaces. *Acc. Chem. Res.* **2010**, *43*, 346–355.

(19) Bent, S. F. Heads or Tails: Which Is More Important in Molecular Self-Assembly? *ACS Nano* **2007**, *1*, 10–12.

(20) Ardalan, P.; Musgrave, C. B.; Bent, S. F. Formation of Alkanethiolate Self-Assembled Monolayers at Halide-Terminated Ge Surfaces. *Langmuir* **2009**, *25*, 2013–2025.

(21) Ardalan, P.; Sun, Y.; Pianetta, P.; Musgrave, C. B.; Bent, S. F.; Engineering, C. Reaction Mechanism, Bonding, and Thermal Stability of 1-Alkanethiols Self-Assembled on Halogenated Ge Surfaces. **2010**, *26*, 8419–8429.

(22) Han, S. M.; Ashurst, W. R.; Carraro, C.; Maboudian, R. Formation of Alkanethiol Monolayer on Ge(111). *J. Am. Chem. Soc.* **2001**, *123*, 2422–2425.

(23) Hohman, J. N.; Kim, M.; Bednar, H. R.; Lawrence, J. A.; McClanahan, P. D.; Weiss, P. S.

Simple, Robust Molecular Self-Assembly on Germanium. *Chem. Sci.* **2011**, *2*, 1334–1343.

(24) Smith, R. K.; Reed, S. M.; Lewis, P. A.; Monnell, J. D.; Clegg, R. S.; Kelly, K. F.; Bumm, L. A.; Hutchison, J. E.; Weiss, P. S. Phase Separation within a Binary Self-Assembled Monolayer on Au{111} Driven by an Amide-Containing Alkanethiol. *J. Phys. Chem. B* **2001**, *105*, 1119–1122.

(25) Kim, M.; Hohman, J. N.; Serino, A. C.; Weiss, P. S. Structural Manipulation of Hydrogen-Bonding Networks in Amide-Containing Alkanethiolate Monolayers via Electrochemical Processing. *J. Phys. Chem. C* **2010**, *114*, 19744–19751.

(26) Love, J. C.; Estroff, L. A.; Kriebel, J. K.; Nuzzo, R. G.; Whitesides, G. M. Self-Assembled Monolayers of Thiolates on Metals as a Form of Nanotechnology. *Chem. Rev.* **2005**, *105*, 1103–1170.

(27) Kim, J.; Rim, Y. S.; Liu, Y.; Serino, A. C.; Thomas, J. C.; Chen, H.; Yang, Y.; Weiss, P. S. Interface Control in Organic Electronics Using Mixed Monolayers of Carboranethiol Isomers. *Nano Lett.* **2014**, *14*, 2946–2951.

(28) Arefi, H. H.; Nolan, M.; Fagas, G. Role of the Head And/or Tail Groups of Adsorbed−[$X^{\text{Head Group}}$]–Alkyl–[$X^{\text{Tail Group}}$] [X = O(H), S(H), $NH_{(2)}$] Chains in Controlling the Work Function of the Functionalized H:Si(111) Surface. *J. Phys. Chem. C* **2015**, *119*, 11588–11597.

(29) Filler, M. A.; Van Deventer, J. A.; Keung, A. J.; Bent, S. F. Carboxylic Acid Chemistry at the Ge(100)-2 × 1 Interface: Bidentate Bridging Structure Formation on a Semiconductor Surface. *J. Am. Chem. Soc.* **2005**, *128*, 770–779.

(30) Hwang, E.; Kim, D. H.; Hwang, Y. J.; Kim, A.; Hong, S.; Kim, S. Bidentate Structures of

Acetic Acid on Ge(100): The Role of Carboxyl Oxygen. *J. Phys. Chem. C* **2007**, *111*, 5941–5945.

(31) Hwang, E.; Jung, S. J.; Kim, S.; Kim, D. H. Chemical Reaction of Benzoic Acid with Ge(100): Effect of a Phenyl Substituent. *J. Phys. Chem. C* **2016**, *120*, 14742–14748.

(32) Long, J. W.; Dunn, B.; Rolison, D. R.; White, H. S. Three-Dimensional Battery Architectures. *Chem. Rev.* **2004**, *104*, 4463–4492.

(33) Min, H.-S.; Park, B. Y.; Taherabadi, L.; Wang, C.; Yeh, Y.; Zaouk, R.; Madou, M. J.; Dunn, B. Fabrication and Properties of a Carbon/Polypyrrole Three-Dimensional Microbattery. *J. Power Sources* **2008**, *178*, 795–800.

(34) L. Prieto, A.; T. Rawls, M.; Dunn, B.; Perre, E.; M. Mosby, J.; Malati, P.; S. Arthur, T.; C. Johnson, D.; J. Bates, D.; Cirigliano, N. Three-Dimensional Electrodes and Battery Architectures. *MRS Bull.* **2011**, *36*, 523–531.

(35) Chamran, F.; Yeh, Y.; Min, H.-S.; Dunn, B.; Kim, C.-J. Fabrication of High-Aspect-Ratio Electrode Arrays for Three-Dimensional Microbatteries. *J. Microelectromechanical Syst.* **2007**, *16*, 844–852.

(36) Ke, F.-S.; Wu, Y.-S.; Deng, H. Metal-Organic Frameworks for Lithium Ion Batteries and Supercapacitors. *J. Solid State Chem.* **2015**, *223*, 109–121.

(37) Song, J. Y.; Wang, Y. Y.; Wan, C. C. Review of Gel-Type Polymer Electrolytes for Lithium-Ion Batteries. *J. Power Sources* **1999**, *77*, 183–197.

(38) Knauth, P. Inorganic Solid Li Ion Conductors: An Overview. *Solid State Ionics* **2009**, *180*, 911–916.

(39) Kim, J. G.; Son, B.; Mukherjee, S.; Schuppert, N.; Bates, A.; Kwon, O.; Choi, M. J.; Chung, H. Y.; Park, S. A Review of Lithium and Non-Lithium Based Solid State Batteries. *J. Power Sources* **2015**, *282*, 299–322.

(40) Bachman, J. C.; Muy, S.; Grimaud, A.; Chang, H.-H.; Pour, N.; Lux, S. F.; Paschos, O.; Maglia, F.; Lupart, S.; Lamp, P.; Giordano, L.; Shao-Horn, Y. Inorganic Solid-State Electrolytes for Lithium Batteries: Mechanisms and Properties Governing Ion Conduction. *Chem. Rev.* **2016**, *116*, 140–162.

(41) Meyer, W. H. Polymer Electrolytes for Lithium-Ion Batteries. *Adv. Mater.* **1998**, *10*, 439–448.

(42) Maier, J. Nanoionics: Ion Transport and Electrochemical Storage in Confined Systems. *Nat. Mater.* **2005**, *4*, 805–815.

(43) Rhodes, C. P.; Long, J. W.; Doescher, M. S.; Fontanella, J. J.; Rolison, D. R. Nanoscale Polymer Electrolytes: Ultrathin Electrodeposited Poly(Phenylene Oxide) with Solid-State Ionic Conductivity. *J. Phys. Chem. B,* **2004**, *108*, 13079–13087.

(44) Duan, J.; Hou, H.; Liu, X.; Liao, Q.; Liu, S.; Meng, R.; Hao, Z.; Yao, Y. Conformal Electrodeposition of Poly(Phenylene Oxide) on TiO_2 Nanotube Arrays with High Performance for Lithium Ion Battery. *J. Appl. Polym. Sci.* **2016**, *133,* 43685.

(45) Chen, C. J. *Introduction to Scanning Tunneling Microscopy*; Brook, R. J.; Heuer, A.; Marks, T. J.; Ruhle, N.; Sutton, A. P.; Cheetham, A.; Hirsch, S. P.; Pettifor, D. G.; Silcox, J.; Tirrell, M. V.; Vitek, V. Eds.; 2nd ed.; Oxford University Press, 2008.

(46) Balke, N.; Kalnaus, S.; Dudney, N. J.; Daniel, C.; Jesse, S.; Kalinin, S. V. Local Detection

of Activation Energy for Ionic Transport in Lithium Cobalt Oxide. *Nano Lett.* **2012**, *12*, 3399–3403.

(47) Okubo, M.; Tanaka, Y.; Zhou, H.; Kudo, T.; Honma, I. Determination of Activation Energy for Li Ion Diffusion in Electrodes. *J. Phys. Chem. B* **2009**, *113*, 2840–2847.

(48) Xiong, J.; Chen, Q.; Edwards, M. A.; White, H. S. Ion Transport within High Electric Fields in Nanogap Electrochemical Cells. *ACS Nano* **2015**, *9*, 8520–8529.

(49) Taghipoor, M.; Bertsch, A.; Renaud, P. An Improved Model for Predicting Electrical Conductance in Nanochannels. *Phys. Chem. Chem. Phys.* **2015**, *17*, 4160–4167.

(50) Watkins, J. J.; White, H. S. The Role of the Electrical Double Layer and Ion Pairing on the Electrochemical Oxidation of Hexachloroiridate(III) at Pt Electrodes of Nanometer Dimensions. *Langmuir* **2004**, *20*, 5474–5483.

(51) Perera, R. T.; Johnson, R. P.; Edwards, M. A.; White, H. S. Effect of the Electric Double Layer on the Activation Energy of Ion Transport in Conical Nanopores. *J. Phys. Chem. C* **2015**, *119*, 24299–24306.

(52) Liu, J.; Banis, M. N.; Li, X.; Lushington, A.; Cai, M.; Li, R.; Sham, T.-K.; Sun, X. Atomic Layer Deposition of Lithium Tantalate Solid-State Electrolytes. *J. Phys. Chem. C* **2013**, *117*, 20260–20267.

(53) Wang, B.; Liu, J.; Sun, Q.; Li, R.; Sham, T.-K.; Sun, X. Atomic Layer Deposition of Lithium Phosphates as Solid-State Electrolytes for All-Solid-State Microbatteries. *Nanotechnology* **2014**, *25*, 504007.

(54) Li, X.; Liu, J.; Banis, M. N.; Lushington, A.; Li, R.; Cai, M.; Sun, X. Atomic Layer

Deposition of Solid-State Electrolyte Coated Cathode Materials with Superior High-Voltage Cycling Behavior for Lithium Ion Battery Application. *Energy Environ. Sci.* **2014**, *7*, 768–778.

(55) Luo, J. Interfacial Engineering of Solid Electrolytes. *J. Mater.* **2015**, *1*, 22–32.

(56) Gowda, S. R.; Reddy, A. L. M.; Shaijumon, M. M.; Zhan, X.; Ci, L.; Ajayan, P. M. Conformal Coating of Thin Polymer Electrolyte Layer on Nanostructured Electrode Materials for Three-Dimensional Battery Applications. *Nano Lett.* **2011**, *11*, 101–106.

(57) Gowda, S. R.; Leela Mohana Reddy, A.; Zhan, X.; Jafry, H. R.; Ajayan, P. M.; Reddy, A. L. M.; Zhan, X.; Jafry, H. R.; Ajayan, P. M. 3D Nanoporous Nanowire Current Collectors for Thin Film Microbatteries. *Nano Lett.* **2012**, *12*, 1198–1202.

(58) Fan, X.; Dou, P.; Jiang, A.; Ma, D.; Xu, X. One-Step Electrochemical Growth of a Three-Dimensional Sn–Ni@PEO Nanotube Array as a High Performance Lithium-Ion Battery Anode. *ACS Appl. Mater. Interfaces* **2014**, *6*, 22282–22288.

(59) Tang, W. S.; Matsuo, M.; Wu, H.; Stavila, V.; Zhou, W.; Talin, A. A.; Soloninin, A. V.; Skoryunov, R. V.; Babanova, O. A.; Skripov, A. V.; Unemoto, A.; Orimo, S.-I.; Udovic, T. J. Liquid-Like Ionic Conduction in Solid Lithium and Sodium Monocarba-Closo-Decaborates Near or at Room Temperature. *Adv. Energy Mater.* **2016**, *6*, 1502237.

(60) Wang, G. T.; Mui, C.; Musgrave, C. B.; Bent, S. F. Competition and Selectivity of Organic Reactions on Semiconductor Surfaces: Reaction of Unsaturated Ketones on Si(100)-2×1 and Ge(100)-2×1. *J. Am. Chem. Soc.* **2002**, *124*, 8990–9004.

(61) Hohman, J. N.; Zhang, P.; Morin, E. I.; Han, P.; Kim, M.; Kurland, A. R.; Mcclanahan, P.

D.; Balema, V. P.; Weiss, P. S. Self-Assembly of Carboranethiol Isomers on Au{111}: Intermolecular Interactions Determined by Molecular Dipole Orientations. *ACS Nano* **2009**, *3*, 527–536.

(62) Gu, J.-E.; Lee, S.; Stafford, C. M.; Lee, J. S. J.-H.; Choi, W.; Kim, B.-Y.; Baek, K.-Y.; Chan, E. P.; Chung, J. Y.; Bang, J.; Lee, J. S. J.-H. Molecular Layer-by-Layer Assembled Thin-Film Composite Membranes for Water Desalination. *Adv. Mater.* **2013**, *25*, 4778–4782.

(63) Wang, L.; Han, Y.; Feng, X.; Zhou, J.; Qi, P.; Wang, B. Metal–organic Frameworks for Energy Storage: Batteries and Supercapacitors. *Coord. Chem. Rev.* **2016**, *307*, 361–381.

(64) Bae, Y.-S.; Farha, O. K.; Spokoyny, A. M.; Mirkin, C. A.; Hupp, J. T.; Snurr, R. Q.; Carborane-Based Metal–Organic Frameworks as Highly Selective Sorbents for CO_2 Over Methane. *Chem. Commun.* **2008**, *20*, 4135.

(65) Anderson, M. E.; Mihok, M.; Tanaka, H.; Tan, L.-P.; Horn, M. W.; McCarty, G. S.; Weiss, P. S. Hybrid Approaches to Nanolithography: Photolithographic Structures with Precise, Controllable Nanometer-Scale Spacings Created by Molecular Rulers. *Adv. Mater.* **2006**, *18*, 1020–1022.

(66) Benson, A. S.; Elinski, M. B.; Ohnsorg, M. L.; Beaudoin, C. K.; Alexander, K. A.; Peaslee, G. F.; DeYoung, P. A.; Anderson, M. E. Metal–Organic Coordinated Multilayer Film Formation: Quantitative Analysis of Composition and Structure. *Thin Solid Films* **2015**, *590*, 103–110.

(67) Ohnsorg, M. L.; Beaudoin, C. K.; Anderson, M. E. Fundamentals of MOF Thin Film Growth via Liquid-Phase Epitaxy: Investigating the Initiation of Deposition and the

Influence of Temperature. *Langmuir* **2015**, *31*, 6114–6121.

(68) Anderson, M. E.; Tan, L. P.; Tanaka, H.; Mihok, M.; Lee, H.; Horn, M. W.; Weiss, P. S. Advances in Nanolithography Using Molecular Rulers. *J. Vac. Sci. Technol. B Microelectron. Nanom. Struct.* **2003**, *21*, 3116–3119.

(69) Gao, X.; Luo, W.; Zhong, C.; Wexler, D.; Chou, S.-L; Liu, H.-K.; Shi, Z.; Chen, G.; Ozawa, K.; Wang, J.-Z.; Novel Germanium/Polypyrrole Composite for High Power Lithium-Ion Batteries. *Sci. Rep.* **2014**, *4*, 6095.

(70) Qie, L.; Yuan, L.-X.; Zhang, W.-X.; Chen, W.-M.; Huang, Y.-H. Revisit of Polypyrrole as Cathode Material for Lithium-Ion Battery. *J. Electrochem. Soc.* **2012**, *159*, A1624–A1629.

(71) Mohammadi, A.; Hasan, M.-A.; Liedberg, B.; Lundström, I.; Salaneck, W. R. Chemical Vapour Deposition (CVD) of Conducting Polymers: Polypyrrole. *Synth. Met.* **1986**, *14*, 189–197.

(72) Gong, Q.; He, Y.-S.; Yang, Y.; Liao, X.-Z.; Ma, Z.-F. Synthesis and Electrochemical Characterization of $LiFePO_4$/C-Polypyrrole Composite Prepared by a Simple Chemical Vapor Deposition Method. *J. Solid State Electrochem.* **2012**, *16*, 1383–1388.

(73) Wu, H.-M.; Shy, H.-J.; Ko, H.-W. Application of Chemical Synthesized Polypyrrole for a Rechargeable Lithium Battery. *J. Power Sources* **1989**, *27*, 59–67.

(74) Xia, J.; Chen, L.; Yanagida, S.; Stangl, R.; Luther, J.; Mallouk, T. E.; Hao, S.; Humphry-Baker, R.; Comte, P.; Péchy, P.; Grätzel, M. Application of Polypyrrole as a Counter Electrode for a Dye-Sensitized Solar Cell. *J. Mater. Chem.* **2011**, *21*, 4644.

(75) Voon, L. C. L. Y.; Sandberg, E.; Aga, R. S.; Farajian, A. A.; Lew Yan Voon, L. C.;

Sandberg, E.; Aga, R. S.; Farajian, A. A. Hydrogen Compounds of Group-IV Nanosheets. *Appl. Phys. Lett.* **2010**, *97*, 163114.

(76) Houssa, M.; Scalise, E.; Sankaran, K.; Pourtois, G.; Afanas'ev, V. V; Stesmans, A. Electronic Properties of Hydrogenated Silicene and Germanene. *Appl. Phys. Lett.* **2011**, *98*, 223107.

(77) Bianco, E.; Butler, S.; Jiang, S.; Restrepo, O. D.; Windl, W.; Goldberger, J. E. Stability and Exfoliation of Germanane: A Germanium Graphane Analogue. *ACS Nano* **2013**, *7*, 4414–4421.

(78) Jiang, S.; Butler, S.; Bianco, E.; Restrepo, O. D.; Windl, W.; Goldberger, J. E. Improving the Stability and Optical Properties of Germanane via One-Step Covalent Methyl-Termination. *Nat. Commun.* **2014**, *5*, 3389.

(79) Liu, Z.; Wang, Z.; Xia, S.; Liu, Y.; Li, Z.; Qin, X.; Wang, G.; Huang, B.; Zhang, X.; Dai, Y.; Lou, Z. GeH: A Novel Material as a Visible-Light Driven Photocatalyst for Hydrogen Evolution. *Chem. Commun.* **2014**, *50*, 11046–11048.

(80) Koski, K. J.; Cui, Y.; Science, M.; States, U.; Sciences, E.; National, S.; Road, S. H.; Park, M.; States, U. The New Skinny in Two-Dimensional. **2013**, 3739–3743.

(81) Restrepo, O. D.; Krymowski, K. E.; Goldberger, J.; Windl, W. A First Principles Method to Simulate Electron Mobilities in 2D Materials. *New J. Phys.* **2014**, *16*, 105009.

(82) Jiang, S.; Arguilla, M. Q.; Cultrara, N. D.; Goldberger, J. E. Improved Topotactic Reactions for Maximizing Organic Coverage of Methyl Germanane. *Chem. Mater.* **2016**, *28*, 4735–4740.

(83) Young, J. R.; Chitara, B.; Cultrara, N. D.; Arguilla, M. Q.; Jiang, S.; Fan, F.; Johnston-Halperin, E.; Goldberger, J. E. Water Activated Doping and Transport in Multilayered Germanane Crystals. *J. Phys. Condens. Matter* **2016**, *28*, 34001.

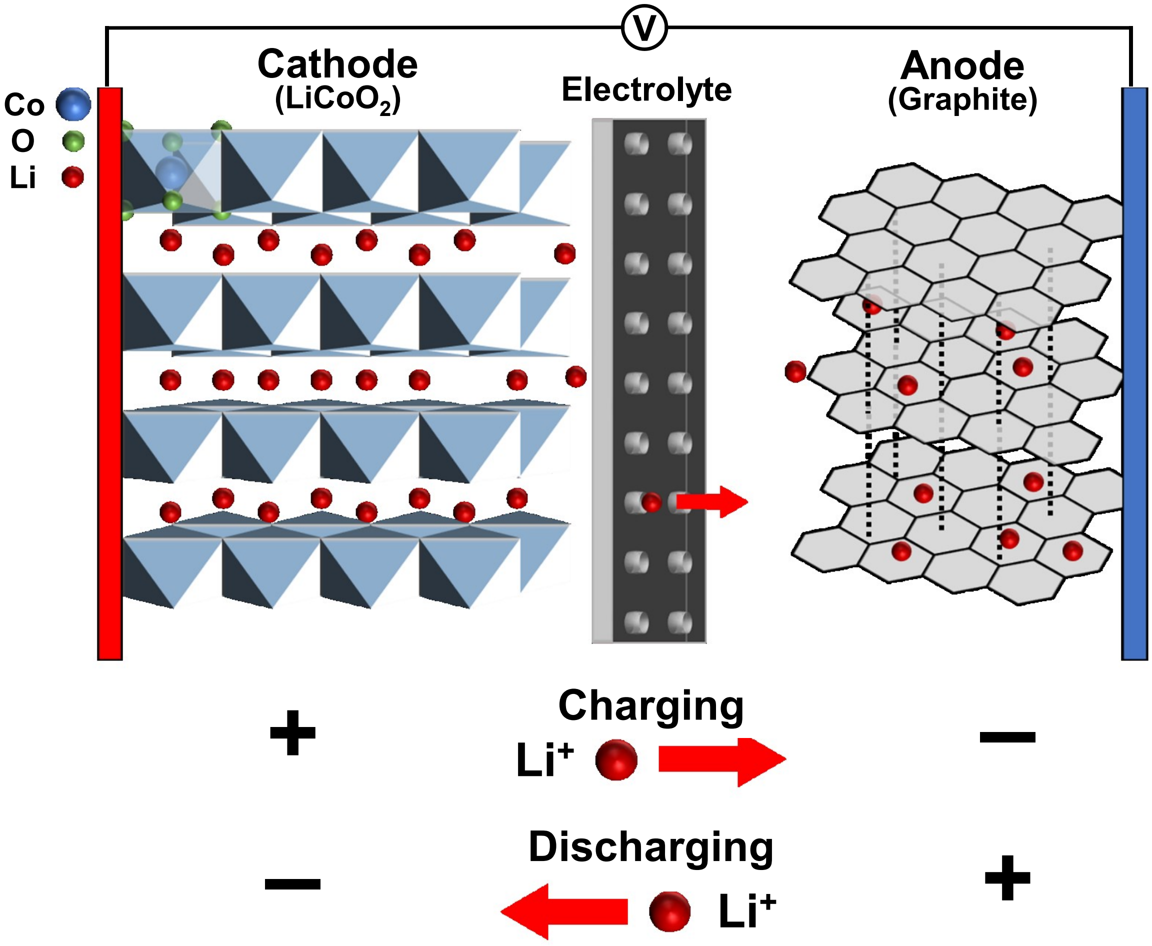

Figure 1.1: Schematic representation of a common lithium-ion battery architecture.

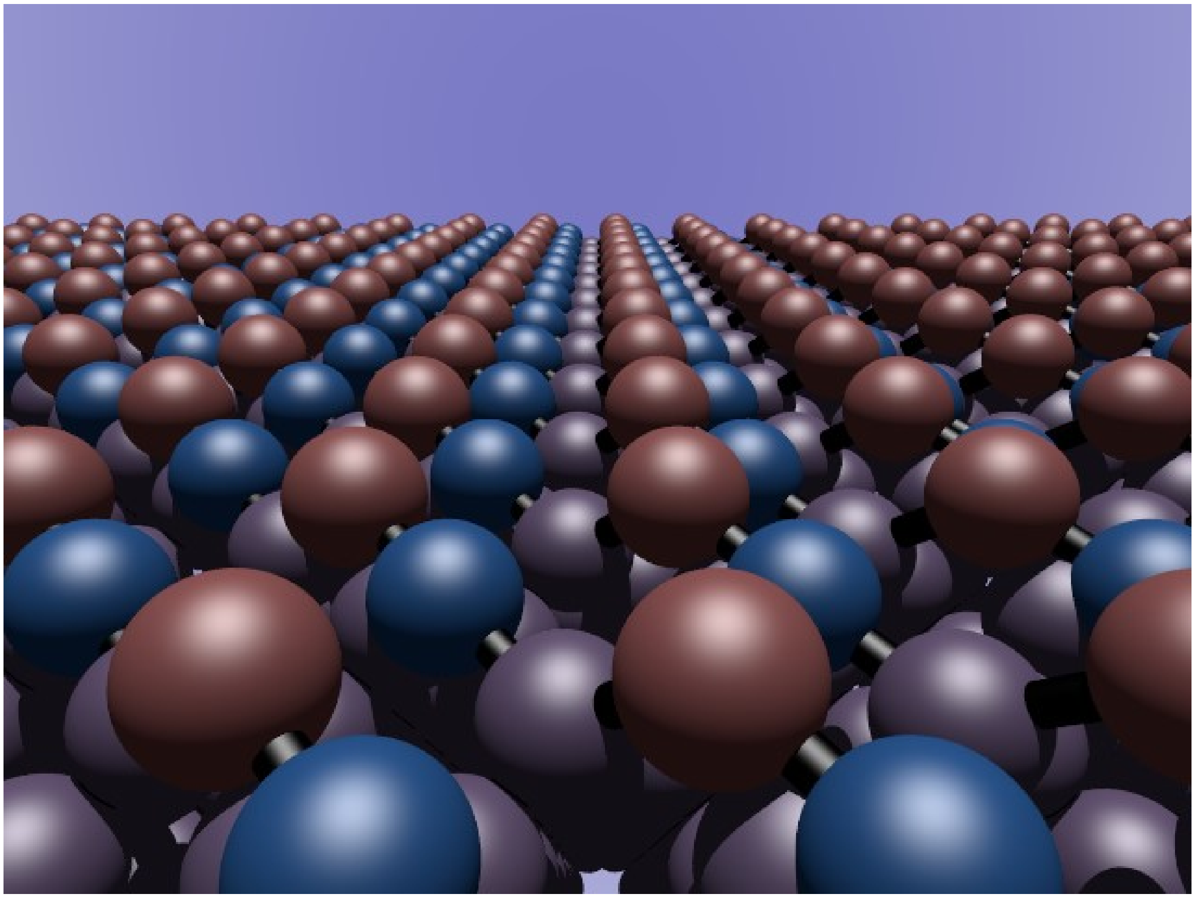

Figure 1.2: Schematic of the Ge(100) – 2 × 1 surface reconstruction over the bulk Ge atoms (purple). The surface reconstructs into rows of dimers, with an electrophilic “down” atom (blue) and a nucleophilic “up” atom (red).[16]

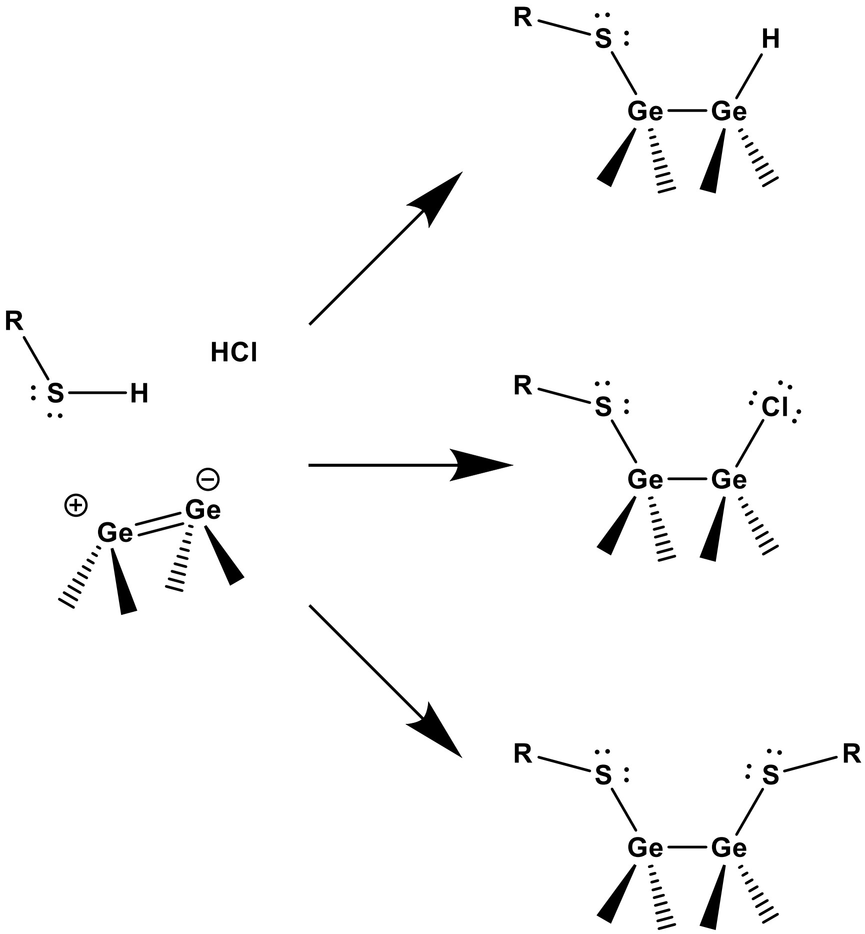

Figure 1.3: Schematic representation of the difference in reactivity between the electrophilic "down" and a nucleophilic "up" atoms. The activation energy required for thiols to bind is lower for the electrophilic atom.[19,20,22]

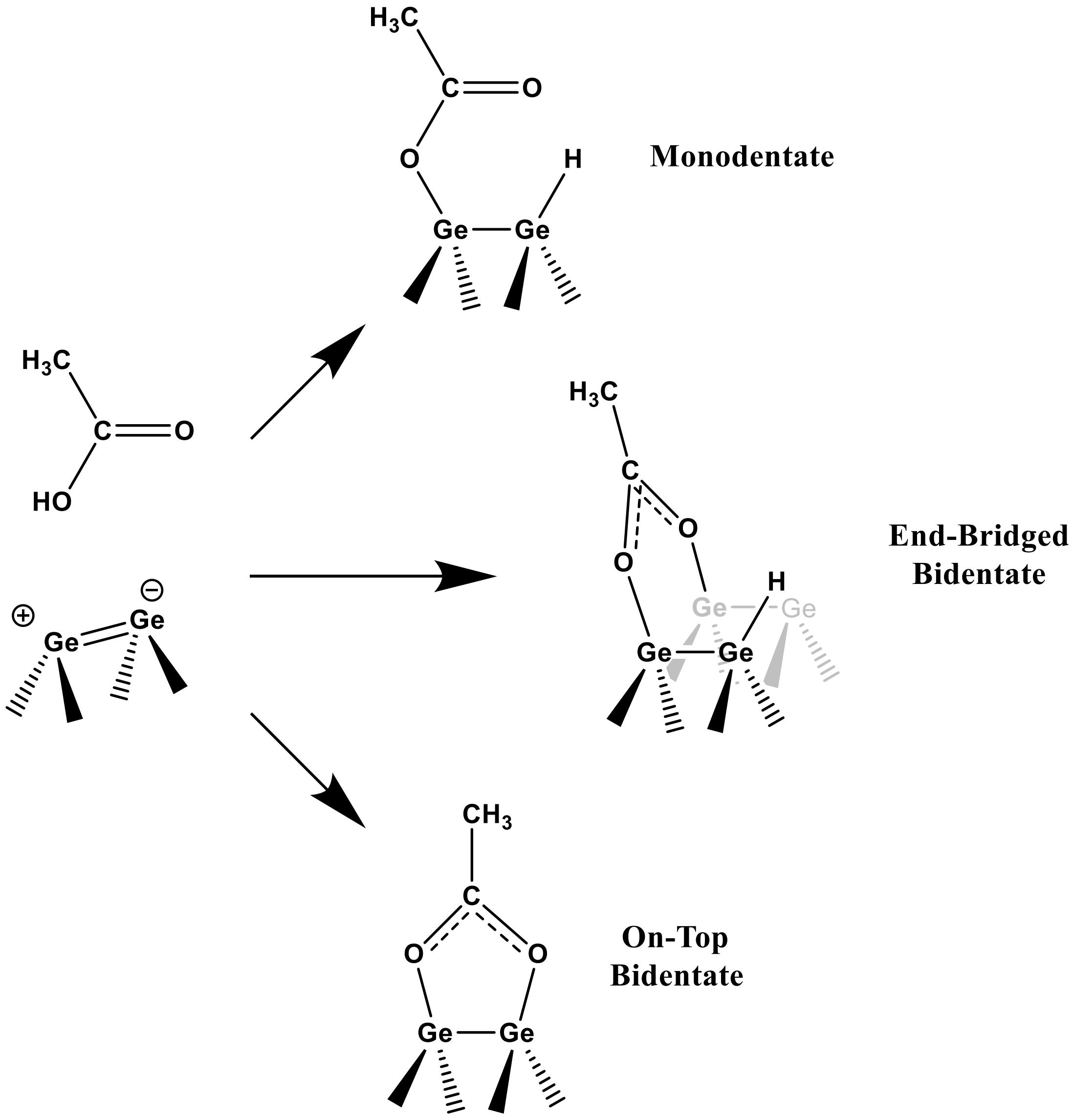

Figure 1.4: Schematic representation of carboxylic acid binding configurations on Ge(100) 2 × 1 surface dimer.[28,29]

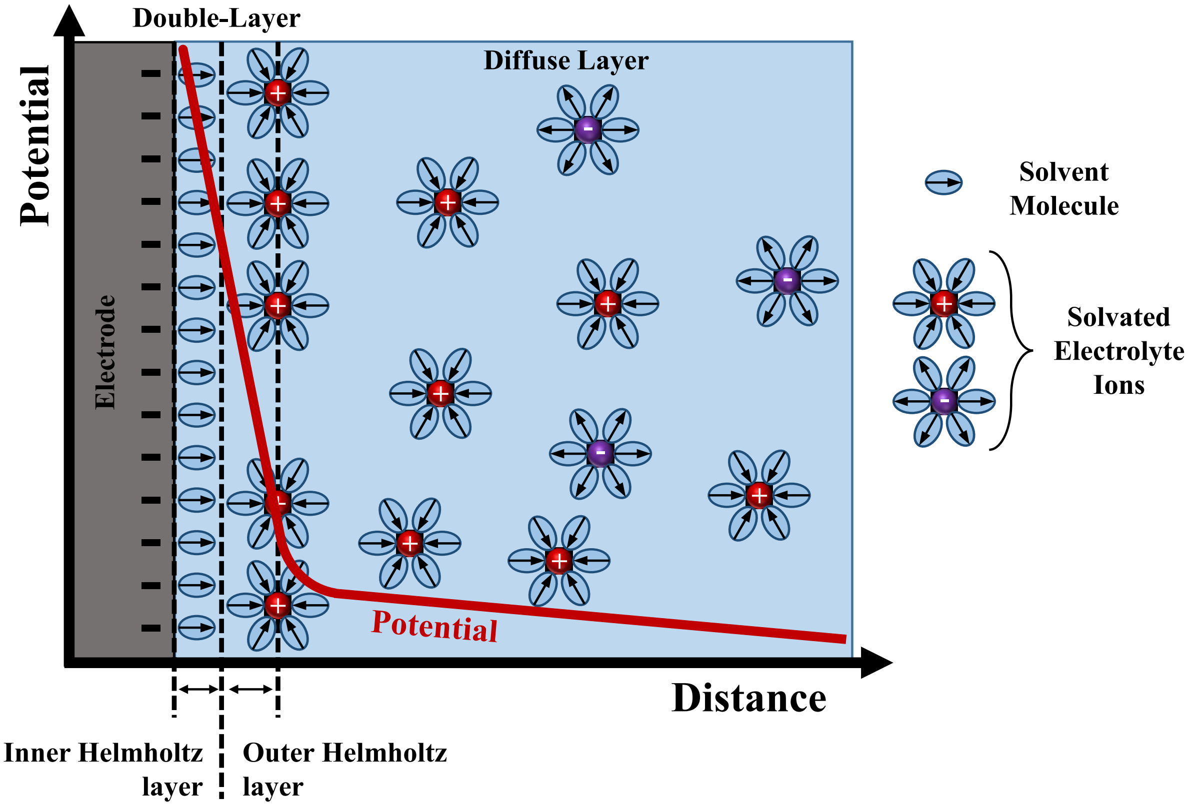

Figure 1.5: Schematic representation of the double-layer capacitance, including the inner and outer Helmholtz layers, and the diffuse layer. The exponential potential drop through the solution is depicted with a red line. The distance this potential extends into solution is described by the Debye length.[1]

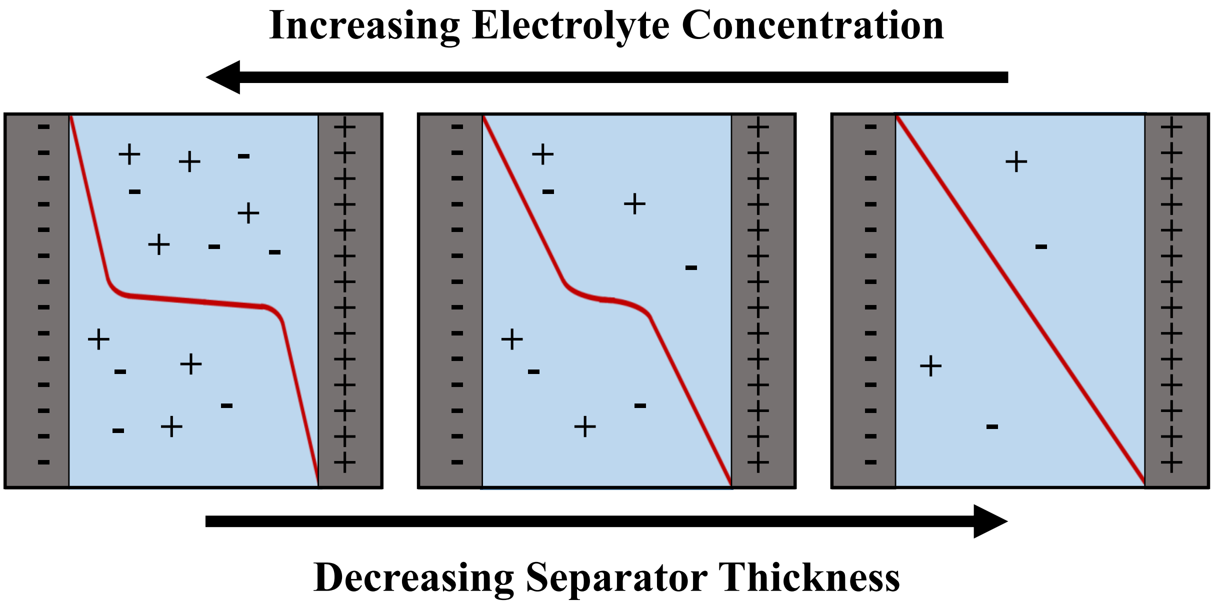

Figure 1.6: Schematic representation of the dependence between degree of potential overlap and electrolyte concentration or separator thickness.[31,33]

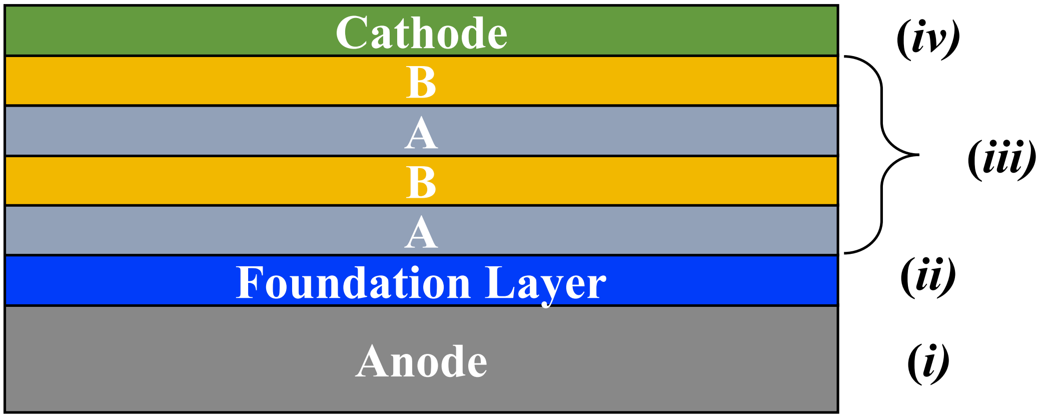

Figure 1.7: Schematic representation of the molecular battery design: (*i*) anode substrate, (*ii*) self-assembled monolayer foundation layer, (*iii*) layer-by-layer assembled of solid-state organic electrolyte, and (*iv*) cathode layer.

CHAPTER 2: Processing of an All-Surface Germanium Nanomaterial

2.1: Introduction

Two-dimensional layered materials have been extensively studied for over a decade due to phenomena that occur when electronic transport is confined within a two-dimensional plane, leading to high technological potential. Novoselov and Geim in 2004 showed that graphite can be mechanically exfoliated to form graphene, an atomically thin layer of carbon that it is stable in ambient conditions, which exhibited novel electronic and other properties unparalleled by known materials systems at the time.[1]

The field has expanded from graphene to many other materials, such as boron nitride, transition metal dichalcogenides, transition metal trichalcogenides, metal halides, oxides, III-V layered semiconductors, layered silicates, layered double hydroxides, and transition metal carbides and nitrides,[2–5] and ranging from metallic, to semi-metallic, semiconducting, and insulating. Each can display unique and interesting electronic behavior, such as superconductivity or charge density wave effects. These materials generally form stacked structures of single two-dimensional sheets that are held together *via* van der Waals interactions, while in-plane atoms are held together by networks of covalent bonds, leading to anisotropic properties. Nanosheets are capable of unique electronic, electrochemical, and photonic properties that have enabled the fabrication of transistors, battery electrodes, magnetic, and optical devices.[3,6]

Silicon has been the leading semiconducting material in the electronic device industry for half a century due to its relatively high electron mobility (~1100 cm^2/V-s) and ease of highly developed processability. Economic forces compel industry to continue to improve upon device performance, which has been done by improving material properties, such as mobility, or by increasing the numbers of transistors on single chips by scaling down the sizes of transistors. Unfortunately, the limit of silicon's capabilities is being reached and new structures and materials are needed to continue improving device performance. Two-dimensional materials offer a possible solution to this problem. While graphene, an sp^2 hybridized carbon material with extremely high carrier mobility, is attractive for device fabrication, it still has problems that limits its capabilities in transistors. For example, it lacks a natural band gap, which creates the need to create one artificially, thereby adding a layer of difficulty and cost, as well as being difficult to dope and to mass-produce.

Germanane shows interesting promise for device applications, with a direct band gap of 1.53 eV, low electron effective mass (0.07 m_e^*), and a high theoretical electron mobility of ~18,000 cm^2/Vs,[1] which is not only higher than bulk germanium (3900 cm^2/Vs) and bulk silicon, but one of the highest mobilities of any material with a band gap.[2] These properties suggest that GeH would be an ideal candidate for next-generation electronics, including transistors, supercapacitors, batteries, and photodetectors.

To capitalize on two-dimensional properties, individual sheets must be isolated *via* exfoliation or other processes, thus greatly increasing the accessible surface area, which is useful for surface-active or catalytic applications,[7,8] as well as confining the electronic transport to two dimensions and reducing the effects of stacked sheets. For many two-dimensional materials, this electron confinement affects the band structure and carrier mobility, and can lead to new interesting phenomena such as superconductivity,[9] spontaneous magnetization,[10] topological insulators,[11] Klein tunneling,[12] and the half-integer quantum Hall effect.[12]

Extensive research has been conducted on a host of two-dimensional materials to increase the success of exfoliation.[12] Large surface area single-sheets can be mechanically exfoliated by adhesive tape, however, this process is slow and unreliable. If two-dimensional materials are going to be commercially viable, they must be able to be scaled up for mass production. Large-scale liquid exfoliation yielding well-dispersed nanosheets of a wide variety of materials can be accomplished by ultrasonication in solvents and surfactants. The weak out-of-plane interactions can be overcome by high-energy vibrations to exfoliate down to a single sheet.[3] Such processes can be enhanced by bubble formation during exfoliation to yield clean separations.[13]

While germanane has garnered a great deal of attention recently due to its favorable electronic and catalytic properties, current synthesis and exfoliation techniques suffer from low yields and produce Ge particle impurities.[8,14–21] Cost-effective and high-throughput processing needs to be developed before GeH can be useful in practical applications.[3] Herein, we report a facile method for large-scale solution exfoliation and purification of GeH sheets using ultrasonication and centrifugation. This technique produces single- and multi-layered GeH structures, which are stabilized in isopropanol (IPA). Surface chemistry can then be done on these sheets in solution owing to better surface accessibility, or be used to directly fabricate devices, such as a lithium-ion anode.

2.2: Fabrication Methods of Pure Germanane Dispersions

2.2.1: Synthesis

All preparation for $CaGe_2$ was done under an argon atmosphere to minimize oxidation (oxygen and water concentrations <1 ppm). Stoichiometric amounts of Ge powder (Alfa Aesar, 99.9999%) and calcium granules (Alfa Aesar, 99.5%) were briefly homogenized *via* ball milling. The subsequent powders were then loaded into an alumina crucible (**Figure 2.1**) and sealed in a quartz ampoule under vacuum, with a typical loading of ~4 g (**Figure 2.2**), using an oxy-methane torch (Type 3A-B Torch, National Torches, Premier Industries), shown in **Figures 2.3** and **2.4**. Samples were annealed above the melting point of the binary elements at 1125 °C for 24 h in a Carbolite RHF 1400 oven (Carbolite Gero Ltd.) and cooled over the next 24 h to room temperature (**Figure 2.4**). Ingots of $CaGe_2$ were carefully selected from the reaction product using tweezers for the subsequent synthesis steps (**Figure 2.5**) to avoid including unreacted Ge and Ca particles. The remaining $CaGe_2$ ingots were intercalated with HCl at -20 °C for 5 days[16] (**Figure 2.6A**) by using a chiller water bath (VWR Polyscience 1167 Chiller / Heating Water Bath). The subsequent product was quickly poured into a vacuum filtration flask, rinsed with water three times, and then rinsed with IPA three times. The layered GeH powder was dried on the filtration flask (**Figure 2.6B**) for an additional 10 min, then dried in a septum-capped vial under vacuum for 12 h to ensure all solvent had been removed (**Figure 2.7**).

2.2.2: Exfoliation and Dispersion

Germanane powder (250 mg) was dispersed in anhydrous IPA (25 mL, Sigma Aldrich, 99.5%), which had been previously purged with nitrogen gas for 1 h. The resulting mixture was sonicated for 4 h in an ultrasonicator water bath (Branson 1510) that was maintained at 10 °C (using the chiller water bath, depicted in **Figure 2.8**) to prevent thermal degradation,[22] producing a shimmering black dispersion that was purified *via* centrifugation for 30 min at 5000 rpm (Eppendorf Centrifuge 5804 R) to remove larger particulates and elemental Ge impurities. The pale red supernatant was saved for further characterization with scanning electron microscopy, transmission electron microscopy, and Raman spectroscopy to assess the degree of exfoliation and purity. Careful handling and storage minimized oxygen exposure and contamination during subsequent processing and experimentation.

X-Ray Diffraction

Powder X-ray diffraction was performed using a Bruker D8 Discover powder X-ray diffractometer using $\mathrm{Cu}_{K\alpha}$ radiation (λ = 1.5418 Å). The XRD spectra were then referenced to the Joint Committee on Powder Diffraction Standards (JCPDS) for phase analysis. Air sensitive samples were packaged in polyethylene terephthalate (PET, Polyester, Ampac) under an Ar atmosphere.

Scanning Electron Microscopy

Germanane, dispersed in IPA, both before and after exfoliation was drop-cast onto *n*-doped Si wafers. Samples imaged with a JEOL JSM-6700F field emission scanning electron microscope with a 5 kV accelerating potential.

Transmission Electron Microscopy

Exfoliated GeH was drop-cast onto carbon-coated copper grids (-300 mesh, Electron Microscopy Sciences) and imaged on a FEI Tecnai T12 transmission electron microscope with a 120 kV accelerating potential.

Raman Spectroscopy

Confocal Raman spectroscopy was conducted with a Renishaw inVia Raman Microscope (Wotton-under-Edge, UK) using a 633 nm source and an 1800 mm^{-1} grating, coupled with a Leica DM2500 optical system and EMCCD detector. Germanane powder was imaged on a glass slide. Isopropanol-dispersed GeH was analyzed by overfilling a polydimethylsiloxane well in a glove box and sealing with a glass coverslip to ensure an air-free environment, taking care to eliminate bubbles. Dried, exfoliated GeH was analyzed by drop-casting ~500 μL IPA-dispersed GeH on a stainless steel current collector with an area of 1 cm × 1 cm until the entire surface was covered by a thin, red film and then dried under vacuum for 5 min. The sample was then sealed in a glass "sleeve" using Kapton tape and glass slides to ensure the sample was not exposed to air during transport or characterization.

2.3: Characterization of Synthesis and Dispersion of Germanane

2.3.1: Synthesis

Our synthesis of GeH sheets is based on a preparation of layered GeH described by Bianco *et al.*[16] Diffraction measurements confirm the identity of the as-synthesized $CaGe_2$ ingots, with X-ray diffraction (XRD) patterns matching reported reference patterns (JCPDS Card #00-013-0299), shown in **Figure 2.9.** There are germanium and calcium oxide impurities due to the high reactivity of calcium with trace oxygen at elevated temperatures. Fortunately, calcium oxide is easily removed in the subsequent HCl etching step. The resultant GeH powder contains layered structures with widths ranging from ~1 µm to 2 mm (**Figure 2.10B**). The XRD spectrum of the layered GeH product (**Figure 2.10C**) matches previously published patterns for GeH,[8,16,22] exhibiting a (002) peak at ~15.4°, corresponding to an interlayer spacing of 5.7 Å (**Figure 2.10A**). However, the spectrum also exhibits evidence for some crystalline Ge.

2.3.2: Impurity Identification

Multiple Raman (see **Figure 2.11A**) spectra of GeH powders taken prior to sonication at random locations (I, II, and III) exhibited a broad range of peaks, which suggests multiple forms of Ge. The peaks around 300 cm^{-1} correspond to the E_2 vibrational modes observed in the spectra of both bulk Ge and layered GeH.[16,22–24] Peaks ranging from 301 to 289 cm^{-1} indicate the presence of other Ge particulates, which are byproducts of the GeH synthesis.[25,26] The GeH Raman spectra also possess two distinct peaks at ~161 and ~228 cm^{-1}, which are found in crystalline Ge and GeH, respectively. In order to assess the lithium storage capabilities of the GeH sheets accurately, any Ge impurities needed to be removed.

2.3.3: Exfoliation and Purification

Ultrasonication has been used extensively as a tool of exfoliation for a variety of layered nanomaterials, and differential centrifugation is a common technique for separating mixed materials with varying solution stability.[3,27] Here, we use ultrasonication to exfoliate GeH, thereby increasing the surface area and solution stability of the nano-sized sheets produced. Larger particulates are subsequently removed from suspension *via* centrifugation. The sonication and centrifugation of as-synthesized GeH yield pale red dispersions (**Figure 2.11B inset**) that are stable for at least 8 months. Raman spectroscopy was used to test the purity of GeH after these processing steps. Isopropanol-dispersed GeH possess Raman peaks at 228.4 and 301.0 cm^{-1} only, while the Ge impurity peaks at 160 cm^{-1} and below 300 cm^{-1} disappear **(Figure 2.11B)**. Germanane that is drop-cast, dried, and sealed in an air-tight, glass sample holder under nitrogen exhibits the same peak at 228.4 cm^{-1} with a slight shift of the in-plane vibration from 301.0 to 302.3 cm^{-1}, which more closely resembles previously reported vibrations for dried and stacked GeH than the IPA-dispersed GeH.[16] The purity of GeH is further supported with XRD (**Figure 2.11C**), where characteristic bulk Ge peaks (shown in **Figure 2.10B**) are not present. The GeH stacking peak observed at 16.86° corresponds to an inter-layer spacing of 5.3 Å, indicating a decrease of ~0.4 Å.

Electron microscopy was used to identify the micro- and nanoscale features of the GeH sheets and assess the degree of degradation and exfoliation. Exfoliated sheets (**Figure 2.12A**) aggregate when dried and show a significant reduction in lateral size due to the forces applied by ultrasonication. **Figures 2.12B and 2.12C** show transmission electron micrographs of exfoliated GeH. While exfoliated GeH tends to aggregate as solvent evaporates, a smaller number of isolated single sheets or multi-layered stacks are found. Polydispersions were found to contain apparent single sheets that ranged in lateral dimensions from ~40 to 200 nm, and multi-sheets that ranged from ~40 nm to 1 μm.

2.4: Air-Instability

Throughout processing, observations were made noting the instability of the dispersions when introduced to air. When a GeH suspension was introduced to air for 30 sec, the nanosheets would flocculate within 24 h, however, we suspected that this result could be humidity dependent. To assess the instability mechanism, we isolated potential degradation causes by focusing on stability changes when either just oxygen or just water is included in a controlled environment.

As-synthesized GeH dispersions in IPA were prepared in 3 separate 1 mL vials, sealed in a nitrogen environment. Next, one sample was purged with oxygen gas for 10 min and 10% (v/v) of deionized water (that had been purge with nitrogen and sonicated for 10 min) was added via syringe to another samples, each vial had a final volume of 1 mL. Samples were then allowed to sit at room temperature in the dark overnight for the first observation, and for one week for the second observation.

Figure 2.13 shows the results of the GeH oxidation study. There appears to be no change upon the addition of O_2 gas after 24 h (**Figure 2.13B**) compared to the GeH (**Figure 2.13A**). The addition of water appears to have made the GeH sheets flocculate (**Figure 2.13C**), however, it is unclear whether this change in stability is due simply to interrupting GeH-IPA interactions or to chemical changes to GeH. After one week, there was no change to the O_2 gas sample, but the water sample appears to have become completely transparent (**Figure 2.13D**).

2.5: Organic Passivation of Germanane Sheets

Surface functionalization of two-dimensional sheets proves to be a promising method for altering both electronic and physical properties, and imparting new functionality (*i.e.,* biological applications).[28] Organic passivation of "all-surface" materials greatly impacts their electronic properties due to the direct influence of the covalent bond of the head group and the molecules tail-group with the entire depth of the sheet. The covalent binding of the head group will cause a shift in both the HOMO and LUMO, thus changing the sheets effective band gap. Additionally, the dipole moment and aromatic nature of the tail group is capable of influencing the Fermi level.[29,30] Surface passivation also changes the physical properties through altering surface energy, and therefore the sheets' dispersibility in various solvents.

Solution exfoliation to create dispersions of two-dimensional materials allows for large-scale surface passivation through solution processing. This process affords the possibility of a quick and cheap method to passivate these materials with various organic ligands to alter the physical and electronic properties. It is foreseeable that a large library of materials is attainable with vastly different electronic properties (*i.e.*, HOMO and LUMO levels, *p*-type and *n*-type doping, magnetics,[31,32] Spin-Hall effects,[33] and superconductivity[34]) and dispersible in a wide variety of solvents using a GeH backbone template.

2.5.1: Procedures

In Solution Passivation

As-synthesized GeH dispersions in IPA were prepared in 1 mL vials under nitrogen. Two separate vials of 1-decanethiol (C10) and 1,8-octanedithiol (C8DT) were prepared and purged under a stream of nitrogen for 5 min. All vials were transferred to an in-house glove bag and were not opened until the humidity of the bag was beneath 10%. Next, C10 and C8DT 10% (v/v) were added to the GeH solutions, each with a final volume of 1 mL. Samples were allowed to sit at room temperature in the dark overnight, although a light red (C10) and dark red (C8DT) precipitate formed after ~6 h of incubation. Next, to test whether the C10-GeH sample could redisperse in a non-polar solvent, the solution was put under vacuum for 48 h and purged with Ar for 1 h. A small liquid aliquot remained and was treated as precipitated GeH-C10. Following the removal of IPA, a hexane solution was prepared by purging anhydrous hexane (Sigma Aldrich) with nitrogen for 5 min along with the addition of molecular sieves to remove residual water. The hexane solution was then syringe injected into the GeH-C10 solution. As a control, GeH powder was sonicated in anhydrous hexane for 4 h.

Substrate Passivation

As-synthesized GeH dispersions in IPA were prepared in sealed vials in a nitrogen environment. A 10 mM C10 solution was prepared in a separate vial and purged under a stream of nitrogen for 5 min. Solvent evaporation was used to deposit a thin layer of GeH on a silicon wafer, where 3 mL of GeH in IPA was filled in a Corning tube with a well-sealed rubber top. A needle attached to a vacuum line was then punctured through the rubber top and evacuated until all IPA evaporated (~24 h). The substrate and C10 were then transferred to an in-house glove bag and were not opened until the relative humidity of the bag was less than 10%. The substrate was next transferred and incubated in the C10 solution for 24 h in the dark.

X-Ray Photoelectron Spectroscopy

Thin films samples were transferred from the glove bag to the XPS vacuum chamber (1×10^{-9} Torr) using a transfer vessel to maintain an air-free environment. Spectra were acquired using a Kratos Axis Ultra DLD photoelectron spectrometer (Manchester, UK) with a monochromatic Al K_{α} source at 300 W and a 300 μm × 700 μm spot size. A pass energy of 20 eV was used with a resolution of 0.1 eV for the high-resolution regions of S 2p and Ge 2p using 20 sweeps per region. All peaks were analyzed using CasaXPS software, fit using Gaussian-Lorentzian line shapes with a Shirley background.

2.5.2: Results and Discussion

In-Solution Passivation

We hypothesize that thiols displace hydrogen atoms on the GeH surface, similar to the observations by Maboudian and coworkers who demonstrated that 1-octadecanethiolate monolayers could be formed on germanium substrates by first passivating in hydrogen. The thiol head group displaced the surface hydrogen.[35] For GeH, we applied a similar method here by adding various alkanethiols to GeH dispersions (**Figure 2.14**). Adding C8DT to GeH dispersions (**Figure 2.14A**) caused sheets to aggregate tightly (**Figure 2.14B**). The addition of C10 also caused sheets to flocculate, however, did not aggregate as tightly (**Figure 2.14C**). Aggregated GeH-C10 could then be redispersed in hexane upon removal of IPA (**Figure 2.14D**). The GeH powder sample that was sonicated in anhydrous hexane was not dispersed.

These preliminary findings suggest that thiols displace hydrogen on the GeH surface. In the case of GeH-C8DT, sheets appear to be bound together by the organic linkers, forming a semiconducting organic framework, however, the exact structure and crystallinity is yet to be determined. Additionally, by displacing with organic monothiols (C10-GeH), the sheet surface energy can be changed, enabling dispersions in other solvents.[36–38] These results indicate that not only is surface passivation in solution possible, but presents opportunities for a wide range of applications.

Substrate Passivation

X-ray photoelectron spectroscopy (XPS) was used to investigate the germanane-thiol binding further (**Figure 2.15**). From the spectra, it is evident that C10 SAMs were formed on the GeH thin films. The S 2p region is shown in **Figure 2.15A**, indicating the presence of 2 sulfur doublets, with the first doublet (S $2p_{1/2}$ and S $2p_{3/2}$) at 162.3 and 163.5 eV corresponding to surface-bound thiolate, making up 78.7% of total thiol on the surface. The second doublet at 163.4 and 164.6 eV corresponds to a small amount of unbound thiol, at 21.3%. It is likely that the unbound thiol remains physisorbed on the surface due to insufficient rinsing. The Ge 2p peak shown in **Figure 2.15B** shows evidence for two germanium oxidation states. The peak at 1212.8 eV corresponds to the Ge^{+1} state, owing to the Ge-H bond present in unmodified GeH.[16] The peak at 1219.7 eV corresponds to the Ge^{+2} oxidation state due to Ge-S bond formation. The XPS results support that 1-decanethiol binds to the GeH surface, however, using this method it is not clear whether the entire available surface is covered with thiolates. The large number of Ge-H bonds present could be due to un-thiolated surface sites or (perhaps more likely) due to buried Ge-H bonds from germanane sheet stacking preventing thiol access. Future work should use XPS to explore GeH sheets that have been passivated in solution, as well as focusing on passivating single-sheet GeH dispersions.

2.6: Controlling Dispersions

Additional centrifugation studies were done to explore the technique's capabilities and whether it was possible to control the number of layered sheets in the dispersion. We hypothesized that dispersions centrifuged at higher speeds will possess larger fractions of smaller sheets, due to the principles behind differential centrifugation, which suggest that less stable particles will crash out more quickly than more stable particles. This difference in stability is due to differences in particle density, surface area, and favorable interactions with the solvent. Therefore, single sheets, with maximized surface area and favorable sheet-solvent interactions, would be the most favorable particle in solution. Higher centrifuge speeds should enable isolation of single-sheets in solution.

1.1.1: Procedures

Materials Processing and Instrumentation

Dispersions of GeH in IPA were centrifuged at 5, 6, 7, 8, 9, 10, 12, and 14 krpm for 10 min (MiniSpin Plus, Eppendorf) in a nitrogen glovebox and the supernatant was saved. Samples were characterized with AFM (Bruker Dimension Icon Scanning Probe Microscope) to measure average particle height and ultraviolet-visible spectroscopy (UV-Vis, Evolution 600 UV-Vis Spectrophotometer, Thermo Scientific, Waltham MA) to measure concentration changes. Three different GeH dispersions (5, 10, and 14 krpm) characterized with AFM (Bruker Dimension Icon Scanning Probe Microscope) were diluted to 1:10 by volume with IPA. Due to the air instability of GeH, an air-tight, Ar flow cell was used. A 15 μL aliquot of a diluted GeH dispersion was drop-cast on a mica substrate and dried under an Ar stream for 15 min. Data were collected using the Peakforce tapping mode with a low argon-flow to maintain a positive pressure.

Thickness and Surface Area Determination

The average thickness of dispersed germanane sheets after centrifugation was determined by analysis of atomic force topographs of sheets drop-cast and dried on a freshly cleaved mica surface under a constant stream of argon gas. A semi-automated image analysis methodology was adopted to process, to count, and to measure the germanane sheets within the image field of view. Images were flattened using a 3-point plane fitting algorithm, followed by applying a constant offset, on a line-by-line basis, such that reference points on the underlying substrate (determined by eye) were all situated at a common height. Germanane sheets were identified using a thresholding approach to select connected regions of pixels above the threshold. The number of sheets in each stack was determined using the average height of the highest 5% of pixels within each region. These heights (scaled by the expected height per germanane sheet, 0.56 nm) were averaged across all germanane stacks observed within a given image, and across multiple images analyzed, to determine the average stack size for a particular centrifugation condition.

2.6.1: Results and Discussion

Atomic force microscopy was used to measure heights of the GeH particles. Average heights and surface areas were extracted from the micrographs using the image processing method described above. Four, four, and two micrographs were used for 5, 10, and 14 krpm samples, respectively (all micrographs and processed images are shown in **Appendix A**), and representative micrographs are shown in **Figure 2.16**. Image processing identified 63, 12, and 33 particles for 5, 10, and 14 krpm samples, respectively, with average heights of 13.1, 1.4, and 2.3 nm, respectively, corresponding to an average layered stack of 23, 2.5, and 4.1 sheets, respectively (**Figure 2.17**). The results indicate that the number of sheets in the layered germanane particles decreases with increasing centrifugation speeds and approaches single-sheet dispersions.

Ultraviolet-visible absorption spectroscopy (UV-Vis) results show a maximum peak intensity at ~305 nm and an absorption offset at ~510 nm, as seen in **Figure 2.18A**. As the centrifuge speed increases, the intensity drops proportionally; this can be visualized better in **Figure 2.18B**, where the maximum intensities at 305 nm from the various spectra is plotted against centrifuge speed. From this plot, there appears to be a linear relationship between centrifuge speed and absorption, corresponding to decreases in GeH concentration.

Germanane sheets are stabilized in IPA through interactions between hydrogens on the GeH surface and the oxygen of the IPA molecule. Due to this hydrogen-binding phenomenon, stability of sheets in solution is surface dependent. Therefore, particles with a higher degree of surface area are more stable in solution. As the centrifugal force is increased (higher centrifugal speeds), less stable particles are pulled from solution at higher rates than more stable particles. While this proves to be a reliable method to producing dispersions with fewer-layered GeH particles, this differential centrifugation causes all particles to gradually precipitate, reducing concentration.

2.7: Conclusions and Prospects

Germanane is a promising material for next-generation devices; however, further steps are required to enable facile, large-scale implementation. In this work, GeH was synthesized in accordance with previously published methods and found to contain bulk germanium particle impurities. Ultrasonication and centrifugation were used to exfoliate and to suspend germanane particles in solution, while simultaneously separating sheets from impurities. This technique was expanded to show that increasing centrifugation speed decreases the number of sheets in dispersed layered GeH particles, indicating that a dispersion of solely single-sheets may be attainable. The mechanism of air-instability, which was only briefly explored, revealed that water causes sheets to flocculate and eventually degrade entirely. This degradation issue needs to be explored in more detail to determine if the initial instability is related to disruption of the interactions between IPA and GeH or due to water-induced oxidation.

Surface functionalization of dispersed GeH nanosheets with organics was also briefly explored. We found evidence to support that displacement of hydrogen on the germanane surface by alkanethiols was possible. This passivation can be exploited to alter surface energy, thereby enabling rediserpsion in other solvents. Specifically, by depositing C10, we could change the suspension solvent from IPA to hexane. Additionally, through the use of C8DT, GeH nanosheets can be bound together, forming a semiconductor organic framework. This surface passivation of sheets while they are dispersed will be useful for large-scale fabrication of germanane nanosheets with various electronic properties and surface energies.

2.8: References

(1) Novoselov, K. S.; Geim, A. K.; Morozov, S. V.; Jiang, D.; Zhang, Y.; Dubonos, S. V.; Grigorieva, I. V.; Firsov, A. A. Electric Field Effect in Atomically Thin Carbon Films. *Science* **2004**, *306*, 666–669.

(2) Lotya, M.; Hernandez, Y.; King, P. J.; Smith, R. J.; Nicolosi, V.; Karlsson, L. S.; Blighe, F. M.; De, S.; Wang, Z.; McGovern, I. T.. Liquid Phase Production of Graphene by Exfoliation of Graphite in Surfactant/Water Solutions. *J. Am. Chem. Soc.* **2009**, *131*, 3611–3620.

(3) Nicolosi, V.; Chhowalla, M.; Kanatzidis, M. G.; Strano, M. S.; Coleman, J. N. Liquid Exfoliation of Layered Materials. *Science* **2013**, *340*, 1226419.

(4) Mashtalir, O.; Naguib, M.; Mochalin, V. N.; Dall'Agnese, Y.; Heon, M.; Barsoum, M. W.; Gogotsi, Y. Intercalation and Delamination of Layered Carbides and Carbonitrides. *Nat. Commun.* **2013**, *4*, 1716.

(5) Urbankowski, P.; Anasori, B.; Makaryan, T.; Er, D.; Kota, S.; Walsh, P. L.; Zhao, M.; Shenoy, V. B.; Barsoum, M. W.; Gogotsi, Y. Synthesis of Two-Dimensional Titanium Nitride Ti4N3 (MXene). *Nanoscale* **2016**, *8*, 11385–11391.

(6) Cunningham, G.; Lotya, M.; Cucinotta, C. S.; Sanvito, S.; Bergin, S. D.; Menzel, R.; Shaffer, M. S. P.; Coleman, J. N. Solvent Exfoliation of Transition Metal Dichalcogenides: Dispersibility of Exfoliated Nanosheets Varies Only Weakly between Compounds. *ACS Nano* **2012**, *6*, 3468–3480.

(7) Osada, M.; Sasaki, T. Two-Dimensional Dielectric Nanosheets: Novel Nanoelectronics From Nanocrystal Building Blocks. *Adv. Mater.* **2012**, *24*, 210–228.

(8) Liu, Z.; Wang, Z.; Xia, S.; Liu, Y.; Li, Z.; Qin, X.; Wang, G.; Huang, B.; Zhang, X.; Dai, Y. GeH: A Novel Material as a Visible-Light Driven Photocatalyst for Hydrogen Evolution. *Chem. Commun.* **2014**, *50*, 11046–11048.

(9) Wilson, J. A.; Yoffe, A. D. The Transition Metal Dichalcogenides Discussion and Interpretation of the Observed Optical, Electrical and Structural Properties. *Adv. Phys.* **1969**, *18*, 193–335.

(10) Clarke, S. J.; Adamson, P.; Herkelrath, S. J. C.; Rutt, O. J.; Parker, D. R.; Pitcher, M. J.; Smura, C. F. Structures, Physical Properties, and Chemistry of Layered Oxychalcogenides and Oxypnictides. *Inorg. Chem.* **2008**, *47*, 8473–8486.

(11) Hasan, M. Z.; Kane, C. L. *Colloquium* : Topological Insulators. *Rev. Mod. Phys.* **2010**, *82*, 3045–3067.

(12) Geim, A. K. Graphene: Status and Prospects. *Science* **2009**, *324*, 1530–1534.

(13) Gao, L.; Ren, W.; Xu, H.; Jin, L.; Wang, Z.; Ma, T.; Ma, L.-P.; Zhang, Z.; Fu, Q.; Peng, L.-M. Repeated Growth and Bubbling Transfer of Graphene with Millimetre-Size Single-Crystal Grains Using Platinum. *Nat. Commun.* **2012**, *3*, 699.

(14) Voon, L. C. L. Y.; Sandberg, E.; Aga, R. S.; Farajian, A. A.; Lew Yan Voon, L. C.; Sandberg, E.; Aga, R. S.; Farajian, A. A. Hydrogen Compounds of Group-IV Nanosheets. *Appl. Phys. Lett.* **2010**, *97*, 163114.

(15) Houssa, M.; Scalise, E.; Sankaran, K.; Pourtois, G.; Afanas'ev, V. V; Stesmans, A. Electronic Properties of Hydrogenated Silicene and Germanene. *Appl. Phys. Lett.* **2011**, *98*, 223107.

(16) Bianco, E.; Butler, S.; Jiang, S.; Restrepo, O. D.; Windl, W.; Goldberger, J. E. Stability and Exfoliation of Germanane: A Germanium Graphane Analogue. *ACS Nano* **2013**, *7*, 4414–4421.

(17) Jiang, S.; Butler, S.; Bianco, E.; Restrepo, O. D.; Windl, W.; Goldberger, J. E. Improving the Stability and Optical Properties of Germanane via One-Step Covalent Methyl-Termination. *Nat. Commun.* **2014**, *5*, 3389.

(18) Koski, K. J.; Cui, Y.; Science, M.; States, U.; Sciences, E.; National, S.; Road, S. H.; Park, M.; States, U. The New Skinny in Two-Dimensional. **2013**, 3739–3743.

(19) Restrepo, O. D.; Krymowski, K. E.; Goldberger, J.; Windl, W. A First Principles Method to Simulate Electron Mobilities in 2D Materials. *New J. Phys.* **2014**, *16*, 105009.

(20) Jiang, S.; Arguilla, M. Q.; Cultrara, N. D.; Goldberger, J. E. Improved Topotactic Reactions for Maximizing Organic Coverage of Methyl Germanane. *Chem. Mater.* **2016**, *28*, 4735–4740.

(21) Young, J. R.; Chitara, B.; Cultrara, N. D.; Arguilla, M. Q.; Jiang, S.; Fan, F.; Johnston-Halperin, E.; Goldberger, J. E. Water Activated Doping and Transport in Multilayered Germanane Crystals. *J. Phys. Condens. Matter* **2016**, *28*, 34001.

(22) Jiang, S.; Bianco, E.; Goldberger, J. E. The Structure and Amorphization of Germanane. *J. Mater. Chem. C* **2014**, *2*, 3185–3188.

(23) Parker, J. H.; Feldman, D. W.; Ashkin, M. Raman Scattering by Silicon and Germanium. *Phys. Rev.* **1967**, *155*, 712–714.

(24) Bermejo, D.; Cardona, M. Raman Scattering in Pure and Hydrogenated Amorphous

Germanium and Silicon. *J. Non. Cryst. Solids* **1979**, *32*, 405–419.

(25) Wang, X.; Shakouri, A.; Yu, B.; Sun, X.; Meyyappan, M. Study of Phonon Modes in Germanium Nanowires. *J. Appl. Phys.* **2007**, *102*, 14304.

(26) Pal, U.; Serrano, J. G. Raman and Infrared Spectroscopy of Ge Nanoparticles Embedded in ZnO Matrix. *Appl. Surf. Sci.* **2005**, *246*, 23–29.

(27) Ko, J. S.; Doan-Nguyen, V. V. T.; Kim, H.; Muller, G. A.; Serino, A. C.; Weiss, P. S.; Dunn, B. S. $Na_2Ti_3O_7$ Nanoplatelets and Nanosheets Derived from a Modified Exfoliation Process for Use as a High Capacity Sodium-Ion Negative Electrode. *ACS Appl. Mater. Interfaces* **2016**, *9*, 1416–1425.

(28) Georgakilas, V.; Otyepka, M.; Bourlinos, A. B.; Chandra, V.; Kim, N.; Kemp, K. C.; Hobza, P.; Zboril, R.; Kim, K. S. Functionalization of Graphene: Covalent and Non-Covalent Approaches, Derivatives and Applications. *Chem. Rev.* **2012**, *112*, 6156–6214.

(29) Arefi, H. H.; Nolan, M.; Fagas, G. Role of the Head And/or Tail Groups of Adsorbed−[$X^{\text{Head Group}}$]–Alkyl–[$X^{\text{Tail Group}}$] [X = O(H), S(H), $NH_{(2)}$] Chains in Controlling the Work Function of the Functionalized H:Si(111) Surface. *J. Phys. Chem. C* **2015**, *119*, 11588–11597.

(30) He, T.; Ding, H.; Peor, N.; Lu, M.; Corley, D. A.; Chen, B.; Ofir, Y.; Gao, Y.; Yitzchaik, S.; Tour, J. M. Silicon/Molecule Interfacial Electronic Modifications. *J. Am. Chem. Soc.* **2008**, *130*, 1699–1710.

(31) Zhao, J.; Zeng, H.; Wang, J.-T.; Lazzeri, M.; Mauri, F.; Li, S.; Huang, H.; Zu, X.; Ahmed, A. S.; Katoch, J. Two-Dimensional Germanane and Germanane Ribbons: Density Functional Calculation of Structural, Electronic, Optical and Transport Properties and the

Role of Defects. *RSC Adv.* **2016**, *6*, 28298–28307.

(32) Sun, M.; Ren, Q.; Zhao, Y.; Wang, S.; Yu, J.; Tang, W. Magnetism in Transition Metal-Substituted Germanane: A Search for Room Temperature Spintronic Devices. *J. Appl. Phys.* **2016**, *113*, 1–7.

(33) Ma, Y.; Dai, Y.; Wei, W.; Huang, B.; Whangbo, M.-H. Strain-Induced Quantum Spin Hall Effect in Methyl-Substituted Germanane $GeCH_3$. *Sci. Rep.* **2015**, *4*, 7297.

(34) Davari Esfahani, M. M.; Oganov, A. R.; Niu, H.; Zhang, J. Superconductivity and Unexpected Chemistry of Germanium Hydrides under Pressure. *Phys. Rev. B* **2017**, *95*, 134506.

(35) Han, S. M.; Ashurst, W. R.; Carraro, C.; Maboudian, R. Formation of Alkanethiol Monolayer on Ge(111). *J. Am. Chem. Soc.* **2001**, *123*, 2422–2425.

(36) Hacker, C. A. Modifying Electronic Properties at the Silicon–Molecule Interface Using Atomic Tethers. *Solid. State. Electron.* **2010**, *54*, 1657–1664.

(37) Kim, J.; Rim, Y. S.; Liu, Y.; Serino, A. C.; Thomas, J. C.; Chen, H.; Yang, Y.; Weiss, P. S. Interface Control in Organic Electronics Using Mixed Monolayers of Carboranethiol Isomers. *Nano Lett.* **2014**, *14*, 2946–2951.

(38) Andrews, A. M.; Liao, W.-S.; Weiss, P. S. Double-Sided Opportunities Using Chemical Lift-Off Lithography. *Acc. Chem. Res.* **2016**, *49*, 1449–1457.

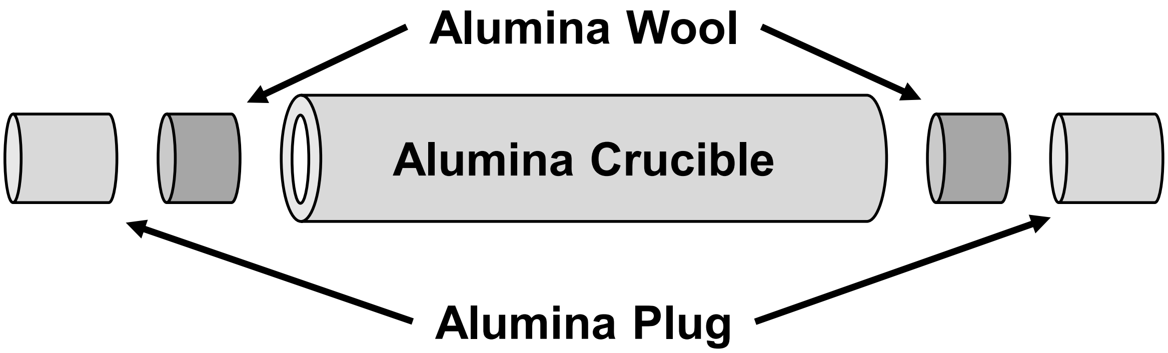

Figure 2.1: Schematic representation of alumina crucible used in the high-temperature solid-state synthesis of $CaGe_2$. One side of the crucible is capped with an alumina plug and alumina wool. Stoichiometric amounts of calcium and germanium powder are then poured into the open end, and capped with alumina wool and an alumina plug. Both the wool and plug are necessary to prevent leaking of molten germanium-calcium during synthesis, as calcium leaks would devitrify the quartz ampule.

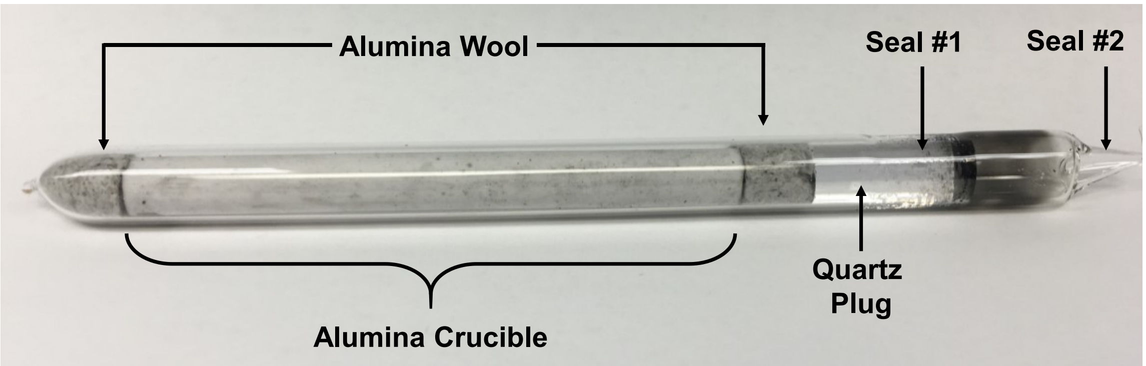

Figure 2.2: Quartz ampule used for high temperature solid-state synthesis of $CaGe_2$. Quartz tubes that are previously sealed on one end (left side of pictured tube) are packed in order from left to right, starting with alumina wool. Next, an alumina tube crucible (that had been previously packed with germanium and calcium powder, as illustrated in **Figure 2.1**) is added, followed by alumina wool, and lastly a quartz plug. Two seals are made with an oxy-methane torch (**Figure 2.3**), starting with a seal around the quartz plug (Seal #1) and then the tube is closed off with Seal #2.

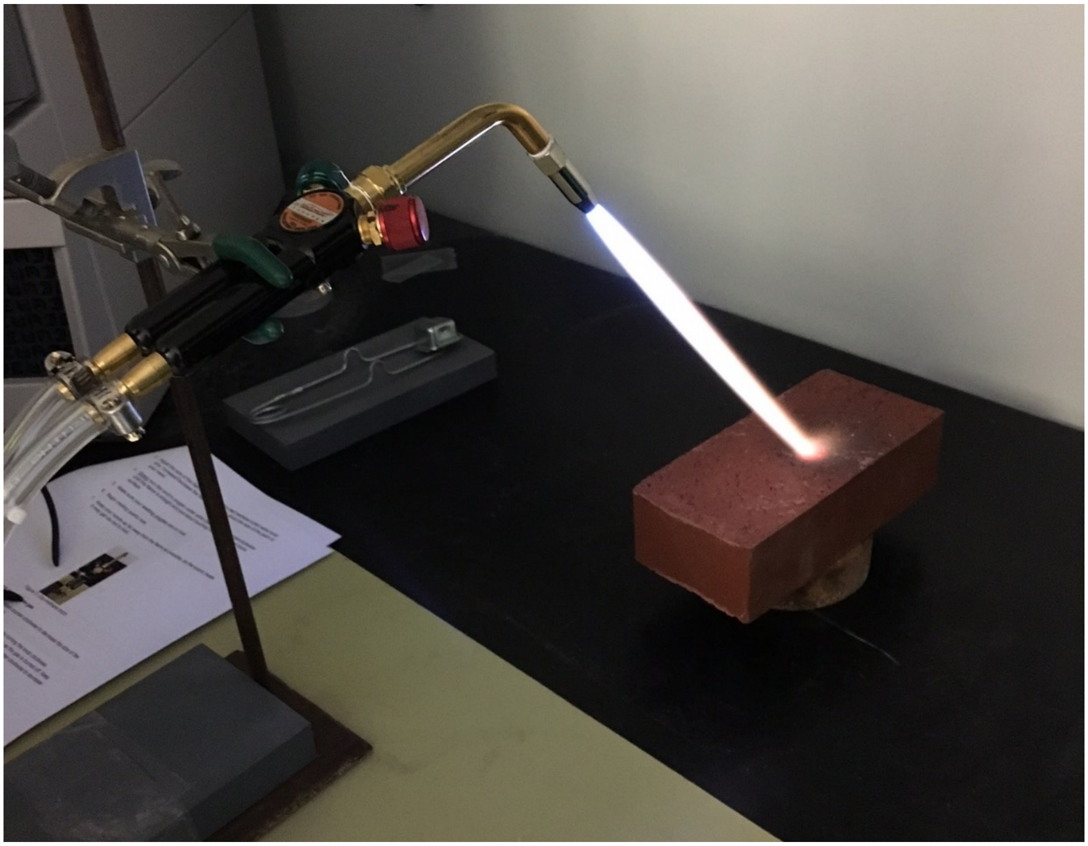

Figure 2.3: Oxy-methane torch used for sealing quartz ampules. The size of the flame is a sufficient indicator of heat produced; the pictured flame size is adequate size. The brick shown here works well as a heat sink.

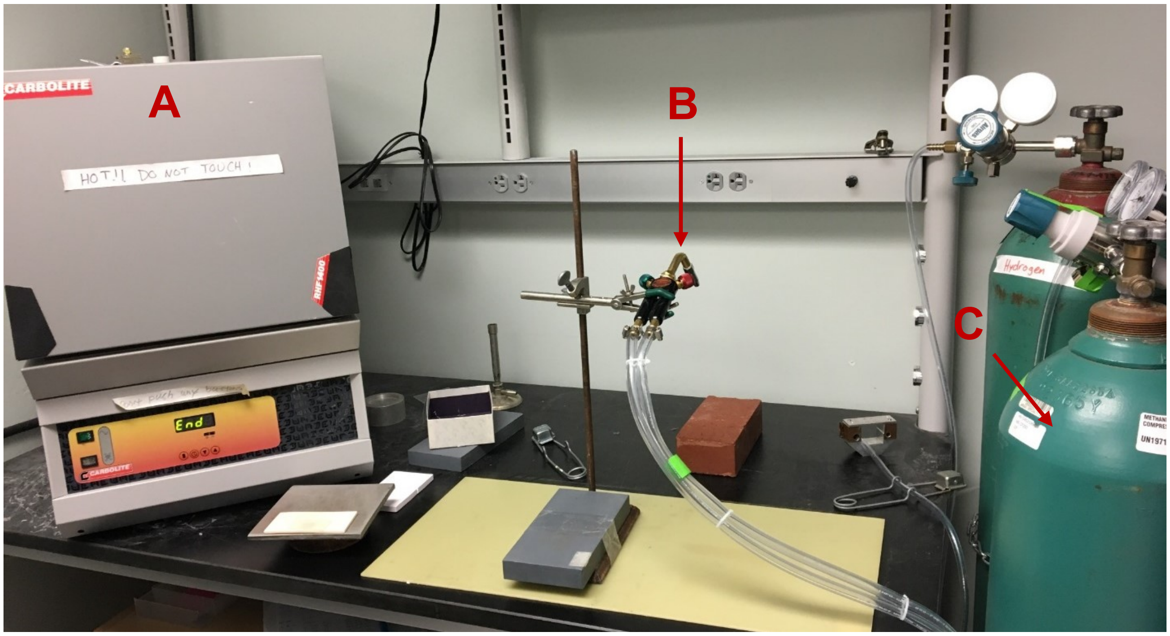

Figure 2.4: Work area including (A) high temperature oven used for synthesis of $CaGe_2$, (B) oxy-methane torch used for sealing quartz ampules, and (C) methane gas used for torch. Oxygen gas is not included in this area due to safety considerations.

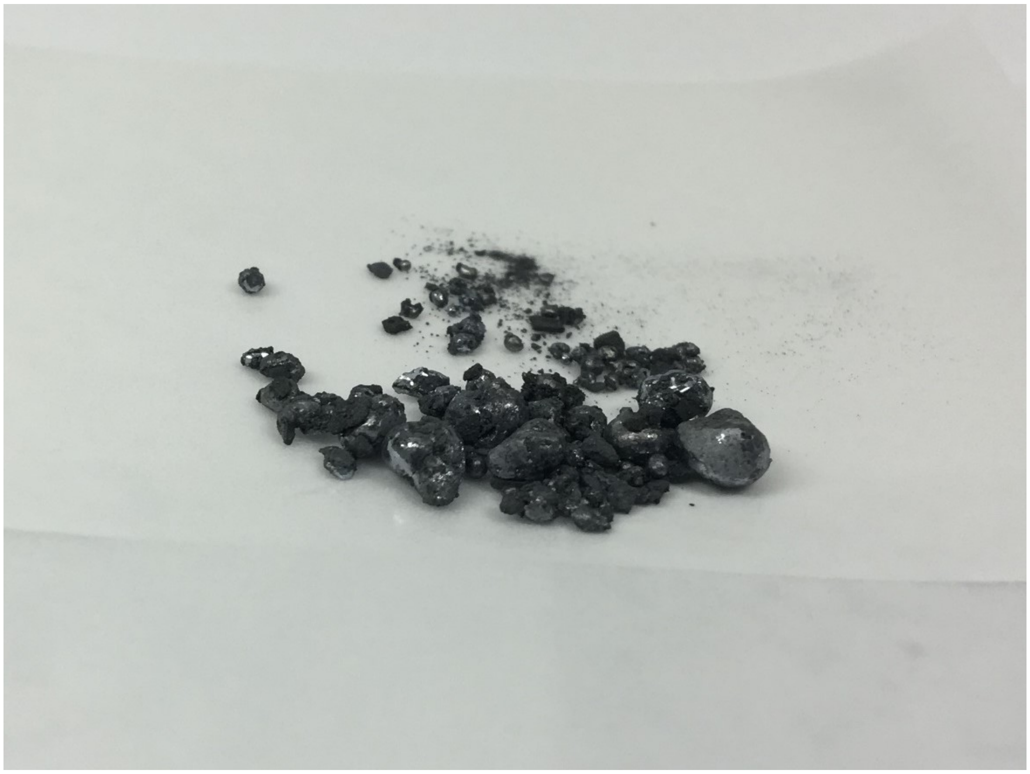

Figure 2.5: Solid-state synthesis of $CaGe_2$ produced many sizes of particles. Larger ingots were selected using tweezers for subsequent synthesis steps in order to reduce the amount of germanium/calcium impurities in later steps.

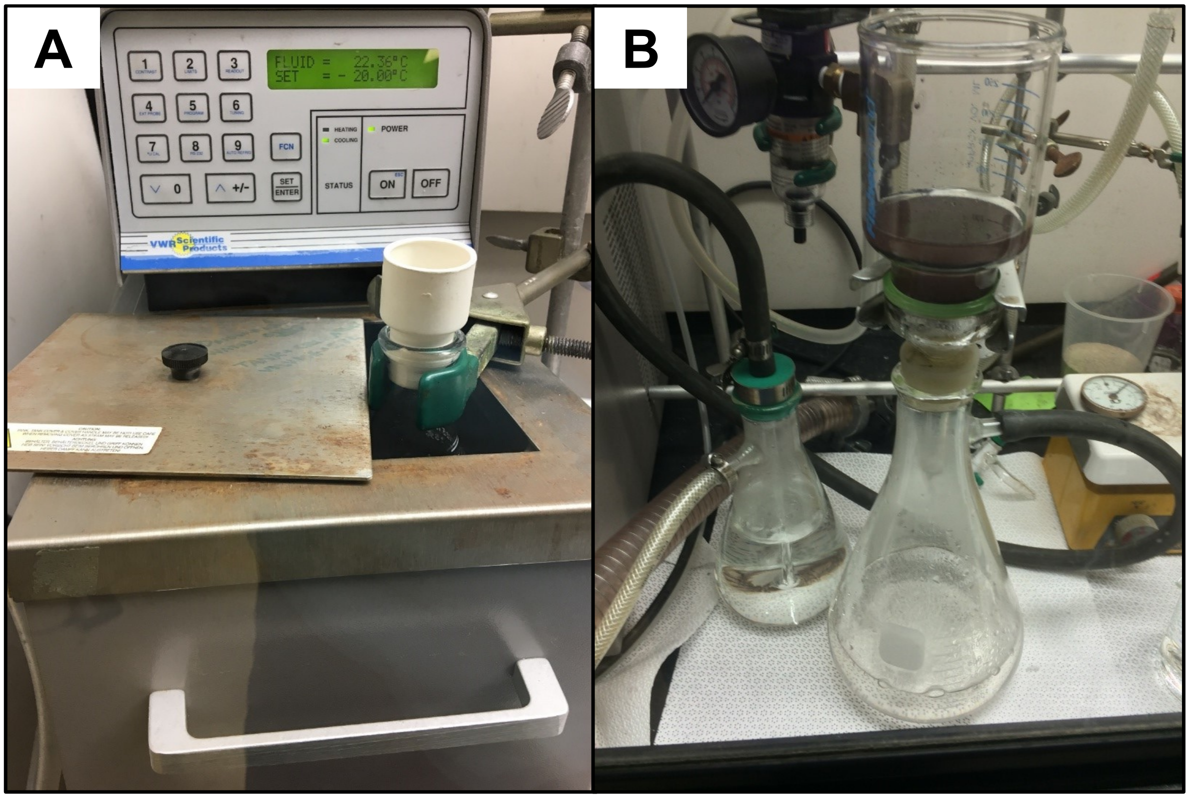

Figure 2.6: (A) The $CaGe_2$ ingots were placed in a 37% HCl bath at -20 ˚C for 5 days. The cooling bath pictured is filled with distilled water and ethylene glycol in a 1:1 ratio. Hydrochloric acid was poured into a 250 mL Erlenmeyer flask and allowed to chill for 12 h prior to adding $CaGe_2$. After the intercalation step (B), the now dispersed product was quickly poured into a vacuum filtration setup. A water bubbler was employed to capture residual HCl.

Figure 2.7: The final germanane (GeH) product is a powder consisting of large and fine flakes.

Figure 2.8: Ultrasonication apparatus used to solution exfoliate germanane sheets. The same bath chiller used previously in the $CaGe_2$ synthesis is used here, except it is filled entirely with deionized water. The chiller cycles water through the bath sonicator to maintain a water temperature of 10 ˚C and prevent thermal degradation of the sheets.

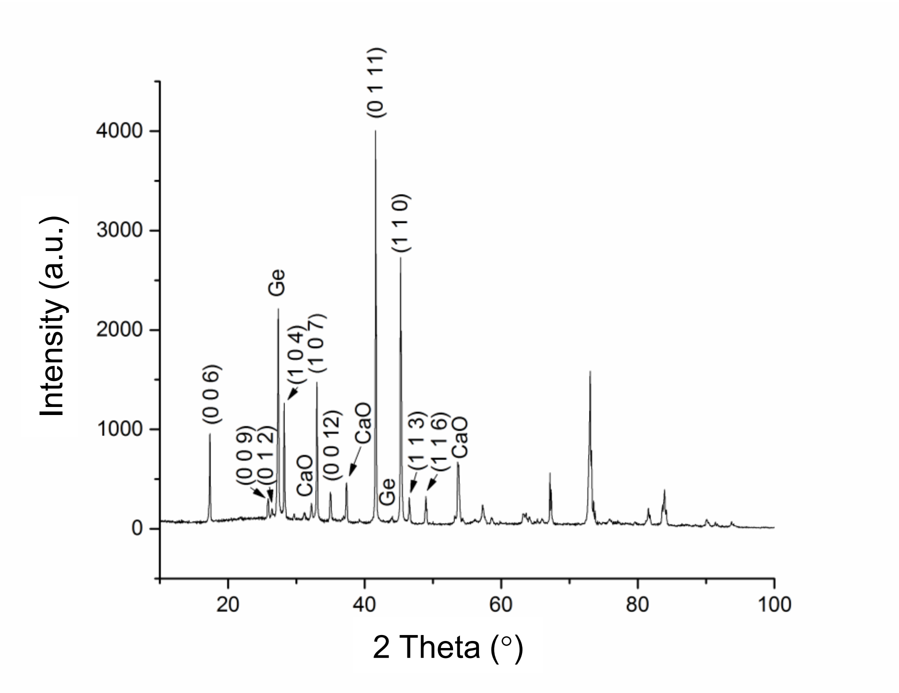

Figure 2.9: Powder X-ray diffraction of a crushed $CaGe_2$ ingot. The peaks index to $CaGe_2$ with some impurity peaks present (CaO and Ge).

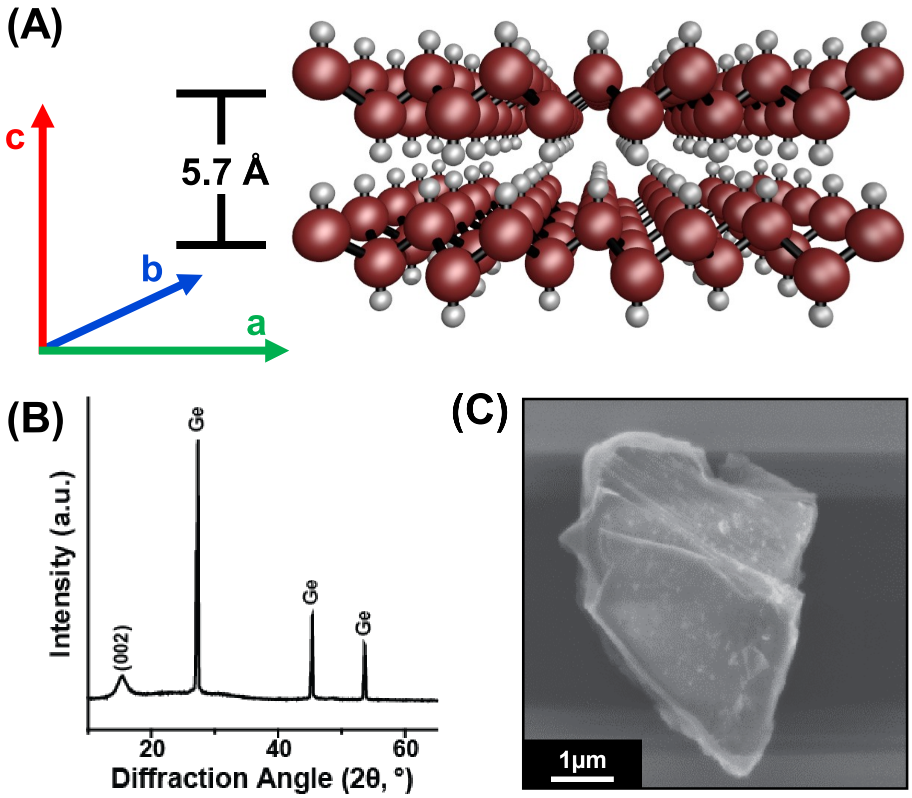

Figure 2.10: (A) Schematic representation of the stacked germanane structure. (B) Scanning electron micrograph of layered germanane. (C) X-ray diffraction spectrum of as-synthesized germanane with a stacking peak at ~15.4° corresponding to an approximate peak spacing of 5.7 Å. The remaining peaks are characteristic of elemental Ge impurities.

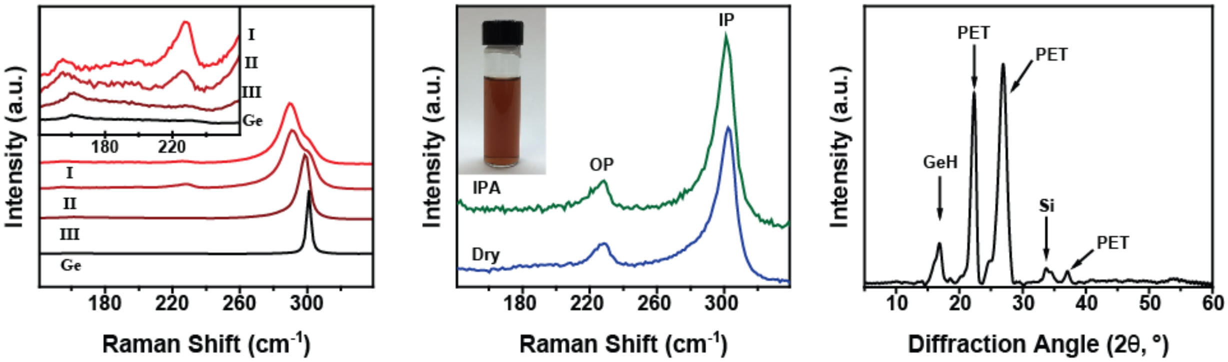

Figure 2.11: (A) Raman spectra of as-synthesized germanane (GeH) powder. Three different regions (I, II, and III) of the powder were sampled and referenced to a bulk Ge wafer (Ge). (B) Raman spectra of exfoliated GeH dispersed in IPA (green, top) and dry GeH (blue, bottom), enclosed between glass slides. The in-plane (IP) and out-of-plane (OP) Ge vibrations are highlighted. The inset is a picture of the pale-red dispersion of GeH in IPA, which is stable for at least 8 months. (C) X-ray diffraction spectra of GeH dried on a Si wafer and sealed in a polyethylene terephthalate (PET) envelope under Ar.

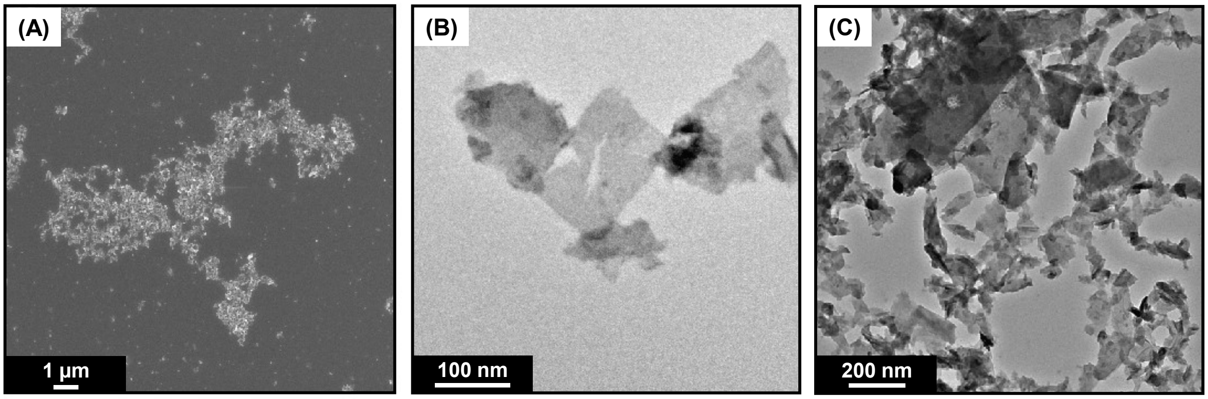

Figure 2.12: (A) Scanning electron micrograph of GeH after sonication and centrifugation. (B, C) Transmission electron micrographs of GeH post-sonication and centrifugation, respectively.

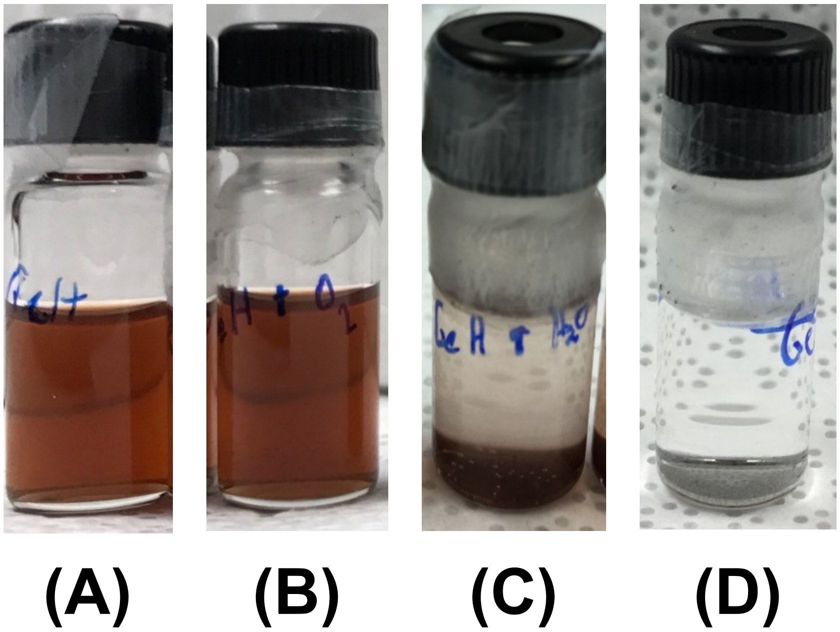

Figure 2.13: Germanane dispersed in isopropanol before (A) and after the addition of (B) O_2 gas after 24 h, (C) deionized water after 24 h, and (D) deionized water after 7 days.

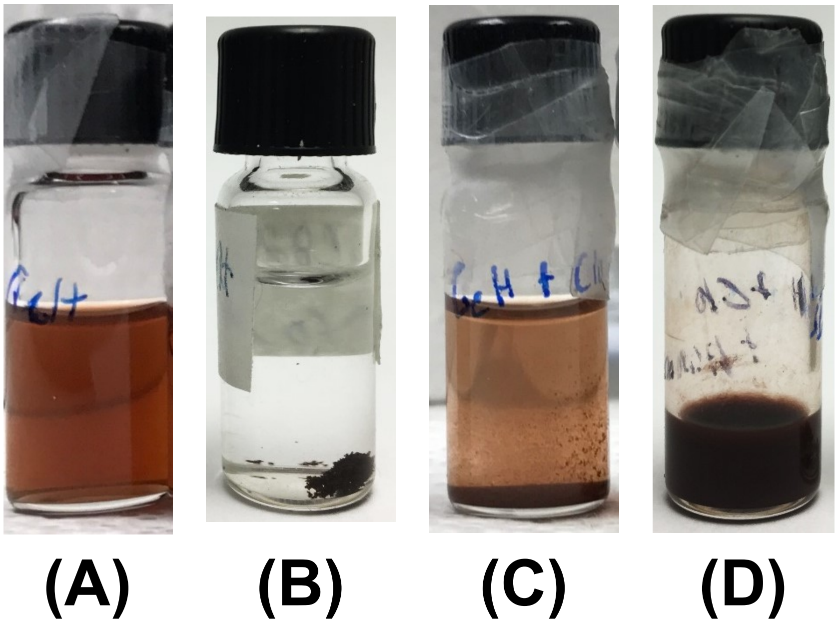

Figure 2.14: (A) Dispersion of germanane with (B) octanedithiol and (C) decanethiol added. The decanethiol germanane sample was dried under vacuum and (D) re-dispersed in anhydrous hexane.

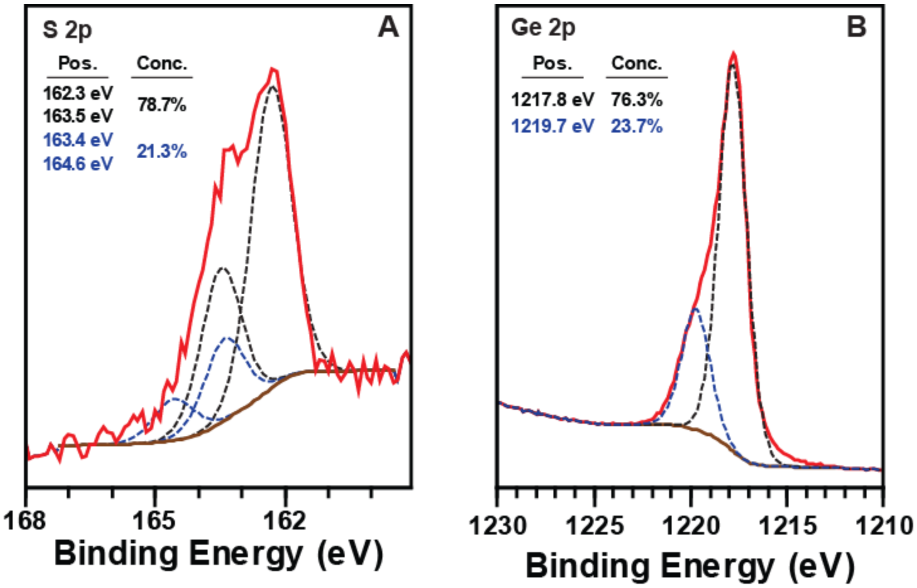

Figure 2.15: High-resolution X-ray photoelectron spectroscopy of thiolated germanane thin films deposited on a silicon wafer substrate, highlighting (A) S 2p and (B) Ge 2p.

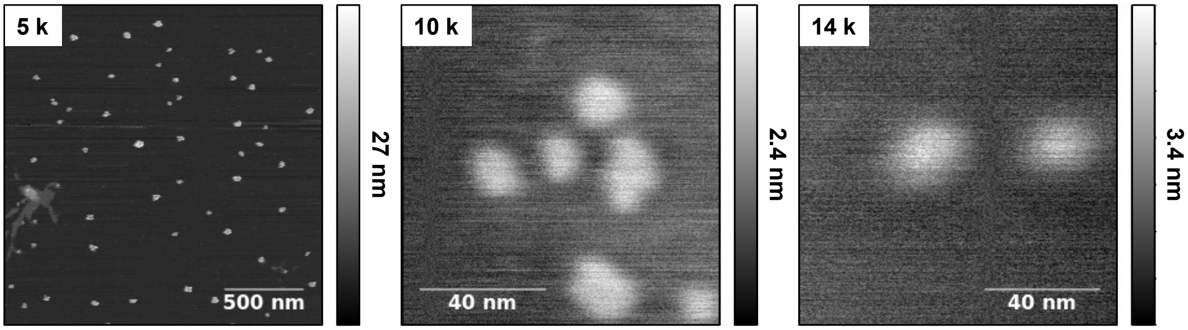

Figure 2.16: Atomic force micrographs of dried germanane dispersions that were previously centrifuged at 5, 10, and 14 krpm.

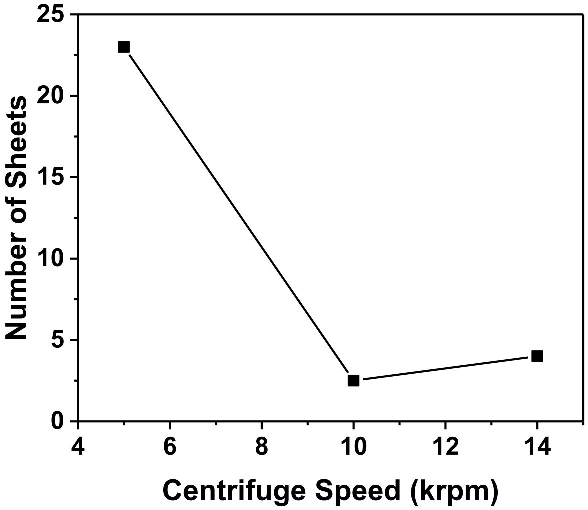

Figure 2.17: The average number of stacked sheets is plotted against centrifuge speed, showing a decrease in stacked sheets with increased speed.

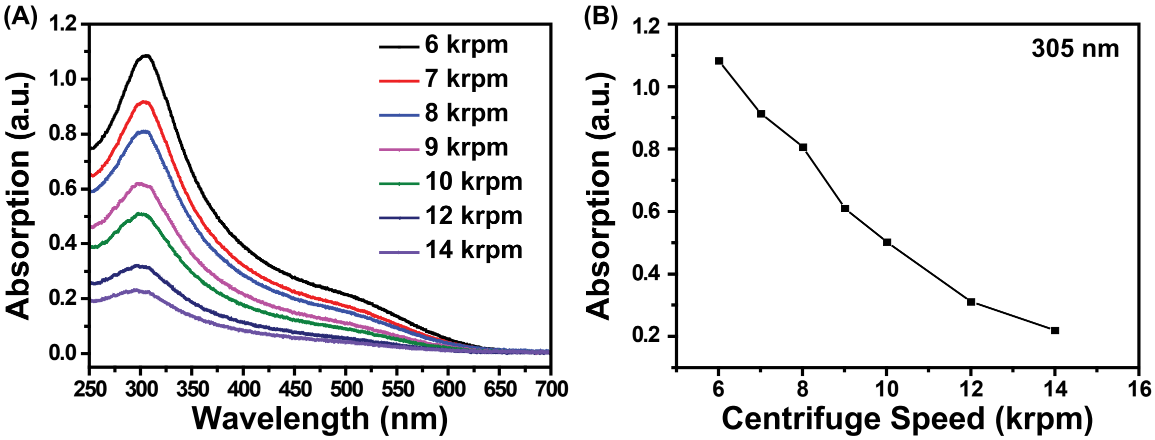

Figure 2.18: (A) Ultraviolet-visible spectrograph containing spectra from germanane dispersions that have been centrifuged at 6, 7, 8, 9, 10, 12, and 14 krpm, represented by black, red, blue, pink, navy blue, and purple lines, respectively. Measurements were done between 250 and 700 nm. (B) The maximum intensities of the various centrifuge speeds are plotted showing a linear relationship.

CHAPTER 3: Germanane as a Lithium-Ion Anode Material

3.1: Introduction

High energy- and power-density batteries are needed for the increasing development and demand of portable devices and electric vehicles. For use, graphite anodes (372 mAh/g) have paved the way for current energy-storage devices. However, to maintain the current trend in battery capabilities, we must continue to explore alternative materials and architectures. Materials like silicon and germanium have relieved immense attention for their high theoretical energy densities, but have notable shortcomings such as capacity fade and low Coulombic efficiencies.[1] Germanium is an attractive anode material for high power density applications owing to its high theoretical capacity (1384 mAh/g) corresponding to a $Li_{15}Ge_4$ phase, high electron and hole mobility (3.25 × Si and 3.8 × Si, respectively),[2,3] and high lithium diffusivity (400× Si).[4,5] While germanium remains more costly than some alternatives due to a lack of concentrated germanium ore deposits, defense and aerospace applications may still benefit from its uniquely high energy and power densities.

Germanium undergoes a 400% volume expansion during lithiation that can cause stress-induced fracture and pulverization, which leads to capacity loss.[5,6] Scaling down the dimensions of the Ge anode (thin films,[7–11] nanoparticles,[12–14] nanowires,[5,15–18] nanotubes,[19] nanocomposite-carbon matrices[6, 11,20,21]) improves performance by decreasing Li ion diffusion distances, leading to higher charge/discharge rates and circumventing fracture.[22] Graphite's ability to mitigate strain through inter-layer expansion upon lithium intercalation, due to a lack of inter-layer chemical bonding, is a leading factor in its relatively long cycle lifetime.[23] In a similar manner, researchers have eliminated bulk diffusion and subsequent potentially damaging phase transformations by developing essentially “all-surface” batteries with two-dimensional materials.[24] Additionally, these materials have the added benefit of drastically increasing surface activity and lowering the energy barrier for diffusion, both of which lead to improved power densities. Recently, researchers have reported the use of silicon nanosheets; however, the reported capacities still fall far short of the theoretical maximum capacity.[25–27]

Here, we investigate GeH, a stable, layered germanium hydride material, as a Li-ion anode material in order to capitalize on its potential for high energy and power density along with increased stability. The initial exploration into germanane as a lithium ion anode material aims to answer several questions: (*i*) what electrochemical reactions occur, (*ii*) is the storage mechanism the same as in bulk germanium, (*iii*) are there any additional storage mechanisms (**Figure 3.1**), (iv) does the stacked structure help compensate stress (**Figure 3.1**), and (*v*) does maximizing surfaces area improve the reaction rate and therefore the power density?

3.2: Fabrication of Germanane-Based Anodes

3.2.1: Assembly Procedures

Thick Film

After exfoliation, 10 wt% carbon nanofiber (CF, Sigma Aldrich) and 10 wt% carbon black (CB, Super P, Alfa Aesar) were added to the GeH dispersion and sonicated at 15 °C for 30 min. Immediately after sonication, the resulting black mixture was drop-cast and dried onto a mortar, which was ground with a pestle for an additional 5 min. Separately, 10 wt% polyacrylic acid (PAA, Sigma Aldrich) was sonicated in 0.5 mL of anhydrous 1-methyl-2-pyrrolidinone (NMP, Sigma Aldrich, 99.5%) for 1 h and added to the GeH / CF / CB powder and ground for an additional 5 min, or until a smooth slurry was formed. We hypothesized that the oxygen atoms in the PAA would help facilitate hydrogen-binding between the binder and the hydrogens on the GeH surfaces. It is worth noting here that the order of assembly matters. Germanane must be dried before adding other components due to IPA-induced segregation. Additionally, PAA must be added after mixing GeH, CF, and CB, and re-dispersing in NMP, otherwise the insulating PAA prevents conduction between sections of the anode.

This slurry was applied to a stainless-steel mesh (Alfa Aesar, 400 mesh) covering an area of 0.5 cm × 0.5 cm and dried under vacuum at room temperature for ~12 h. The electrode covering 0.5 cm × 0.5 cm was then folded onto itself and pressed under 10,000 lbs. of force. The mass loading of the GeH mixture on the electrodes was approximately 0.5 – 1 mg. A control sample was prepared in a similar manner using pure Ge powder (-100 mesh, ≥ 99.999% trace metal basis, Sigma Aldrich), however, the powder mixture of CF and CB was only ground and not sonicated.

Thin Film

Dried, exfoliated GeH was analyzed by drop-casting ~500 µL IPA-dispersed GeH on a stainless steel current collector with an area of 1 cm × 1 cm until the entire surface was covered by a thin, red film and then dried under vacuum for 5 min.

Scanning Electron Microscopy

Scanning electron microscopy was used to image thick film germanane anode composites. Carbon nanofiber, carbon black, and a mixture of carbon nanofiber, carbon black, polyacrylic acid, and germanane in a ratio of 10:10:10:70 were pressed onto *n*-doped Si wafers. Samples were imaged with a JEOL JSM-6700F field emission scanning electron microscope with a 5 kV accelerating potential.

3.2.2: Anode Characterization and Discussion

Thick Film

Scanning electron micrographs of carbon nanofiber, carbon black, and a mixture of carbon nanofiber, carbon black, polyacrylic acid, and germanane in a ratio of 10:10:10:70 are shown in **Figure 3.2A,B,C**, respectively. Images demonstrate the advantages of fillers. Each carbon nanofiber (**Figure 3.2A**) has an approximate average diameter of 100 nm with length on the order of several microns. This high-surface area, conductive filament is useful for maintaining long-range conduction and structure throughout the cycle-lifetime of the anode. The nano-sized carbon black (**Figure 3.2B**) has an approximate average spherical diameter of 80 nm, and therefore larger surface area per volume than the carbon nanofiber. This is useful for maintaining closer contact to germanane sheets, and ensuring sufficient conduction. The advantages of each additive can be seen more clearly when combined (**Figure 3.2C**). The germanane nanosheets are too small to be seen at this resolution, but they coat the small CB particles, CF can be seen maintaining conduction over long distances, and PAA coats everything, holding it together. Additionally, the CF helps the PAA maintain integrity over long ranges, preventing sections from breaking off during cycling.

Thin Film

Due to air instability, no thin films samples were characterized by microscopy. However, will appear similar to **Figure 2.12A** with higher concentrations. Electrical contact is maintained by inter-sheet interactions and contact to the stainless steel current collector. Thin film anodes offer poor structural and electrical support when cycled, but are easily characterization pre- and post-cycling. Thin film samples were used for later characterization with Raman spectroscopy and X-ray diffraction.

3.3: Germanane Anode Performance

3.3.1: Experimental Procedures

Electrochemical Measurements

Electrochemical characterization was carried out in 3-electrode cells (**Figure 3.3**) using a BioLogic VMP-3 potentiostat in an argon-filled glovebox with moisture and oxygen levels <1 ppm. Lithium-ion cycling was done in an electrolyte solution of $LiClO_4$ (1.0 M) in a 95:5 mixture of anhydrous PC and anhydrous fluoroethylene carbonate (FEC). Using FEC as an additive has been shown to enhance the stability of the SEI layer.[28] Lithium metal foils (99.9%, Sigma Aldrich) served as both auxiliary and reference electrodes. Cyclic voltammetry was performed within a window of 2.5 and 0.1 V *vs*. Li/Li^+. Respective electrodes were swept at rates between 0.1 to 10 $mV{\cdot}s^{-1}$. Galvanostatic cycling (GC) experiments were performed using cutoff voltages of 2.5 and 0.1 V *vs*. Li/Li^+ and cycled at various constant currents between C/10 to 2×C, where $C/h = 1384$ mAh/g, the weight normalized maximum theoretical current for Ge per hour.

X-ray diffraction

Powder X-ray diffraction was performed using a Bruker D8 Discover powder X-ray diffractometer using $Cu_{K\alpha}$ radiation ($\lambda = 1.5418$ Å). The XRD pattern was then referenced to the Joint Committee on Powder Diffraction Standards for phase analysis. A thin film germanane anode sample was packaged in PET under an argon atmosphere.

Raman spectroscopy

Confocal Raman spectroscopy was conducted with a Renishaw inVia Raman Microscope using a 633 nm source and an 1800 mm^{-1} grating, coupled with a Leica DM2500 optical system and EMCCD detector. Thin film GeH samples were sealed in a glass "sleeve" using Kapton tape and glass slides to ensure the sample was not exposed to air during transport or characterization. Lithiation-induced structural changes were characterized using the thin film GeH-coated stainless steel samples, electrochemically cycled between 0.1 and 2.5 V *vs*. Li/Li$^+$, at a rate of 0.1 mV·s^{-1}. After a single, full cycle, the sample was rinsed with anhydrous propylene carbonate (PC, 99.7% Sigma-Aldrich) three times, dried under an argon gas stream, and then under vacuum for 5 min. The sample was finally sealed in a new glass "sleeve" for analysis.

3.3.2: Second Cycle Electrochemical Properties

Cyclic voltammograms (CVs) of GeH and bulk Ge anodes at 0.1 mV/s from the second cycle are shown in **Figure 3.4A**. There are two peaks associated with lithiation: a broad peak at ~0.3 V and a sharp peak at 0.1 V. Delithiation is indicated by a broad peak between 0.4 V and 0.6 V.[29] These peaks correspond to the formation of several different Ge_xLi_y phases during the lithium insertion/extraction process. There is a low intensity, broad oxidation peak at 0.95 V during the first few cycles that decreases in intensity for subsequent cycles of the GeH sample that is not present in CVs using bulk Ge anodes. Lithiation of Ge follows **Equation 3.1**, but there are several lithiation steps along the way to a completely lithiated system,[10,30] which occur at different electrochemical potentials. Complete delithiation of crystalline $Li_{15}Ge_4$ results in an amorphous Ge structure. The similarity between second cycle CVs of GeH and bulk Ge indicate that GeH follows the same cycle.

$$Ge + Li \xrightarrow{Lithation} Li_{15}Ge_4 \xrightarrow{Delithiation} Ge_{amorphous} + Li \qquad \textbf{(3.1)}$$

Ex situ confocal Raman was used to identify structural changes in GeH after cycling against lithium metal, as shown in **Figure 3.4B**. The pristine GeH anode exhibits characteristic peaks at

227.1 and 302.3 cm^{-1}, corresponding to the out-of-plane (OP) A_1 and in-plane (IP) E_{2g} Ge vibrations, with a broad peak at ~526 cm^{-1} that corresponds to a hydrogen vibrational mode ((Ge-H)$_w$).[31] There is no evidence for hydrogen bending (~800 cm^{-1}) or stretching (1890 and 1975 cm^{-1}), possibly due to the low sensitivities of these modes. After cycling the GeH anode against lithium, its Raman spectrum changes significantly. The OP peak disappears and the IP peak broadens and shifts to 269.5 cm^{-1}, a shift that is known to signal the phase transition of Ge from a crystalline to an amorphous phase. Additionally, the hydrogen wag at ~526 cm^{-1} disappears, suggesting the removal of hydrogen upon lithium alloying. A structural change indicative of amorphization is further supported by XRD in **Figure 3.5**, where the germanane stacking peak disappears. These results indicate that the crystalline order of the anode is lost following the initial lithiation/delithiation cycle, becoming an amorphous Ge nanomaterial.

3.3.3: Galvanostatic Cycling

Constant current measurements (**Figure 3.6**) were used to determine the lithium insertion/extraction behavior at various cycling rates and to explore the observed phase transitions in the electrode material. The second cycle is shown in **Figure 3.6A** as it more accurately reflects material performance. A multitude of side reactions occur during the first charging/discharging cycle as evidenced by the large changes in measured capacity and Coulombic efficiency (**Figure 3.6B**). Galvanostatic charging at C/10 shows a maximum capacity of 1108 mAh/g. Plateaus near 0.16 V correspond to a phase boundary at room temperature between amorphous Ge nanomaterials and $Li_{15}Ge_4$. This phenomenon is described by Gibbs' phase rule, which precludes changes in cell voltage during a phase transformation.[8,28]

The maximum capacities for both lithiation and de-lithiation, and corresponding Coulombic efficiencies at various C rates are plotted in **Figure 3.6B**. The initial capacity of

1533 mAh/g at C/10 is greater than the theoretical maximum for Ge at room temperature. A large portion of this measured capacity is likely a result of electrolyte breakdown and subsequent SEI formation, therefore not representative of reversible anode performance. The extent of SEI formation can be visualized more clearly with the irreversible capacity loss between the first and second cycles, as shown in **Figure 3.7**. Interestingly, irreversible redox peaks were observed during first CV cycle of GeH, which is explored further in a following section. These additional redox peaks may contribute to overall charge storage in the first cycle, however the exact source of this redox peak is worth further investigation.

3.3.4: Kinetics

The kinetics of the germanane anode were investigated with cyclic voltammetry, as shown in **Figure 3.8A**, with cycling at rates from 0.2 to 50 mV/s. As the rate increases, the anodic and cathodic peaks broaden and the cathodic peak shifts to the right. Similar effects can be seen with bulk germanium (**Figure 3.5B**). This shift in potentials limits our ability to conduct b-value analysis. Nonetheless, we can infer the charge-storage mechanism at different charge/discharge rates by assessing the shape of the cyclic voltammogram curve. As the rate increases, the redox peaks of the GeH anode **(Figure 3.8A**) begin to match those of the carbon matrix **(Figure 3.8C**). This result suggests that the rate is too high for Ge-Li alloying to occur and carbon dominates any charge storage. The bulk Ge CVs broaden and have a peak shift as well; however, much of the original peak shape is maintained at higher sweep rates (**Figure 3.8B**). An advantage of the nanostructures is better depicted in **Figure 3.8D**, where it is evident that a higher capacity is achievable at higher charge/discharge rates. These results support the hypothesis that the amorphous nanosheet structure of GeH maintains a higher reaction rate by reducing diffusion-based limitations; however, definitive conclusions cannot be made due to the instability of both bulk germanium and germanane anodes.

3.3.5: Long Term Performance

The cycling performance of GeH cycled at 1C is shown in **Figure 3.9**, where capacity is retained through 100 cycles. The GeH anode shows charge capacities of 819, 530, 527, 542, 525, 438, and 341 mAh/g for cycle 1, 2, 5, 10, 50, and 100, respectively. The long-term cycling for both GeH and bulk Ge anodes are shown in **Figures 3.10A** and **3.10B**, respectively, where insertion and extraction are plotted together, along with the Coulombic efficiency, which stabilizes at ~99% for both GeH and bulk Ge anodes at high cycle numbers. Previously reported silicon nanosheet work shows rapid degradation, which is attributed to inter-layer SEI formation,[25,26,32,33] a similar mechanism may be responsible for the decay in the GeH system.

3.3.6: First Cycle Electrochemical Properties

The results discussed thus far focus on the performance of the germanane anode after the second electrochemical cycle, yet it would be more accurate to describe them as amorphous germanium nanosheets due to the structural change that occurs during the Ge-Li alloying/de-alloying reaction after the first cycle. A cyclic voltammogram of germanane during the first cycle is shown in **Figure 3.11A**, with distinctive reduction and oxidation peaks at 0.53 and 0.93 V, respectively, and the Coulombic efficiency between these two peaks is ~95%. To investigate the source of these peaks, a pristine GeH anode was swept from the open circuit voltage to 0.45 V *vs.* Li/Li^+ (below the previously tested voltage of the first peak) and its Raman spectrum was immediately measured (**Figure 3.11B**). *Ex situ* analysis of this sample showed that the germanane had become amorphous by this potential. From these data, it appears that the reduction reaction is reversible within the first cycle and that the sample undergoes oxidation after the structure becomes amorphous and hydrogens are removed. However, the reduction reaction no longer occurs after the lithium-induced structural change. It is unclear what the source of this extra redox reaction is, whether it is structural or hydrogen related. Additional studies are needed in order to elucidate the exact mechanism for these redox peaks.

The capacity retention stabilizes at ~1110 mAh/g after the first few cycles. The total charge storage decreases as the rate is increased, with capacities of 893, 720, 530, and 265 mAh/g for C/5, C/2, 1C, and 2C, respectively. This capacity loss at higher rates is similar to other Ge nanomaterial anodes,[5,28] and is likely a result of kinetic limitations of the host matrix. The kinetics are explored further in the earlier kinetics section (section 3.3.4). The capacity recovered to its initial cycling capacity when the rate was returned to C/10. The Coulombic efficiency stabilized after the first five cycles and averaged ~98%. The large initial reduction in efficiency during the first five cycles is most likely related to SEI formation, but the exact cause was not tested here.

3.4: Conclusions and Prospects

Herein, we report a method for purifying GeH sheets, by exfoliating and dispersing them in isopropanol. The purified dispersions created are stable for at least 8 months, which given GeH's favorable electronic properties, could be useful for many device applications where a solution-processable material is beneficial. Here, we use the purified GeH dispersion to fabricate a GeH-carbon composite for use as a Li-ion battery anode. Results present a promising first step with high energy densities of ~1100 mAh/g and stability over 100 charge/discharge cycles, which compares well to previously reported nano-architectures. Scale-up and purification of the synthesis as well as optimizing carbon composites will need to be further developed for this purpose and to explore kinetic capabilities alongside extra redox reactions. Thus far, the high energy density and stability bode well for using GeH in energy storage applications.

3.5: References

(1) McDowell, M. T.; Lee, S. W.; Nix, W. D.; Cui, Y. 25th Anniversary Article: Understanding the Lithiation of Silicon and Other Alloying Anodes for Lithium-Ion Batteries. *Adv. Mater.* **2013**, *25*, 4966–4985.

(2) Prince, M. B. Drift Mobilities in Semiconductors. II. Silicon. *Phys. Rev.* **1954**, *93*, 1204–1206.

(3) Prince, M. B. Drift Mobilities in Semiconductors. I. Germanium. *Phys. Rev.* **1953**, *92*, 681–687.

(4) McIlwrath, K.; Cui, Y.; Huggins, R. A.; Zhang, X. F.; Chan, C. K.; Peng, H.; Liu, G. High-Performance Lithium Battery Anodes Using Silicon Nanowires. *Nat. Nanotechnol.* **2008**, *3*, 31–35.

(5) Kennedy, T.; Mullane, E.; Geaney, H.; Osiak, M.; Dwyer, C. O.; Ryan, K. M. High-Performance Germanium Nanowire-Based Lithium-Ion Battery Anodes Extending over 1000 Cycles Through in Situ Formation of a Continuous Porous Network. **2014**, *14*, 716–723.

(6) Seng, K. H.; Guo, Z. P.; Liu, H. K.; Park, M. M.-H.; Cho, J.; Guo, Z. P.; Liu, H. K.; Cho, J. Self-Assembled Germanium/Carbon Nanostructures as High-Power Anode Material for the Lithium-Ion Battery. *Angew. Chemie Int. Ed.* **2012**, *51*, 5657–5661.

(7) Graetz, J.; Ahn, C. C.; Yazami, R.; Fultz, B. Nanocrystalline and Thin Film Germanium Electrodes with High Lithium Capacity and High Rate Capabilities. *J. Electrochem. Soc.* **2004**, *151*, 698–702.

(8) Baggetto, L.; Hensen, E. J. M.; Notten, P. H. L. In Situ X-Ray Absorption Spectroscopy of Germanium Evaporated Thin Film Electrodes. *Electrochim. Acta* **2010**, *55*, 7074–7079.

(9) Laforge, B.; Levan-Jodin, L.; Salot, R.; Billard, A. Study of Germanium as Electrode in Thin-Film Battery. *J. Electrochem. Soc.* **2008**, *155*, 181–188.

(10) Baggetto, L.; Notten, P. H. L. Lithium-Ion (De)Insertion Reaction of Germanium Thin-Film Electrodes: An Electrochemical and In Situ XRD Study. *J. Electrochem. Soc.* **2009**, *156*, 169–175.

(11) Cui, G.; van Aken, P. A.; Maier, J.; Kaskhedikar, N.; Zhi, L.; Gu, L.; Müllen, K.; Zhi, L.; Kaskhedikar, N.; van Aken, P. A.; Müllen, K.; Maier, J. A Germanium--Carbon Nanocomposite Material for Lithium Batteries. *Adv. Mater.* **2008**, *20*, 3079–3083.

(12) Kim, J.; Cho, J.; Kim, K.; Park, M. Flexible Dimensional Control of High- Capacity Li-Ion- Battery Anodes: From 0D Hollow to 3D Porous Germanium Nanoparticle Assemblies. *Adv. Mater.* **2010**, *22*, 415–418.

(13) Seo, S.-D.; Lee, J.-H.; Hwang, I.-S.; Kim, J.-C.; Lee, S.; Kim, D.-W. A Binder-Free Ge-Nanoparticle Anode Assembled on Multiwalled Carbon Nanotube Networks for Li-Ion Batteries. *Chem. Commun.* **2012**, *48*, 7061–7063.

(14) DiLeo, R. A.; Frisco, S.; Ganter, M. J.; Rogers, R. E.; Raffaelle, R. P.; Landi, B. J. Hybrid Germanium Nanoparticle Single-Wall Carbon Nanotube Free-Standing Anodes for Lithium Ion Batteries. *J. Phys. Chem. C* **2011**, *115*, 22609–22614.

(15) Seo, M.-H.; Park, M.; Lee, K. T.; Kim, K.; Kim, J.; Cho, J. High Performance Ge Nanowire Anode Sheathed with Carbon for Lithium Rechargeable Batteries. *Energy Environ. Sci.*

2011, *4*, 425–428.

(16) Liu, X. H.; Huang, S.; Picraux, S. T.; Li, J.; Zhu, T.; Huang, J. Y. Reversible Nanopore Formation in Ge Nanowires during Lithiation–Delithiation Cycling: An In Situ Transmission Electron Microscopy Study. *Nano Lett.* **2011**, *11*, 3991–3997.

(17) Yuan, F.-W.; Yang, H.-J.; Tuan, H.-Y. Alkanethiol-Passivated Ge Nanowires as High-Performance Anode Materials for Lithium-Ion Batteries: The Role of Chemical Surface Functionalization. *ACS Nano* **2012**, *6*, 9932–9942.

(18) Wang, J.; Du, N.; Zhang, H.; Yu, J.; Yang, D. Cu–Ge Core–shell Nanowire Arrays as Three-Dimensional Electrodes for High-Rate Capability Lithium-Ion Batteries. *J. Mater. Chem.* **2012**, *22*, 1511–1515.

(19) Park, M.-H.; Cho, Y.; Kim, K.; Kim, J.; Liu, M.; Cho, J. Germanium Nanotubes Prepared by Using the Kirkendall Effect as Anodes for High-Rate Lithium Batteries. *Angew. Chemie Int. Ed.* **2011**, *50*, 9647–9650.

(20) Hwang, C.-M.; Park, J.-W. Electrochemical Characterization of a Ge-Based Composite Film Fabricated as an Anode Material Using Magnetron Sputtering for Lithium Ion Batteries. *Thin Solid Films* **2010**, *518*, 6590–6597.

(21) Seng, K. H.; Park, M.; Guo, Z. P.; Liu, H. K.; Cho, J. Catalytic Role of Ge in Highly Reversible GeO_2/Ge/C Nanocomposite Anode Material for Lithium Batteries. *Nano Lett.* **2013**, *13*, 1230–1236.

(22) Liu, X. H.; Zhong, L.; Huang, S.; Mao, S. X.; Zhu, T.; Huang, J. Y. Size-Dependent Fracture of Silicon Nanoparticles during Lithiation. *ACS Nano* **2012**, *6*, 1522–1531.

(23) Mukhopadhyay, A.; Tokranov, A.; Sena, K.; Xiao, X.; Sheldon, B. W. Thin Film Graphite Electrodes with Low Stress Generation During Li-Intercalation. *Carbon* **2011**, *49*, 2742–2749.

(24) Muller, G. A.; Cook, J. B.; Kim, H.-S.; Tolbert, S. H.; Dunn, B. High Performance Pseudocapacitor Based on 2D Layered Metal Chalcogenide Nanocrystals. *Nano Lett.* **2015**, *15*, 1911–1917.

(25) Lu, Z.; Zhu, J.; Sim, D.; Zhou, W.; Shi, W.; Hng, H. H.; Yan, Q. Synthesis of Ultrathin Silicon Nanosheets by Using Graphene Oxide as Template. *Chem. Mater.* **2011**, *23*, 5293–5295.

(26) Kim, W.; Hwa, Y.; Shin, J.; Yang, M.; Sohn, H. Scalable Synthesis of Silicon Nanosheets from Sand as an Anode for Li-Ion Batteries. **2014**, 4297–4302.

(27) Xu, K.; Ben, L.; Li, H.; Huang, X. Silicon-Based Nanosheets Synthesized by a Topochemical Reaction for Use as Anodes for Lithium Ion Batteries. *Nano Res.* **2015**, *8*, 2654–2662.

(28) Chockla, A. M.; Klavetter, K. C.; Mullins, C. B.; Korgel, B. A. Solution-Grown Germanium Nanowire Anodes for Lithium-Ion Batteries. *ACS Appl. Mater. Interfaces* **2012**, *4*, 4658–4664.

(29) Klavetter, K. C.; Wood, S. M.; Lin, Y.-M.; Snider, J. L.; Davy, N. C.; Chockla, A. M.; Romanovicz, D. K.; Korgel, B. A.; Lee, J.-W.; Heller, A.; Mullins, C. B. A High-Rate Germanium-Particle Slurry Cast Li-Ion Anode with High Coulombic Efficiency and Long Cycle Life. *J. Power Sources* **2013**, *238*, 123–136.

(30) Lim, L. Y.; Liu, N.; Cui, Y.; Toney, M. F. Understanding Phase Transformation in Crystalline Ge Anodes for Li-Ion Batteries. *Chem. Mater.* **2014**, *26*, 3739–3746.

(31) Bermejo, D.; Cardona, M. Raman Scattering in Pure and Hydrogenated Amorphous Germanium and Silicon. *J. Non. Cryst. Solids* **1979**, *32*, 405–419.

(32) Sun, L.; Su, T.; Xu, L.; Liu, M.; Du, H.-B. Two-Dimensional Ultra-Thin SiO_x ($0 < X < 2$) Nanosheets with Long-Term Cycling Stability as Lithium Ion Battery Anodes. *Chem. Commun.* **2016**, *52*, 4341–4344.

(33) Ryu, J.; Hong, D.; Choi, S.; Park, S. Synthesis of Ultrathin Si Nanosheets from Natural Clays for Lithium-Ion Battery Anodes. *ACS Nano* **2016**, *10*, 2843–2851.

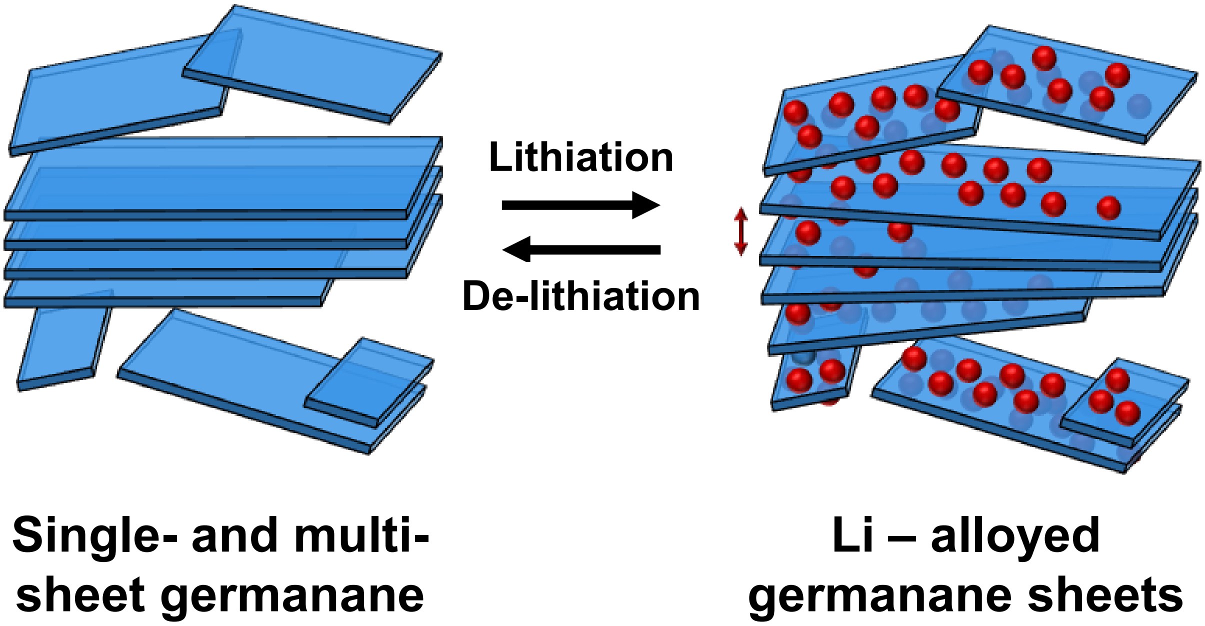

Figure 3.1: Schematic representing a proposed germanane Li-ion storage mechanism. Upon lithium insertion, any remaining stacked sheets separate out-of-plane to alleviate stress. Additionally, part of these experiments looks to identify if these sheets store through an intercalation mechanism.

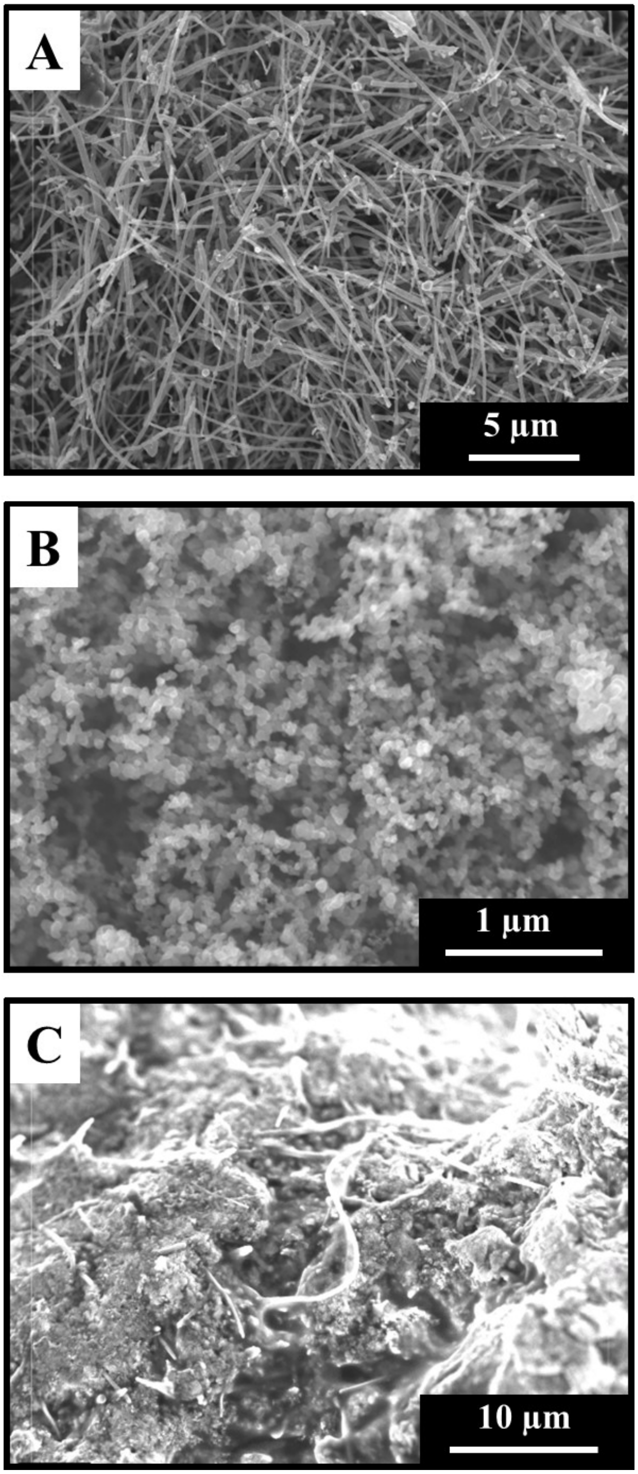

Figure 3.2: Scanning electron micrographs of (A) carbon nanofiber (CF), (B) carbon black (CB), and (C) a mixture of germanane (GeH), CF, CB, and polyacrylic acid (PAA) pressed onto a *n*-Si substrate.

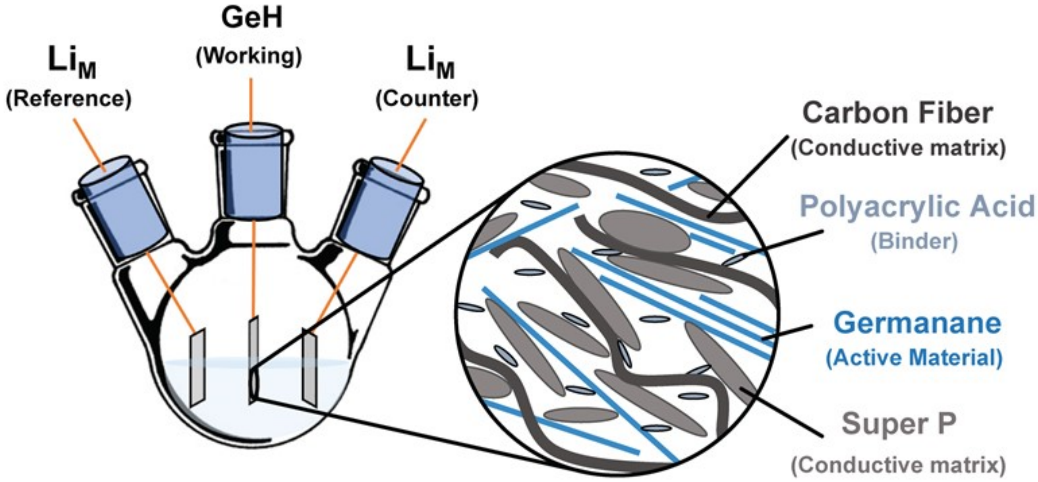

Figure 3.3: Schematic of the electrochemical setup for germanane electrode testing. Thick film germanane composites are depicted here, however the same setup is used for thin film testing.

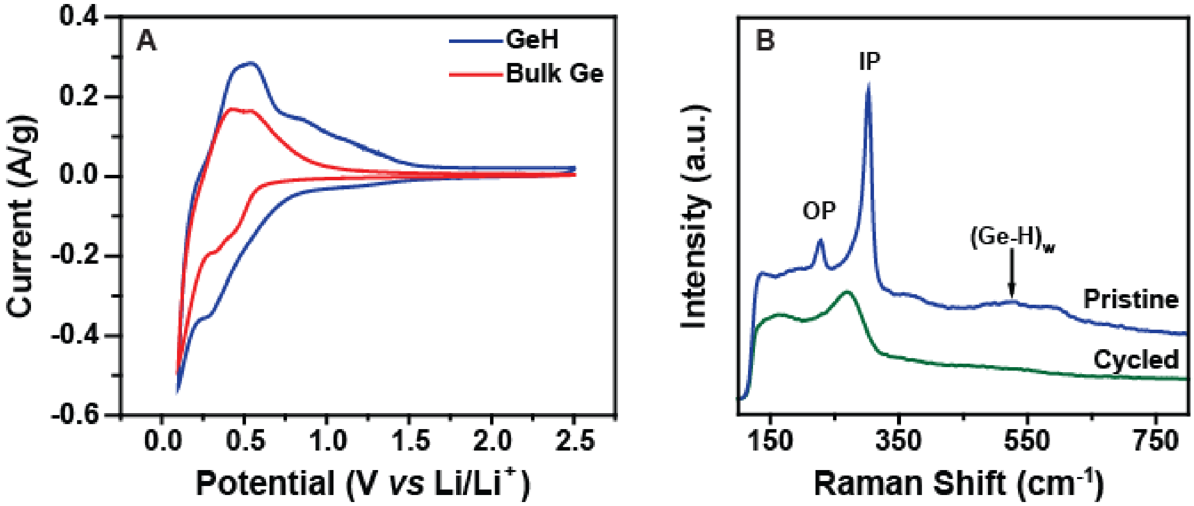

Figure 3.4: (A) Cyclic voltammograms comparing germanane (GeH) and bulk Ge anodes and (B) *ex situ* confocal Raman spectra of pristine (blue, top) and Li-cycled (green, bottom) GeH anodes show evidence for structural changes associated with delithiation-driven amorphization of the GeH sheets. The E_{2g} in-plane (IP) and A_1 out-of-plane (OP) Ge vibrations and hydrogen wag ($(\text{Ge-H})_w$) are highlighted.

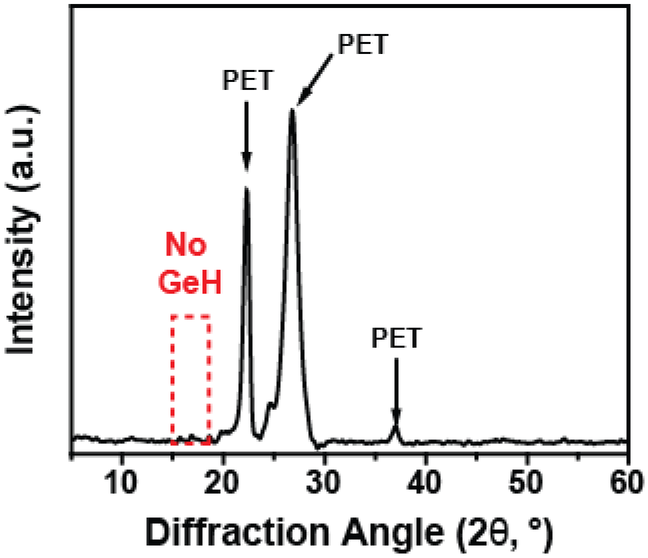

Figure 3.5: Powder X-ray diffraction of germanane after cycling against lithium. Germanane was drop-cast out of isopropanol onto a stainless steel electrode. The electrode was cycled using cyclic voltammetry from 2.5 to 0.1 V at 0.1 mV/s. Following completion, the sample was immediately rinsed with propylene carbonate, dried under an Ar stream, and sealed in a polyethylene terephthalate (PET) envelope to prevent oxidation. A stainless steel background was subtracted from this spectrum for clarity.

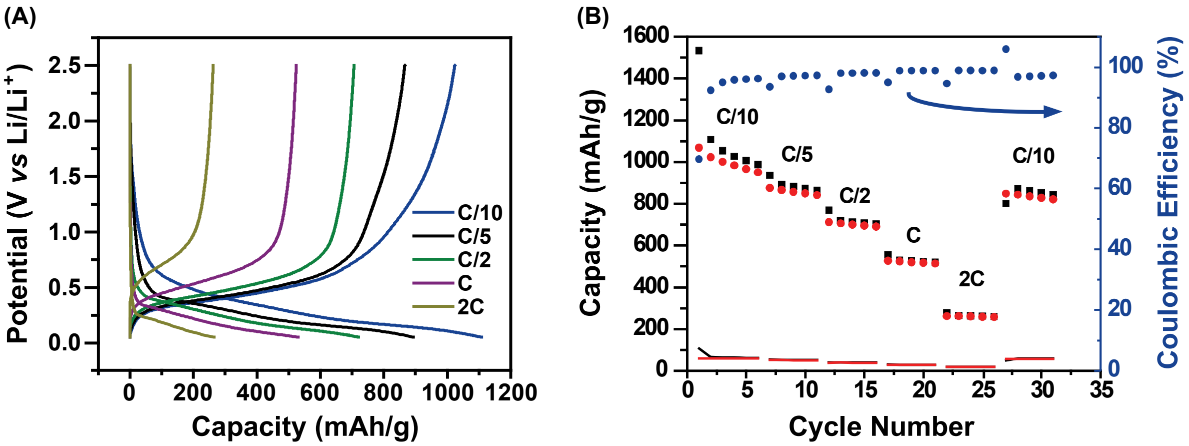

Figure 3.6: (A) Galvanostatic cycling of a GeH anode at various charge/discharge (C) rates. (B) The maximum insertion and extraction capacities for the GeH anode are plotted in black squares and red circles, respectively, with the corresponding Coulombic efficiency plotted in blue circles; the contributions of carbon nanofiber/carbon black and PAA binder to insertion and extraction capacity plotted in black and red lines, respectively, and represent only a small fraction of the overall capacity.

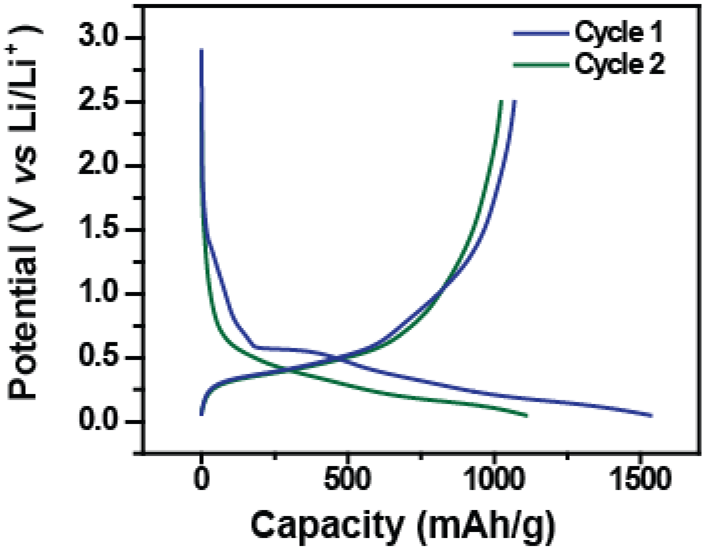

Figure 3.7: Galvanostatic charge/discharge curves at C/10 of germanane for the first and second cycles, in the voltage window of 2.5 and 0.1 V *vs.* Li/Li$^+$, show solid-electrolyte-interphase (SEI) layer formation.

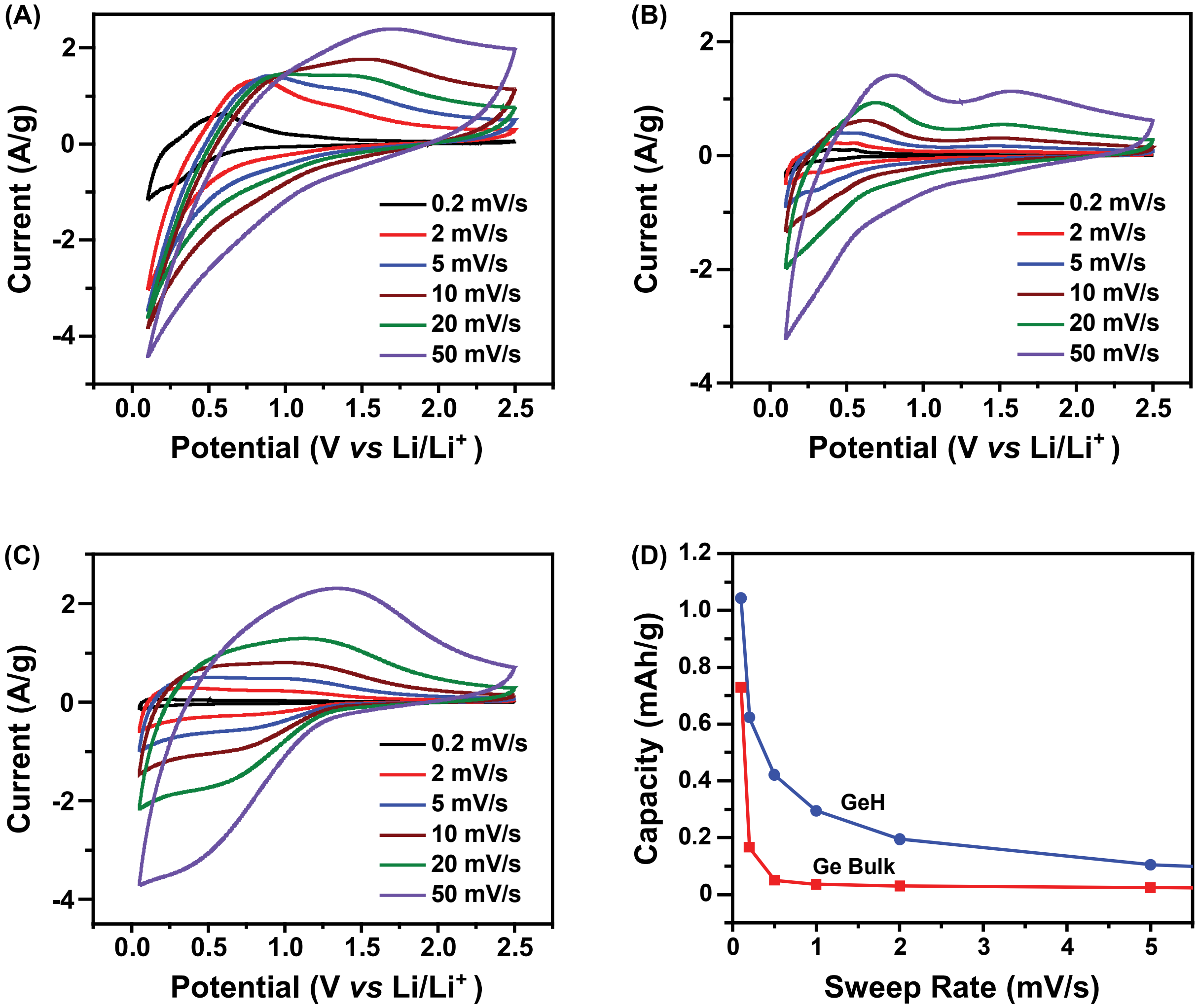

Figure 3.8: Cyclic voltammograms (second cycles) for (A) germanane (GeH), (B) bulk Ge, and (C) carbon matrix cycled at 0.2, 2, 5, 10, 20, and 50 mV/s between 2.5 and 0.1 V *vs*. Li/Li$^+$. Reductive capacity at different sweep rates (D) is plotted against sweep rate for GeH and bulk Ge.

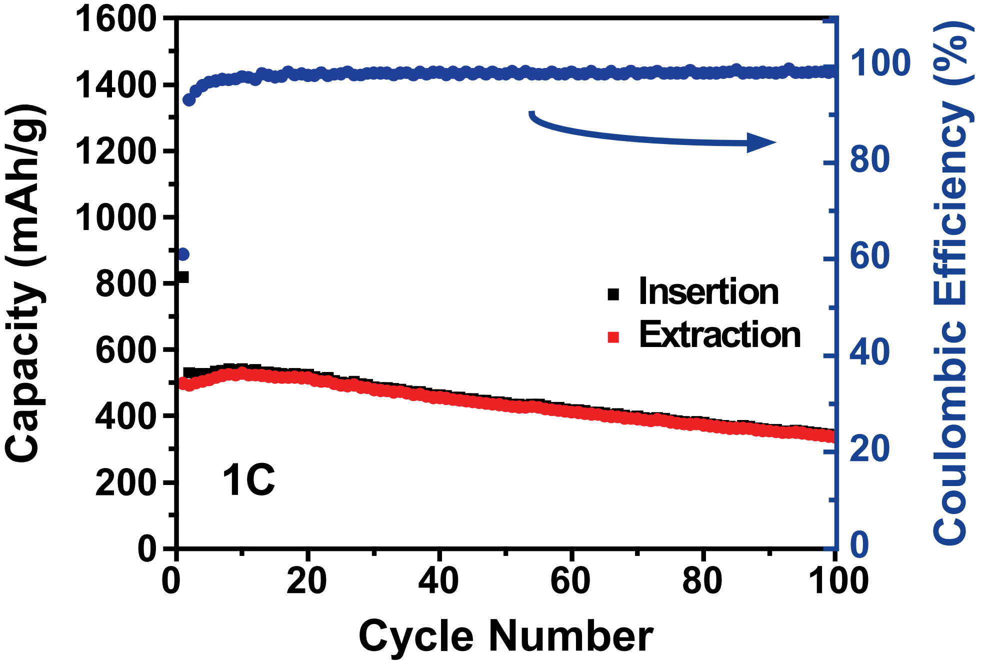

Figure 3.9: Long-term galvanostatic cycling of GeH at 1 C, showing the charge capacity (black), discharge capacity (red), and Coulombic efficiency (blue).

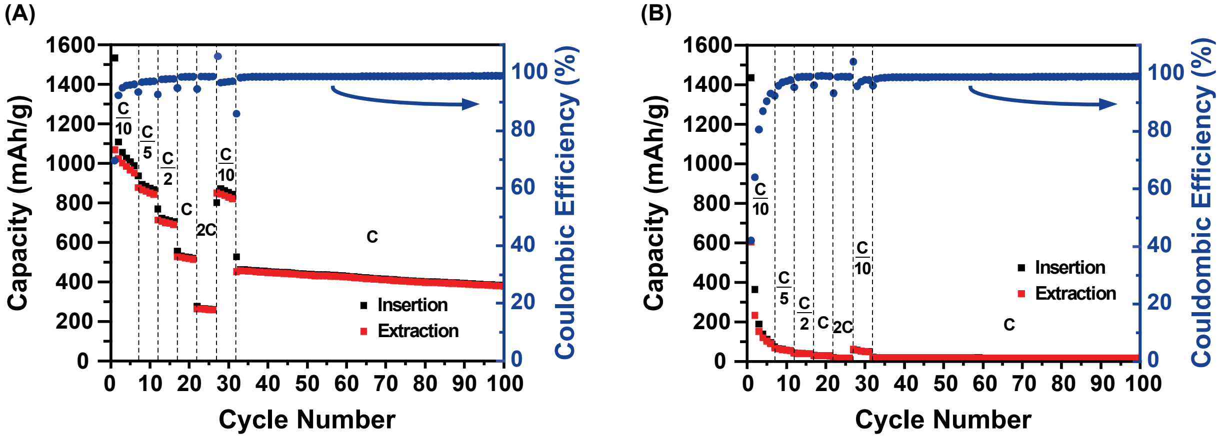

Figure 3.10: Capacities for each galvanostatic charge/discharge curve for (A) germanane and (B) bulk Ge cycled at rates of C/10, C/5, C/2, C, 2C, C/10, and finally cycled to 100 cycles at a rate of 1C within a voltage window of 2.5 and 0.1 V *vs*. Li/Li$^+$. Plots also contain the Coulombic efficiencies for each complete cycle.

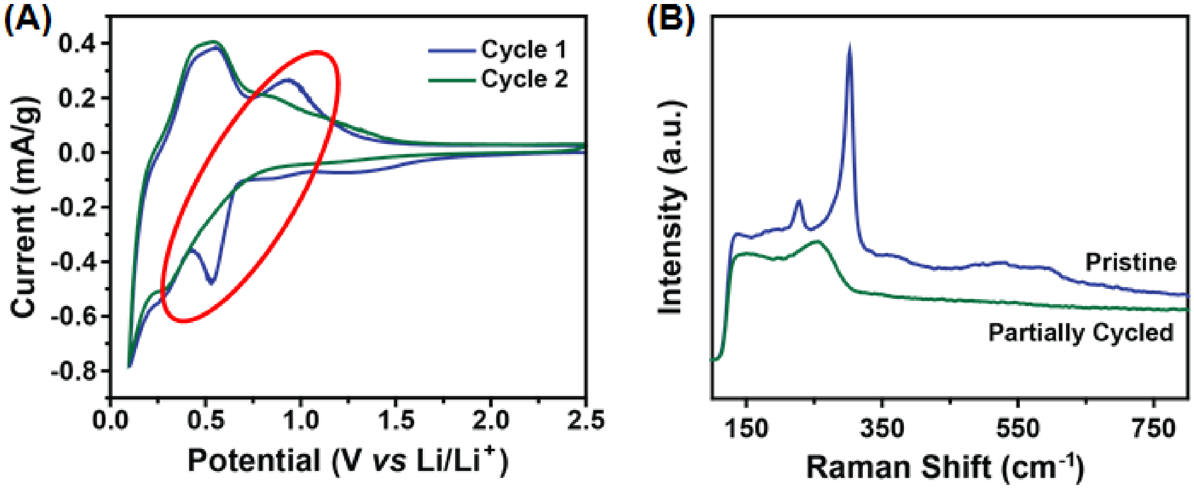

Figure 3.11: (A) Cyclic votlammogram of cycle 1 and 2 of a germanane thin film, cycled between 2.5 and 0.1 V *vs*. Li/Li$^+$ at 0.1 mV/s. Red circle highlights germanane specific redox peaks. (B) Raman spectra of pristine GeH (top, blue) and partially cycled GeH, where a thin film of GeH was swept to 0.45 mV *vs.* Li/Li$^+$.

CHAPTER 4: Work Function Control of Germanium through Carboxyl-Carborane Surface Passivation

4.1: Introduction

Recent advances in interface engineering for semiconductors have contributed to significant improvements for electronic devices, such as transistors, photovoltaics, and sensors.[1—10] Many of these architectures require precise control of energy levels at the interface between materials. Alignment of these energy levels provides low-resistance contacts, whereas large misalignment causes band bending that generates internal electric fields. This internal field can be helpful for preventing electron-hole recombination in heterojunction photovoltaics. Band engineering can be accomplished by controlling surface work functions (WFs), which has been demonstrated by passivating surfaces with covalently bound organic monolayers possessing different dipole magnitudes and orientations.[2,3] However, these monolayers also often alter the surface energy, adding complications to the device fabrication process by changing the wetting or adhesive properties at the material interface.[8–11] The ability to tune energy level alignment with a simple and reliable method without influencing surface energy and wetting will greatly reduce complications across industries.[12]

Recently, our group modified gold and silver surfaces with carboranethiols to tune band alignment and thus interfacial charge-transfer resistance between metal contacts and a polymer semiconductor with minimal effects on surface energy and wetting at the interface.[12] By changing both the placement of the carbon atoms within the cluster and the head group position on the carborane cage, it is possible to tune the dipole moment magnitude and orientation while leaving the chemical environment identical between isomers.[13–16] This feature makes carboranes an attractive option for tuning surface WFs. Translating the carborane system from metal to semiconductor systems would aid in rapid-prototyping of semiconductor devices by enabling precision band engineering with minimal impact on processing.[17]

Germanium is a promising candidate for semiconductor-based technologies owing to its small band gap (0.67 eV) and high carrier mobility, roughly twice that of silicon. These properties are useful for faster devices and an absorption spectrum that extends into the infrared. Unfortunately, germanium's defect-rich, intrinsic oxide keeps it from making a large impact on today's devices.[18] Researchers have investigated methods for removing germanium's oxide layer, commonly through etching, and then depositing an organic monolayer to suppress oxide formation. Maboudian and coworkers demonstrated this removal by etching the oxide with HF and simultaneously passivating the surface with hydrogen. Monolayers of 1-octadecanethiolate were subsequently formed by displacing the surface hydrogens.[19] Bent and coworkers applied this alkanethiol deposition to halogenated Ge(111) and Ge(100) surfaces.[20] They removed the germanium oxide by H_2O_2 and HCl or HBr etches, leaving behind halogen-passivated surfaces. The halogen layer was then displaced by octanethiol or octadecanethiol, resulting in organic monolayers that are stable in ambient conditions for several days. Many head groups have been explored for Ge, however, thiol passivation remains a prominent wet chemical method for organic SAM formation.[21]

While exploring head group–surface interactions, Bent and coworkers revealed a significant difference in halogen and sulfur concentrations between the Ge(100) and Ge(111) surfaces, which they attributed to the unique characteristics of the Ge(100) surface.[20–22] In order to reduce the number of dangling bonds, the Ge(100) surface reconstructs into a 2 × 1 structure, resulting in the creation of surface dimers. The major difference in surface reactivity is attributed to the nucleophilic top Ge atom and the electrophilic bottom Ge atom. This reactivity difference has been studied with other possible head group chemistries on sputter-cleaned surfaces in ultra-high vacuum. For example, alcohols and carboxylic acids were found to chemisorb selectively to Ge(100), and not Ge(111), through hydrogen dissociation and reaction between the oxygen and the electrophilic bottom atom in the surface dimer.[23,24]

Herein, we investigate the deposition of icosahedral carboranes with different head groups on Ge(100) surfaces using an H_2O_2 and HCl pretreatment. Specifically, boron clusters with thiol, hydroxyl, and carboxylic acid head groups attached at various vertices were studied in order to determine suitable head group chemistries for chemisorption of carborane SAMs on germanium with the ultimate goal of tuning the WF with minimal perturbations to surface energy. While there are established methods for germanium SAM formation using thiol head groups,[18–21] our work indicates these are not suited for the carborane system and instead present evidence for carboxylic acid binding to the germanium surface. **Figure 4.1A** contains a schematic depicting the various head groups and carborane isomers used in this study. Initial experiments focused on binding positions where the head group was bound to boron vertices, specifically, 9-*o*-carborane (**O9**) and 9-*m*-carborane (**M9**), as this would reduce lateral dipole-dipole interactions that could aid in assembly and instead enable focus on head group surface reactivity.

4.2: Head Group Identification

4.2.1: Procedures

Synthesis

All molecule synthesis is described in **Appendix A.**

Surface Preparation

Single-side polished, undoped Ge(100) wafers (MTI Corporation, Richmond, CA) wafers were cleaned by sonicating in acetone for 20 min and dried under a nitrogen gas stream. They were then rinsed with deionized water at 18.2 MΩ-cm resistivity (Milli-Q from Millipore, Billerica, MA), submerged in 30% hydrogen peroxide (Sigma Aldrich, St. Louis, MO) for 5 min, rinsed with water again, and submerged in 37% HCl (Sigma Aldrich) for 5 min. That etch cycle was repeated 2 more times. Care was taken to ensure that there was no mixing between HCl and H_2O_2 solutions, due to potentially hazardous byproducts. After the last HCl step, the samples were quickly dried under a nitrogen gas stream, and immediately transferred to a nitrogen glovebox with an oxygen content ~0.1ppm. Solvents were purged with nitrogen for 30 min prior to use. All self-assembled monolayer solutions were made in the glovebox in anhydrous benzene (Sigma Aldrich, St. Louis, MO) at a concentration of 1 mM, using molecules 1-COOH-*o*-carborane (O1COOH), 9-COOH-*o*-carborane (O9COOH), 9-OH-*m*-carborane (M9OH), 9-SH-*o*-carborane (O9SH), described above, and 9-SH-*m*-carborane (M9SH, Sigma Aldrich).

Both chlorine- and SAM- modified germanium surfaces were held in solution until just before analysis, and were immediately rinsed in benzene only or benzene and anhydrous isopropanol (IPA, Sigma Aldrich, St. Louis, MO) and dried with a nitrogen gas stream. The rinsing and drying steps were done 3 times.

X-Ray Photoelectron Spectroscopy

Samples were transferred from the glovebox to the XPS vacuum chamber (1×10^{-9} Torr) using a transfer vessel to maintain an air-free environment. Spectra were acquired using a Kratos

Axis Ultra DLD photoelectron spectrometer with a monochromatic Al K_{α} source at 300 W and a 300 µm × 700 µm spot size. A pass energy of 20 eV was used with a resolution of 0.1 eV for the high-resolution regions of Ge 2p, C 1s, Cl 2p, B 1s, and O 1s, using between 5 and 20 sweeps per region. Energy scales were corrected to the C-C binding energy of 284.8 eV. All peaks were analyzed using CasaXPS software, fit using Gaussian-Lorentzian line shapes with a Shirley background, and finally smoothed using a Savotzky-Golay quadratic.

4.2.2: Results

X-ray photoelectron spectroscopy was used to investigate head groups binding on germanium surfaces by taking high-resolution spectra of B 1s (**Figure 4.1B**) and S 2p (**Figure 4.2**). For both 9-SH-*m*-carborane and 9-SH-*o*-carborane (O9SH), the lack of peaks in both the B 1s and S 2p spectra indicate that neither bind. Expanding to the two other possible head groups, (hydroxyl and carboxylic acid), we find that 9-OH-*m*-carborane (M9OH) did not show any evidence for binding, however, presence of boron for 9-COOH-*o*-carborane (O9COOH) suggests SAM formation.

With the success of O9COOH, we examined its isomer 1-COOH-*o*-carborane (O1COOH), where the head group is bound to a carbon vertex instead of boron. This isomer also shows evidence of SAM formation, however, the relative quantity of boron signal observed on the surface by XPS analysis was lower than what was observed for O9COOH (**Figure 4.1B**). We hypothesize that a strong vertically oriented dipole moment might facilitate multi-layering through head-tail attraction. To test this possibility, we rinsed O1COOH and O9COOH Ge surfaces with a polar solvent, isopropanol, after the benzene rinse to disrupt dipole-dipole interactions. This procedure resulted in decreases in B 1s signal for O9COOH (**Figure 4.3A**) so that both O1COOH and O9COOH are present in similar quantities, consistent with of our multi-layering hypothesis. After extensive rinsing with both polar and nonpolar solvents, the presence of boron suggests that the carborane carboxyl SAM is chemisorbed.

High-resolution XPS spectra of carboxylic acid carborane SAMs on germanium, shown in **Figure 4.3**, highlight the regions for (A) B 1s, (B) Cl 2p, (C) C 1s, (D) O 1s, and (E) Ge 2p. Ge(100) surfaces modified by HCl (black trace), O9COOH (red trace), and O1COOH (blue trace) are all shown for comparison, with fitted peak positions in the **Table 4.1**. These data show that the H_2O_2/HCl pre-treatment successfully leaves a relatively oxide-free surface by etching away germanium oxide and passivating the germanium surface with chlorine atoms.

Figure 4.3B highlights the chlorine region, showing that after deposition chlorine is still present on the surface, with Cl $2p_{1/2}$ and $2p_{3/2}$ XPS features at 198.6 and 200.3 eV, respectively. Note that there is overlap between Cl 2p peaks and the Ge 3s plasmon peak (fitted with the purple dotted line). The chlorine peak decreases upon O1COOH and O9COOH SAM formation, relative to the Ge 3s plasmon background, while the chlorine peak position remains unchanged. This reduction in signal could be a result of the displacement of chlorine ions with carboxyl groups, attenuation from the organic monolayer, or a combination of both.

The C 1s spectra (**Figure 4.3C**) shows evidence for multiple carbon species. The presence of carbon on the HCl-treated sample is attributed to C-C/C-H bonds from adventitious carbon (284.5 eV). A similar carbon signal, slightly shifted to higher binding energies (284.8 eV), is observed for both carborane isomers, which may be due to the higher electropositive nature of carboranes. In addition, the peaks at 286.4 and 286.5 eV for O1COOH and O9COOH, respectively, correspond to a C-B bond from the carborane cluster.[25] The slight difference in binding energy between isomers may be a result of different bonding configurations. The peaks at 288.5 and 288.2 eV for O1COOH and O9COOH, respectively, are a result of the presence of the carboxyl functional group (O-C=O) on the surface. This small difference correlates to the electronegativity difference between isomers, with the C-C bond in O1COOH increasing binding energy and C-B bond in O9COOH decreasing binding energy.

Both carborane systems change the O 1s spectra (**Figure 4.3D**) from the chlorine-passivated system in a similar fashion. The HCl-etched control sample shows a small amount of residual oxygen. After assembly of carborane SAMs, there are increases in peak intensity at 531.7 and 531.6 eV for O1COOH and O9COOH, respectively, due to the presence of the carboxyl groups.[26] The Cl-passivated surface contains two peaks in the Ge 2p spectra (**Figure 4.3E**), 1217.7 and 1218.3 eV, corresponding to elemental Ge and Ge-Cl, respectively. Samples show evidence for Ge-O bond formation upon deposition of O1COOH and O9COOH, with shifts to higher binding energy by 0.4 eV and 0.2 eV, respectively. The shifts observed for the isomers correspond to a change in oxidation state from Ge^{+1} to Ge^{+2}.[27,28] This apparent peak shift for both carborane samples suggests that the carboxyl group is binding through a Ge-O-C bond.[26]

The cause of the carboxyl group binding may be due to the presence of surface dimers on the Ge(100) surface,[26,29] the electronic structure of the carborane cage, or a combination of both. Previous work with 11-mercaptoundecanoic acid has shown that the thiol group binds to Cl-terminated Ge(111) surfaces preferentially over the carboxyl-group.[20,30] Aromatic backbones in molecules have shown to have an effect on head group reactivity in metal systems;[31] and a similar mechanism may be responsible here, where the electronic nature of the carborane backbone influences head group reactivity.[32] To address this issue, we deposited O1COOH monolayers on Ge(111) using similar surface preparation procedures, and characterized samples with XPS. The Ge(111) surface has a 1 × 1 structure, and therefore does not contain surface dimers. High-resolution spectra show (**Figure 4.4**) that both boron and chlorine are still present on the Ge(111) surface, indicating that the carborane backbone, not surface dimers, likely induce carboxyl binding.

4.3: Work Function Control

4.3.1: Procedures

Density Functional Theory

All density functional theory procedures and results are detailed in **Appendix A**.

Ultraviolet Photoelectron Spectroscopy

Measurements were performed using a Kratos Axis Ultra DLD after XPS analysis, using a He I excitation source (21.2 eV). The spectra energy scales were calibrated to the Fermi level of freshly evaporated Au. To obtain clean germanium surfaces, chlorine terminated germanium surfaces were Ar ion etched using a 3.8 kV accelerating voltage, 100 μA extractor current, and a beam current of 1.159 μA.

Contact Angle

Dynamic contact angle measurements were obtained using an automated FTA1000 Analyzer System (First Ten Angstroms, Inc., Portsmouth, VA) equipped with a 500 μL gas tight #1750 syringe (Hamilton Co., Reno, NV) and a 27 gauge flat-tip stainless steel needle. Control and analysis software utilized was FTA32 version 2.1.

Using the dynamic sessile drop method, the sample is brought into close proximity to the substrate and a 4 μL droplet of deionized water is deposited on the sample with the tip needle maintaining contact to the drop. To obtain advancing angle values, 2.5 μL of deionized water is added and then the same volume is withdrawn to obtain receding angle values. The volume change occurs over a 1.25 sec time period and then the drop is static for 8.75 sec. A cycle of volume increase and decrease is repeated a total of 8 times with 5 photographs captured per sec. The angle between the surface and the drop was analyzed for the final 6 cycles with 30 frames after each volume increase collected and averaged to obtain advancing contact angle as well as the same after each volume decrease to determine receding contact angle. The standard deviation for the majority of individual droplets throughout the analyzed cycles was found to be less than 1°. For both O1COOH and O9COOH, four germanium substrates were passivated and characterized by dynamic contact angle goniometry with at least two droplets per sample analyzed to determine advancing and receding angles. Reported error is the standard deviation on the average advancing (or receding) contact angles for the nine droplets analyzed for each sample type.

4.3.2: Results

Ultraviolet photoelectron spectroscopy (**Figure 4.5A**) was used to determine WF changes on the Ge(100) surface through the chemisorption of carborane carboxylic acid. The WF is calculated using **Equation 4.1**, where *hv* is the excitation energy of the He I photon (21.2 eV) and E_{cutoff} is the high binding energy (BE) cutoff of the spectrum.[1] This sharp intensity drop in the spectrum corresponds to the energy level at which electrons can no longer escape.

$$WF = hv - E_{cutoff} \tag{4.1}$$

The total WF change is a summation of both chemical bonding and molecular dipole effects, but due to the similarity of the binding between O1COOH and O9COOH isomers, we can directly compare how the molecular dipole affects surface WF. Using density functional theory (**Appendix A, Table A2**) with B3LYP functional,[12] we determined the dipole magnitudes and orientations to be 3.24 D oriented towards the head group for O1COOH (**Figure 4.5B**) and 5.14 D oriented away from the head group (**Figure 4.5C**) for O9COOH. These differences in dipole moment manifest themselves in a 5.22 pKa difference between O1COOH and O9COOH, with O9COOH having a more electron-rich and O1COOH a more electron-poor head group.[32] While the net dipole of the molecules chemisorbed on the Ge surface will change, these values are useful in making qualitative comparisons.

All surface treatments (O1COOH, O9COOH, and HCl) examined here cause increases in the low-energy cutoff region of the spectra due to the strong effect that chemical binding has on the Ge WF.[3] For reference, the clean Ge(100) surface and HCl-etched Ge(100) surface exhibit a WF of 4.56 eV (BE of 16.65 eV) and 4.13 eV (BE of 17.08 eV), respectively. Upon modifying the HCl-etched Ge(100) surface with O1COOH and O9COOH SAMs, the WF increased to 4.39 eV (BE of 16.82 eV) and decreased to 3.99 eV (BE of 17.22 eV), respectively. This result shows that the different dipole between carborane isomers influence the WF of the germanium surface in a similar fashion to Au and Ag.[12] Relative to the Ge-Cl surface, the vertical component of O1COOH points into the surface increasing the WF by 0.26 eV while the vertical component of the O9COOH points away from the surface decreasing the WF by 0.14 eV. These data indicate that the WF can shift by ~±0.2 eV relative to the Ge-Cl surface WF. The WF change with carborane dipole direction agrees with past work of carboranethiol SAMs on Au and Ag.[12] Additionally, following that work, these data suggest that a mixed monolayer of carborane carboxyls could tune the WF of Ge over a 0.4 eV range centered around 4.19 eV. Lastly, the correlation between dipole orientation and WF change offers further verification that these carboranes are tethered to the surface through the carboxylic acid head groups.

The advancing and receding contact angles for the O1COOH and O9COOH (shown in **Table 4.2**), indicate that the wetting properties and surface energy of the two are not significantly different. The O1COOH has the smaller contact angle and a smaller molecular dipole of the isomers used, consistent with data for M1 and M9 thiol on gold. Monolayers of M1 thiol on gold have a smaller dipole moment (1.06 D) relative to monolayers of M9 (4.08 D) thiol on gold, corresponding to static contact angles found to be 77.7° and 85.8°, respectively.[12] The reduced contact angle observed for the O1COOH and O9COOH may be due to substrate roughness (discussed in more detail in **Appendix i**), lower molecular packing density, or differences in molecular orientation.[26,29] The nonpolar solvent hexadecane was used as well, and similarly to the carboranethiol-Au system, the surface was completely wetted and no contact angle was attainable.[12]

The difference between the advancing and receding contact angle is hysteresis, which is indicative of the roughness. For both the O1COOH and O9COOH samples, the hysteresis is approximately 17°. This is only 2-3 times higher than what was observed for alkanethiols passivating germanium substrates using the facile water/ethanol solvent deposition method that is known to maintain the substrate roughness (~0.3 nm).[S17] The similarity of the hysteresis values indicates that this roughening is consistent between the two samples.

4.4: Conclusions and Prospects

In summary, carborane carboxyl monolayers were formed on germanium surfaces to modify surface WF with minimal effects to surface energy. This study finds that the carborane cluster affects head group surface reactivity, where carboxylic acid tethers assemble rather than thiol and hydroxyl head groups. This affinity for carboxylic acid is hypothesized to be induced by the unique electronic character of the carborane cluster. The carborane SAMs on Ge present the opportunity for surface WF to be tailored over a 0.4 eV range while the integrity of surface properties, such as wetting and adhesion, are maintained. How binding angle may influence these surface properties and whether this angle can be controlled with an annealing phase are areas for further exploration.[26,29] The results presented herein motivate future experimental and theoretical investigations to understand how the carborane clusters affect head group–surface binding chemistries, and whether other head group chemistries may be affected. Additionally, with the successful WF modulation presented here, it is worth exploring how carborane SAMs may benefit other semiconductor device systems, such as silicon[33] and metal oxides.[34]

4.5: References

(1) Greiner, M. T.; Helander, M. G.; Tang, W.-M.; Wang, Z.-B.; Qiu, J.; Lu, Z.-H. Universal Energy-Level Alignment of Molecules on Metal Oxides. *Nat. Mater.* **2011**, *11*, 76–81.

(2) He, T.; Ding, H.; Peor, N.; Lu, M.; Corley, D. A.; Chen, B.; Ofir, Y.; Gao, Y.; Yitzchaik, S.; Tour, J. M. Silicon/Molecule Interfacial Electronic Modifications. *J. Am. Chem. Soc.* **2008**, *130*, 1699–1710.

(3) Arefi, H. H.; Nolan, M.; Fagas, G. Role of the Head And/or Tail Groups of Adsorbed−$[X^{\text{Head Group}}]$–Alkyl–$[X^{\text{Tail Group}}]$ [X = O(H), S(H), $NH_{(2)}$] Chains in Controlling the Work Function of the Functionalized H:Si(111) Surface. *J. Phys. Chem. C* **2015**, *119*, 11588–11597.

(4) Jeong, S.; Garnett, E. C.; Wang, S.; Yu, Z.; Fan, S.; Brongersma, M. L.; McGehee, M. D.; Cui, Y. Hybrid Silicon Nanocone–Polymer Solar Cells. *Nano Lett.* **2012**, *12*, 2971–2976.

(5) Mäkinen, A. J.; Kushto, G. P. Monolayer-Induced Band Bending in the Near-Surface Region of Ge(111). *Phys. Rev. B* **2011**, *83*, 245315.

(6) Hacker, C. A. Modifying Electronic Properties at the Silicon–Molecule Interface Using Atomic Tethers. *Solid. State. Electron.* **2010**, *54*, 1657–1664.

(7) Avasthi, S.; Lee, S.; Loo, Y.-L.; Sturm, J. C. Role of Majority and Minority Carrier Barriers Silicon/Organic Hybrid Heterojunction Solar Cells. *Adv. Mater.* **2011**, *23*, 5762–5766.

(8) Paniagua, S. A.; Hotchkiss, P. J.; Jones, S. C.; Marder, S. R.; Mudalige, A.; Marrikar, F. S.; Pemberton, J. E.; Armstrong, N. R. Phosphonic Acid Modification of Indium−Tin Oxide Electrodes: Combined XPS/UPS/Contact Angle Studies. *J. Phys. Chem. C* **2008**, *112*, 7809–7817.

(9) Zhou, Y.; Fuentes-Hernandez, C.; Shim, J.; Meyer, J.; Giordano, A. J.; Li, H.; Winget, P.; Papadopoulos, T.; Cheun, H.; Kim, J.; Fenoll, M.; Dindar, A.; Haske, W.; Najafabadi, E.; Khan, T. M.; Sojoudi, H.; Barlow, S.; Graham, S.; Brédas, J.-L.; Marder, S. R.; Kahn, A.; Kippelen, B. A Universal Method to Produce Low–Work Function Electrodes for Organic Electronics. *Science* **2012**, *336*, 327–332.

(10) Giordano, A. J.; Pulvirenti, F.; Khan, T. M.; Fuentes-Hernandez, C.; Moudgil, K.; Delcamp, J. H.; Kippelen, B.; Barlow, S.; Marder, S. R. Organometallic Dimers: Application to Work-Function Reduction of Conducting Oxides. *ACS Appl. Mater. Interfaces* **2015**, *7*, 4320–4326.

(11) Jradi, F. M.; Kang, X.; O'Neil, D.; Pajares, G.; Getmanenko, Y. A.; Szymanski, P.; Parker, T. C.; El-Sayed, M. A.; Marder, S. R. Near-Infrared Asymmetrical Squaraine Sensitizers for Highly Efficient Dye Sensitized Solar Cells: The Effect of π-Bridges and Anchoring Groups on Solar Cell Performance. *Chem. Mater.* **2015**, *27*, 2480–2487.

(12) Kim, J.; Rim, Y. S.; Liu, Y.; Serino, A. C.; Thomas, J. C.; Chen, H.; Yang, Y.; Weiss, P. S. Interface Control in Organic Electronics Using Mixed Monolayers of Carboranethiol Isomers. *Nano Lett.* **2014**, *14*, 2946–2951.

(13) Hohman, J. N.; Zhang, P.; Morin, E. I.; Han, P.; Kim, M.; Kurland, A. R.; Mcclanahan, P. D.; Balema, V. P.; Weiss, P. S. Self-Assembly of Carboranethiol Isomers on Au{111}: Intermolecular Interactions Determined by Molecular Dipole Orientations. *ACS Nano* **2009**, *3*, 527–536.

(14) Grimes, R. N. *Carboranes*; Birtcher, K., Ed.; 3rd ed.; Academic Press, 2016.

(15) Thomas, J. C.; Schwartz, J. J.; Hohman, J. N.; Claridge, S. A.; Auluck, H. S.; Serino, A. C.;

Spokoyny, A. M.; Tran, G.; Kelly, K. F.; Mirkin, C. A.; Gilles, J.; Osher, S. J.; Weiss, P. S. Defect-Tolerant Aligned Dipoles within Two-Dimensional Plastic Lattices. *ACS Nano* **2015**, *9*, 4734–4742.

(16) Schwartz, J. J.; Mendoza, A. M.; Wattanatorn, N.; Zhao, Y.; Nguyen, V. T.; Spokoyny, A. M.; Mirkin, C. A.; Baše, T.; Weiss, P. S. Surface Dipole Control of Liquid Crystal Alignment. *J. Am. Chem. Soc.* **2016**, *138*, 5957–5967.

(17) Yan, H.; Hohman, J. N.; Li, F. H.; Jia, C.; Solis-Ibarra, D.; Wu, B.; Dahl, J. E. P.; Carlson, R. M. K.; Tkachenko, B. A.; Fokin, A. A.; Schreiner, P. R.; Vailionis, A.; Kim, T. R.; Devereaux, T. P.; Shen, Z.-X.; Melosh, N. A. Hybrid Metal–Organic Chalcogenide Nanowires with Electrically Conductive Inorganic Core through Diamondoid-Directed Assembly. *Nat. Mater.* **2017**, *16*, 349–355.

(18) Hohman, J. N.; Kim, M.; Bednar, H. R.; Lawrence, J. A.; McClanahan, P. D.; Weiss, P. S. Simple, Robust Molecular Self-Assembly on Germanium. *Chem. Sci.* **2011**, *2*, 1334–1343.

(19) Han, S. M.; Ashurst, W. R.; Carraro, C.; Maboudian, R. Formation of Alkanethiol Monolayer on Ge(111). *J. Am. Chem. Soc.* **2001**, *123*, 2422–2425.

(20) Ardalan, P.; Musgrave, C. B.; Bent, S. F. Formation of Alkanethiolate Self-Assembled Monolayers at Halide-Terminated Ge Surfaces. *Langmuir* **2009**, *25*, 2013–2025.

(21) Loscutoff, P. W.; Bent, S. F. Reactivity of the Germanium Surface: Chemical Passivation and Functionalization. *Annu. Rev. Phys. Chem.* **2006**, *57*, 467–495.

(22) Ardalan, P.; Sun, Y.; Pianetta, P.; Musgrave, C. B.; Bent, S. F.; Engineering, C. Reaction Mechanism, Bonding, and Thermal Stability of 1-Alkanethiols Self-Assembled on

Halogenated Ge Surfaces. **2010**, *26*, 8419–8429.

(23) Kachian, J. S.; Bent, S. F. Sulfur versus Oxygen Reactivity of Organic Molecules at the Ge(100)-2×1 Surface. *J. Am. Chem. Soc.* **2009**, *131*, 7005–7015.

(24) Lin, T.-H.; Lin, B.-Y.; Hao, T.; Chien, H.-Y.; Wang, J.-H.; Hung, W.-H. Adsorption and Thermal Reaction of Short-Chain Alcohols on Ge(100). *J. Phys. Chem. C* **2013**, *117*, 2760–2768.

(25) Baše, T.; Bastl, Z.; Plzák, Z.; Grygar, T.; Plešek, J.; Carr, M. J.; Malina, V.; Šubrt, J.; Večerníková, J. B. E.; Kříž, O. Carboranethiol-Modified Gold Surfaces. A Study and Comparison of Modified Cluster and Flat Surfaces. *Langmuir* **2005**, *21*, 7776–7785.

(26) Filler, M. A.; Van Deventer, J. A.; Keung, A. J.; Bent, S. F. Carboxylic Acid Chemistry at the Ge(100)-2 × 1 Interface: Bidentate Bridging Structure Formation on a Semiconductor Surface. *J. Am. Chem. Soc.* **2005**, *128*, 770–779.

(27) Lu, Z. H. Air–Stable Cl–Terminated Ge(111). *Appl. Phys. Lett.* **1998**, *68*, 520–522.

(28) Bodlaki, D.; Yamamoto, H.; Waldeck, D. H.; Borguet, E. Ambient Stability of Chemically Passivated Germanium Interfaces. *Surf. Sci.* **2003**, *543*, 63–74.

(29) Hwang, E.; Kim, D. H.; Hwang, Y. J.; Kim, A.; Hong, S.; Kim, S. Bidentate Structures of Acetic Acid on Ge(100): The Role of Carboxyl Oxygen. *J. Phys. Chem. C* **2007**, *111*, 5941–5945.

(30) Cai, Q.; Xu, B.; Ye, L.; Tang, T.; Huang, S.; Du, X.; Bian, X.; Zhang, J.; Di, Z.; Jin, Q.; Zhao, J. Stable Functionalization of Germanium Surface and Its Application in Biomolecules Immobilization. *Appl. Surf. Sci.* **2014**, *316*, 46–53.

(31) DiBenedetto, S. A.; Facchetti, A.; Ratner, M. A.; Marks, T. J. Molecular Self-Assembled Monolayers and Multilayers for Organic and Unconventional Inorganic Thin-Film Transistor Applications. *Adv. Mater.* **2009**, *21*, 1407–1433.

(32) Bregadze, V. I. Dicarba-Closo-Dodecaboranes $C_2B_{10}H_{12}$ and Their Derivatives. *Chem. Rev.* **1992**, *92*, 209–223.

(33) Hwang, H. -N.; Baik, J. Y.; An, K. -S.; Lee, S. S.; A.; Kim, Y.; Hwang, C. C.; Kim, B. Selectivity of the Chemisorption of Vinylacetic Acid on the Si(001)2×1 Surface. *J. Phys. Chem. B* **2004**, *108*, 8379–8384.

(34) Jadhav, S. A. Self-Assembled Monolayers (SAMs) of Carboxylic Acids: An Overview. *Cent. Eur. J. Chem.* **2011**, *9*, 369–378.

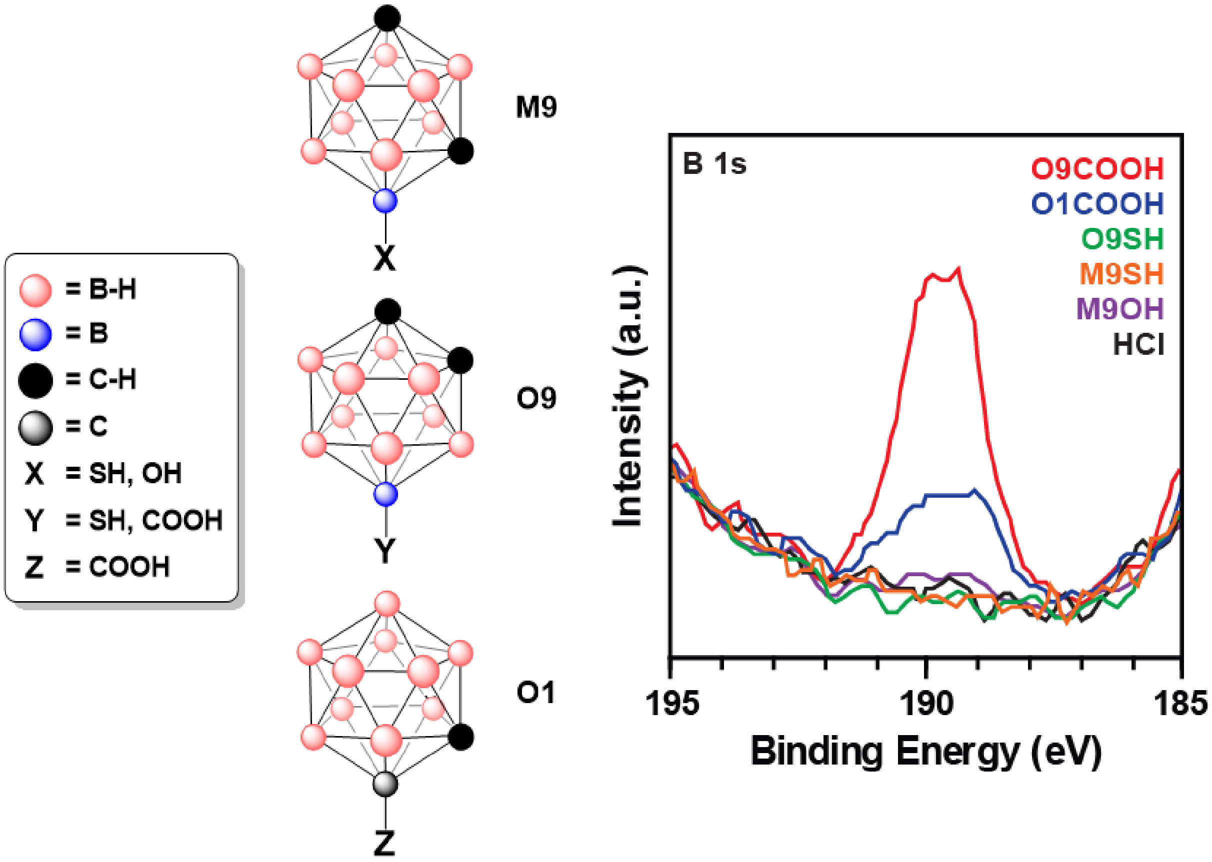

Figure 4.1: Schematic representation of 9-*m*-carborane (M9) with thiol and hydroxyl head groups (M9SH and M9OH, respectively), 9-*o*-carborane (O9) with thiol and carboxylic acid head groups (O9SH and O9COOH, respectively), and 1-*o*-carborane (O1) with a carboxylic acid head group (O1COOH). X-ray photoelectron spectra of the B 1s electron indicates only the presence of O9COOH and O1COOH on Ge(100).

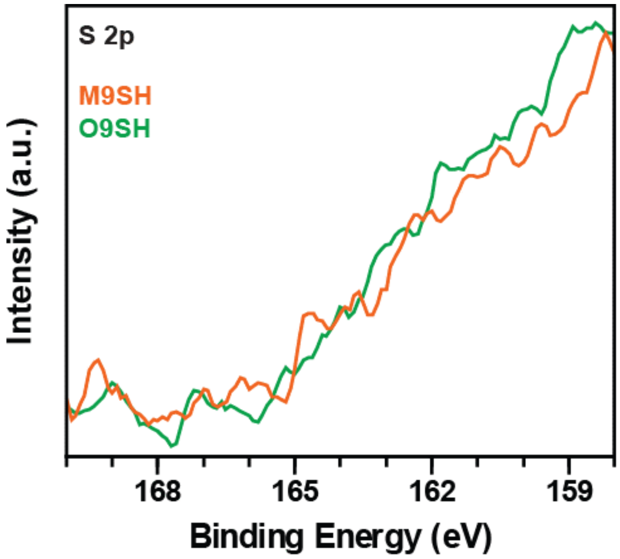

Figure 4.2: X-ray photoelectron spectroscopy of M9SH and O9SH on Ge (100), highlighting the S 2p region. Any signal from the presence sulfur is below instrument detection.

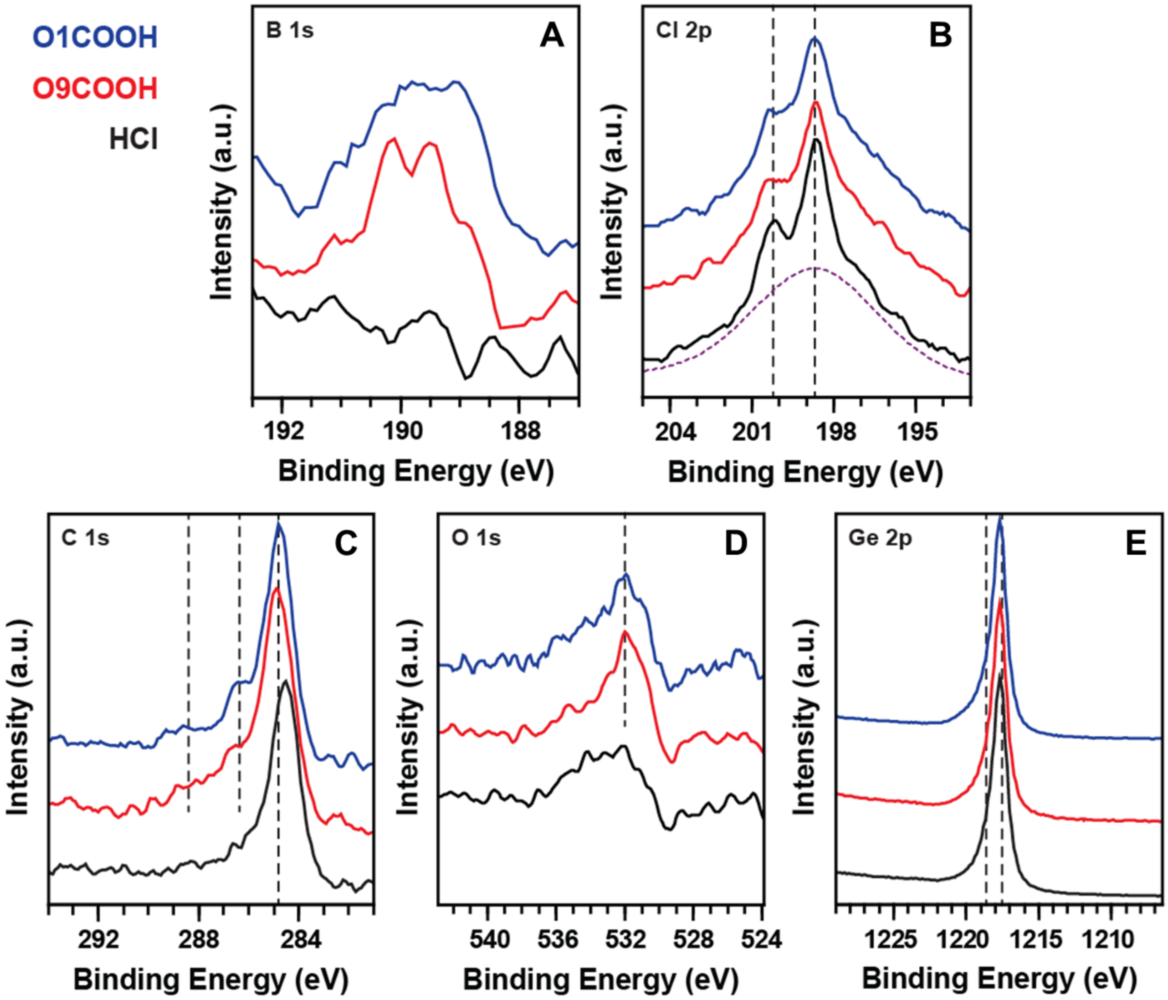

Figure 4.3: X-ray photoelectron spectroscopy of 1-COOH-*o*-carborane (O1COOH, blue trace), 9-COOH-*o*-carborane (O9COOH, red trace), and HCl etched (black trace) on Ge(100), highlighting the (A) B 1s, (B) Cl 2p, (C) C 1s, (D) O 1s, and (E) Ge 2p regions. Dotted purple line (B) outlines the Ge plasmon peak. Dotted black lines highlight specific peak positions.

	B 1s	**O 1s**	**Ge 2p**	**Cl $2p_{1/2}$**	**C 1s**
HCl	-	-	1217.68 eV 1218.58 eV	198.64 eV	284.5 eV 285.99 eV
O1COOH	189.61 eV	531.7 eV	1217.72 eV 1218.96 eV	198.68 eV	284.76 eV 286.38 eV 288.45 eV
O9COOH	189.68 eV	531.6 eV	1217.71 eV 1218.77 eV	198.64 eV	284.82 eV 286.53 eV 288.17 eV

Table 4.1: Summation of peak positions from X-ray photoelectron spectroscopy of HCl-etched (HCl), o-1-carborane carboxylic acid-passivated (O1COOH), and o-9-carborane carboxylic acid-passivated (O9COOH) Ge(100) surfaces.

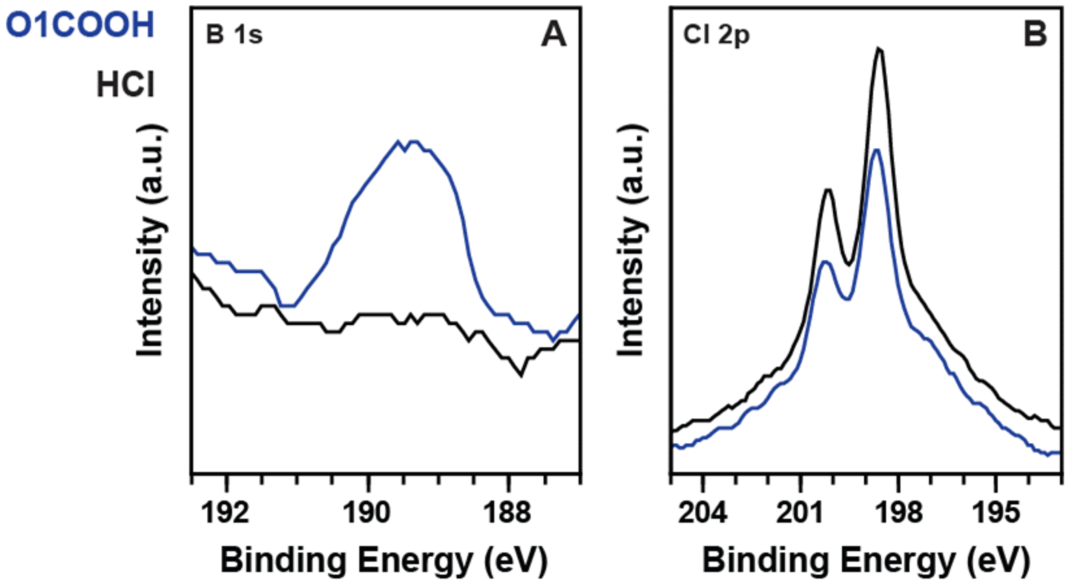

Figure 4.4: X-ray photoelectron spectroscopy of 1-COOH-o-carborane (O1COOH, blue trace) and chlorine (HCl, black trace) modified Ge (111). The (A) B 1s region shows that O1COOH is present and the (B) Cl 2p region shows a relative decrease in intensity of Cl between Cl-passivated and O1COOH-passivated surfaces.

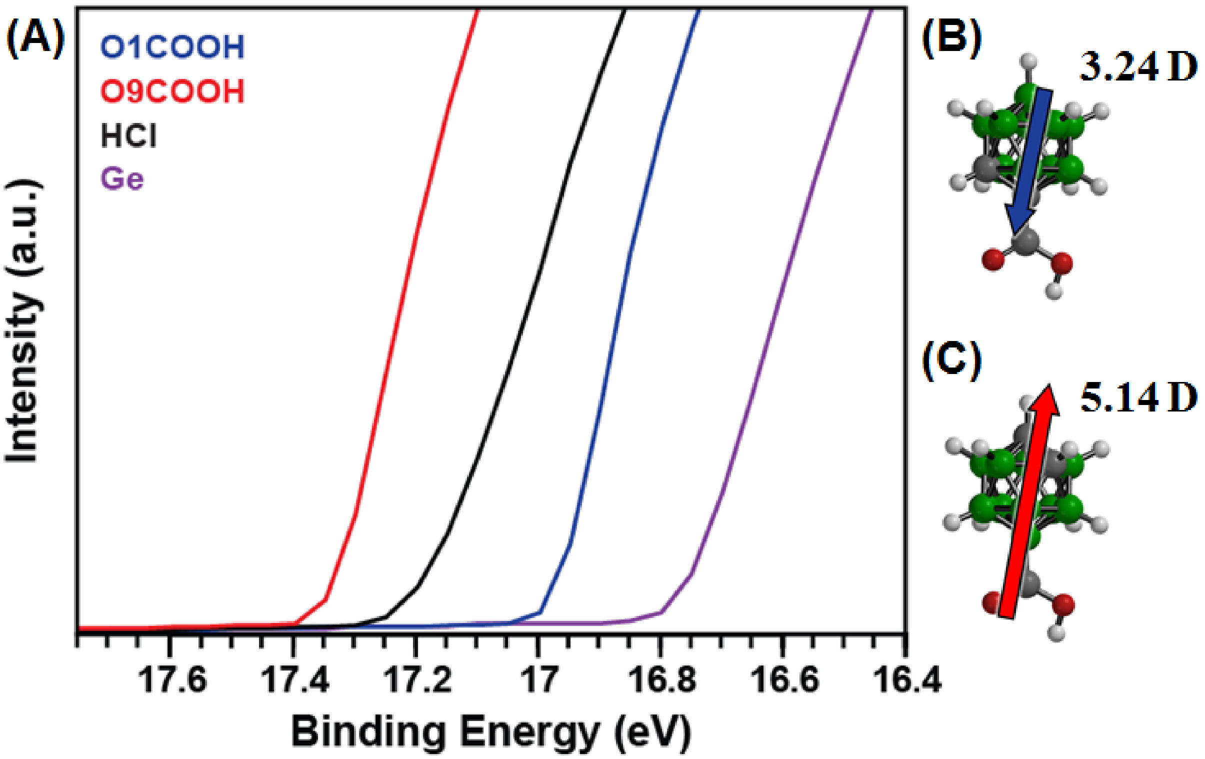

Figure 4.5: (A) Ultraviolet photoelectron spectroscopy of Ge(100) surfaces modified by 1-COOH-*o*-carborane (O1COOH, blue trace), 9-COOH-*o*-carborane (O9COOH, red trace), and chlorine (HCl, black trace), and Ar-ion-etched Ge(100) surface Ge, teal trace). Surface modification by O1COOH and O9COOH show a shift of ±0.2 eV from chlorine passivated Ge with both shifted lower from germanium's native work function. Schematic representations of (B) O1COOH and (C) O9COOH with calculated dipole magnitudes and orientations.

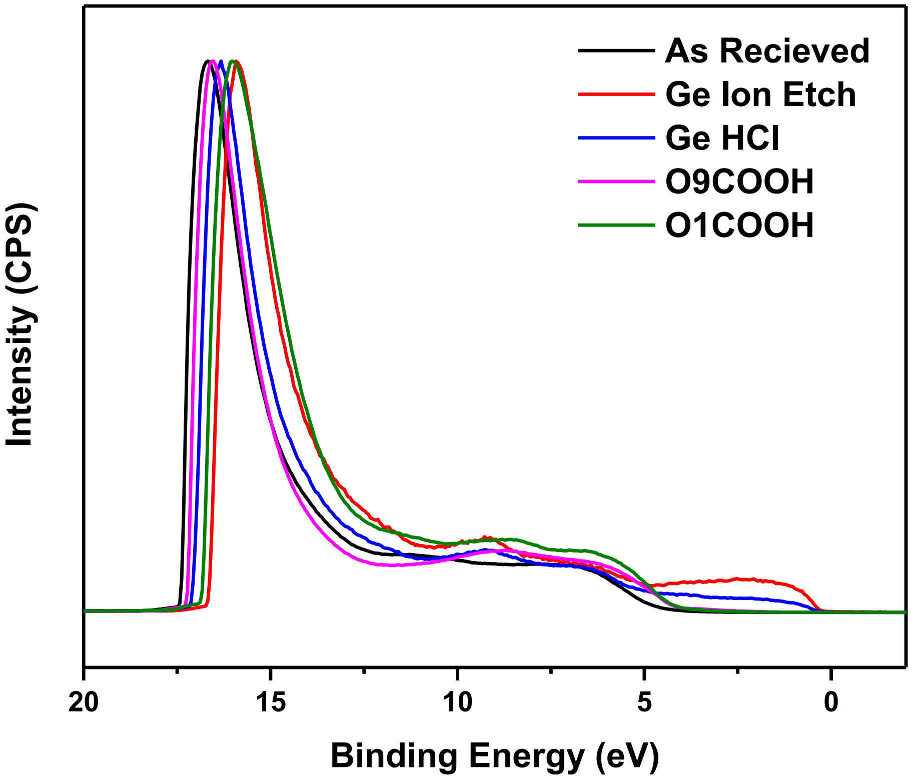

Figure 4.6: Full ultraviolet photoelectron spectra of a new (as received, black trace), Ar-ion-etched (Ge Ion Etch, red trace), HCl-etched (Ge HCl, blue trace), o-*9*-carborane carboxylic acid-passivated (O9COOH, pink trace), and o-*1*-carborane carboxylic acid-passivated (O1COOH, green trace) Ge(100) wafer surfaces.

	Advancing θ	**Receding θ**
O1COOH	**56.8 ± 5.5**	**39.9 ± 3.6**
O9COOH	**59.5 ± 4.6**	**42.3 ± 6.9**

Table 4.2: Advancing and receding contact angles for 1-COOH-*o*-carborane (O1COOH), 9-COOH-*o*-carborane (O9COOH) on Ge(100) surfaces.

CHAPTER 5: Progress towards the Molecular Battery

5.1: Introduction: Metal-Organic Coordinated Thin Films

The ultimate goal of fabricating a molecular battery requires ultrathin film layers of organics on germanium (< 50 nm) with 1−3 nm control in thickness and low surface roughness. There are a few approaches to achieving such structures (*i.e.*, anion-cation assembly,[1] condensation reaction,[2] and metal-organic coordinated films[3,4]) utilizing LBL assembly method. The LBL approach enables tailoring film thickness by the length of the molecule used. For example, LBL growth of metal-organic multilayers composed of bi-functional alkyl chains, specifically 16-mercaptohexadecanoic acid (MHDA, **Figure 5.1 and 5.2A**), with copper (II) ion coordination deposited on Au/Si substrates produces film thickness that can be increased by 17 Å per layer.[5,6] Additionally, these films maintain uniformity with each subsequent layer, with a film roughness (~1.8 nm, averaged over 30 layers) comparable to that of the substrate (~1.5 nm).[3,7] However, these multilayer films may lack the porosity that would allow the storage and flow of lithium ions necessary for battery applications.

Metal-organic frameworks (MOFs) also involve metal cations bound to organic linkers through metal coordination. Frameworks self-assemble into high-porosity structures that can be tailored by altering the length of the organic linker backbone. Additionally, the chemical nature of the MOF can be altered by changing the metal ion or chemical components of the organic linker. Together, these properties have made MOFs attractive materials for gas storage,[8] catalysis,[9] and batteries.[10]

While much of the research with MOFs is done with bulk powders, the use of surface-anchored metal organic frameworks (SurMOFs) is a promising means to fulfill the stringent requirements of a molecular battery. Previous work has shown that LBL growth of SurMOFs produces uniform ultrathin films.[11] Tri-functional molecular linkers that assemble with copper ions to form porous films, as in the case with Cu(II) with 1,3,5-benzenetricarboxylate (BTC), which belongs to the HKUST-1 system, have been explored (**Figure 5.1**).[4] These molecules can be tethered to surfaces using alkanethiols like MHDA (**Figure 5.2B**).[4,12–14] A central feature for the HKUST-1 structure is the copper-paddlewheel configuration, which binds two Cu^{2+} ions with four organic linker molecules, forming a "node" in the crystal structure. Much of the work performed to date on tethering HKUST-1 and MHDA multilayers has focused on understanding film growth and its driving forces, leaving much of the backbone chemical alterations and applications fairly unexplored. Here, we employ techniques used for the assembly of carboranes in metal-organic multilayers (depicted in **Figure 5.5A**) and the formation of SurMOFs with other organic linkers in an attempt to fabricate ultrathin films with precise control of thickness and a low degree of surface roughness, as, which can be implemented as an organic, solid-state battery separator.

5.2: Metal-Organic Multilayers of Carboranes

5.2.1: Introduction

Designing a well-ordered, layer-by-layer structure requires control over assembly and the ability to minimize defects. The first layer is an important first step in identifying and addressing defect sources, as any defects may propagate up through subsequent layers. Additionally, the first layer is an ideal system to test the effects that different electronic or physical properties have on electrochemical performance.

The thiol-Au system has been heavily exploited to study how various tail groups affect assembly.[15] For example, C12 on Au{111} adopts a 30° tilt from the surface normal, creating distinct domains and grain boundaries (**Figure 3A**).[15] This could be problematic for a molecular battery due to the large number of defects. Conversely, carboranethiols assemble on Au{111} with minimal defects (**Figure 5.3B**). This assembly is due to a spherical tail-group that defines the structure and prevents any surface tilt, resulting in a low-defect density, close-packed assembly.[16] Additionally, the electronic structure of carboranes can be altered without influencing the chemical environment (**Figure 5.4**). This electronic structure tailoring can be accomplished by altering the position of the carbon atoms relative to the host boron cluster can be changed to create *meta*-, *ortho*-, and *para*-carborane isomers (**Figure 5.4A,B,C**, respectively) and by adding functional groups (*i.e.*, head groups) to a number of vertices. Additionally, one (**Figure 5.4D**) or both (**Figure 5.4E**) carbons can be replaced by boron atoms to create anionic clusters with net -1 and -2 charges, respectively. This ability to alter electronic environment has enabled carboranes to impact surface alteration (see previous chapter),[17] gas sensing,[18] gas storage,[19] and battery applications.[20,21] These favorable physical and electronic properties make carboranes an attractive option for molecular battery studies.

The planned route for fabricating a molecular battery device is from the bottom-up, starting with SAM formation of carboranes on a germanium surface. A possible avenue for this assembly is discussed in the previous chapter. The next step in assembly is layer-by-layer deposition of carboranes. Recently, carboranes have been implemented in MOF systems for gas storage applications,[19] however, they have yet to be used as SurMOFs. Here, we investigate the assembly of bifunctional carboranes into metal-organic multilayer thin films for their eventual usage in a molecular battery.

5.2.2: Materials and Methods

Surface Preparation

Here, we used the reliable and well-studied thiol/Au system for LBL studies.[15] Gold substrates were prepared by first evaporating (CHA Solution – Metal Deposition e-Beam, CHA Industries, Fremont, CA) a 5 nm Ti wetting layer on undoped, single-side-polished, 4” Si(100) wafers (Silicon Quest Int., San Jose CA), followed immediately by evaporating 100 nm of Au. The molecule carboxy-1,12-*para*-carboranethiol (PCB, synthesized by the Prof. Tomáš Baše group at the Czech Academy of Science, Prague, Czech Republic), shown in **Figure 5.1 and 5.5A**, was used for these studies, following the same established protocol as the MHDA LBL multilayer system, due to the favorable thiol-metal bond and vertical orientation. Here, the *para*-carborane configuration places both the carbons and functional groups on opposite sides of the carborane cage, consequently, reducing the dipole moment of the molecule. Any dipole moment in the PCB structure will be solely due to electronegativity differences between the COOH and SH functional groups, reducing the dipole moment’s effect on assembly by limiting dipole-dipole interactions with neighboring entities both lateral and normal to assembly. This reduction in dipole influence will allow us to study the strength of the metal coordination with carboxyl and sulfhydryl functional groups. Several samples were prepared to identify the optimal parameters for multilayer formation, exploring deposition time, phase, and temperature.

Three solutions were prepared for this work to identify optimal deposition procedures for formation of carboranes multilayers, by exploring dependence on solvent for the organic linker (benzene or ethanol), deposition time (1 or 24 h), deposition phase (solution or vapor), and deposition temperature (room temperature or 70 ˚C). Solutions of 1 mM PCB in benzene (PCB/B), 1 mM PCB in ethanol (PCB/E), and 10 mM copper (II) perchlorate hexahydrate in ethanol were made. Gold substrates were placed in either the PCB/B (samples A-C, E) or PCB/E solution (sample D). After the molecular deposition, substrates were rinsed in ethanol, blown dry with nitrogen, and then placed in the ethanolic copper salt solution. Each subsequent layer deposition followed this PCB/Cu deposition procedure. After the desired deposition cycle, rinsing with ethanol, and drying with nitrogen, sample thickness was immediately characterized *via* ellipsometry.

Ellipsometry

Ellipsometry was carried out using a Gaertner LSE Stokes Ellipsometer with a HeNe laser (632.8 nm) in ambient conditions. Index of refraction (n_s) and extinction coefficient (k_s) for the gold substrate were modeled using these values, $n_s = 0.25$, $k_s = 3.46$, for evaporated gold films. Optical properties for organic films are assumed to be $n_f = 1.5$, $k_f = 0$. These are commonly accepted values for films < 100 nm.[7,22,23]

5.2.3: Results and Discussion

Representative ellipsometry data are shown in **Figure 5.5B** for five different sample preparation methods for the assembly of carborane multilayers. Sample A (black trace) was prepared *via* solution-phase deposition at room temperature using PCB/B, each layer was deposited for 1 h. Sample B (red trace) was prepared *via* solution-phase deposition at room temperature using PCB/B, each layer was deposited for 24 h. Sample C (blue trace) was prepared *via* vapor-phase deposition at room temperature using PCB/B, each layer was deposited for 24 h. Sample D (purple trace) was prepared *via* solution-phase deposition at room temperature using PCB/E, each layer was deposited for 24 h. Finally, sample E (green trace) was prepared *via* solution-phase deposition at 70 ˚C using PCB/B, each layer was deposited for 1 h.

Previous studies on LBL SurMOFs show that the film thickness increases linearly with deposition cycle, and the slope of progression is comparable to the organic-linker length.[24] The data presented in **Figure 5.5B** reveals that these PCB molecules do *not* follow the same trend. In fact, it appears that only single and bilayers formed on the surface, corresponding to thicknesses of ~5 and ~10 Å, respectively. It is evident from the plot that the variations in parameters tested had no significant effect on film thickness. From this study, it appears that the Cu coordination alone is not enough to promote LBL assembly with the deposition parameters used.

5.3: Metal-Organic Thin Films of MOF-14 and MOF-399

5.3.1: Introduction

As discussed above, the pore size in MOFs can be expanded by increasing the size of the organic linker backbone; for example, HKUST-1 can be extended to the copper (II) with organic linkers 1,3,5-tris(4- carboxyphenyl) benzene (BTB)[25] or 1,3,5-tris(4'-carboxy[1,1'-biphenyl]-4-yl)benzene (BBC)[26] as seen in the MOF-14 and MOF-399 systems, respectively. (**Figure 5.1**) with additional benzene rings. Anderson and coworkers have shown that SurMOFs can be created with these molecules, yielding films with thickness tunability and surface roughness comparable to that of MHDA.[11] Both of these organic linkers have a copper-paddlewheel configuration, similar to the HKUST-1 system. Additionally, Long and coworkers have shown that a similar MOF organic linker, 2,5-dihydroxyterephthalic acid, is capable of acting as a lithium ion conductor for battery applications.[27] Here, we investigate the capabilities of MOF-14 and MOF-399 for battery separator applications.

5.3.2: SurMOF Films

Samples were prepared through a similar bottom-up approach to that of HKUST-1 SurMOF films.[4] First a layer of MHDA (1 mM MHDA in ethanol) is deposited on evaporated Au (100 nm with Ti adhesion layer) on Si substrates (Platypus Technologies, LLC, Madison WI), and then alternating solution-phase deposition between an ethanolic solution of the organic component (either BTB or BBC, at a concentration of 0.1 mM) and an ethanolic solution of the inorganic component (1 mM of copper (II) acetate monohydrate). Film thickness and roughness values were determined by ellipsometry and atomic force microscopy (AFM), respectively.

Results indicate that, on average, MOF-14 increases thickness by ~1.9 nm/layer with a roughness of 1.5 nm (**Figure 5.6 and 5.7**) and MOF-399 increases thickness by ~3.2 nm/layer with a roughness of 1.6 nm (**Figure 5.6 and 5.8**). While the porosity of these films is yet to be determined, the precision in thickness control combined with an extremely low surface roughness is promising for molecular battery applications. Here, we explore the potential of these films for molecular battery applications by looking at lithium permittivity, *via* XPS, AFM, and cyclic voltammetry, and electronic/ionic conduction, *via* electrochemical impedance spectroscopy (EIS).

5.3.3: Soaking MOF-14 in a Lithium Salt Solution

Initial experiments started with MOF-14, due to its superior thickness control. Film degradation when exposed to a common battery electrolyte solvent and whether lithium could be physically inserted by soaking in a lithium salt solution was investigated with AFM and with AFM and XPS.

5.3.3.1: Materials and Methods

Sample Preparation

To test the stability of the SurMOF in the common battery electrolyte solutions, Au on Si substrates coated in 8 layers of MOF-14 (including underlying MHDA SAM) were investigated. One sample was submerged in an equal part solution of ethylene carbonate (EC) and diethyl carbonate (DEC) for 24 h (DEC:EC – 24 h), another in a 1 M solution of $LiClO_4$ in DEC:EC for 24 h ($LiClO_4$ – 24 h), and a third sample in a 1 M solution of $LiClO_4$ in DEC:EC for 48 h ($LiClO_4$ – 48 h). A MOF-14 sample was kept out of solution and used as a control (Pristine). Samples were then rinsed in a DEC:EC solution and dried with nitrogen gas. Characterization of surfaces was carried out with ellipsometry, AFM, and XPS to quantify film thickness, surface roughness and film integrity, and to qualify chemical environment, respectively.

Atomic Force Microscopy

Samples were imaged by AFM using a Bruker Dimension Icon Scanning Probe Microscope. The topography and mechanical properties of these substrates were simultaneously measured using the PeakForce Quantitative Nanomechanical Property Mapping (PeakForce QNM) mode. ScanAsyst-Air cantilevers (Bruker, spring constant of 0.4 ± 0.1 N/m) were used for all of the measurements. The peak force set point was chosen and adjusted automatically through the ScanAsyst® imaging mode.

X-Ray Photoelectron Spectroscopy

Spectra were acquired using a Kratos Axis Ultra DLD photoelectron spectrometer (Kratos Analytical, Manchester, UK) with a monochromatic Al K_α source at 300 W and a 300 μm × 700 μm spot size in an ultrahigh vacuum chamber (1×10^{-9} Torr). A pass energy of 20 eV was used with a resolution of 0.1 eV for the high-resolution regions of C 1s, Cu 3p, Li 1s, Cl 2p, and O 1s, using between 5 and 20 sweeps per region. Energy scales were corrected to the C-C binding energy of 284.8 eV. All peaks were analyzed using CasaXPS software, fit using Gaussian-Lorentzian line shapes with a Shirley background, and finally smoothed using a Savotzky-Golay quadratic.

5.3.3.2: Results

Ellipsometric data were plotted in a bar graph, shown in **Figure 5.9** (left), with error bars corresponding to the deviation in thickness between 5 different positions analyzed on the same sample. The DEC:EC – 24 h sample shows a small decrease in film thickness (14.9 ± 0.2 nm), compared to the Pristine sample (16.1 ± 0.3 nm), possibly due to the removal of some surface species or restructuring of the film. The $LiClO_4$ – 24 h and $LiClO_4$ – 48 h samples show slight increases in film thickness (16.1 ± 0.4 nm and 17.2 ± 0.6 nm, respectively) over the DEC:EC – 24 h sample. This change may be due to swelling that may occur when lithium is inserted into the film and increasing the soaking time enables increased lithium insertion. The topography of the films, as obtained by AFM, is shown in **Figure 5.9** (right). Surface roughness values of 1.75, 1.67, 1.57, and 1.51 nm corresponding to Pristine, DEC:EC – 24 h, $LiClO_4$ – 24 h, and $LiClO_4$ – 48 h samples, respectively. These AFM results, coupled with ellipsometry results, support that film integrity is maintained throughout deposition. Some protrusions are observed in the $LiClO_4$ – 48 h sample, possibly indicating that lithium salt deposits are forming on the surface of the film with prolonged exposure to the lithium salt solution. These protrusions may also increase the measured film thicknesses.

The chemical environment of the $LiClO_4$ – 24 h sample was investigated with XPS; results are shown in **Figure 5.10**. The lower deposition time sample was used to avoid any possible signal from salt deposits, as seen in $LiClO_4$ – 48 h. The C 1s region, **Figure 5.10A**, shows evidence for four different carbon bonds on the surface. The strongest peak at 284.8 eV corresponds to a C-C bond, common with adventitious carbon on the surface. The shoulder at 285.9 eV corresponds to a C-O-C bond, which indicates that DEC:EC solvent molecules are still present after drying with nitrogen and exposure to the ultrahigh vacuum environment in the XPS chamber. It is possible that the solvent molecules are located in pores, counterbalancing Li-ion charge.[27] The last strong peak at 288.7 eV corresponds to the presence of a O-C=O group, due to the carboxyl groups in the MOF-14 structure. The last feature on this spectrum is the presence of a small hump at 291.0 eV, from π-π* transitions, indicating the presence of sp^2 carbon. This last feature is expected due to the presence of delocalized electrons in the benzene rings of MOF-14.

Spectra highlighting Cu 3p, Li 1s, and Cl 2p regions is shown in **Figure 5.10B, C, and D**, respectively. These spectra show that all three elements are present in this film, however, it is difficult to make claims as to the oxidation states for these elements due to the low concentrations present and large full-width-half-max (FWHM). The Cu 3p peak is centered at 77.8 eV, corresponding to Cu^{+2}, which is expected from the salt ($Cu(ClO_4)_2 \cdot 6H_2O$) used for deposition. The Li 1s peak appears centered at 59.1 eV, corresponding to an oxidation state of +1. The Cl 2p peak is a doublet consisting of a Cl $2p_{3/2}$ and $2p_{1/2}$, which adds to the size of the FWHM. The presence of Cl is due to ClO_4, possibly from both the copper and lithium salts. Lastly, the oxygen peak (**Figure 5.10E**) shows evidence for two different oxygen species on the surface, with peaks centered at 531.8 and 532.9 eV corresponding to C-O and C=O, respectively. Unfortunately, different oxidation environments of oxygen are difficult to distinguish due to a low degree of shifting. We expect to see other oxygen group in this spectra (*i.e.*, ClO_4), however they are likely hidden under the other peaks. The XPS results presented are promising, showing that not only the

MOF-14 structure is present and maintained after exposure to Li salt solutions, but that lithium is also present. These results suggest that lithium is capable of moving through the MOF-14 thin film.

5.3.4: Impedance Spectroscopy of MOF-14

Electrochemical impedance spectroscopy is a method to measure the electrical impedance of a material as a function of the frequency of an applied electrical current. The technique can be used broadly to investigate electronic and ionic conductivity and resistivity sources within a sample. The shape and magnitude of the resulting spectrum gives information as to the degree of conductivity. For example, a semi-circular plot indicates conduction is occurring within the material; if there is a linear response, the material is insulating and behaving like a dielectric. Plots can be modeled to equivalent circuits to give information about contact resistance (R_Ω) and charge transfer resistance (R_{CT}). The contact resistance is a summation of total resistance in the circuit, while charge transfer resistance corresponds to electrochemical processes at the interface of an electrode.[28] From these resistances, conductivity (σ) can be calculated using **Equation 5.1**, where *t* is the thickness of the separator and *A* is the area of the electrode.

$$\boldsymbol{\sigma = \frac{t}{R_{CT}A}} \tag{5.1}$$

Here, we use EIS to identify whether films of MOF-14 are ionically and electronically conductive. While high ionic conductivity is favorable for battery applications, any electronic conduction would be detrimental for future prospects as a separation layer in a molecular battery, as this electrical conduction would create electronic shorts.

5.3.4.1: MOF-14 Materials and Methods

Sample Preparation

Several samples of 8-layer MOF-14 films (with underlying MHDA SAM) on Au were analyzed by EIS (Pristine). Several more 8-layer MOF-14 samples were heated to 130 ˚C for 2 h under vacuum (Annealed) to remove any possible water contamination, and then analyzed by EIS to look for conduction changes. Heating of MOF-14 films on Au using this method has been shown by infrared spectroscopy to remove water from the framework and AFM of heated samples has shown that the morphology remains unchanged.[11] Preliminary data collected by Anderson *et al.* shows the same is true at higher heating temperatures (150 and 180 ˚C) and longer heat exposures (4 and 6 h).[11] Additionally, to identify whether soaking in a lithium salt solution increases conductivity, 8-layer MOF-14 samples were annealed at 130 ˚C for 2 h under vacuum, soaked in 1 M $LiClO_4$ in EC:DEC for 24 h (Li 24 h), and then analyzed by EIS.

Electrochemical Impedance Spectroscopy

Electrochemical impedance spectra were collected at room temperature in an Ar glovebox with O_2 and H_2O concentrations <1 ppm using a Solartron 1252 frequency response analyzer at a frequency range of 100 kHz−100 mHz and a 10 mV (rms) potential. Contacts to the MOF were made using hanging mercury drop electrodes with contact areas of 0.0707−0.017 cm^2 (corresponding to drops of 3 and 1.5 mm in diameter, respectively). An alligator clip was used to make contact to the Au substrate.

5.3.4.2: MOF-14 Results

The EIS data for MOF-14 are plotted in **Figure 5.11A**, showing multiple 8-layer MOF-14: Pristine films (black traces), 8-layer MOF-14 films annealed at 130 ˚C for 2 h (red traces), and 12-

layer MOF-14 films soaked in a 1 M $LiClO_4$ EC:DEC solution for 24 h (blue traces). The semicircle shape indicates that there is some degree of conduction for all samples, with large resistance changes between similar samples and different positions on the same sample. Interestingly, resistance does not seem to be affected by the annealing step, indicating that water is not responsible for conduction. Additionally, soaking in a lithium salt solution does not improve the conductivity of these films to any noticeable degree. From these results, we hypothesize that these films are showing electronic conduction, due to electron hopping.[29] From **Equation 1**, the data presented in **Figure 5.11A**, a SurMOF thickness of 16.1 nm, and an average surface area of ~ 0.044 cm^2 we can calculate the approximate range of conductivities for each sample. The conductivities are 1.87 ± 0.01 µS/m – 11.23 ± 0.09 µS/m, 1.67 ± 0.02 µS/m – 6.98 ± 0.05 µS/m, and 1.47 ± 0.02 µS/m – 2.44 ± 0.01 µS/m, for pristine, annealed, and lithium-soaked samples, respectively. It is worth noting that these conductivities are estimations as surface areas are different between samples. Film thicknesses tend to be slightly different with heating and Li salt solution soaking processing steps and based on previous height change observations, which may affect conductivity by <10%. Nonetheless, the overall degree of electrical conductivity renders all MOF-14 films tested ineffective as an electrolyte separator. Additionally, while we expected the conductivity to increase upon addition of lithium ions, it is unclear whether these films are permeable to lithium ions due to the negligible change in conductivity when lithium salt is added. The negligible change in conductivity may be a result of either the non-permeability of Li through the MOF or that the electrical conductivity is much larger than any ionic conductivity, overwhelming any signal due to ionic conduction. Nonetheless, if a MOF is to be used for future battery work, an electrically insulating, ionically conductive system must be identified.

5.3.5: Impedance Spectroscopy of MOF-399

Next, we explored the possibility of MOF-399 as a battery separator by characterizing the conduction of the film on Au with EIS. With the same EIS procedures as for MOF-14, three different 12-layer MOF-399 on Au samples were tested: Pristine, annealed at 130 ˚C for 2 h under vacuum (Annealed), and annealed at 130 ˚C for 2 h under vacuum and soaked in 1 M $LiClO_4$ in EC:DEC for 24 h (Li 24 h). The plot of all samples (**Figure 5.11B**) shows differences in line shape compared to MOF-14. These results are characteristic of a dielectric response, indicating that there is no electronic or ionic conduction through the films.[28] Moreover, soaking films in lithium showed no significant improvement to conductivity. This indicates that while lithium may be present, it is not mobile. It is unclear why the conduction between MOF-399 and MOF-14 is different. It may be a result of the longer organic spacer, which increases the spacing between copper ions, or a much thicker film. The film thicknesses of the samples tested were 16.9 and 35.1 nm for 8L MOF14 and 12L MOF399, respectively. While the lack of conduction is promising for molecular battery purposes, the lithium conductivity requires further investigation.

5.4: Using MOF-399 as a Germanium Anode Surface Coating

With the promising EIS results from the MOF-399 films on Au substrates, we moved to investigating lithium conductivity through cyclic voltammetry by employing a Li-active anode material, specifically germanium. With cyclic voltammetry, a potential is applied between the Ge/MOF-399 electrode (working electrode) and lithium metal (counter electrode). Since germanium typically lithiates between 0.5 – 0.05 V *vs* Li/Li^+, the potential applied may drive lithium through the MOF thin film. We suspect that if there is Li conduction, it will be greatly reduced compared to bare germanium, due to the kinetic limitations of diffusing through a close-packed organic framework.

5.4.1: Construction of a Ge/MOF-399 Anode

5.4.1.1: Metal Contact Formation

The Ge/MOF-399 fabrication procedures are detailed in **Figure 5.12**. For these experiments a *p*-type Ge(100) wafer with a Ni metal contact was used due to the low-resistance contact that is formed with Ni. Single-side polished, 4” diameter, *p*-type Ge(100) wafers (resistivity < 1 Ω-cm) were etched in 30% hydrofluoric acid for 5 min, rinsed quickly with deionized water, then dried under a nitrogen gas stream. Wafers were stored in a nitrogen environment while transporting for further processing. Nickel was evaporated on the unpolished backside of the Ge(100) wafers using a CHA Solution – Metal Deposition e-Beam (CHA Industries). Wafers were then annealed using an MPTC Rapid Thermal Process – 600XP – Rapid Thermal Annealer (Modular Process Technology Corp) at 500 ˚C for 5 min at atmospheric pressure.

5.4.1.2: MOF-399 Layer-by-Layer

The MOF-399 thin film follows procedures discussed previously for Au. However, initial SAM formation of MHDA on Ge(100) follows previously published work by Hohman *et al.*[30] Samples were prepared by first depositing a layer of MHDA (1 mM MHDA in ethanol, mixed with deionized water in a 1:1 ratio) on Ge(100) surfaces for 24 h at room temperature. Next, the MOF-399 layers were formed by an alternating solution-phase deposition between a solution if 0.1 mM BBC in ethanol and a solution of 1 mM of copper (II) acetate monohydrate in ethanol. Two different film thicknesses were created: 4-layer and 12-layer. Film thickness and roughness values were determined by ellipsometry and AFM, respectively.

5.4.1.3: Experimental Methods

Ellipsometry

Ellipsometry was carried using a Gaertner LSE Stokes Ellipsometer with a HeNe laser (632.8 nm) in ambient conditions. The germanium substrate was modeled using $n_s = 5.45$ and $k_s = 0.85$ for bulk germanium. Optical properties for organic films are assumed to be $n_f = 1.5$, $k_f = 0$.[7,22,23]

Atomic Force Microscopy

As described in section 5.3.3.

Cyclic Voltammetry

The Ni side of the Ge anode substrates were mounted on stainless steel current collectors using nickel paste. Electrochemical characterization of MOF-399 films on Ge and bare Ge samples were conducted in a 3-electrode cell using a BioLogic VMP-3 potentiostat at room temperature in an Ar glovebox with O_2 and H_2O concentrations < 1 ppm. Lithium cycling was done in an electrolyte solution of 1M $LiClO_4$ in an equal part mixture of EC and DEC. Lithium metal foil (99.9%, Sigma Aldrich) served as both auxiliary and reference electrodes. Samples were scanned within a window of 2.5 and 0.1 V *vs.* Li/Li^+.

X-Ray Photoelectron Spectroscopy and Depth Profiling

Immediately after the 10 CV cycles on pristine Ge and Ge/MOF-399 samples, the sample surfaces were rinsed with EC:DEC and transferred to the XPS analysis chamber. Spectra were acquired using a Kratos Axis Ultra DLD photoelectron spectrometer (Kratos Analytical, Manchester, UK) with a monochromatic Al K_α source at 300 W and a 300 µm × 700 µm spot size in an ultrahigh vacuum chamber (1×10^{-9} Torr). A pass energy of 20 eV was used with a resolution of 0.1 eV for the high-resolution regions of C 1s, Ge 3d, Li 1s, O 1s, and Cu 2p using between 5 and 30 sweeps per region. The resulting spectra uncorrected. Depth profiling was performed with Ar-etching with an accelerating voltage of 3.8 kV, a beam current of 1.15 μA, an extractor current of 100 μA, and a raster size of 3 × 3 mm^2. High-resolution XPS was performed prior to Ar-etching, then after every 90 s of Ar-etching, with a total etch time of 360 s.

5.4.1.4: Results and Discussion

Ellipsometry and AFM results indicate that MOF-399 films were successfully grown on Ge(100) surfaces (**Figure 5.13**). Prior to processing, the bare Ge(100) surface has a low surface roughness of 0.35 nm (**Figure 5.13A**). The 4-layer MOF-399 has a thickness of 15.0 ± 1.0 nm and surface roughness of 1.3 nm (**Figure 5.13B)**, while the 12-layer has a thickness of 35.1 ± 1.6 nm and a surface roughness of 0.88 nm (**Figure 5.13C)**. This growth corresponds to a rate ~3.0 nm/layer with a roughness of ~1.5 nm, which is comparable to MOF-399 growth on Au surfaces. While there were only two different deposition cycles tested for this analysis, it shows promise for migration of MOF-399 to other surfaces.

Cyclic voltammetry was used to identify whether the MOF-399 multilayer film is Li-ion permeable under applied potentials. Lithiation of a pristine Ge(100) wafer is shown in **Figure 5.14A**. The first cycle involves a lithiation process that induced a phase change from crystalline Ge to $Li_{15}Ge_4$ and a delithation process forming amorphous Ge (described by **Equation 3.1**). The first lithiation process occurs between 0.31 and 0.1 V *vs*. Li/Li$^+$, and its corresponding CV peak is sharp. The de-lithation process occurs at 0.65 V *vs*. Li/Li$^+$ and the corresponding CV peak is much broader. Peak broadening occurs as a result of amorphism. The following lithiation/delithiation cycles show increasing peak broadening corresponding to an increasing degree of amorphousness, and appear to stabilize at cycle 8.

The cyclic voltammogram of the 12-layer film of MOF-399 on Ge(100) cycled against Li metal is shown in **Figure 5.14B**. This sample was cycled down to 0.05 V at 0.05 mV/s due to the lower currents obtained. The onset of a Ge-Li alloying reaction occurs at 0.31 V *vs*. Li/Li$^+$ in the first cycle and continues to increase in reaction rate (evident by an increase in current) until 0.05 V *vs*. Li/Li$^+$. The de-alloying reaction occurs at 0.61 V *vs*. Li/Li$^+$. Peak widths of both the reduction and oxidation peaks for the Ge/MOF-399 sample match those of the pristine sample. However, the peak intensity and width of the Ge/MOF-399 sample increase slowly with initial subsequent cycles, and then rapidly after cycle 8.

The presence of peaks associated with Ge-Li alloying reactions indicates that the MOF-399 multilayer is Li-permeable when an electric field is applied. The increase in peak current in the pristine Ge sample is a result of a decrease in atomic packing density and a subsequent increase in Li-permeability. The same phenomenon is present in the Ge/MOF-399 sample, however, the degree of the effect is larger. This increase in Li-permeability indicates that the structure of the multilayered film has expanded. Additionally, the smaller peak intensity for the MOF-399 coated Ge surface indicates that the film acts as an impeding force for lithiation.

Depth profiling using XPS and Ar etching revealed distinct differences between the pristine Ge sample and the Ge/MOF-399 sample. The C 1s spectra for the pristine Ge sample are shown in **Figure 5.15A**. At t = 0 (prior to starting an etch) the sample shows evidence for C-C and C-O carbon components that are common for physisorbed solvent (EC:DEC), as well as a large C=O component that is common for breakdown of carbonates during SEI formation.[31] At t = 90 s (after the first etch cycle) evidence for the physisorbed components decreases substantially and the C=O peak remains prominent. This C=O peak is likely the primary carbon component forming the SEI layer. As etching continues to t = 360 s, the C=O peak intensity decreases substantially indicating that the majority of the carbon interfacial layer has been etched away. It is worth noting that there is a large shift in binding energy after the first 90 s of etching. This shift is most likely a result of charging phenomena. Normally, this peak shift is calibrated internally using an unaltered element in the sample, however, that is not possible here due to the uncertainty of SEI formation and large variability that immerges from side reactions that occur during lithiation.

Spectra from the C 1s region for the Ge/MOF-399 sample is shown in **Figure 5.15B**. The $t = 0$ s spectrum is similar to that of the pristine sample with a large presence of C-C and C-O, however, with reduced C=O concentration. The presence of all carbon entities decreases as etch time increases, reaching near-zero concentration at $t = 360$ s, which is similar to the carbon layer on the pristine Ge sample. The similar etch times to remove the carbon layer between the pristine Ge and Ge/MOF-399 samples indicates that the thickness of the carbon layers is likely similar. Additionally, the small initial amount of C=O that is present at the surface of the film likely indicates a degree of electrolyte solution decomposition, but minimal compared with pristine Ge at $t \geq 0$.

Spectra for the Ge 3d regions for pristine Ge and Ge/MOF-399 are shown in **Figure 5.15C** and **5.15D**, respectively. Both samples show no evidence for the presence of Ge initially, and increased Ge concentration as etch time increases. The pristine Ge sample shows a large degree of GeO_2, which is a result of the native oxide layer on Ge. The lack of GeO_2 for the Ge/MOF-399 is due to the oxide removal step during MHDA deposition. As stated previously, solution decomposition at an electrode interface creates an insulating interfacial layer. Solution decomposition continues until the resistance is large enough where the potential at the SEI layer-solution interface is below the breakdown voltage of the electrolyte solution. Germanium oxide is an insulating material and contributes to the insulating component of the SEI. Therefore, the overall SEI layer for the pristine Ge sample is likely a combination of germanium oxide and carbon-based layers, where the Ge/MOF-399 sample is just carbon-based. This result indicates that the overall SEI layer is thicker for the pristine Ge sample than the Ge/MOF-399 sample.

The Li 1s spectra are shown in **Figure 5.15E** and **5.15F** for pristine Ge and Ge/MOF-399, respectively. These results are similar between the two samples and show that Li is present within the surface films. Spectra for the O 1s regions for prinstine Ge and Ge/MOF-399 are shown in **Figure 5.15G** and **5.15H**, respectively. These results complement the C 1s spectra, showing that oxygen is present, specifically carbon-bound oxygen, and that the concentration decreases with increases etch time. Additionally, as the concentration of carbon-bound oxygen decreases for pristine Ge, the concentration of metal-bound oxygen increases, which is a result of germanium oxide presence.

Lastly, the Cu 2p region for Ge/MOF-399 is shown in **Figure 5.16**. At t = 0, there is no presence of Cu, indicating that any Cu was removed from the surface or is covered by SEI formation as a result of solution decomposition. As etch time increases, the Cu signal appears and persists with similar concentrations throughout the Ar etch, and then decreases at t = 360 s.

The stark difference in carbon species between pristine and MOF-399–coated Ge combined with the presence of copper throughout the carbon layer indicate that the MOF-399 multilayer survived the lithiation process. Additionally, while there was some evidence for solution decomposition at the surface of the Ge/MOF-399 sample, it did not appear to substantially increase the overall SEI layer thickness. Lastly, the presence of germanium oxide hints that the MOF-399 layer may act as a more stable artificial SEI than the solution decomposition-driven SEI as the overall SEI thickness was larger for the pristine Ge sample than the MOF-399–coated Ge sample.

However, several more controls are needed before concrete conclusions can be drawn. Characterization of a pristine (no lithium cycling) 12-layer MOF-399 film on Ge *via* depth profile XPS would be beneficial for comparing chemical composition before and after lithiation. This experiment will enable a more definitive analysis of the effect of lithiation and whether the film is chemically altered. Additionally, characterization of a MHDA-passivated Ge sample would give insight into whether germanium oxide influences solution decomposition-driven SEI film thickness and if the MOF-399 film is more stable.

5.5: Conclusions and Prospects

In the presented work, we explored several possible systems for fabricating organic films to be used as separators in molecular batteries. We used a thiol/carboxyl *para*-carborane with copper in an attempt to assemble multilayer carboranes and found this design to be inadequate. After several deposition cycles, we were only able to form layers up to ~ 10 Å, which corresponds to a bilayer. We hypothesize that the lack of interaction strength within the multilayer prevented formation of thicker films. Unfortunately, these thicknesses are insufficient for application in a molecular battery. However, it would be ideal to use carboranes if possible; therefore, it is worth exploring other designs that increase interaction strengths. For example, by altering the placement of carbon atoms within the carborane cage to induce dipole-dipole interactions or by using tri-functional carboxylic acid groups, similar to the HKUST-1 system, to increase the degree of copper coordination.

We also explored the conductivity of multilayers of MOF-14 and MOF-399 on Au through electrochemical impedance spectroscopy. Ideally, films should exhibit ionic conduction and electrical insulation to be applicable in a molecular battery. Here, we found that MOF-14 showed signs of electronic conduction while MOF-399 was electronically insulating. From these results we concluded MOF-399 to be a more promising candidate to explore lithium permeability. To conduct this measurement, we deposited MOF-399 on Ge and cycled against lithium using CV. These results showed that while the MOF-399 film impeded Li-ion diffusion, the film was still lithium permeable. Depth profiling with XPS and Ar-etching indicate that the MOF-399 film is likely intact after cycling, prevents solution decomposition and further SEI formation, and is a more stable artificial-SEI layer than a solution-decomposition–formed SEI layer. The results presented herein support that MOF-399 is a promising candidate for a molecular battery insulator and for fabricating an artificial SEI layer. Moreover, metal-organic, coordinated multilayering appears to be a possible avenue for fabrication. This work lays the foundation for exploring metal-organic, coordinated multilayering with other organic backbones, whose large-scale MOF counterparts show large Li-ion conductivities.

5.6: References

(1) Tang, T.; Qu, J.; Müllen, K.; Webber, S. E. Molecular Layer-by-Layer Self-Assembly of Water-Soluble Perylene Diimides through π −π and Electrostatic Interactions. *Langmuir* **2006**, *22*, 26–28.

(2) Gu, J.-E.; Lee, S.; Stafford, C. M.; Lee, J. S. J.-H.; Choi, W.; Kim, B.-Y.; Baek, K.-Y.; Chan, E. P.; Chung, J. Y.; Bang, J.; Lee, J. S. J.-H. Molecular Layer-by-Layer Assembled Thin-Film Composite Membranes for Water Desalination. *Adv. Mater.* **2013**, *25*, 4778–4782.

(3) Benson, A. S.; Elinski, M. B.; Ohnsorg, M. L.; Beaudoin, C. K.; Alexander, K. A.; Peaslee, G. F.; DeYoung, P. A.; Anderson, M. E. Metal–Organic Coordinated Multilayer Film Formation: Quantitative Analysis of Composition and Structure. *Thin Solid Films* **2015**, *590*, 103–110.

(4) Ohnsorg, M. L.; Beaudoin, C. K.; Anderson, M. E. Fundamentals of MOF Thin Film Growth via Liquid-Phase Epitaxy: Investigating the Initiation of Deposition and the Influence of Temperature. *Langmuir* **2015**, *31*, 6114–6121.

(5) Anderson, M. E.; Mihok, M.; Tanaka, H.; Tan, L.-P.; Horn, M. W.; McCarty, G. S.; Weiss, P. S. Hybrid Approaches to Nanolithography: Photolithographic Structures with Precise, Controllable Nanometer-Scale Spacings Created by Molecular Rulers. *Adv. Mater.* **2006**, *18*, 1020–1022.

(6) Hatzor, A.; Weiss, P. S. Molecular Rulers for Scaling Down Nanostructures. *Science* **2001**, *291*, 1019–1020.

(7) Evans, S. D.; Ulman, A.; Goppert-Berarducci, K. E.; Gerenser, L. J. Self-Assembled Multilayers of Ω.-Mercaptoalkanoic Acids: Selective Ionic Interactions. *J. Am. Chem. Soc.* **1991**, *113*, 5866–5868.

(8) Barea, E.; Montoro, C.; Navarro, J. A. R.; Speakman, S.; Straut, C. M.; Wilusz, E.; Hatton, T. A.; Su, Z.-M.; Lemaire, J.; Keita, B.; Nadjo, L.; Dolbecq, A.; Navarro, J. A. R.; Horcajada, P.; Serre, C. Toxic Gas Removal – Metal–Organic Frameworks for the Capture and Degradation of Toxic Gases and Vapours. *Chem. Soc. Rev.* **2014**, *43*, 5419–5430.

(9) Falkowski, J. M.; Sawano, T.; Zhang, T.; Tsun, G.; Chen, Y.; Lockard, J. V.; Lin, W. Privileged Phosphine-Based Metal–Organic Frameworks for Broad-Scope Asymmetric Catalysis. *J. Am. Chem. Soc.* **2014**, *136*, 5213–5216.

(10) Ke, F.-S.; Wu, Y.-S.; Deng, H. Metal-Organic Frameworks for Lithium Ion Batteries and Supercapacitors. *J. Solid State Chem.* **2015**, *223*, 109–121.

(11) Ohnsorg, M. L. *Metal-Organic Coordinated Thin Film Systems*; Holland, 2016.

(12) Shekhah, O.; Wang, H.; Kowarik, S.; Schreiber, F.; Michael Paulus; Tolan, M.; Sternemann, C.; Evers, F.; Zacher, D.; Fischer, R. A.; Wöll, C. Step-by-Step Route for the Synthesis of Metal−Organic Frameworks. *J. Am. Chem. Soc.* **2007**, *129*, 15118–15119.

(13) Munuera, C.; Shekhah, O.; Wang, H.; Wöll, C.; Ocal, C.; Kaskel, S.; Woll, C.; Evers, F.; Zacher, D.; Fischer, R. A.; Woll, C. The Controlled Growth of Oriented Metal–organic Frameworks on Functionalized Surfaces as Followed by Scanning Force Microscopy. *Phys. Chem. Chem. Phys.* **2008**, *10*, 7257.

(14) Zacher, D.; Shekhah, O.; Wöll, C.; Fischer, R. A.; Akita, Y.; Kitagawa, H.; Dutta, P.; Boom,

M. E. van der; Zacher, D.; Fischer, R. A.; Wöll, C. Thin Films of Metal–Organic Frameworks. *Chem. Soc. Rev.* **2009**, *38*, 1418.

(15) Love, J. C.; Estroff, L. A.; Kriebel, J. K.; Nuzzo, R. G.; Whitesides, G. M. Self-Assembled Monolayers of Thiolates on Metals as a Form of Nanotechnology. *Chem. Rev.* **2005**, *105*, 1103–1170.

(16) Hohman, J. N.; Zhang, P.; Morin, E. I.; Han, P.; Kim, M.; Kurland, A. R.; Mcclanahan, P. D.; Balema, V. P.; Weiss, P. S. Self-Assembly of Carboranethiol Isomers on Au{111}: Intermolecular Interactions Determined by Molecular Dipole Orientations. *ACS Nano* **2009**, *3*, 527–536.

(17) Kim, J.; Rim, Y. S.; Liu, Y.; Serino, A. C.; Thomas, J. C.; Chen, H.; Yang, Y.; Weiss, P. S. Interface Control in Organic Electronics Using Mixed Monolayers of Carboranethiol Isomers. *Nano Lett.* **2014**, *14*, 2946–2951.

(18) Bae, Y.-S.; Farha, O. K.; Spokoyny, A. M.; Mirkin, C. A.; Hupp, J. T.; Snurr, R. Q. Carborane-Based Metal–Organic Frameworks as Highly Selective Sorbents for CO_2 Over Methane. *Chem. Commun.* **2008**, *20*, 4135.

(19) Kennedy, R. D.; Krungleviciute, V.; Clingerman, D. J.; Mondloch, J. E.; Peng, Y.; Wilmer, C. E.; Sarjeant, A. A.; Snurr, R. Q.; Hupp, J. T.; Yildirim, T.; Farha, O. K.; Mirkin, C. A. Carborane-Based Metal–Organic Framework with High Methane and Hydrogen Storage Capacities. *Chem. Mater.* **2013**, *25*, 3539–3543.

(20) Yoshida, K.; Sato, T.; Unemoto, A.; Matsuo, M.; Ikeshoji, T.; Udovic, T. J.; Orimo, S. Fast Sodium Ionic Conduction in $Na_2B_{10}H_{10}$–$Na_2B_{12}H_{12}$ Pseudo-Binary Complex Hydride and Application to a Bulk-Type All-Solid-State Battery. *Appl. Phys. Lett.* **2017**, *110*, 103901.

(21) Tang, W. S.; Matsuo, M.; Wu, H.; Stavila, V.; Zhou, W.; Talin, A. A.; Soloninin, A. V.; Skoryunov, R. V.; Babanova, O. A.; Skripov, A. V.; Unemoto, A.; Orimo, S.-I.; Udovic, T. J. Liquid-Like Ionic Conduction in Solid Lithium and Sodium Monocarba-Closo-Decaborates Near or at Room Temperature. *Adv. Energy Mater.* **2016**, *6*, 1502237.

(22) Daniel, T. A.; Uppili, S.; McCarty, G.; Allara, D. L. Effects of Molecular Structure and Interfacial Ligation on the Precision of Cu-Bound A,ω-Mercaptoalkanoic Acid "Molecular Ruler" Stacks. *Langmuir* **2006**, *23*, 638-648.

(23) Shi, J.; Hong, B.; Parikh, A. N.; Collins, R. W.; Allara, D. L. Optical Characterization of Electronic Transitions Arising from the Au/S Interface of Self-Assembled N-Alkanethiolate Monolayers. *Chem. Phys. Lett.* **1995**, *246*, 90–94.

(24) Anderson, M. E.; Tan, L. P.; Tanaka, H.; Mihok, M.; Lee, H.; Horn, M. W.; Weiss, P. S. Advances in Nanolithography Using Molecular Rulers. *J. Vac. Sci. Technol. B Microelectron. Nanom. Struct.* **2003**, *21*, 3116–3119.

(25) Chen, B.; Eddaoudi, M.; Hyde, S. T.; O'Keeffe, M.; Yaghi, O. M. Interwoven Metal-Organic Framework on a Periodic Minimal Surface with Extra-Large Pores. *Science* **2001**, *291*, 1021-1023.

(26) Furukawa, H.; Go, Y. B.; Ko, N.; Park, Y. K.; Uribe-Romo, F. J.; Kim, J.; O'Keeffe, M.; Yaghi, O. M. Isoreticular Expansion of Metal–Organic Frameworks with Triangular and Square Building Units and the Lowest Calculated Density for Porous Crystals. *Inorg. Chem.* **2011**, *50*, 9147–9152.

(27) Wiers, B. M.; Foo, M.-L.; Balsara, N. P.; Long, J. R. A Solid Lithium Electrolyte via Addition of Lithium Isopropoxide to a Metal–Organic Framework with Open Metal Sites.

J. Am. Chem. Soc. **2011**, *133*, 14522–14525.

(28) Bard, A. J.; Faulkner, L. R. *Electrochemical Methods: Fundamentals and Applications*; 1st ed.; John Wiley & Sons, Inc.: New York, 1980.

(29) Stavila, V.; Talin, A. A.; Allendorf, M. D. MOF-Based Electronic and Opto-Electronic Devices. *Chem. Soc. Rev.* **2014**, *43*, 5994–6010.

(30) Hohman, J. N.; Kim, M.; Lawrence, J. A.; McClanahan, P. D.; Weiss, P. S. High-Fidelity Chemical Patterning on Oxide-Free Germanium. *J. Phys. Condens. Matter* **2012**, *24*, 164214.

(31) Nakai, H.; Kubota, T.; Kita, A.; Kawashima, A. Investigation of the Solid Electrolyte Interphase Formed by Fluoroethylene Carbonate on Si Electrodes. *J. Electrochem. Soc.* **2011**, *158*, A798.

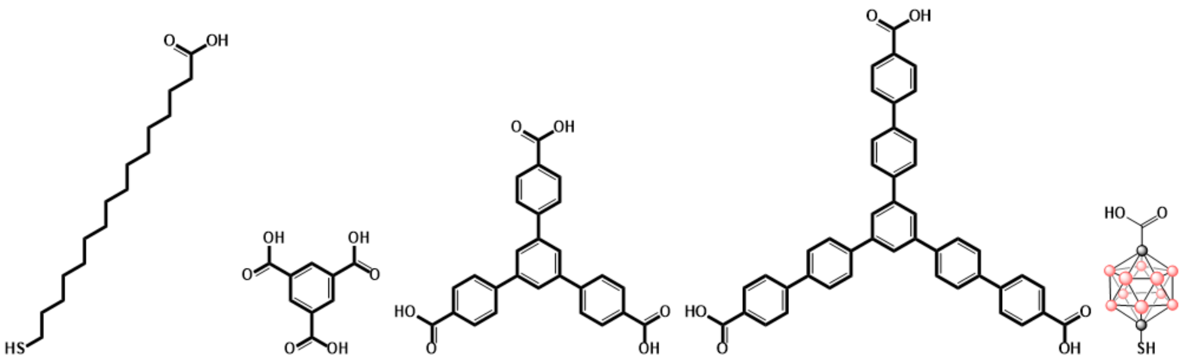

MHDA **HKUST-1** **MOF-14** **MOF-399** **PCB**

Figure 5.1: Schematic representation of molecules utilized for metal-organic coordinated thin films: 16-mercaptohexadecanoic acid (MHDA), 1,3,5-benzenetricarboxylate (BTC, used in HKUST-1), 1,3,5-Tris(4-carboxyphenyl) benzene (BTB, used in MOF-14), 1,3,5-Tris(4'-carboxy[1,1'-biphenyl]-4-yl)benzene (BBC, used in MOF-399), and 1-SH, 12-COOH *para*-carborane (PCB).

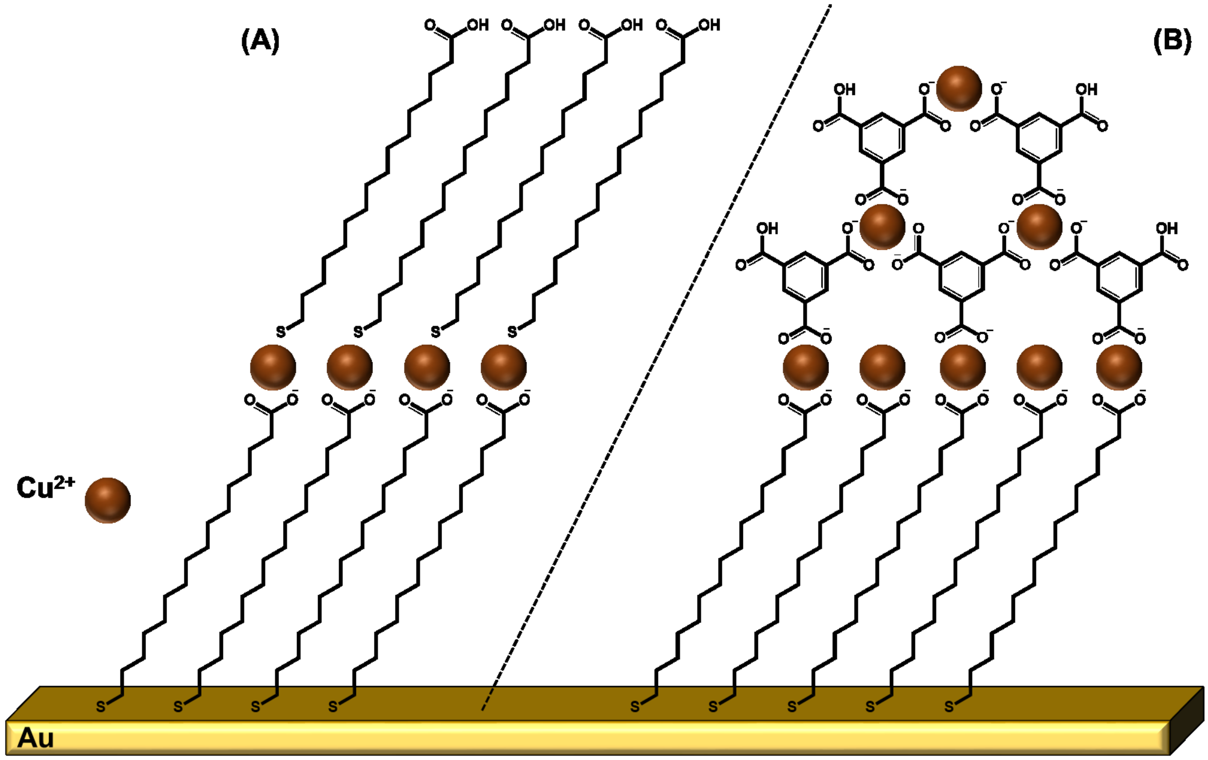

Figure 5.2: Schematic representation of metal-organic-framework assemblies of (A) 16-mercaptohexadecanoic acid (MHDA), and (B) copper (II) coordinated 1,3,5-benzenetricarboxylate ($Cu_3(BTC)_2$, HKUST-1) on MHDA.

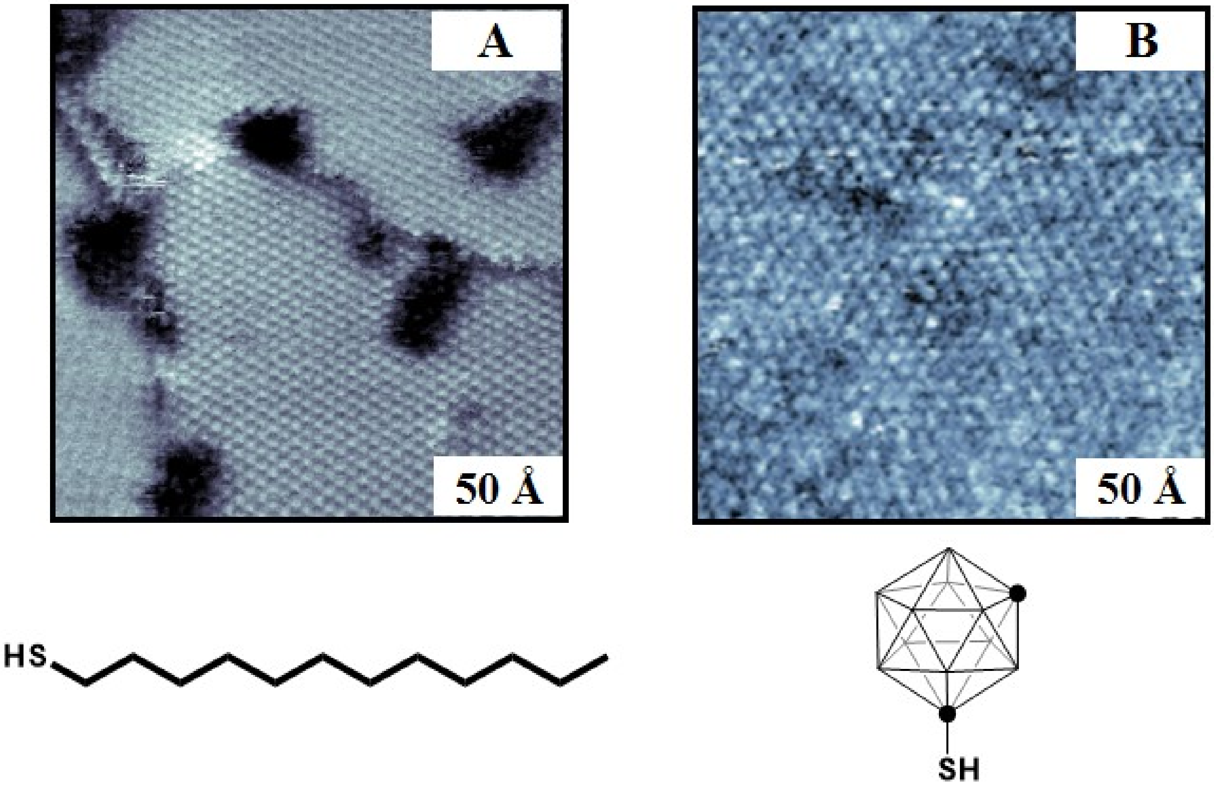

Figure 5.3: Scanning tunneling microscopy of (A) 1-dodecanethiol and (B) *m*-1-carboranethiol assembled on Au{111} shows topography of molecular assemblies. Schematic representations of both molecules are underneath their respective micrographs. Micrographs are reproduced with permission.[16]

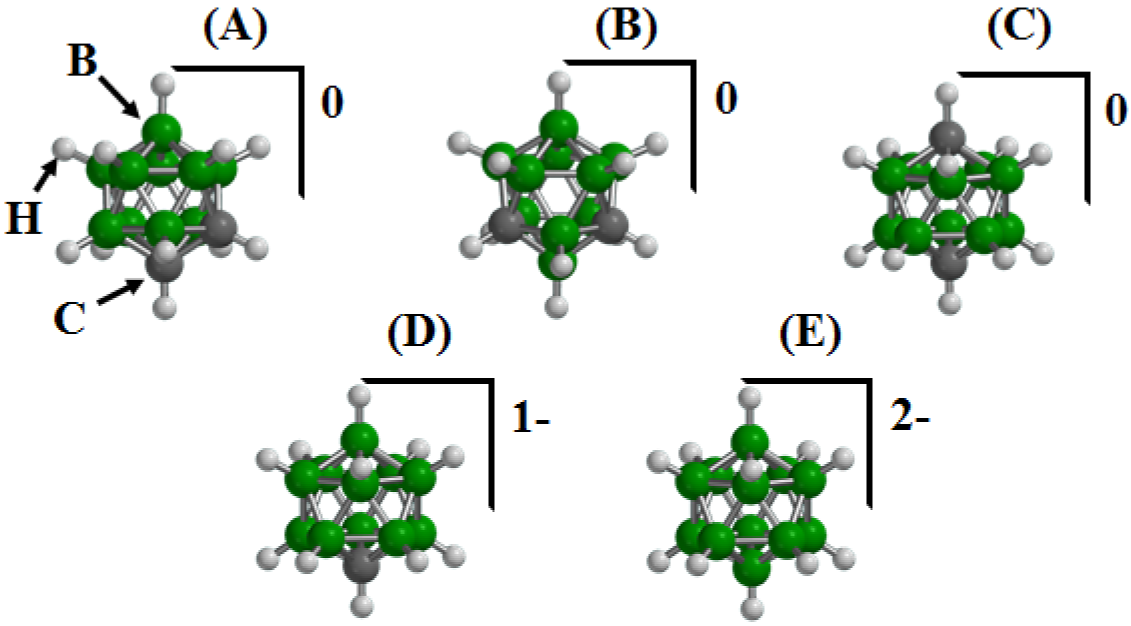

Figure 5.4: Schematic representations of (A) *ortho*-, (B) *meta*-, and (C) *para*-carborane, all possessing a neutral net charge, (D) carborane monoanion, possessing a net charge of -1, and (E) dodecaborate, possessing a net charge of -2.

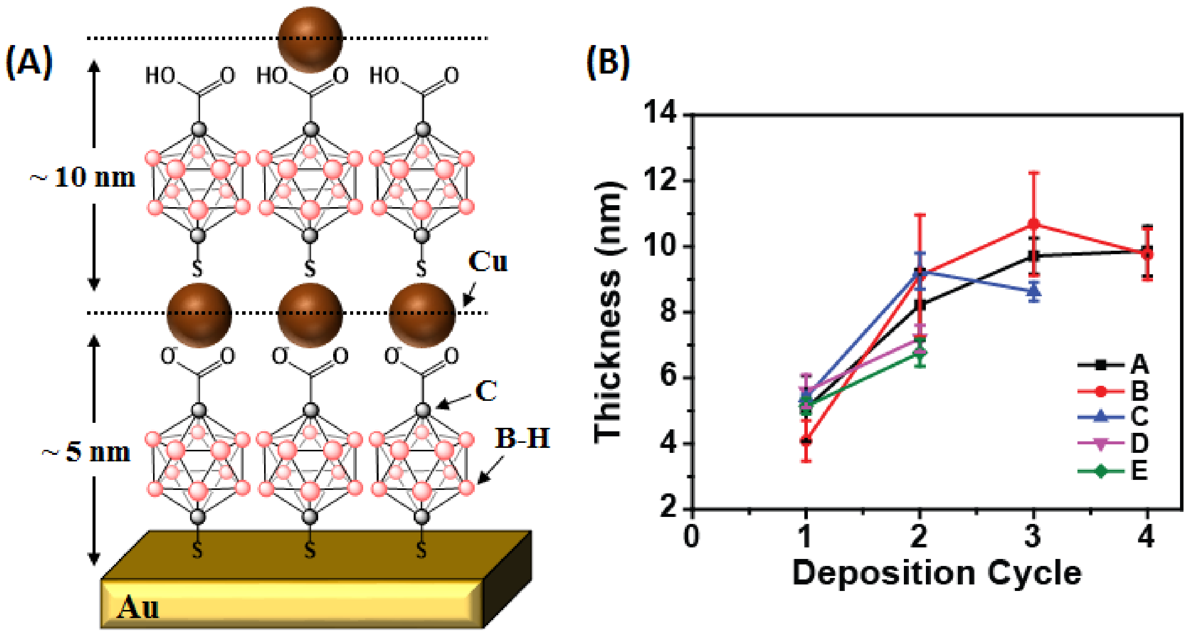

Figure 5.5: (A) Schematic representation of metal-organic-framework assemblies of carboxy-1,12-*para*-carboranethiol (PCB) with Cu^{2+}. (B) Thicknesses of PCB samples A (black trace) prepared by solution-phase deposition for 1 h at room temperature using PCB in benzene, B (red trace) prepared by solution-phase deposition for 24 h at room temperature using PCB in benzene, C (blue trace) prepared *via* vapor-phase deposition for 24 h at room temperature using PCB in benzene, D (purple trace) prepared by solution-phase deposition for 24 h at room temperature using PCB in ethanol, and E (green trace) prepared by solution-phase deposition for 1 h at 70 ˚C using PCB in benzene. Data were collected *via* ellipsometry. Results indicate that film thickness up to 10 Å formed, with error bars representing deviation in thickness on the same sample (n=5).

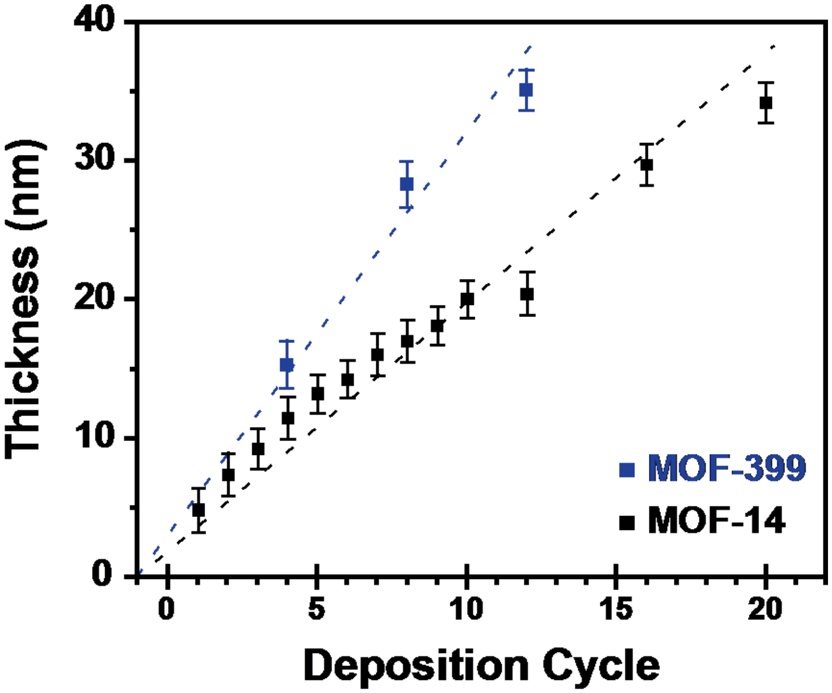

Figure 5.6: Thickness as determined by ellipsometry plotted with respect to the deposition cycle for MOF-14 (black) and MOF-399 (blue) with dotted trend lines. The roughness of each deposition cycle is plotted as the error bar.

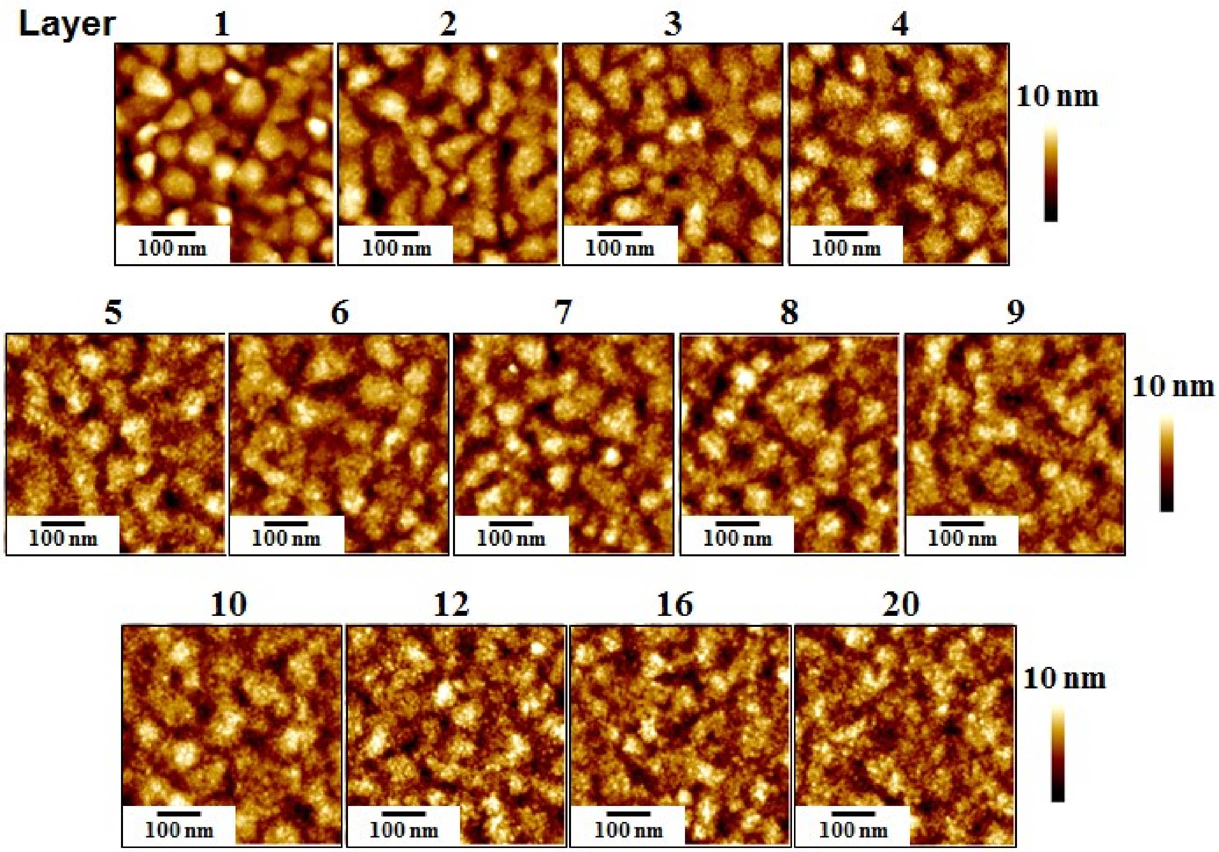

Figure 5.7: Atomic force micrographs of MOF-14 thin films grown on Au on Si.

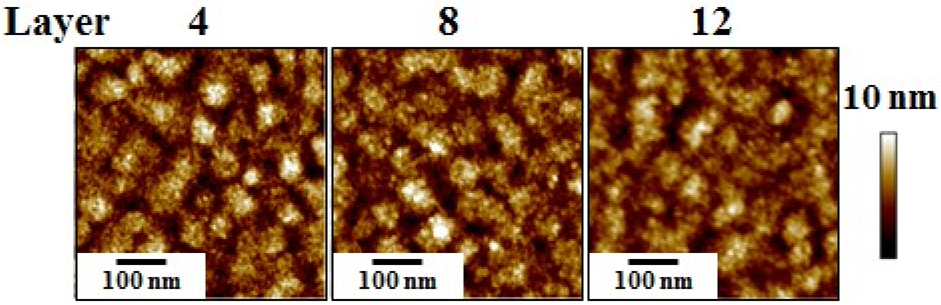

Figure 5.8: Atomic force micrographs of MOF-399 thin films grown on Au on Si.

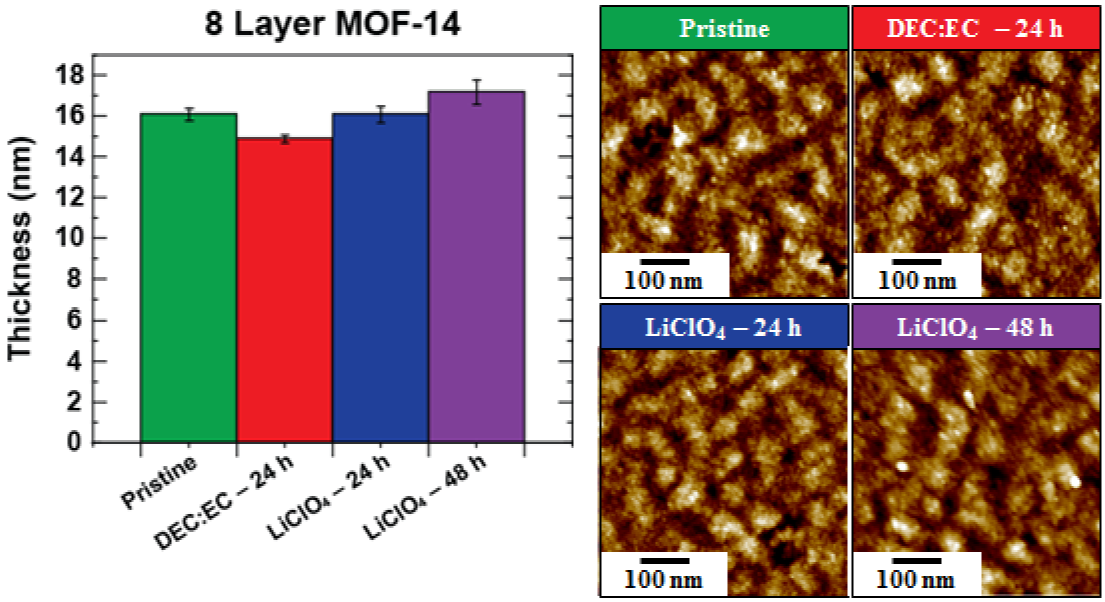

Figure 5.9: Bar graph (left) shows the thickness four MOF-14 film on Au samples, pristine, submerged in an equal part solution of ethylene carbonate (EC) and diethyl carbonate (DEC) for 24 h (DEC:EC – 24 h), a 1 M solution of $LiClO_4$ in DEC:EC for 24 h ($LiClO_4$ – 24 h), and a 1 M solution of $LiClO_4$ in DEC:EC for 48 h ($LiClO_4$ – 48 h). The error bar is deviation in height across the same sample (n=5). Atomic force micrographs (right) of the four samples show film topography is maintained.

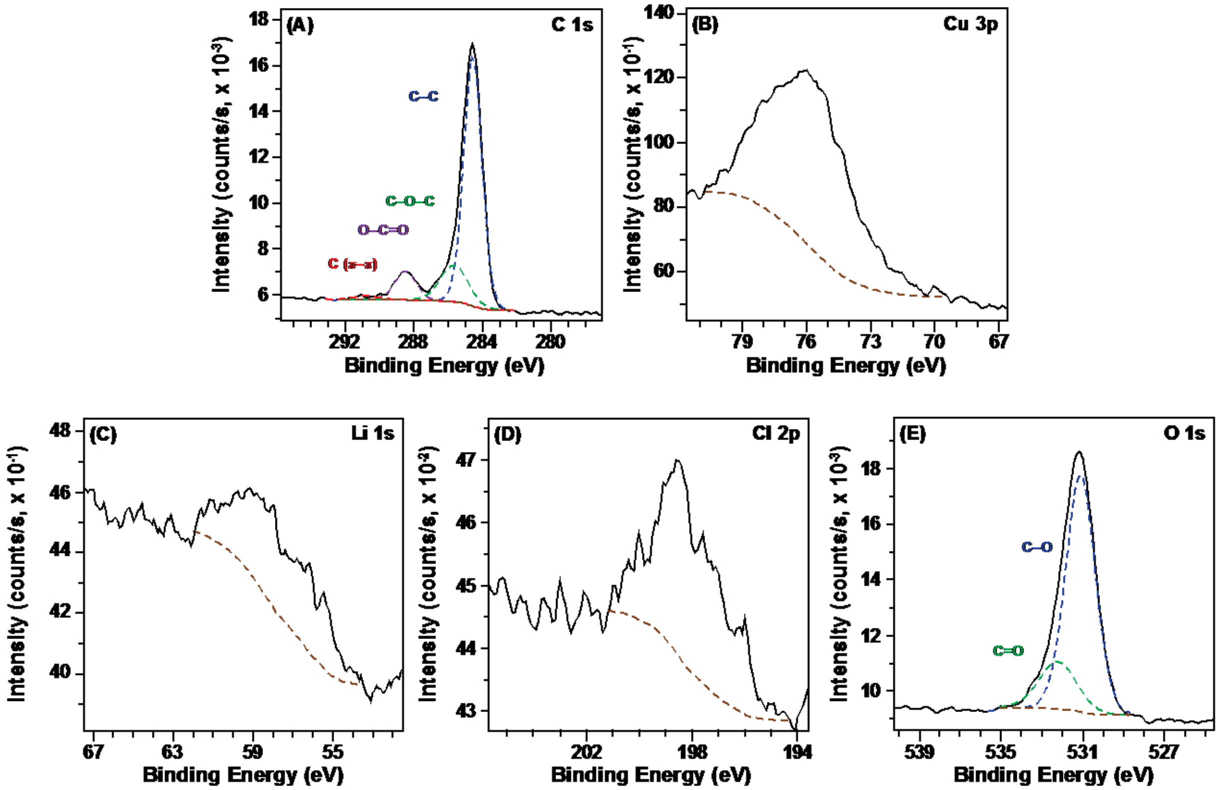

Figure 5.10: X-ray photoelectron microscopy of MOF-14 that was soaked in a solution of 1 M $LiClO_4$ in DEC:EC for 24 h, highlighting the (A) C 1s, (B) Cu 3p, (C) L1 1s, (D) Cl 2p, and (E) O 1s regions. The baseline is fitted using a Shirley background line shape (brown dashed-line).

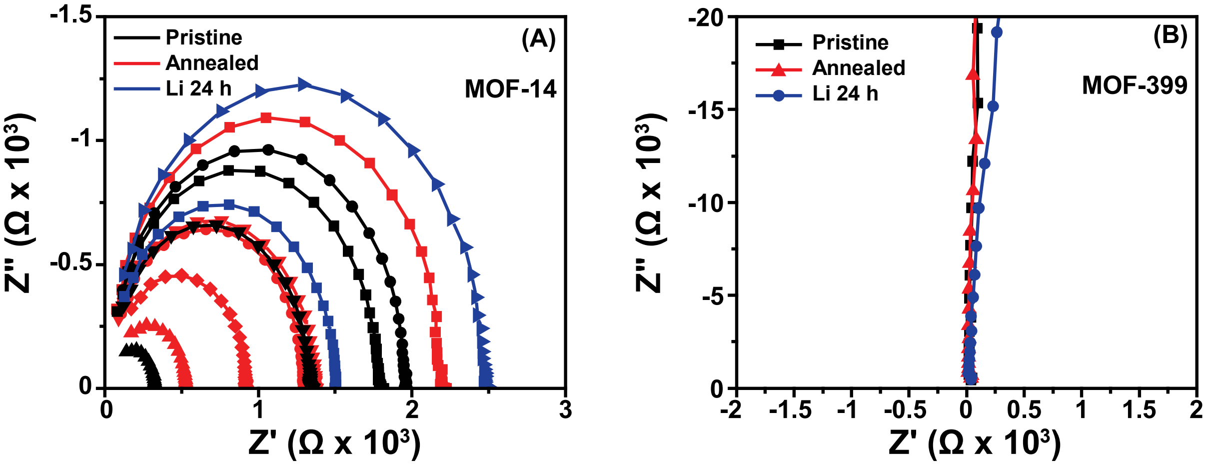

Figure 5.11: Electrochemical impedance spectroscopy (EIS) for (A) three 8-layer MOF-14 films on Au samples: pristine (black trace), annealed at 130 ˚C for 2 h (red traced), and soaked in lithium salt solution (1 M $LiClO_4$ in EC:DEC) (blue trace). Spectra of (B) three 12-layer MOF-399 films on Au samples: pristine (black trace), annealed at 130 ˚C for 2 h (red traced), and soaked in lithium salt solution (1 M $LiClO_4$ in EC:DEC) soaked (blue trace).

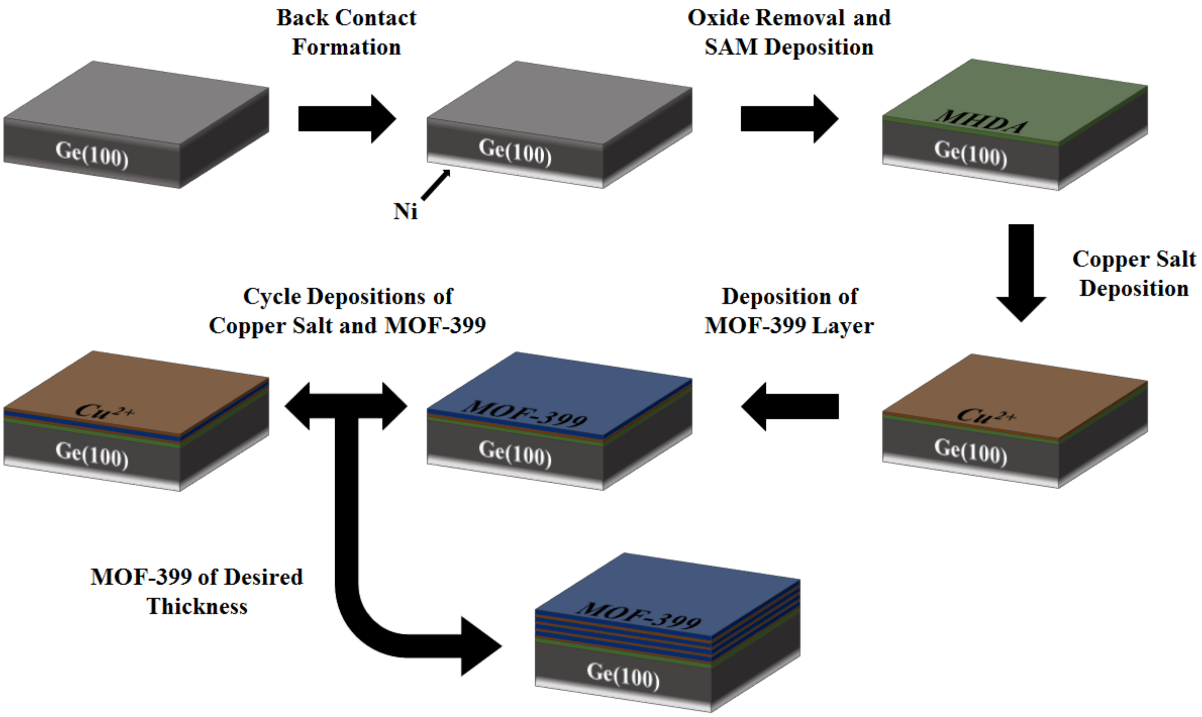

Figure 5.12: Schematic representation of the Ge anode / MOF-399 formation process.

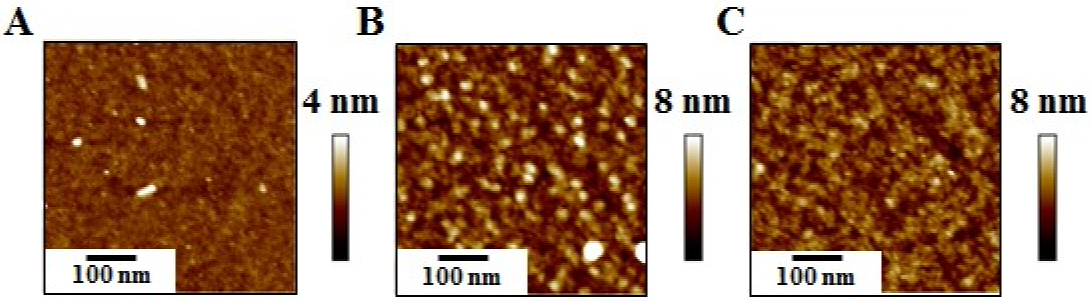

Figure 5.13: Atomic force micrographs of (A) bare Ge(100), (B) 4 layers of MOF-399 on Ge(100), and (C) 12 layers of MOF-399 on Ge(100). Sample characterization revealed (A) roughness of 0.35 nm, (B) thickness of 15.0 ± 1.0 nm as measured by ellipsometry with a roughness of 1.3 nm as measured by AFM, and (C) a thickness of 35.1 ± 1.6 nm and a roughness of 0.88 nm.

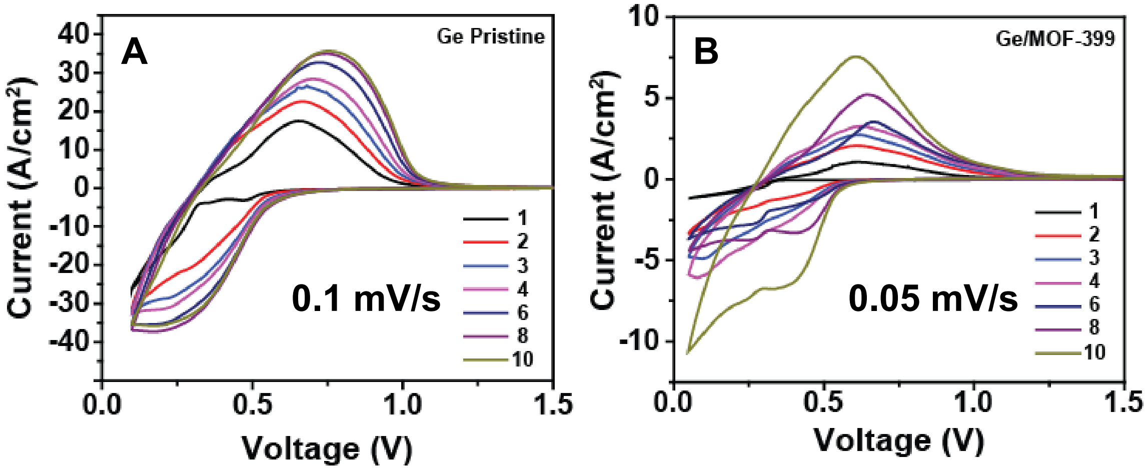

Figure 5.14: Cyclic voltammograms of (A) a pristine Ge(100) wafer and (B) a Ge(100) wafer coated with 12 layers of MOF-399. Scans were run for 10 cycles between 1.5 and 0.1 V *vs*. Li/Li$^+$ at 0.1 mV/s for pristine Ge and between 1.5 and 0.05 V *vs*. Li/Li$^+$ at 0.05 mV/s for Ge with a MOF-399 thin film coating.

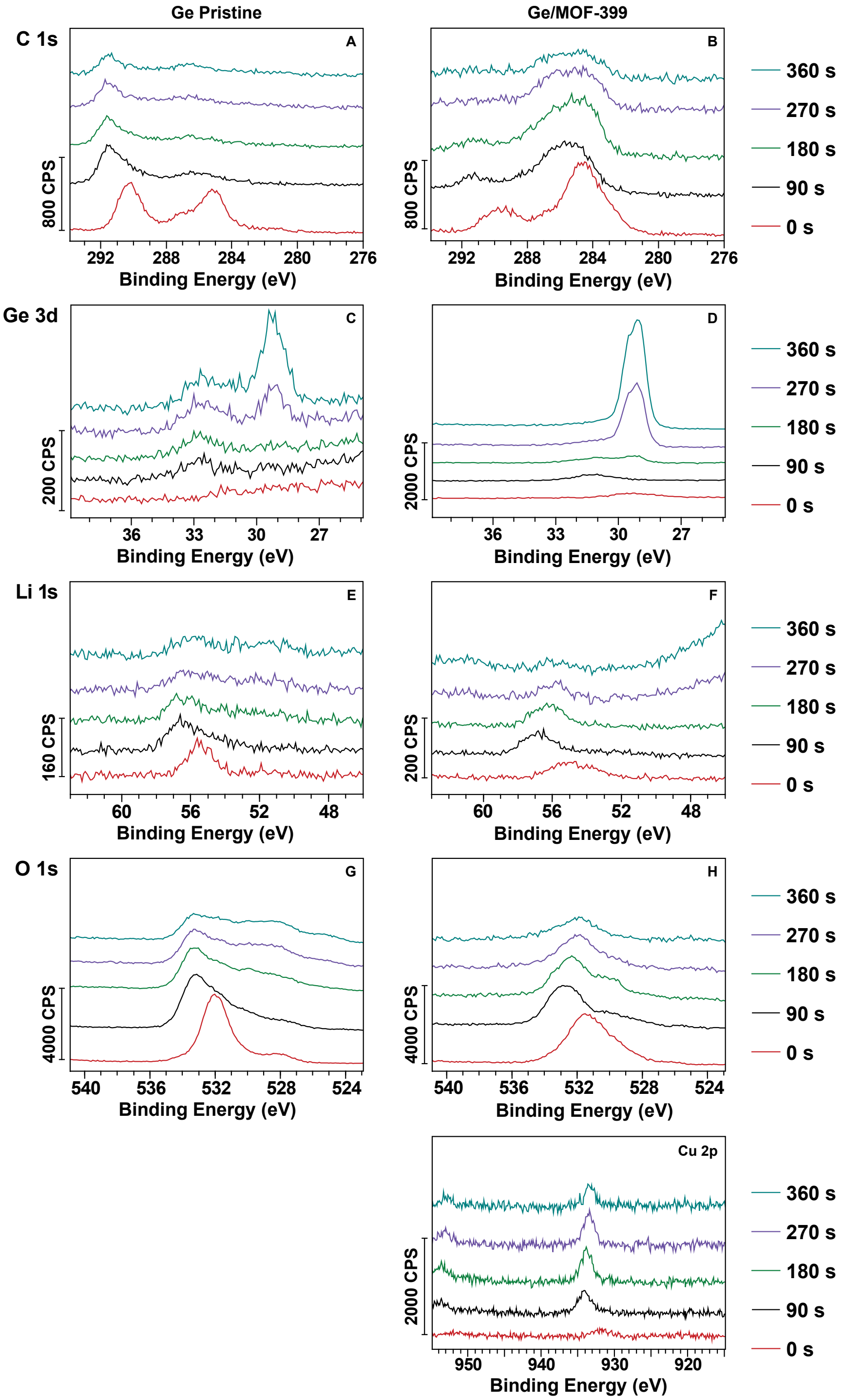

Figure 5.15: X-ray photoelectron micrographs of (A, C, E, and G) a pristine Ge substrate and (B, D, F, and H) a Ge substrate coated with MOF-399 multilayers after 10 lithition/delithiation cycles. High-resolution spectra were taken of the C 1s (A and B), Ge 3d (C and D), Li 1s (E and F), and O 1s (G and H) regions.

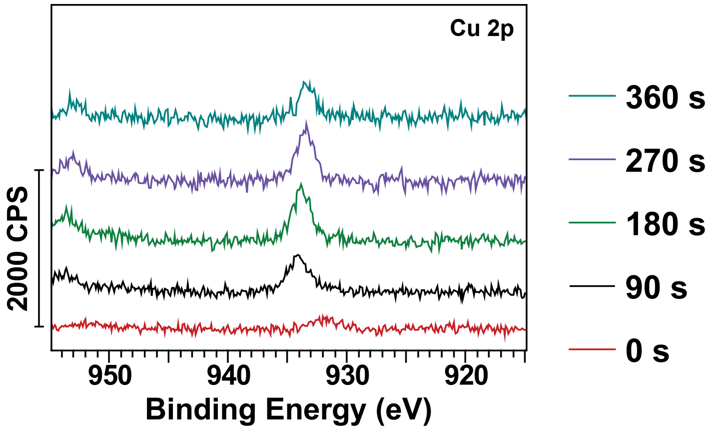

Figure 5.16: X-ray photoelectron micrographs a Ge substrate coated with MOF-399 multilayers after 10 lithition/delithiation cycles, highlighting the Cu 2p region.

CHAPTER 6: Conclusions and Prospects

In this dissertation, we have explored the importance of surfaces for devices, focusing on germanium and lithium-ion batteries. Specifically, we have used an “all-surface” form of germanium, germanane, as well as taken steps towards fabricating a molecular battery from an understanding of germanium surface chemical control. This latter work led to the development of a method to control the germanium surface work function through carborane SAMs. From the experiments presented herein, it is evident that material surfaces play an important role in device performance. The ability to control surfaces through organic passivation enables us to manipulate various material properties as well as fabricate intricate nanostructures.

Here, germanane was explored for use as a Li-ion anode material. However, established synthesis routes failed to produce the purity required for precision analysis of GeH-based anodes. We used sonication and centrifugation as a means of creating large-scale dispersions of germanane. This method proved useful for selectively dispersing GeH nanosheets, separating bulk germanium impurities from solution. Additionally, the large-scale dispersions created, which will be useful for further solution-processing techniques common to other two-dimensional materials. For example, we have shown how GeH surfaces can be passivated with alkanethiols, thus altering the surface energy of GeH nanosheets. This passivation technique may prove useful for controlling air-instability issues or electronic properties of the sheets at a large scale. Additionally, this solution processibility enables development of thin-film devices, a promising direction for this material, due to its high carrier mobility and direct band gap of 1.53 eV.

The GeH dispersions were used to fabricate pure thin-film and carbon-GeH composite thick-film anodes. We hypothesized that the volume-induced degradation will be reduced due to directionally-limited volume expansion. Representative GeH anode electrodes were found to have a reversible Li-ion capacity of ~1100 mAh/g when cycled between 0.1 to 2 V *vs.* Li/Li$^+$, which is near the theoretical maximum for germanium (1384 mAh/g). Additionally, these preliminary experiments show that nanosheets are capable of high cycling rates, with 80% capacity retention over 100 cycles, and 99% Coulombic efficiency.

While nanostructuring can improve performance of Li-ion anodes, the increased surface area has the adverse effect of increasing solid-electrolyte-interphase formation. As stated above, SEI forms on the surface of electrodes whose potentials are greater than the breakdown voltages of the electrolyte solution. This SEI layer is then comprised of decomposed components of the solution and other surrounding materials (*i.e.*, anode or cathode), and acts as an electronic "resistor" that continues to grow until the voltage drop across it is below the breakdown voltage of the electrolyte solution. This SEI layer can impede ion flow and electrically isolate active electrode materials, and thus be detrimental to battery performance. Therefore, increasing the surface area of the electrodes increases the amount of SEI build-up, and subsequent SEI-specific complications. However, the increased propensity for a larger degree of SEI formation with the increased surface area of nanostructures does not negate the advantages of nanostructuring, but instead illustrates the importance of controlling electrode-electrolyte interfaces (*i.e.*, artificial SEIs) or using electrolyte solutions that are stable in the battery's operating voltage window (*i.e.*, ionic liquids). Implementation of these strategies would not only benefit commercial battery systems, but would also aid in removing variables in the characterization of new material and architecture performance. Future work should explore germanane performance compared to other germanium nanomaterials with ionic liquids to characterize structure-specific advantages.

Additionally, organic passivation may prove useful in fabricating artificial SEI layers. Various head- and tail-group chemistries should be explored to create films that adhere strongly to germanium anodes, are permeable to lithium ions, adapt to bulk volume changes, and prevent solution degradation. This study may require using additional organic layers over the organic passivation, where there are strong interactions between overlayers and passivation layers. It is possible that the metal-organic films explored in **Chapter 5** may prove useful for this area. These systems can be tested initially on germanium thin films, and then extrapolated to germanium nanomaterials.

Previous work we have conducted showed that the work function of Au and Ag surfaces could be tuned while maintaining surface energy by using SAMs of different carboranethiol isomers. Here, we expanded on that work to Ge surfaces. Previous research indicated that thiol chemistry would be sufficient for anchoring carborane cages to the Ge surface, however, our results indicate otherwise. Carboranes with different head groups (thiol, hydroxyl, and carboxylic acid) were studied in order to identify which head groups facilitated SAM formation. Carboxylic acid proved to be the only head group of those tested, to bind to both (100) and (111) surfaces. We hypothesize that this selectivity in binding is due to a combination of steric and electronic effects. Future work could explore this selectivity by testing different carborane isomers to study the effects of pK_a on binding, as well as studying molecules like benzenethiol and benzoic acid. Additionally, our work showed that the Ge surface work function could be tailored by 0.4 eV without significantly changing wetting properties. These results mirror the study of carboranethiols on Au and Ag, and highlight a large advantage that carboranes can bring to electronic devices. Carboranes offer the potential to tune energy level alignment of a wide range of materials, without influencing wetting properties. This would aid in rapid prototyping of devices by greatly reducing complications in development. To support this claim further, a larger list of materials systems must be established, which might include using the carborane carboxylic acid molecule in other popular semiconductor systems, such as indium oxide.

Finally, we introduced the molecular battery as a potential answer to the miniaturization demands for Li-ion batteries. The requirements and a potential design were outlined by using a layer-by-layer deposition of organic molecules and metal-ion coordination. With the successful deposition of carboranes on Ge surfaces, we explored carborane-based metal-organic multilayering on Au{111} surface and found that only bilayer was capable of forming. Additionally, we investigated benzene-based organic linkers, specifically BTB (from MOF-14) and BBC (from MOF-399) on Au{111} using EIS and found the BTB and BBC to be electrically conductive and insulating, respectively. From this work, we continued to explore BBC on the Ge(100) surface to investigate the films ionic conductivity using cyclic voltammetry. Preliminary results indicate that multilayer films of BBC are ionically conductive under an applied potential and are stable after several cycles. The results presented indicate a positive first step towards realizing a molecular battery by presenting a working system (MOF-399) as well as supporting the feasibility of using metal-organic coordination for molecular-deposition. Given the lithium permeability of multilayered MOF-399, it is worth exploring full molecular battery assembly. This construction can be achieved by depositing films of polypyrrole doped with a Li^+ salt over the MOF-399 film using organic chemical vapor deposition. Full cell battery tests could evaluate overall performance of this system and allow us to study how performance changes by altering the number of layers of the separator.

Germanium’s predisposition to oxidize creates a number of challenges in processing. In order to study Ge derived materials, atmospheric controls are required, which creates difficulties in scaling up. However, the methods presented here offer a good starting point. We have highlighted several areas where surface control, and thus oxide control, can benefit devices and how these controls can be implemented. From this work, a strong foundation has been laid to explore germanium surfaces as well as other semiconductor surfaces for controlling properties and fabricating nanomaterials and nanoscale devices, such as germanane and the molecular battery.

APPENDIX A: Germanane Centrifugation Supporting Information

A.1: Atomic Force Micrographs of Dried Germanane Dispersions

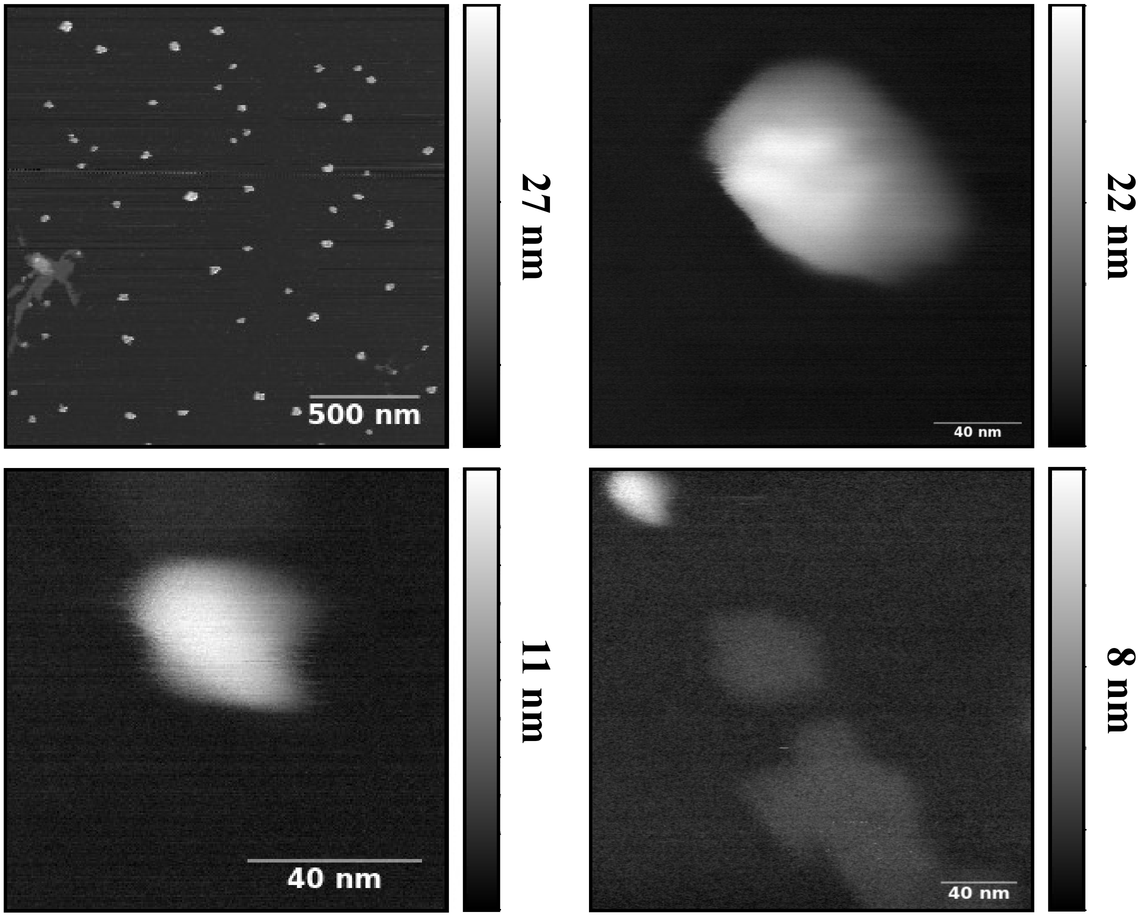

Figure A.1: Atomic force micrographs of dried germanane-isopropanol dispersions that were centrifuged previously at 5 krpm for 30 min.

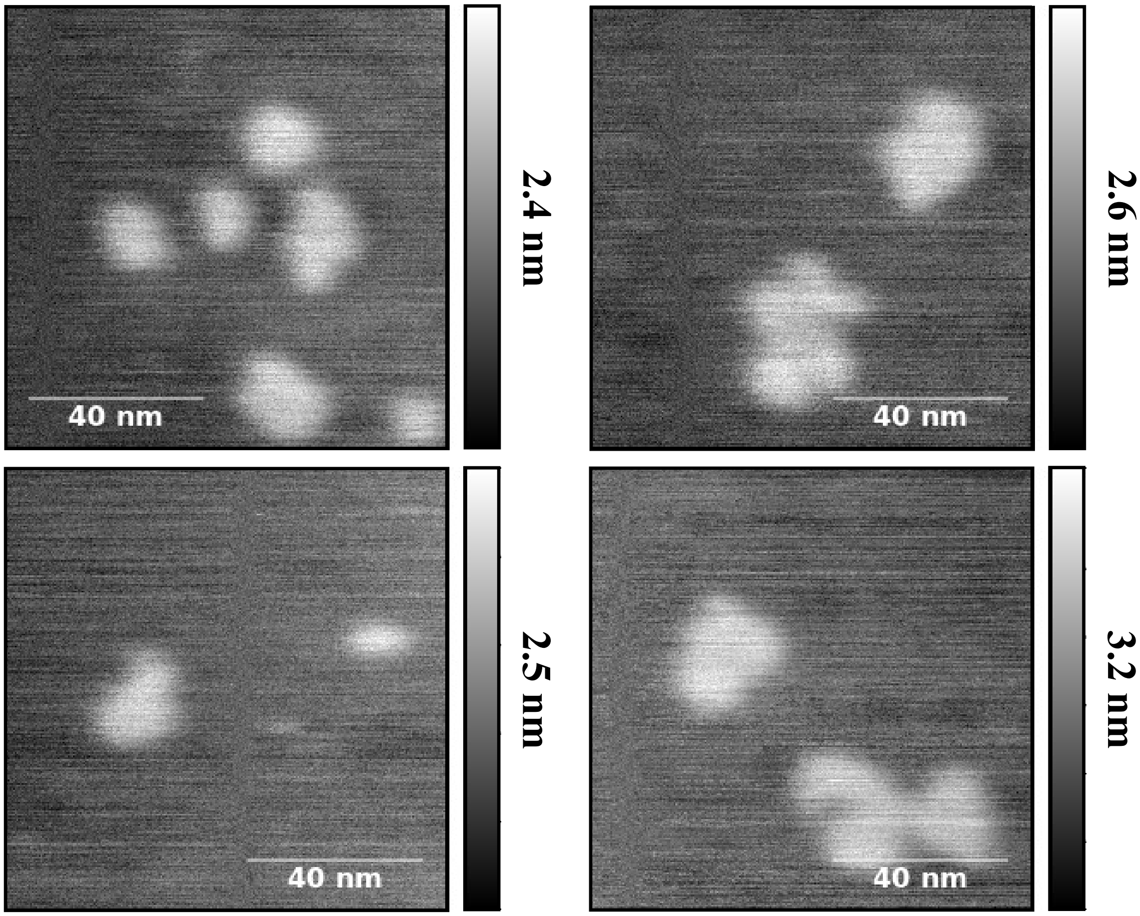

Figure A.2: Atomic force micrographs of dried germanane-isopropanol dispersions that were centrifuged previously at 10 krpm for 30 min.

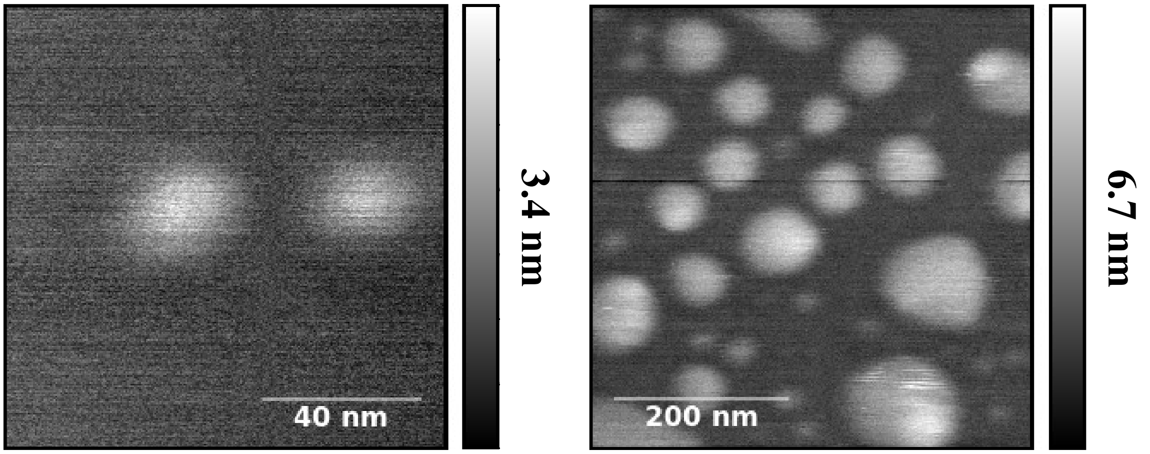

Figure A.3: Atomic force micrographs of dried germanane-isopropanol dispersions that were centrifuged previously at 14 krpm for 30 min.

A.2: Processed Germanane Atomic Force Micrographs

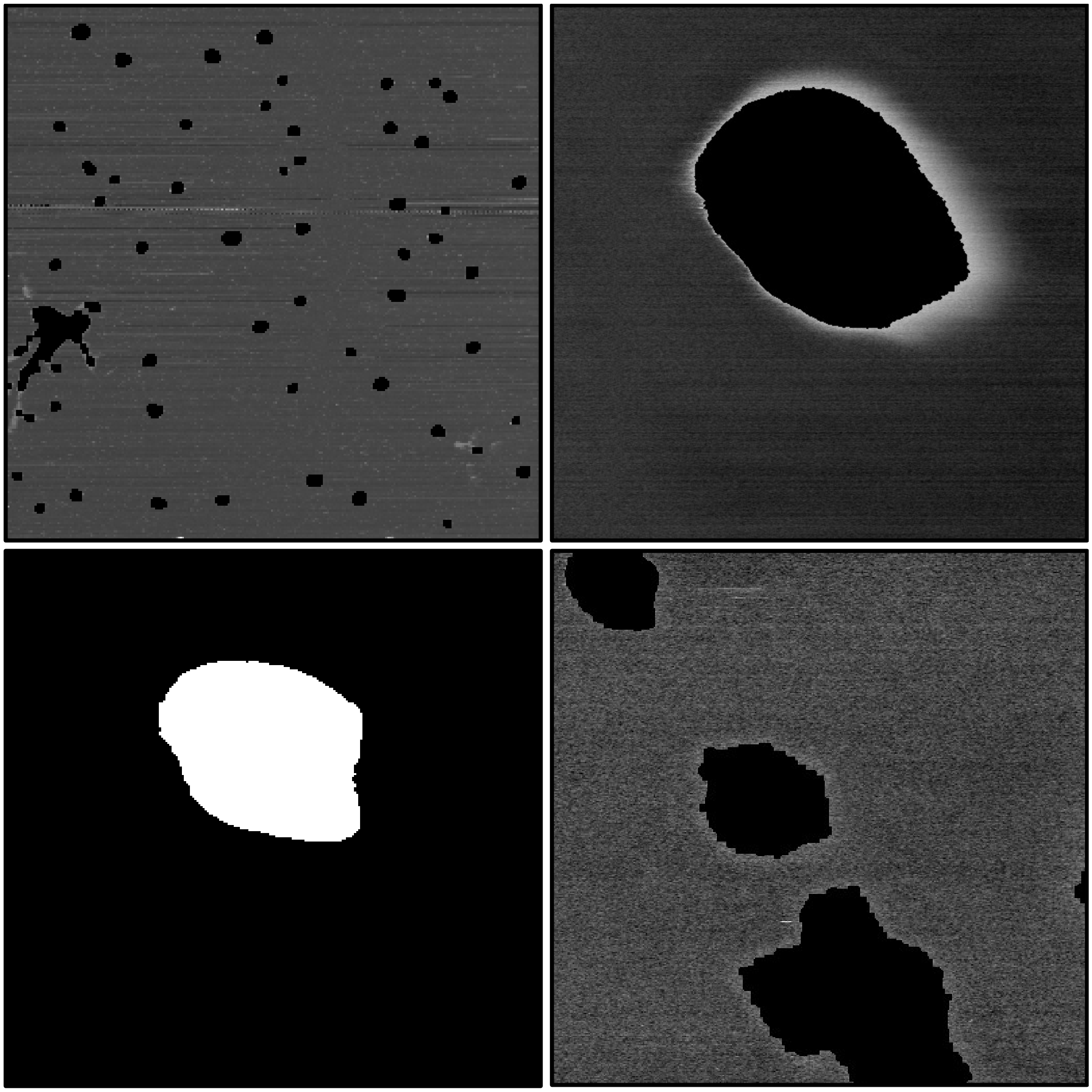

Figure A.4: Processed atomic force micrographs of 5 krpm samples highlighting particles.

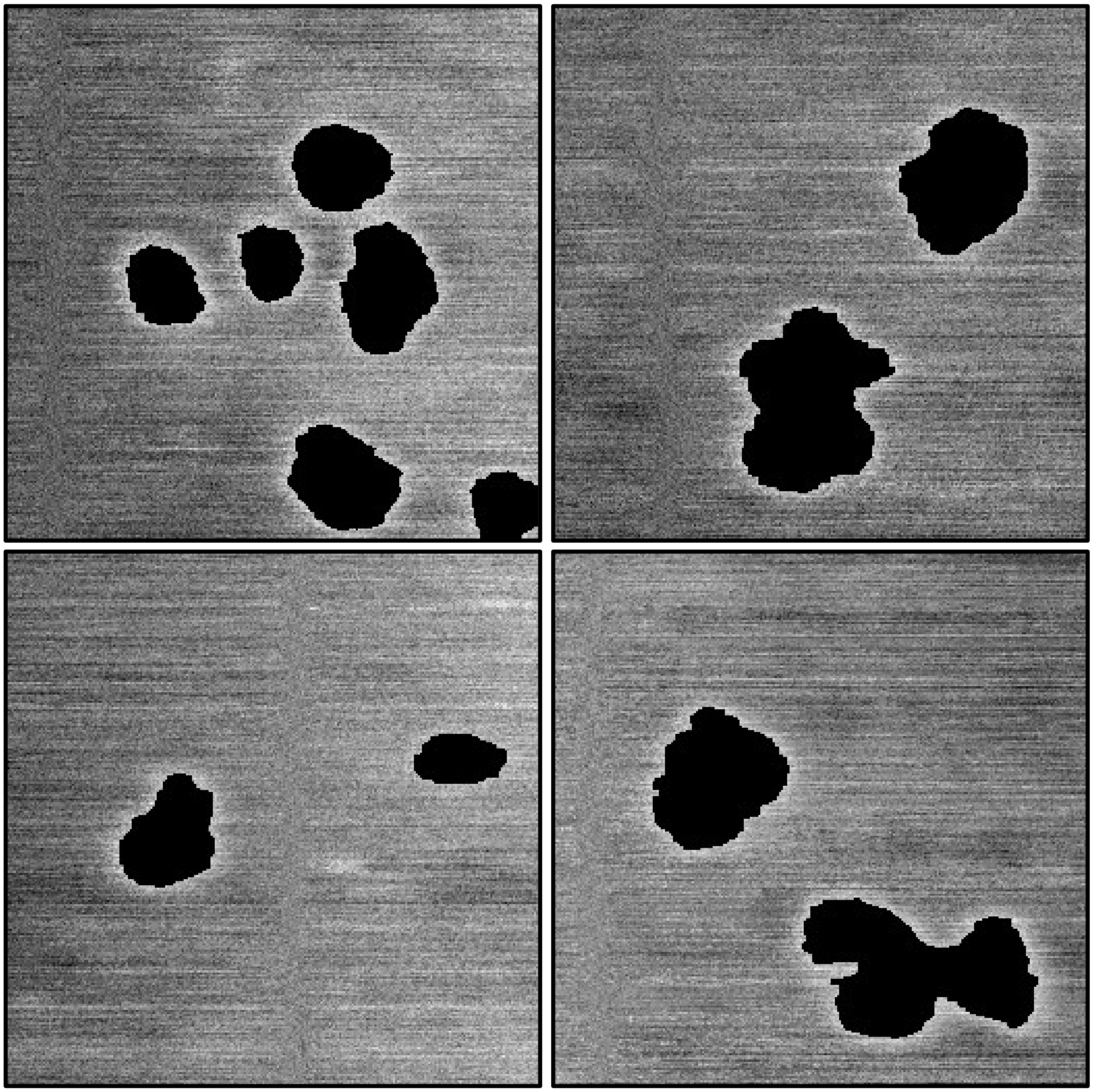

Figure A.5: Processed atomic force micrographs of 10 krpm samples highlighting particles.

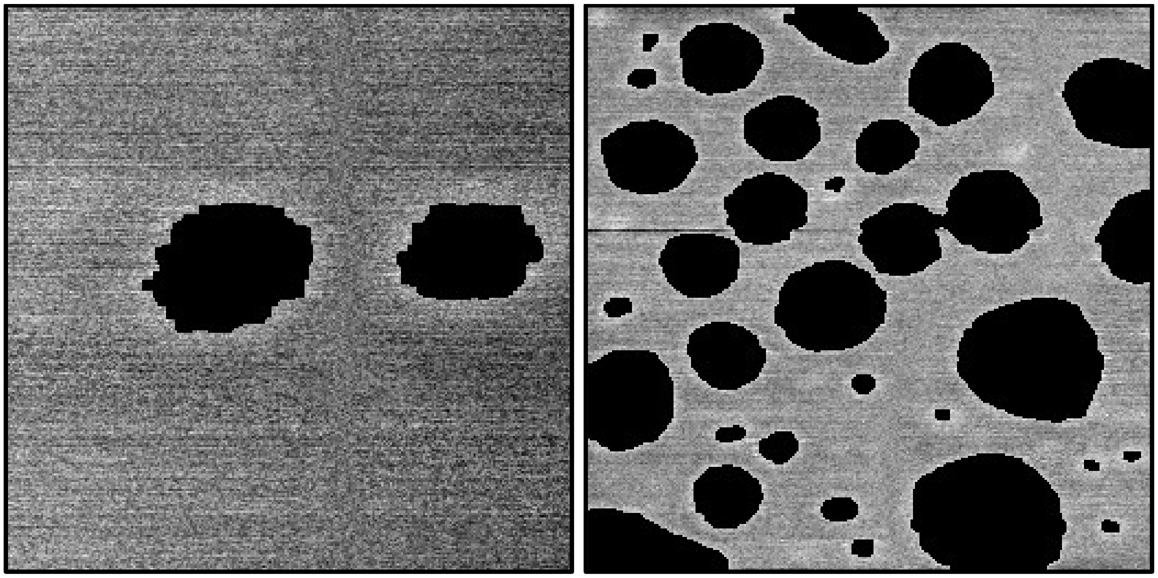

Figure A.6: Processed atomic force micrographs of 14 krpm samples highlighting particles.

APPENDIX B: Carborane Supporting Information

B.1: Synthesis of Carborane Molecules

1-COOH-o-carborane: From the synthesis reported by Kahl and co-workers.[1] To a cooled (-78 °C) solution of *o*-carborane (1.0 g, 6.9 mmol) in Et_2O (9.5 mL) was added ^{n}BuLi (4.8 mL, 7.68 mmol, 1.6 M in hexanes) in a dropwise fashion. The resultant solution was then allowed to stir for 20 min at -78 °C, after which crushed dry ice (approx. 2.0-2.5 g) was quickly added to the reaction mixture and allowed to continue stirring at -78 °C for 1 h before warming to room temperature. All the volatiles were removed under reduced pressure and water was added to the remaining residue. Hexanes (2 x 15 mL) were added to the aqueous mixture to extract any unreacted *o*-carborane. Following this, the aqueous layer was acidified with 3 M HCl and the title compound was extracted with hexanes (4 x 15 mL). The combined extracts were dried over Na_2SO_4 and all the volatiles removed under reduced pressure to give the title compound as a white solid (**O1COOH, Figure B1 and B2**).

Yield: 0.8 g (61 %). **^{1}H NMR (500 MHz, $CDCl_3$):** δ 1.50-3.20 (m, 10H, B*H*), 4.05 (s, 1H, $C_{carborane}$-*H*) 8.59 (1H, COO*H*); **^{11}B NMR (160 MHz):** δ -2.07 (d, 2B, $^{1}J_{BH}$ = 148 Hz), -8.42 (d, 2B, $^{1}J_{BH}$ = 152 Hz), -11.61 (d, 4B, $^{1}J_{BH}$ = 173 Hz), -13.27 (d, 2B, $^{1}J_{BH}$ = 178 Hz) Note: Due to the presence of acid in $CDCl_3$, the position for the resonance corresponding to COO*H* changes depending on the concentration of acid.

***9-COOH-o-carborane*:** From the synthesis reported by Craciun and Custelcean.[2] CrO_3 (2.6 g, 32.5 mmol) was slowly added to a solution of 9-ethyl-*o*-carborane[3] (1.0 g, 5.8 mmol) in glacial acetic acid (14 mL) and concentrated sulfuric acid (1.4 mL) in an ice bath (5-15 °C). The solution was stirred in the ice bath for 1 h and subsequently heated at 65 °C for 2 h. After cooling to room temperature, the solution was poured into ice cold water to give a white precipitate. The white crystals were filtered off and recrystallized from methanol to give the title compound as a white solid (**O9COOH**, **Figure B3 and B4**).

Yield: 0.63 g (57%). **^{1}H NMR (400.1 MHz, DMSO-d$_6$):** δ 1.24-3.02 (m, 9H, B*H*), 5.00 (s, 2H, $C_{carborane}$-*H*), 11.39 (s, 1H, COO*H*); **^{11}B NMR (128.4 MHz):** δ -0.46 (s, 1B), -3.41 (d, 2B, $^1J_{BH}$ = 148 Hz), -9.65 (d, 4B, $^1J_{BH}$ = 145 Hz), -14.60 (m, 6B)

9-OH-m-carborane: From the synthesis reported by Spokoyny and co-workers.[4] SPhos (20.5 mg, 5 mol%), SPhos-Pd-G3 precatalyst (39.8 mg, 5 mol%), 9-Br-*m*-carborane (223 mg, 1 mmol) were added to an oven-dried reaction tube and sealed with a PTFE septum cap. The reaction tube was evacuated and backfilled with N_2 four times. 1,4-dioxane (2 mL) and a 1 M K_3PO_4 solution in water (2 mL, deoxygenated by sparging with N_2 for 30 min) were injected. The rapidly stirring reaction mixture was heated at 80 °C for 1 h in an oil bath. Upon completion, the reaction mixture was extracted with Et_2O (4 x 5 mL), the organics were filtered through a silica plug and solvent removed under reduced pressure. The resulting dark brown oil was loaded onto a silica column and washed with a 50:50 CH_2Cl_2:hexanes mixture, the product was eluted from the column using a 50:50 Et_2O:hexanes mixture. The product containing fractions were combined and solvent removed under reduced pressure to yield a white solid (**M9OH**, **Figures B5 and B6**).

Yield: 83 mg (52%). **^{1}H NMR (500 MHz, CDCl$_3$):** δ 1.40-3.10 (m, 9H, B*H*), 1.61 (s, 1H, -O*H*), 2.74 (s, 2H, $C_{carborane}$-*H*); **^{11}B NMR (160 MHz):** δ 8.6 (s, 1B), - 8.1 (d, 2B, $^1J_{BH}$ = 162 Hz), -11.7 (d, 1B, $^1J_{BH}$ = 151 Hz), -15.0 (d, 2B, $^1J_{BH}$ = 162 Hz), - 16.9 (d, 2B, $^1J_{BH}$ = 164 Hz), -20.5 (d, 1B, $^1J_{BH}$ = 182 Hz), -27.1 (d, 1B, $^1J_{BH}$ = 182 Hz).

9-SH-*o*-carborane: Adapted from references 5,6. To a suspension of *o*-carborane (1.44 g, 10.0 mmol) and $AlCl_3$ (1.33 g, 10.0 mmol) in 30 mL dichloromethane at -78 °C, a solution of sulfur monochloride (0.40 mL, 5.0 mmol) in dichloromethane (5 mL) was added dropwise under an inert atmosphere. The reaction mixture was magnetically stirred overnight before quenching with water. Extractions were performed with dichloromethane before the organic layers were combined and removed under reduced pressure. The resulting solids were resuspended in a solution of hydrochloric acid prior to the careful introduction of zinc dust. After stirring overnight, the reaction mixture was quenched with water and the resulting precipitates were filtered and purified via sublimation at 130 °C and silica column chromatography with 1:1 CH_2Cl_2:hexanes as eluent (**O9SH**, **Figure B7 and B8**).

Yield: 194 mg (12%). **^{1}H NMR (400.1 MHz, CD_2Cl_2)**: δ 0.42(d, $^2J_{B\text{-}H}$= 4.05 Hz 1H, S-*H*), 1.6-3.1 (m, 9H, B-*H*), 3.5 (s, 1H, $C_{carborane}$-*H*), 3.7 (s, 1H, $C_{carborane}$-*H*); **^{11}B{H} NMR (128.4 MHz)**: δ 4.8, -1.5, -8.0, -13.3, -14.3, -15.3.

B.2: Characterization of Carboranes by Nuclear Magnetic Resonance

Nuclear Magnetic Resonance Procedures

^{1}H and ^{11}B NMR spectra were recorded on AV 500 and AV 400 spectrometers in ambient conditions. Bruker Topspin V3.5 software was used to process the FID data and visualize the spectra. ^{1}H were referenced to residual solvent resonances in deuterated solvents and are reported relative to tetramethylsilane ($\delta = 0$ ppm). ^{11}B NMR spectra were referenced to $Et_2O \cdot BF_3$ in a sealed capillary ($\delta = 0$ ppm).

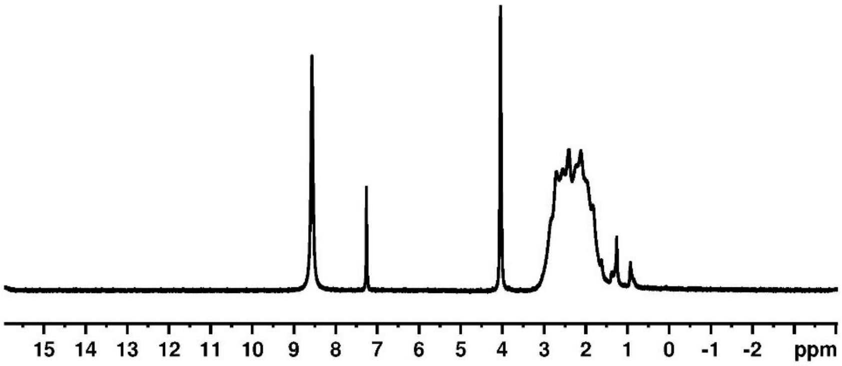

Figure B.1 Hydrogen nuclear magnetic resonance of 1-COOH-*o*-carborane in $CDCl_3$.

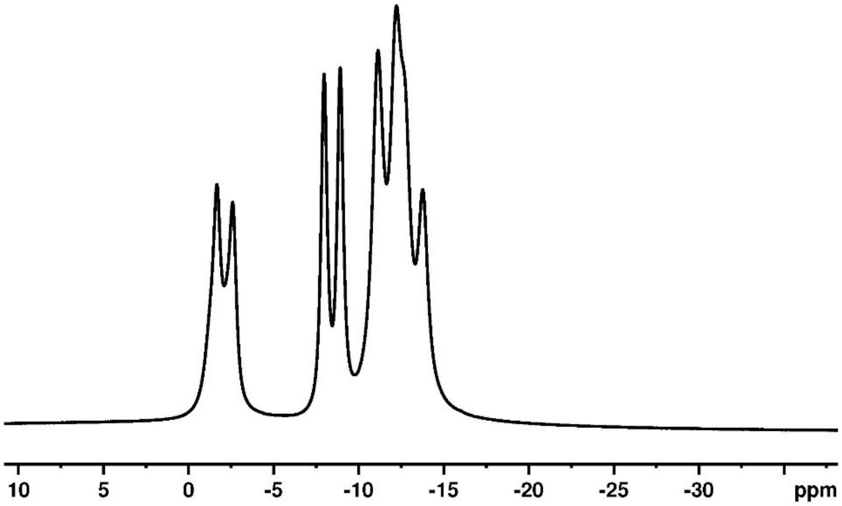

Figure B.2: Boron nuclear magnetic resonance of 1-COOH-*o*-carborane.

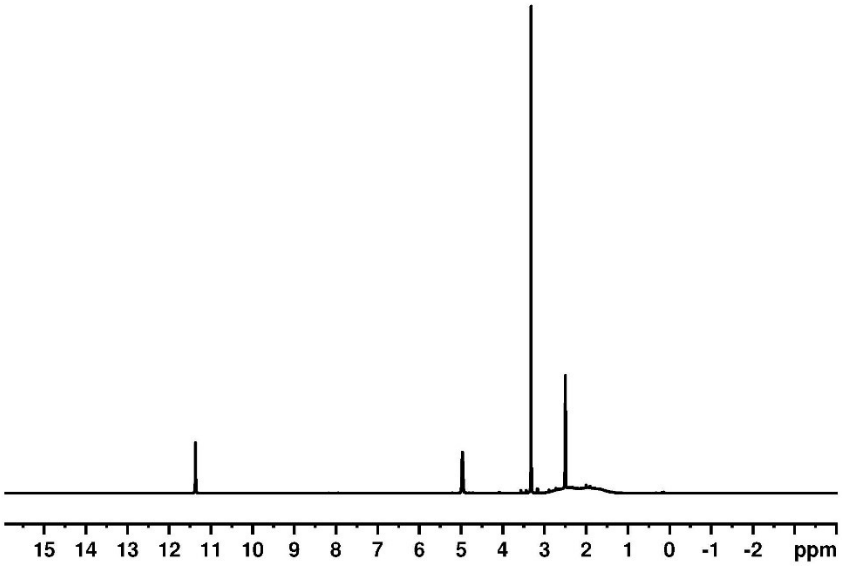

Figure B.3: Hydrogen nuclear magnetic resonance of 9-COOH-*o*-carborane in DMSO-d_6.

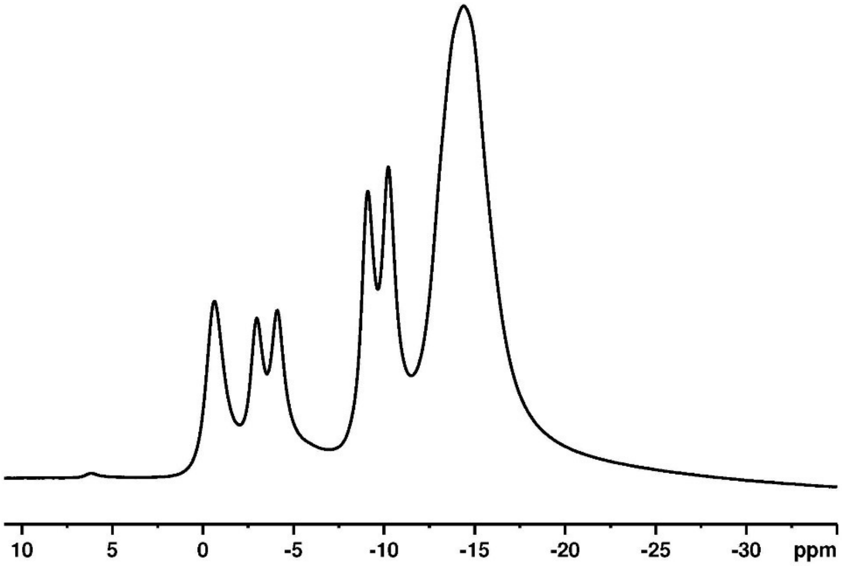

Figure B.4: Boron nuclear magnetic resonance of 9-COOH-*o*-carborane.

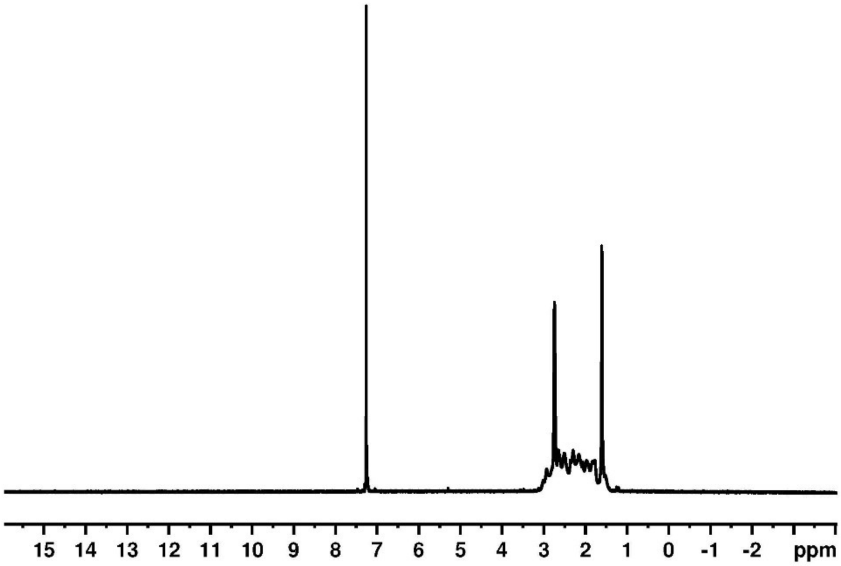

Figure B.5: Hydrogen nuclear magnetic resonance of 9-OH-*m*-carborane in $CDCl_3$.

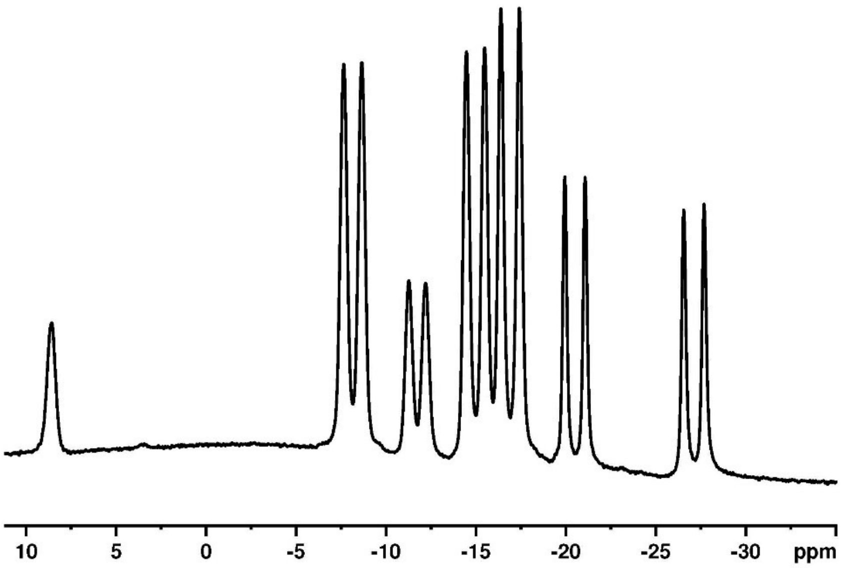

Figure B.6: Boron nuclear magnetic resonance of 9-OH-*m*-carborane.

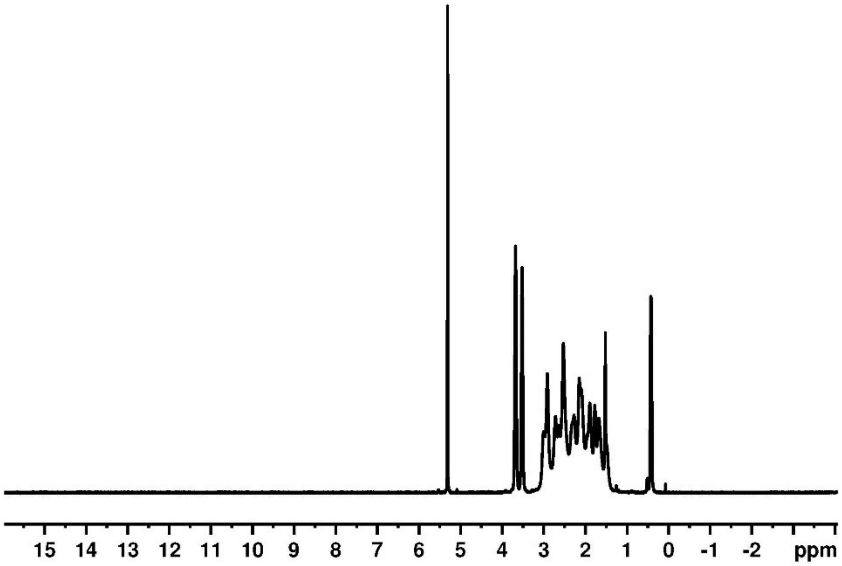

Figure B.7: Hydrogen nuclear magnetic resonance of 9-SH-*o*-carborane in CD_2Cl_2.

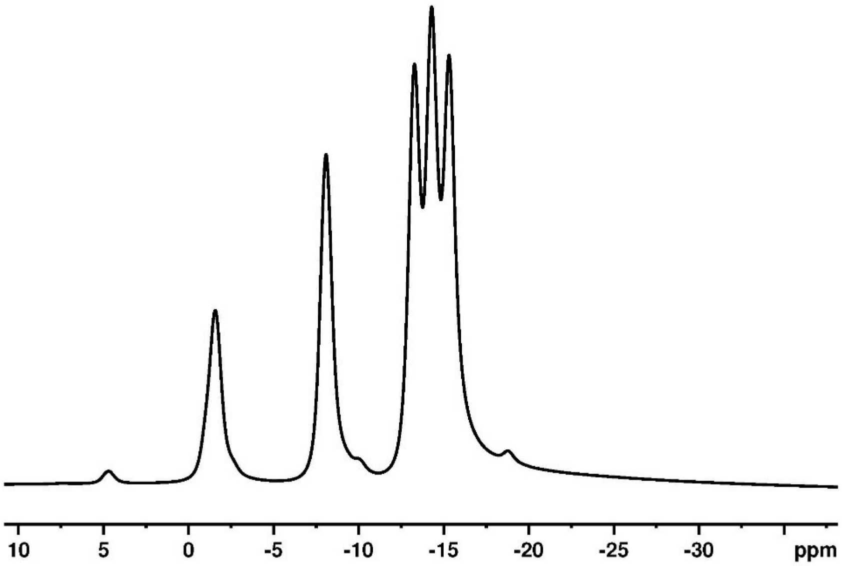

Figure B.8: Boron nuclear magnetic resonance of 9-SH-*o*-carborane.

B.3: Density Functional Theory

Dipole moment calculations were performed with ADF 2014 Suite version 2014.04[7-9] using TZP basis sets (Slater-type orbitals: double zeta core, triple zeta valence + 1 polarization function). Geometry optimizations and single point calculations were performed using PBE-D3(BJ),[10,11] B3LYP-D3(BJ),[10,12-14] PBE0,[15] and M06,[16] density functionals. Dipole moment orientations for each density functional and carborane are listed in **Table B1**. Single point calculations were performed with the substituted vertex and the antipodal vertex defining the Z-axis, and the YZ plane defining the mirror plane of each functionalized carborane as listed in **Table B2**. The Cartesian coordinates for all modeled carboranes are listed in **Table B3**.

O1	**Dipole**	**[x]**	**[y]**	**[z]**
SH				
PBE-D3(BJ)	3.75	0.69761753	-2.02337790	3.08190783
B3LYP-D3(BJ)	3.76	0.69857707	-2.03926806	3.07998822
PBE0	3.80	0.72607085	-2.05040678	3.12155451
M06	3.76	0.68633331	-1.96946353	3.13057304
COOH				
PBE-D3(BJ)	3.36	0.02519714	-0.67689966	3.29034758
B3LYP-D3(BJ)	3.24	-0.01342170	0.65789447	3.17322952
PBE0	3.37	0.01815419	-0.66460536	3.30156895
M06	3.37	0.00588162	-0.63440538	3.31077017
O9	**Dipole**	**[x]**	**[y]**	**[z]**
SH				
PBE-D3(BJ)	5.24	0.64446826	-2.36186256	4.63162036
B3LYP-D3(BJ)	5.44	0.65385386	-2.37582172	4.85123856
PBE0	5.43	0.69030422	-2.38601933	4.83088071
M06	5.11	0.59454144	-1.92794277	4.69062735
COOH				
PBE-D3(BJ)	5.02	-0.94344730	-1.43560061	4.71673395
B3LYP-D3(BJ)	5.14	-0.68261308	-1.15677534	4.95928961
PBE0	5.17	-0.89359993	-1.31769858	4.91653076
M06	4.97	-0.83310996	-1.20083782	4.74997079
M1	**Dipole**	**[x]**	**[y]**	**[z]**
SH				
PBE-D3(BJ)	1.96	0.52416668	-1.75154639	0.70188432
B3LYP-D3(BJ)	1.95	0.52204147	-1.76139729	0.66157757
PBE0	1.98	0.54561792	-1.77090327	0.68899967
M06	1.81	0.35575413	-1.59927981	0.76714709
M9	**Dipole**	**[x]**	**[y]**	**[z]**
SH				
PBE-D3(BJ)	3.41	0.38944325	-0.83447575	3.27979973
B3LYP-D3(BJ)	3.59	0.38465372	-0.84122027	3.47001511
PBE0	3.56	0.39787710	-0.82292237	3.43715650
M06	3.46	0.36310995	-0.85397928	3.33393794
Carborane	**Dipole**	**[x]**	**[y]**	**[z]**
ortho-CB				
PBE-D3(BJ)	4.23	0.00035560	-2.23669758	3.58883336
B3LYP-D3(BJ)	4.27	0.00169187	-2.25599379	3.62271532
PBE0	4.31	0.00164996	-2.27739567	3.66292793
M06	4.19	0.00004628	-2.21287112	3.56061348
meta-CB				
PBE-D3(BJ)	2.68	-0.00148343	-2.27703813	1.40894095
B3LYP-D3(BJ)	2.70	-0.00050187	-2.29386751	1.42176463
PBE0	2.73	-0.00002894	-2.32236334	1.43464539
M06	2.65	0.00142062	-2.24758244	1.39847908

Table B.1: Dipole magnitudes and orientations calculated using density functional theory.

	[0,0,0]	**[0,0,Z]**	**[0,Y,Z]**
O1-R	B(12)	C(1)	C(2)
O9-R	B(9)	C(2)	C(1)
M1-R	B(12)	C(1)	C(7)
M9-R	B(9)	B(2)	B(3)
***o*-carborane**	B(12)	C(1)	C(2)
***m*-carborane**	B(12)	C(1)	C(7)

Table B.2: The vertices that define the origin, Z axis, and YZ plane for DFT dipole moment calculations in the reported carborane molecules.

1-COOH-*o*-carborane: B3LYP-D3(BJ)

H	1.47066970	-1.99326466	3.11395219
B	-0.88772284	1.22189709	0.92877854
H	-1.47365773	2.16608620	0.53899187
C	0.00000000	0.00000000	3.22137113
C	0.00883851	0.20302729	4.71806646
H	2.32650464	0.87284171	3.09948569
C	0.00000000	1.37505472	2.35822913
B	0.88780802	-1.22602368	2.43968556
B	-1.45715891	0.46459508	2.42626277
H	-2.32562892	0.87579493	3.10225097
B	-1.44878288	-0.46528512	0.93746501
H	-2.47391866	-0.77671238	0.44297010
B	0.00000000	0.00000000	0.00000000
H	-0.00119936	0.02126492	-1.17998258
B	0.88827292	1.22116510	0.92924827
H	1.47583970	2.16405959	0.53892601
B	-0.89072320	-1.22480644	2.43975764
H	-1.47495015	-1.99206509	3.11285274
B	-0.00064168	-1.51074540	0.93512310
B	1.44811608	-0.46719794	0.93738123
H	2.47277320	-0.77951138	0.44250411
B	1.45641663	0.46238461	2.42544950
H	-0.00207054	-2.57873895	0.43279872
H	0.00221523	2.27232379	2.95609048
O	-0.00515878	-0.96912193	5.36966633
O	0.02983732	1.28593414	5.24557796
H	0.00711656	-0.76402587	6.32083379

1-COOH-*o*-carborane: M06

H	-1.46940761	1.98218771	3.11148650
B	0.88327821	-1.21843862	0.92796416
H	1.47131608	-2.16250728	0.54513985
C	0.00000000	0.00000000	3.20715880
C	0.00048961	-0.21138825	4.70134818
H	-2.30619628	-0.87687483	3.10622540
C	0.00000000	-1.36476267	2.35149764
B	-0.88450167	1.22049135	2.43313377
B	1.44216838	-0.46473975	2.42570933

H	2.30654874	-0.87583392	3.10629654
B	1.43995130	0.46404938	0.93371502
H	2.46566022	0.77262086	0.44202576
B	0.00000000	0.00000000	0.00000000
H	0.00029348	-0.02513391	-1.17872620
B	-0.88294799	-1.21852035	0.92778823
H	-1.47091200	-2.16233625	0.54426395
B	0.88397806	1.22084805	2.43298302
H	1.46880227	1.98263230	3.11122939
B	-0.00042874	1.50449129	0.92947547
B	-1.44025591	0.46365230	0.93355425
H	-2.46596536	0.77189489	0.44155962
B	-1.44226684	-0.46520804	2.42547042
H	-0.00070130	2.57129376	0.42746470
H	-0.00063456	-2.26227092	2.95377023
O	0.00580432	0.94878551	5.35036355
O	-0.00337583	-1.29256587	5.21460998
H	0.00569989	0.73748748	6.29667503

1-COOH-*o*-carborane: PBE-D3(BJ)

H	-1.47643756	2.00185458	3.12645953
B	0.88822549	-1.22364859	0.93077251
H	1.48226766	-2.17645899	0.53901424
C	0.00000000	0.00000000	3.23088408
C	0.00183630	-0.21332648	4.73299922
H	-2.33530333	-0.87927867	3.11466418
C	0.00000000	-1.38002374	2.36291918
B	-0.88719620	1.22858250	2.44335012
B	1.45962500	-0.46660595	2.42927611
H	2.33658567	-0.88137379	3.11310221
B	1.44873475	0.46661883	0.93635076
H	2.48419700	0.77995706	0.43768009
B	0.00000000	0.00000000	0.00000000
H	-0.00040403	-0.02421647	-1.19093258
B	-0.88913406	-1.22312610	0.93275604
H	-1.48508516	-2.17494179	0.54152345
B	0.89178496	1.22607364	2.44278515
H	1.48423711	1.99941761	3.12261335
B	0.00141604	1.51219092	0.93548551
B	-1.44810055	0.46888560	0.93908904

H	-2.48410402	0.78207368	0.44153063
B	-1.45768882	-0.46232975	2.43326164
H	0.00199595	2.59093113	0.43012984
H	-0.00083076	-2.28446008	2.96810300
O	0.02598248	0.97044899	5.38511552
O	-0.01534515	-1.30631216	5.26243876
H	0.02378437	0.74790181	6.34267393

1-COOH-*o*-carborane: PBE0

H	-1.47231433	1.99483266	3.11891264
B	0.88614016	-1.22028143	0.93215381
H	1.47437679	-2.17198934	0.54695944
C	0.00000000	0.00000000	3.21701024
C	-0.00613086	-0.20354364	4.71371357
H	-2.32407690	-0.87670751	3.10761289
C	0.00000000	-1.36627810	2.36047401
B	-0.88711593	1.22479663	2.43901149
B	1.45279351	-0.46237386	2.42729300
H	2.32379444	-0.87776502	3.10818795
B	1.44658017	0.46666394	0.93552876
H	2.47773399	0.77829987	0.44055576
B	0.00000000	0.00000000	0.00000000
H	0.00066412	-0.02433215	-1.18556218
B	-0.88631763	-1.22021936	0.93226943
H	-1.47484308	-2.17180280	0.54705465
B	0.88791191	1.22461489	2.43887836
H	1.47353787	1.99478129	3.11827987
B	0.00002760	1.51045613	0.93309294
B	-1.44666614	0.46723027	0.93588981
H	-2.47784959	0.77928086	0.44105700
B	-1.45270496	-0.46188329	2.42704417
H	0.00042026	2.58367146	0.42869976
H	-0.00103908	-2.26479289	2.96165726
O	0.00867753	0.96215624	5.35841730
O	-0.02448893	-1.28438710	5.23732003
H	0.00175243	0.75483502	6.30645804

9-COOH-*o*-carborane: B3LYP-D3(BJ)

H	-2.46556794	0.77827481	0.41197171
H	2.46576654	0.77023286	0.40904497
H	1.46969445	-2.16513361	0.50396247
B	-0.00137621	1.51156431	0.92805722
B	0.89107512	1.21500568	2.42692347
H	1.48055175	1.98385808	3.09670964
H	-1.47379499	1.98482612	3.10652206
H	-2.32904863	-0.88250192	3.07711966
H	0.00015870	-0.10908060	4.27027114
H	-1.47382729	-2.16002815	0.50273006
H	-0.00212321	-2.29333873	2.91055051
B	-0.89001443	-1.22314326	0.91132970
C	0.00000000	-1.37825391	2.34075917
B	0.00000000	0.00000000	0.00000000
B	1.45284537	-0.47002699	2.41478684
B	0.89221729	-1.22775949	0.91628664
B	-0.88953702	1.21601331	2.43247080
B	-1.45390170	-0.46665676	2.41149338
B	1.45045715	0.46022332	0.92202706
H	2.32762257	-0.88355134	3.08215612
H	0.00125302	2.57147880	0.41244564
C	0.00000000	0.00000000	3.19786240
B	-1.45011580	0.46883041	0.92456161
C	0.03418620	-0.06022027	-1.59355387
O	-0.62938934	0.97464691	-2.18832705
O	0.58505186	-0.91708143	-2.25217214
H	-0.53806474	0.83776263	-3.14858524

9-COOH-*o*-carborane: M06

H	-2.45899428	0.76893902	0.41495500
H	2.45955743	0.76085434	0.41266580
H	1.47261805	-2.15930825	0.51462187
B	-0.00163031	1.50477920	0.92378809
B	0.88523177	1.21296240	2.42265618
H	1.47584785	1.97492739	3.09579379
H	-1.47277051	1.97504869	3.10252123
H	-2.31585604	-0.87912495	3.07613777
H	0.00081407	-0.10852993	4.26351363
H	-1.47422414	-2.15673363	0.51696125

H	-0.00381718	-2.28499674	2.91253954
B	-0.88425519	-1.22007911	0.91244484
C	0.00000000	-1.37014473	2.33869474
B	0.00000000	0.00000000	0.00000000
B	1.43696964	-0.47079660	2.41902476
B	0.88841797	-1.22386677	0.91778091
B	-0.88414921	1.21408575	2.42649546
B	-1.43769118	-0.46696996	2.41555340
B	1.44208188	0.45811005	0.92212879
H	2.31298726	-0.88051997	3.08370347
H	-0.00066992	2.56432847	0.40865683
C	0.00000000	0.00000000	3.18903213
B	-1.44122632	0.46557274	0.92339916
C	0.05287398	-0.05544182	-1.59168782
O	-0.72968436	0.87652484	-2.18261972
O	0.71388304	-0.82936719	-2.23819144
H	-0.61194647	0.75555310	-3.13862128

9-COOH-*o*-carborane: PBE-D3(BJ)

H	-2.47927747	0.77981050	0.41970416
H	2.47719079	0.77206217	0.41355845
H	1.48026823	-2.17278705	0.50876230
B	-0.00407910	1.51217925	0.93175306
B	0.89206967	1.21647955	2.43587870
H	1.48843549	1.99075648	3.11348019
H	-1.48332774	1.99098722	3.12404451
H	-2.33858160	-0.88765616	3.09593040
H	-0.00041752	-0.10979324	4.29457831
H	-1.48692062	-2.16994527	0.50979401
H	-0.00068124	-2.30720779	2.92348202
B	-0.89387438	-1.22361809	0.91753407
C	0.00000000	-1.38325845	2.34977746
B	0.00000000	0.00000000	0.00000000
B	1.45207236	-0.46909438	2.42680475
B	0.89383983	-1.22692558	0.92329420
B	-0.89072371	1.21591198	2.44336992
B	-1.45455750	-0.46794674	2.42344392
B	1.45078815	0.46155438	0.92939828
H	2.33579398	-0.88849073	3.09952153

H	-0.00351699	2.58562550	0.41668455
C	0.00000000	0.00000000	3.21261709
B	-1.45174164	0.46862702	0.93270664
C	0.05177289	-0.06255140	-1.59893607
O	-0.91797590	0.70482008	-2.19990206
O	0.85453165	-0.70961984	-2.25592356
H	-0.77208178	0.58500882	-3.16642559

9-COOH-*o*-carborane: PBE0

H	-2.47254396	0.77794501	0.41913236
H	2.47123441	0.77062516	0.41400125
H	1.47088566	-2.16995756	0.51661872
B	-0.00238896	1.51114459	0.92910036
B	0.88868208	1.21453653	2.43016714
H	1.47881754	1.98508436	3.10715175
H	-1.47261426	1.98695751	3.11705561
H	-2.32528893	-0.88251490	3.09059285
H	0.00044212	-0.10686388	4.27217117
H	-1.47784611	-2.16532123	0.51854532
H	-0.00152120	-2.28735784	2.91562244
B	-0.89023380	-1.21963410	0.91861735
C	0.00000000	-1.36951306	2.34577391
B	0.00000000	0.00000000	0.00000000
B	1.44731396	-0.46696380	2.42019443
B	0.89068335	-1.22391871	0.92240864
B	-0.88762337	1.21655731	2.43552741
B	-1.44842732	-0.46331421	2.41906069
B	1.44854972	0.46127558	0.92523101
H	2.32353401	-0.88388832	3.09368005
H	-0.00026470	2.57902749	0.41561847
C	0.00000000	0.00000000	3.19710964
B	-1.44948370	0.46943530	0.92966142
C	0.03802531	-0.05278454	-1.59813744
O	-0.81998566	0.81926942	-2.18044962
O	0.74666755	-0.77647408	-2.25888270
H	-0.70125576	0.70479184	-3.13774956

1-SH-*o*-carborane: B3LYP-D3(BJ)

H	-1.46703333	1.98407301	3.12140909
B	0.88507512	-1.22875758	0.91872509
H	1.47842652	-2.16723758	0.52486033
C	0.00000000	0.00000000	3.24948926
S	-0.09410610	-0.15976527	5.03551996
H	-2.31674982	-0.88465344	3.09915629
C	0.00000000	-1.39634432	2.34351442
B	-0.88300683	1.21753256	2.44642091
B	1.43952058	-0.48460353	2.43434028
H	2.32079567	-0.90232958	3.09157072
B	1.44908070	0.45457747	0.94734281
H	2.47768322	0.76338892	0.45751393
B	0.00000000	0.00000000	0.00000000
H	0.00115211	-0.01323904	-1.18030538
B	-0.88910740	-1.22351820	0.92305603
H	-1.49004519	-2.15744168	0.53064897
B	0.89209734	1.20864275	2.45209721
H	1.48603252	1.97247475	3.12336315
B	0.00605949	1.50415838	0.94242050
B	-1.44403148	0.46464319	0.94605034
H	-2.47051307	0.77683756	0.45472268
B	-1.43691081	-0.47132475	2.43772501
H	0.01287857	2.57569718	0.44711965
H	-0.00560170	-2.30349658	2.92693241
H	1.22904349	-0.03952196	5.24708043

1-SH-*o*-carborane: M06

H	-1.46976310	1.97205936	3.11854436
B	0.88146811	-1.22335196	0.92048310
H	1.47725803	-2.16290847	0.53686220
C	0.00000000	0.00000000	3.22779992
S	-0.06864134	-0.15621739	5.00971474
H	-2.30181259	-0.88512319	3.10490017
C	0.00000000	-1.38107691	2.34091402
B	-0.88356115	1.21376606	2.43617926
B	1.42860600	-0.47924717	2.43038820

H	2.30443349	-0.89357888	3.09635563
B	1.43967633	0.45714351	0.94186003
H	2.46931553	0.76464379	0.45703073
B	0.00000000	0.00000000	0.00000000
H	0.00198518	-0.01920981	-1.17895928
B	-0.88385448	-1.22102945	0.92376990
H	-1.48334320	-2.15759160	0.53895933
B	0.88242580	1.20848355	2.44236020
H	1.47131819	1.96587810	3.12551152
B	0.00223223	1.49991847	0.93429003
B	-1.43818991	0.46145350	0.93898880
H	-2.46546003	0.76765821	0.44858197
B	-1.42853459	-0.47107991	2.43518588
H	0.00645031	2.57071536	0.44006987
H	-0.00285906	-2.28516227	2.93321762
H	1.24920881	0.04017991	5.19702423

1-SH-*o*-carborane: PBE-D3(BJ)

H	-1.47580952	1.98916409	3.13462606
B	0.88610660	-1.23086361	0.91945709
H	1.48847252	-2.17572684	0.51974688
C	0.00000000	0.00000000	3.25778645
S	-0.09333536	-0.16277901	5.04468347
H	-2.32424483	-0.89139671	3.11672217
C	0.00000000	-1.40335955	2.34522225
B	-0.88472687	1.21688172	2.45123340
B	1.44095463	-0.48592687	2.43783795
H	2.33232207	-0.90921952	3.10069783
B	1.44895786	0.45605979	0.94597756
H	2.48910270	0.76641087	0.45431956
B	0.00000000	0.00000000	0.00000000
H	-0.00091630	-0.01595574	-1.19127605
B	-0.89035851	-1.22636133	0.92395099
H	-1.49809767	-2.17045240	0.53093454
B	0.89285271	1.20960551	2.45527967
H	1.49340457	1.97901532	3.13481768
B	0.00499907	1.50556895	0.94438205
B	-1.44522545	0.46457002	0.94757534
H	-2.48465147	0.77662340	0.45650861
B	-1.43858696	-0.47517612	2.44348057

H	0.00924554	2.58960523	0.44936059
H	-0.00218993	-2.31691432	2.93614907
H	1.24458882	-0.04961020	5.24167005

1-SH-*o*-carborane: PBE0

H	-1.46547253	1.98728095	3.12645333
B	0.88302591	-1.22590249	0.92338379
H	1.47693198	-2.17366588	0.53563794
C	0.00000000	0.00000000	3.24238499
S	-0.10124629	-0.16028449	5.01927978
H	-2.31402810	-0.88300649	3.10883644
C	0.00000000	-1.38265489	2.34829191
B	-0.88119488	1.21886468	2.44318886
B	1.43725380	-0.47971921	2.43381998
H	2.32008892	-0.90042646	3.09815257
B	1.44699156	0.45658424	0.94350656
H	2.48157443	0.76464033	0.45272320
B	0.00000000	0.00000000	0.00000000
H	0.00063355	-0.01867510	-1.18576957
B	-0.88731189	-1.22080074	0.92763772
H	-1.48903264	-2.16430626	0.54210576
B	0.89007926	1.20988561	2.44894303
H	1.48541580	1.97658117	3.12632555
B	0.00623070	1.50426344	0.93823220
B	-1.44193914	0.46637459	0.94280462
H	-2.47510986	0.77755805	0.45166483
B	-1.43478416	-0.46632704	2.43763271
H	0.01264738	2.58099762	0.44079221
H	-0.00515481	-2.29094108	2.93423725
H	1.22022649	-0.03404832	5.23465768

9-SH-*o*-carborane: B3LYP-D3(BJ)

H	-2.46069026	0.76796958	0.43184973
H	2.46648409	0.77270513	0.43901747
H	1.47345868	-2.16363000	0.53419719
B	0.00334154	1.51000092	0.95325921
B	0.88885635	1.21405213	2.45652624
H	1.47907585	1.98156489	3.12738084

H	-1.48111842	1.98295120	3.11886468
H	-2.32934635	-0.88183866	3.10031576
H	0.00026434	-0.10801659	4.29802764
H	-1.46714081	-2.16894504	0.53462180
H	0.00375331	-2.29248248	2.94244547
B	-0.88608183	-1.22951712	0.94132724
C	0.00000000	-1.37749463	2.37198403
B	0.00000000	0.00000000	0.00000000
B	1.45279501	-0.46744577	2.43497612
B	0.88627413	-1.22525149	0.93689947
B	-0.88855446	1.21526174	2.45079255
B	-1.45049324	-0.47081810	2.43649024
B	1.44610699	0.46559562	0.94590610
H	2.33072308	-0.88175127	3.09831731
H	0.00183892	2.57051691	0.43790124
C	0.00000000	0.00000000	3.22547536
B	-1.44291725	0.45869817	0.94246136
S	-0.09365405	0.00118882	-1.86263987
H	1.18545127	-0.35325576	-2.07747632

9-SH-*o*-carborane: M06

H	-2.45875233	0.76708493	0.43474690
H	2.45403478	0.75951070	0.42933997
H	1.46589072	-2.16511815	0.53876574
B	-0.00368721	1.50437459	0.94504352
B	0.88335268	1.21258989	2.44171290
H	1.47735821	1.97562472	3.11185266
H	-1.47326751	1.97578892	3.12099316
H	-2.31602610	-0.87949121	3.09769226
H	0.00186212	-0.10633936	4.28568794
H	-1.46916957	-2.16028699	0.53826748
H	-0.00491555	-2.28270240	2.93932465
B	-0.88226219	-1.22119245	0.93579360
C	0.00000000	-1.36813945	2.36510652
B	0.00000000	0.00000000	0.00000000
B	1.43608949	-0.47039619	2.43686197
B	0.88192946	-1.22642250	0.94053171
B	-0.88319929	1.21243246	2.44774437
B	-1.43960753	-0.46727934	2.43374922
B	1.43373438	0.45637468	0.93877067

H	2.31477153	-0.87999005	3.09944097
H	-0.00326669	2.56466303	0.42928427
C	0.00000000	0.00000000	3.21135412
B	-1.43890149	0.46325332	0.94187332
S	-0.03330198	-0.04881697	-1.86130912
H	1.21638311	0.42281124	-2.01316924

9-SH-*o*-carborane: PBE-D3(BJ)

H	-2.47394779	0.76792566	0.43718598
H	2.47953473	0.77480864	0.44451609
H	1.48404486	-2.17469395	0.54208198
B	0.00223772	1.51115667	0.95851295
B	0.88989588	1.21566116	2.46586740
H	1.48676857	1.98806765	3.14567070
H	-1.49183418	1.98922516	3.13363464
H	-2.33898621	-0.88849960	3.11550976
H	-0.00088062	-0.10862903	4.32136117
H	-1.47743177	-2.18106603	0.53984249
H	0.00449947	-2.30535667	2.95797188
B	-0.88806773	-1.23250322	0.94711350
C	0.00000000	-1.38292825	2.38158696
B	0.00000000	0.00000000	0.00000000
B	1.45279299	-0.46778753	2.44561618
B	0.88752378	-1.22731589	0.94438305
B	-0.88958903	1.21547718	2.46030447
B	-1.45098841	-0.47372809	2.44507756
B	1.44670273	0.46677899	0.95234548
H	2.34011721	-0.88697318	3.11449144
H	0.00064518	2.58305394	0.44041121
C	0.00000000	0.00000000	3.23959505
B	-1.44283508	0.45878007	0.94767359
S	-0.09427131	-0.00827739	-1.86106495
H	1.19093887	-0.39196719	-2.05609664

9-SH-*o*-carborane: PBE0

H	-2.46609138	0.76901244	0.43758797
H	2.47365079	0.77192919	0.44534824

H	1.47467441	-2.17141062	0.55042908
B	0.00378763	1.51048453	0.95563863
B	0.88746016	1.21341219	2.46028473
H	1.47908072	1.98178466	3.13889058
H	-1.47930344	1.98470215	3.12996893
H	-2.32543450	-0.88189171	3.11258169
H	0.00008447	-0.10779372	4.29926803
H	-1.47004549	-2.17404804	0.54846000
H	0.00307355	-2.28514801	2.95008258
B	-0.88501724	-1.22718199	0.94886185
C	0.00000000	-1.36901282	2.37720548
B	0.00000000	0.00000000	0.00000000
B	1.44813430	-0.46580597	2.44036356
B	0.88472319	-1.22406073	0.94477615
B	-0.88566831	1.21556695	2.45439274
B	-1.44555068	-0.46740516	2.44206180
B	1.44483258	0.46546401	0.94915962
H	2.32651487	-0.88353833	3.11120781
H	0.00356462	2.57772488	0.44078704
C	0.00000000	0.00000000	3.22435918
B	-1.44082495	0.46053855	0.94658662
S	-0.10320019	-0.00456946	-1.85715660
H	1.18261909	-0.32908450	-2.07350388

1-SH-*m*-carborane: B3LYP-D3(BJ)

H	-2.38555720	0.76334501	3.06835952
B	1.43996603	-0.46546218	0.92799391
H	2.38924796	-0.91399409	0.39414802
C	0.00000000	0.00000000	3.23778383
S	-0.04856247	-0.07593329	5.04495297
H	-1.41908477	-2.08253668	2.99786010
B	0.89355352	-1.20781444	2.42661421
B	-1.44410139	0.48003848	2.42239131
B	1.44078407	0.46354178	2.42929463
H	2.38716895	0.74797192	3.07028299
B	0.89458442	1.22276198	0.92220495
H	1.53274916	2.06908953	0.40344441
B	0.00000000	0.00000000	0.00000000
H	-0.00193536	-0.14580162	-1.16893777

C	0.00000000	-1.37504872	1.01017144
H	-0.00717036	-2.35121407	0.54989034
B	-0.00134395	1.51136769	2.41931623
H	0.00532069	2.49627051	3.06507320
B	-0.89054033	1.22578736	0.91244042
B	-1.44203440	-0.45896182	0.93383126
H	-2.39048073	-0.91062872	0.40178924
B	-0.88918095	-1.19602222	2.43741111
H	-1.52018605	2.07408976	0.38775373
H	1.41857222	-2.09474336	2.98816882
H	0.94081050	0.81476154	5.23174153

1-SH-*m*-carborane: M06

H	-2.37867030	0.74934875	3.06843454
B	1.43072321	-0.46477615	0.92195927
H	2.37979320	-0.91481092	0.39248942
C	0.00000000	0.00000000	3.22081129
S	-0.02194812	-0.08541011	5.02094212
H	-1.41621139	-2.07791141	2.99403521
B	0.88727491	-1.20621628	2.41887907
B	-1.43813228	0.47360480	2.41871647
B	1.43299278	0.46023135	2.42603302
H	2.37522208	0.73666436	3.07535247
B	0.88962240	1.21847050	0.92526364
H	1.52813670	2.06534037	0.41132441
B	0.00000000	0.00000000	0.00000000
H	0.00044346	-0.14450287	-1.16771256
C	0.00000000	-1.36497935	1.00581910
H	-0.00395828	-2.34257707	0.54541853
B	-0.00343444	1.50028995	2.42353763
H	-0.00062151	2.48018596	3.07796967
B	-0.88709252	1.22022904	0.91616350
B	-1.43267176	-0.46057721	0.92649083
H	-2.38053164	-0.91380653	0.39745889
B	-0.88433604	-1.19520002	2.43009565
H	-1.51835038	2.06841000	0.39570981
H	1.41162871	-2.09223731	2.98190443
H	0.65931766	1.06114095	5.19347957

1-SH-mCB-PBE-D3(BJ)

H	-2.39660812	0.76507190	3.08106130
B	1.44063626	-0.46700879	0.92941706
H	2.40110203	-0.91975517	0.39388311
C	0.00000000	0.00000000	3.24706183
S	-0.05604076	-0.08230019	5.05473987
H	-1.42815216	-2.09384255	3.00819109
B	0.89267198	-1.21241876	2.43240087
B	-1.44485861	0.48173133	2.42870329
B	1.44144553	0.46430124	2.43596717
H	2.39914802	0.74619323	3.08339273
B	0.89600877	1.22393618	0.92756477
H	1.54296252	2.07665759	0.40469910
B	0.00000000	0.00000000	0.00000000
H	-0.00208722	-0.14619296	-1.18014090
C	0.00000000	-1.37767243	1.01044025
H	-0.00790154	-2.36285938	0.54775303
B	-0.00065187	1.51464499	2.42773063
H	0.00462315	2.50828707	3.08166496
B	-0.88960762	1.22773936	0.91728094
B	-1.44262045	-0.45927410	0.93630256
H	-2.40257981	-0.91335347	0.40175495
B	-0.89064566	-1.19982103	2.44190642
H	-1.52704939	2.08309750	0.38784384
H	1.42520276	-2.10682832	3.00088712
H	0.95266546	0.80476191	5.23514853

1-SH-*m*-carborane: PBE0

H	-2.38545701	0.76170017	3.07461070
B	1.43628799	-0.46518090	0.92577295
H	2.38982029	-0.91816388	0.39105992
C	0.00000000	0.00000000	3.23438449
S	-0.05380207	-0.08462649	5.03046266
H	-1.41791329	-2.08724396	2.99645251
B	0.88948647	-1.20733226	2.42378466
B	-1.43974261	0.47915893	2.42381803
B	1.43706120	0.46348715	2.43035929
H	2.38935750	0.74473326	3.07509164
B	0.89369317	1.22306881	0.92313585

H	1.53651185	2.07223935	0.40264416
B	0.00000000	0.00000000	0.00000000
H	-0.00281615	-0.14774791	-1.17419045
C	0.00000000	-1.36982570	1.00782005
H	-0.00701558	-2.34823441	0.54730822
B	-0.00081962	1.50941916	2.42212528
H	0.00371208	2.49759634	3.07382785
B	-0.88906848	1.22642733	0.91452954
B	-1.43808184	-0.45932285	0.93256642
H	-2.39152861	-0.91386501	0.39986154
B	-0.88636246	-1.19536274	2.43390154
H	-1.52433551	2.07806481	0.38945504
H	1.41740857	-2.09947685	2.98689283
H	0.93615840	0.80298584	5.22247566

9-SH-*m*-carborane: B3LYP-D3(BJ)

H	-1.57157562	-2.07080450	0.50994543
H	0.00572179	2.57465831	0.43741465
H	2.49430170	0.71950788	0.52282680
B	-1.42511169	0.47256613	0.95709711
B	-0.87799868	1.22279623	2.46971211
H	-1.57037327	1.97757379	3.05061780
H	-2.21055640	-0.74026671	2.88343570
H	-0.00669333	-2.51885777	3.04456339
H	-0.00121323	-0.10340337	4.55344059
H	1.57778104	-2.07860503	0.51647023
H	2.20783336	-0.74484372	2.89712680
B	0.88871820	-1.22839357	0.94874710
C	1.29907879	-0.43884559	2.40265036
B	0.00000000	0.00000000	0.00000000
B	0.88713541	1.21892756	2.46201100
B	1.42855735	0.45795495	0.95115620
C	-1.30003705	-0.43044040	2.39398368
B	0.00000000	-1.51267820	2.43827809
B	0.00137809	1.51493751	0.95579353
H	1.58357310	1.97002732	3.04284275
H	-2.48725771	0.73296449	0.52290693
B	0.00000000	0.00000000	3.38314967
B	-0.87952159	-1.22156352	0.94018033
S	-0.06262747	-0.08231753	-1.86237736

H	0.70142749	1.00241390	-2.07884898

9-SH-*m*-carborane: M06

H	-1.56859196	-2.07098456	0.51181710
H	-0.00018361	2.56101327	0.42054892
H	2.48766411	0.71622467	0.51203322
B	-1.42731134	0.46587334	0.95036799
B	-0.88069285	1.21445428	2.45538024
H	-1.57137382	1.96631110	3.03891084
H	-2.20334809	-0.73554469	2.87446334
H	-0.00452575	-2.50649631	3.04238490
H	-0.00048508	-0.10108464	4.53612883
H	1.57328648	-2.07592185	0.51776110
H	2.20162877	-0.73813041	2.88119316
B	0.88646303	-1.22337501	0.94661226
C	1.29163234	-0.43194417	2.38539741
B	0.00000000	0.00000000	0.00000000
B	0.88295529	1.21344108	2.44693031
B	1.42413916	0.45546494	0.94473975
C	-1.29403286	-0.42628729	2.37949898
B	0.00000000	-1.50365672	2.43321721
B	-0.00321455	1.50552820	0.94650946
H	1.57643082	1.96526296	3.02735649
H	-2.48995171	0.72124143	0.51515776
B	0.00000000	0.00000000	3.36723268
B	-0.87953032	-1.21758691	0.93758088
S	-0.02879705	-0.04648838	-1.85888290
H	0.75375454	1.03601548	-2.01392430

9-SH-*m*-carborane: PBE-D3(BJ)

H	-1.57659526	-2.08545007	0.51661581
H	0.00552912	2.58709276	0.43944215
H	2.50877258	0.72514343	0.52597042
B	-1.42937110	0.47277853	0.96277503
B	-0.88143377	1.22450795	2.47656068
H	-1.57771034	1.98759393	3.06547551
H	-2.22159331	-0.74319343	2.89701371

H	-0.00725823	-2.53069151	3.06045335
H	-0.00150146	-0.10136363	4.57748879
H	1.58411414	-2.09170012	0.52268252
H	2.21708737	-0.74599670	2.91329211
B	0.89135678	-1.22953979	0.95725506
C	1.30229581	-0.43755747	2.41100025
B	0.00000000	0.00000000	0.00000000
B	0.88805496	1.22110178	2.46830684
B	1.43250269	0.45916368	0.95791735
C	-1.30490002	-0.42935133	2.40145873
B	0.00000000	-1.51337970	2.44972418
B	0.00094167	1.51645026	0.96164320
H	1.58748464	1.98163208	3.05696504
H	-2.50144317	0.73619527	0.52256812
B	0.00000000	0.00000000	3.39464981
B	-0.88186575	-1.22290483	0.94864959
S	-0.06125182	-0.08953850	-1.86133636
H	0.72940635	0.99193999	-2.06477271

9-SH-*m*-carborane: PBE0

H	-1.57529459	-2.07609894	0.52108725
H	0.00526913	2.58096977	0.44126526
H	2.50180141	0.72207795	0.53169435
B	-1.42604521	0.47098237	0.96244403
B	-0.87949197	1.22039508	2.47149518
H	-1.57441939	1.97735050	3.05802801
H	-2.20891933	-0.73865622	2.88693660
H	-0.00616473	-2.51778330	3.05339601
H	-0.00028666	-0.10381443	4.56022199
H	1.58117528	-2.08325005	0.52676555
H	2.20632652	-0.74172639	2.89947277
B	0.88899027	-1.22560208	0.95519901
C	1.29645159	-0.43489015	2.40266638
B	0.00000000	0.00000000	0.00000000
B	0.88644384	1.21688674	2.46398158
B	1.42858572	0.45853009	0.95643741
C	-1.29731612	-0.42741236	2.39572154
B	0.00000000	-1.50703812	2.44366662
B	0.00094116	1.51424220	0.95843963
H	1.58477930	1.97078478	3.05041350

H	-2.49579906	0.73081789	0.53027180
B	0.00000000	0.00000000	3.38409014
B	-0.88015830	-1.21934407	0.94782892
S	-0.06573282	-0.09467828	-1.85662868
H	0.68573657	0.99650344	-2.07767882

***o*-carborane: B3LYP-D3(BJ)**

C	0.00000000	0.00000000	3.21487885
B	0.00000000	0.00000000	0.00000000
H	-0.00054870	-0.01883287	-1.18023879
B	-1.45096818	-0.46736207	2.42902843
H	-2.32521836	-0.88383818	3.09614526
H	0.00124647	-0.10943722	4.28740257
B	-1.44821965	0.46263350	0.93670728
H	-2.47163758	0.77251534	0.43787821
B	-0.88918467	-1.22264826	0.92620728
H	-1.47452253	-2.16618967	0.53251908
B	0.88974034	-1.22261621	0.92699932
H	1.47645189	-2.16500969	0.53269412
B	1.44785199	0.46314056	0.93691750
H	2.47004952	0.77594641	0.43676375
B	-0.00101216	1.50843268	0.93957368
H	-0.00196119	2.57690963	0.43775936
C	0.00000000	-1.37859970	2.35629795
H	0.00106336	-2.29345076	2.92662408
B	1.45133921	-0.46708384	2.42945503
B	0.88894429	1.21525912	2.44549223
H	-1.47527775	1.98272597	3.11979328
B	-0.88965966	1.21470707	2.44536701
H	2.32717707	-0.88206318	3.09572458
H	1.47398403	1.98524786	3.11821463

***o*-carborane: M06**

C	0.00000000	0.00000000	3.20103153
B	0.00000000	0.00000000	0.00000000
H	0.00074495	-0.02420238	-1.17894806
B	-1.43895485	-0.46759677	2.42845760

H	-2.31148250	-0.88278861	3.09617647
H	0.00053809	-0.11048808	4.27509091
B	-1.44003246	0.46095579	0.93390843
H	-2.46523317	0.76778716	0.43978143
B	-0.88420062	-1.21936180	0.92682756
H	-1.47130228	-2.16314832	0.54062818
B	0.88471702	-1.21895882	0.92699941
H	1.47238445	-2.16236885	0.54058276
B	1.43993020	0.46142191	0.93383097
H	2.46460050	0.76898871	0.43904358
B	-0.00061623	1.50275556	0.93367152
H	-0.00114840	2.57047211	0.43317342
C	0.00000000	-1.36712368	2.35168305
H	-0.00121291	-2.28127950	2.92628114
B	1.43872135	-0.46720603	2.42855803
B	0.88423356	1.21198535	2.43734997
H	-1.47239459	1.97570521	3.11200542
B	-0.88471354	1.21148208	2.43734329
H	2.31132156	-0.88144021	3.09674034
H	1.47130079	1.97634600	3.11242896

***o*-carborane: PBE-D3(BJ)**

C	0.00000000	0.00000000	3.22382471
B	0.00000000	0.00000000	0.00000000
H	-0.00036805	-0.02281436	-1.19106066
B	-1.45378184	-0.46991381	2.43455265
H	-2.33721405	-0.89043986	3.10762040
H	0.00060735	-0.11050345	4.30524003
B	-1.44811594	0.46350972	0.93745627
H	-2.48224118	0.77569476	0.43614575
B	-0.88977568	-1.22489569	0.92864600
H	-1.48254159	-2.17720918	0.53312723
B	0.89098786	-1.22435740	0.92832214
H	1.48413809	-2.17616458	0.53188702
B	1.44945108	0.46442891	0.93800843
H	2.48373575	0.77779797	0.43724944
B	-0.00075935	1.51024856	0.94138202
H	-0.00179905	2.59004373	0.43816771
C	0.00000000	-1.38440103	2.36081766
H	0.00069856	-2.30700032	2.93565609

B	1.45251183	-0.46921007	2.43542004
B	0.88939559	1.21609967	2.45009493
H	-1.48473005	1.98862270	3.13094208
B	-0.89123150	1.21456699	2.45046416
H	2.33603381	-0.88870304	3.10920571
H	1.48095327	1.99174712	3.13077902

***o*-carborane: PBE0**

C	0.00000000	0.00000000	3.20890406
B	0.00000000	0.00000000	0.00000000
H	-0.00074381	-0.02229572	-1.18585054
B	-1.44704714	-0.46614620	2.42997550
H	-2.32203424	-0.88623623	3.10424220
H	0.00111040	-0.10957453	4.28371463
B	-1.44654900	0.46363339	0.93562105
H	-2.47644482	0.77377191	0.43698298
B	-0.88712238	-1.22098631	0.92931949
H	-1.47431943	-2.17223609	0.53985720
B	0.88797928	-1.22060147	0.92933448
H	1.47646211	-2.17061242	0.53867089
B	1.44656230	0.46456254	0.93579027
H	2.47585255	0.77619257	0.43625913
B	-0.00051641	1.50841300	0.93832111
H	-0.00177612	2.58248309	0.43528438
C	0.00000000	-1.37008804	2.35678773
H	0.00125331	-2.28612454	2.92953317
B	1.44708261	-0.46525046	2.43036638
B	0.88695198	1.21490029	2.44415881
H	-1.47616349	1.98287339	3.12548216
B	-0.88800843	1.21393165	2.44444951
H	2.32365091	-0.88342040	3.10385043
H	1.47383656	1.98577260	3.12436625

***m*-carborane: B3LYP-D3(BJ)**

H	-2.38999972	0.75290851	3.06617721
B	1.44163292	-0.46381755	0.93018599
H	2.39023623	-0.91215370	0.39468212
C	0.00000000	0.00000000	3.21366399

H	0.00036591	-0.01328029	4.29269884
H	-1.42297387	-2.09264783	2.98638579
B	0.89138030	-1.20288809	2.43237530
B	-1.44194974	0.47080303	2.42657234
B	1.44146529	0.47090552	2.42755957
H	2.38954498	0.75504408	3.06610033
B	0.89306729	1.22462188	0.91629307
H	1.52664894	2.06936710	0.38935562
B	0.00000000	0.00000000	0.00000000
H	-0.00093823	-0.14445494	-1.16943638
C	0.00000000	-1.37812426	1.00791688
H	-0.00086503	-2.35314111	0.54535567
B	0.00014819	1.51052914	2.41804609
H	0.00213266	2.49770193	3.06152420
B	-0.89371425	1.22445650	0.91561803
B	-1.44145901	-0.46401686	0.92929741
H	-2.38974398	-0.91282191	0.39390393
B	-0.89046906	-1.20363818	2.43184740
H	-1.52703893	2.06876211	0.38849801
H	1.42447824	-2.09070642	2.98777774

_m_-carborane: M06

H	2.37832855	-0.91490820	0.39240847
B	-1.43190391	0.46825575	2.42490848
H	-2.37836550	0.74769838	3.06566674
C	0.00000000	-1.36466671	1.00308008
H	0.00056326	-2.34004226	0.53884301
H	1.41699610	-2.09018194	2.97531526
B	-0.88405509	-1.20130980	2.42479717
B	1.43261958	-0.46226535	0.92592830
B	-1.43182960	-0.46410367	0.92686204
H	-2.37878281	-0.91398037	0.39299100
B	-0.88857527	1.22009602	0.91836871
H	-1.52372113	2.06386446	0.39482960
B	0.00007385	1.50407057	2.41895516
H	-0.00008312	2.48687610	3.06668363
C	0.00000000	0.00000000	3.19967038
H	-0.00070700	-0.01570111	4.27999280
B	0.00000000	0.00000000	0.00000000
H	-0.00133684	-0.14538150	-1.16794051

B	0.88799114	1.22071781	0.91849423
B	1.43239031	0.46828830	2.42458792
H	2.37893492	0.74708007	3.06540681
B	0.88475280	-1.20157306	2.42298660
H	1.52195310	2.06414690	0.39308928
H	-1.41398852	-2.09127039	2.97693788

***m*-carborane: PBE-D3(BJ)**

H	-2.40200060	0.75460880	3.07690297
B	1.44255716	-0.46452439	0.93222988
H	2.40177206	-0.91714601	0.39444475
C	0.00000000	0.00000000	3.22228044
H	0.00006304	-0.01560663	4.31040828
H	-1.43136887	-2.10395949	2.99578717
B	0.89086447	-1.20589105	2.43818904
B	-1.44316549	0.47196867	2.43285835
B	1.44160998	0.47212328	2.43351191
H	2.40038068	0.75650225	3.07690379
B	0.89362955	1.22583725	0.92105240
H	1.53535268	2.07722959	0.38998404
B	0.00000000	0.00000000	0.00000000
H	-0.00021712	-0.14564467	-1.18062900
C	0.00000000	-1.38017569	1.00896081
H	-0.00059056	-2.36407916	0.54397165
B	-0.00016714	1.51317881	2.42621711
H	0.00085243	2.50970988	3.07587039
B	-0.89333073	1.22549208	0.92020221
B	-1.44212866	-0.46467192	0.93171425
H	-2.40067495	-0.91723615	0.39289775
B	-0.89170159	-1.20669701	2.43692272
H	-1.53396118	2.07705661	0.38833273
H	1.43005151	-2.10189337	2.99912233

***m*-carborane: PBE0**

H	-2.39008732	0.75129543	3.07189256
B	1.43794911	-0.46343780	0.92853936
H	2.39066418	-0.91629877	0.39106955
C	0.00000000	0.00000000	3.20822178

H	0.00035730	-0.01575456	4.28927785
H	-1.42137781	-2.09633926	2.98592054
B	0.88756254	-1.20184331	2.42898753
B	-1.43811869	0.47003248	2.42680897
B	1.43735742	0.47015069	2.42763206
H	2.38955851	0.75293059	3.07152659
B	0.89185606	1.22425068	0.91713336
H	1.53025067	2.07234578	0.38854191
B	0.00000000	0.00000000	0.00000000
H	-0.00069265	-0.14719304	-1.17502437
C	0.00000000	-1.37228033	1.00647220
H	-0.00047554	-2.34945823	0.54367226
B	0.00003412	1.50783325	2.41981234
H	0.00094206	2.49756784	3.07019963
B	-0.89229567	1.22415194	0.91690052
B	-1.43776512	-0.46406399	0.92828854
H	-2.39019621	-0.91743438	0.39117592
B	-0.88742684	-1.20194387	2.42880420
H	-1.53048714	2.07264512	0.38886766
H	1.42119826	-2.09560897	2.98698531

Table B.3: Cartesian coordinates for all simulated carboranes as calculated by density functional theory using B3LYP-D3(BJ), M06, PBE-D3(BJ), and PBE0.

B.4: Schematics of Carborane Molecule Examples

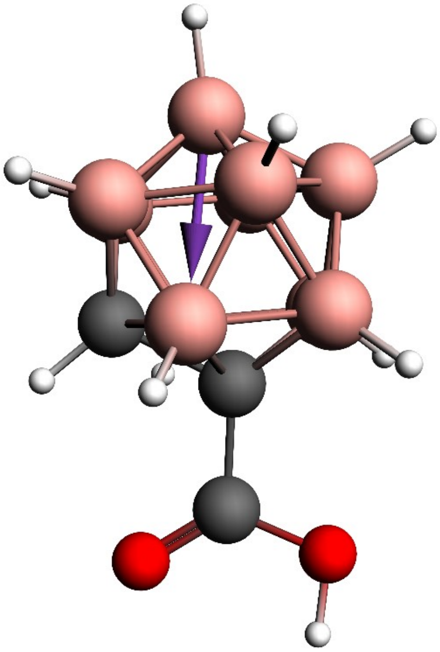

Figure B.9: Schematic of 1-COOH-*o*-carborane, with boron, carbon, oxygen, and hydrogen depicted in pink, grey, red, and white, respectively. Dipole orientation depicted with purple arrow.

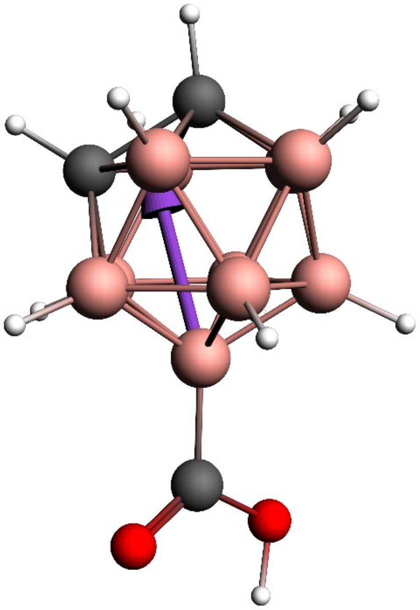

Figure B.10: Schematic of 9-COOH-*o*-carborane, with boron, carbon, oxygen, and hydrogen depicted in pink, grey, red, and white, respectively. Dipole orientation depicted with purple arrow.

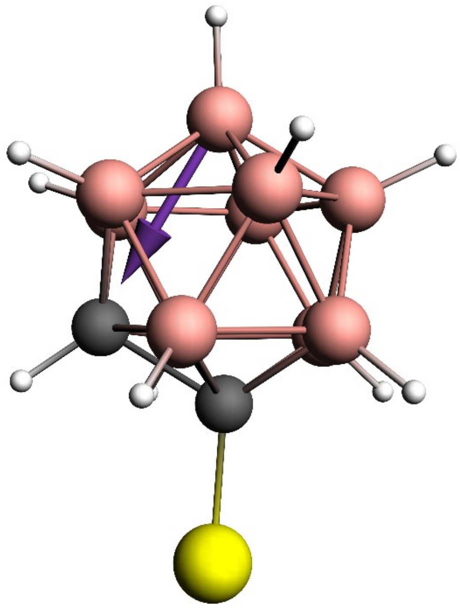

Figure B.11: Schematic of 1-SH-*o*-carborane, with boron, carbon, sulfur, and hydrogen depicted in pink, grey, yellow, and white, respectively. Dipole orientation depicted with purple arrow.

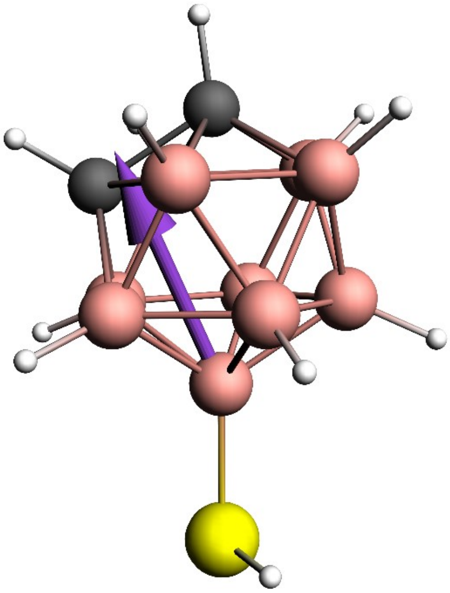

Figure B.12: Schematic of 9-SH-*o*-carborane, with boron, carbon, sulfur, and hydrogen depicted in pink, grey, yellow, and white, respectively. Dipole orientation depicted with purple arrow.

B.5: References

(1) Kasar, R. A.; Knudsen, G. M.; Kahl, S. B. Synthesis of 3-Amino-1-carboxy-*o*-carborane and an Improved, General Method for the Synthesis of All Three C-Amino-C-Carboxycarboranes. *Inorg. Chem.* **1999**, *38*, 2936-2940.

(2) Craciun, L.; Custelcean, R. Syntheses and Crystal Structures of 9-Acetyl- and 9-Cyano-1,2-dicarbadodecaborane: Supramolecular Association in Carboranyl C-H Hydrogen-Bonded α-Networks. *Inorg. Chem.* **1999,** *38,* 4916-4919.

(3) Zakharkin, L. I.; Kovredov, A. I.; Olshevskaya, V. A.; Shaugumbekova, Z. S. Synthesis of B-Organo-substituted 1,2-, 1,7-, and 1,12-Dicarbaclosododecaboranes(12). *J. Organomet. Chem*. **1982**, *226*, 217-222.

(4) Dziedzic, R.; Saleh, L.; Axtell, J.; Martin, J.; Stevens, S.; Royappa, A.; Rheingold, A.; Spokoyny, A. M. B-N, B-O, and B-CN Bond Formation via Palladium-Catalyzed Cross-Coupling of B-Bromo-Carboranes. *J. Am. Chem. Soc.* **2016**, *138*, 9081-9084.

(5) Plesěk, J.; Janousěk, Z.; Herm̆ańek, S. Synthesis and Properties of Some Icosahedral Carborane B,B'-Dithiols. *Collect. Czech. Chem. Commun.* **1980**, *45*, 1775−1779.

(6) Spokoyny, A. M.; Machan, C. W.; Clingerman, D. J.; Rosen, M. S.; Wiester, M. J.; Kennedy, R. D.; Stern, C. L.; Sarjeant, A. A.; Mirkin, C. A. A Coordination Chemistry Dichotomy for Icosahedral Carborane-Based Ligands. *Nat. Chem.* **2011**, *3*, 590−596.

(7) Velde, G. te; Bickelhaupt, F. M.; Baerends, E. J.; Fonseca Guerra, C.; van Gisbergen, S. J. A.; Snijders, J. G.; Ziegler, T. Chemistry with ADF. *J. Comput. Chem.* **2001**, *22*, 931-967.

(8) Fonseca Guerra, C.; Snijders, J. G.; te Velde, G.; Baerends, E. J. Towards an Order-N DFT Methods. *Theor. Chem. Acc.* **1998**, *99*, 391-403.

(9) ADF2014, SCM, Theoretical Chemistry, Vrije Universiteit, Amsterdam, The Netherlands, http://www.scm.com.

(10) Grimme, S.; Huenerbein, R.; Ehrlich, S. On the Importance of the Dispersion Energy for the Thermodynamic Stability of Molecules. *ChemPhysChem* **2011**, *12*, 1258-1261.

(11) Perdew, J. P.; Burke, K.; Ernzerhof, M. General Gradient Approximation Made Simple. *Phys. Rev. Lett.* **1996**, *77*, 3865-3868.

(12) Lee, C.; Wang, W.; Parr, R. G. Development of the Colle-Salvetti Correlation-energy Formula into a Functional of the Electron Density. *Phys. Rev. B* **1998**, *37*, 785-789.

(13) Becke, A. D. Density-functional Thermochemistry. III. The Role of Exact Exchange. *J. Chem. Phys.* **1993**, *98*, 5648-5652.

(14) Stephens, P. J.; Devlin, F. J.; Chabalowski, C. F.; Frisch, M. J. *Ab Initio* Calculation of Vibrational Absorption and Circular Dichroism Spectra Using Density Functional Force Fields. *J. Phys. Chem.* **1994**, *98*, 11623-11627.

(15) Adamo, C.; Barone, V. Toward Reliable Density Functional Methods Without Adjustable Parameters: The PBE0 Model. *J. Chem. Phys*. **1999**, *110*, 6158-6170.

(16) Zhao, Y.; Truhlar, D. G. The M06 Suite of Density Functional for Main Group Thermochemistry, Thermochemical Kinetics, Noncovalent Interactions, Excited States, and Transition Elements: Two New Functionals and Systematic Testing of Four M06-class Functionals and 12 Other Functionals. *Theor. Chem. Acc.* **2008**, *120*, 215-241.